

DISS. ETH No. 14379

**A GREEN'S TENSOR APPROACH TO
LIGHT SCATTERING AND PROPAGATION
IN STRATIFIED MEDIA:
THEORY AND APPLICATIONS**

A dissertation submitted to the
SWISS FEDERAL INSTITUTE OF TECHNOLOGY
ZURICH

for the degree of
Doctor of Natural Sciences

presented by
MICHAEL PAULUS
Dipl. Physiker, Universität Augsburg
born October 23, 1971
citizen of Germany

accepted on the recommendation of
Prof. Dr. R. Vahldieck, examiner
Prof. Dr. O. J. F. Martin, co-examiner
Dr. B. Michel, co-examiner

2001

Abstract

An accurate and self-consistent technique is presented for computing the electromagnetic field that propagates and is scattered in structures formed by bodies embedded in a stratified background. The scatterers can be three-dimensional, with a finite extension in all three directions, or two-dimensional, extending infinitely in one direction. The background is composed of an arbitrary number of layers with different permittivities (including complex permittivities for absorbing dielectric media and metals).

This fully vectorial technique is based on the electric field integral equation and utilizes the Green's tensor associated with the multilayered background. The explicit formulas for the computation of the Green's tensor are derived for both three-dimensional and two-dimensional geometries and the practical implementation is discussed in detail. In particular, we show how to efficiently handle the singularities occurring in Sommerfeld integrals, by deforming the integration path in the complex plane. Examples assess the accuracy of this approach and illustrate the physical substance of the Green's tensor, which represents the field radiated by three orthogonal dipoles embedded in the multilayered medium. The advantage of this approach for scattering calculations lies in the fact that only the scatterers must be discretized, the stratified background being accounted for in the Green's tensor. Further, the boundary conditions at the different material interfaces as well as at the edges of the computation window are perfectly and automatically fulfilled.

The Green's tensor technique is then applied to several scattering problems in complex structures. The potential and limitations of light-coupling masks for high-resolution optical contact lithography are discussed by calculating the electric field distribution in the photoresist. The influence of the illumination polarization is studied and the ultimate resolution with a 248 nm illumination wavelength is determined for both isolated and packed structures. In the latter case, crosstalk effects can limit the maximum pattern density. Further, it is shown how a bottom antireflection coating can be used to efficiently suppress in-

terfering backreflections from the substrate. Light-coupling masks are compared with a different contact lithography mask type and optimized mask dimensions are found for which the contrast and the depth of focus are increased. In a second application the interaction of a mode propagating in a planar waveguide with a three-dimensional defect in the structure or a two-dimensional grating on top of the structure is studied. The scattering by the defect disturbs the propagation of the mode and optical energy is coupled out of the waveguide. Similarly, the interaction of a surface plasmon-polariton propagating along a metal-vacuum interface with a dielectric defect is investigated. This illustrates the utilization of the Green's tensor technique for the study of the optics of metals. Our method is then applied to simulate scanning near-field optical microscopy. It is shown that the metal roughness has a dramatic impact on the emission characteristics of an aperture probe and, in particular, on its polarization sensitivity. Finally, numerical experiments of light scattering by a circular dielectric cylinder embedded in a stratified background are presented and the dependence on the illumination angle is discussed.

Zusammenfassung

Die vorliegende Doktorarbeit stellt eine exakte und selbstkonsistente Methode zur Berechnung elektromagnetischer Felder in geschichteten Strukturen vor. Die Felder breiten sich in einem geschichteten Hintergrund aus und streuen an Objekten, die in dem Hintergrund eingeschlossen sind. Die Streukörper können dreidimensional mit endlichen Abmessungen in allen drei Raumrichtungen sein, sie können aber auch zweidimensional sein und sich in eine Richtung unendlich ausdehnen. Der Hintergrund besteht aus einer beliebigen Anzahl von Schichten mit unterschiedlichen Permittivitäten (einschliesslich komplexen Permittivitäten für absorbierende dielektrische Materialien und Metalle).

Die vollständig vektorielle Methode beruht auf einer Volumenintegralgleichung für das elektrische Feld und benutzt den Greenschen Tensor für den geschichteten Hintergrund. Die expliziten Formeln für die Berechnung des Greenschen Tensors werden sowohl für drei- als auch für zweidimensionale Geometrien hergeleitet und ihre praktische Implementierung wird ausführlich diskutiert. Insbesondere zeigen wir, dass die in Sommerfeld–Integralen auftretenden Singularitäten effizient behandelt werden können, indem der Integrationsweg in die komplexe Ebene hinein verlagert wird. Beispiele untermauern die Genauigkeit unserer Methode und veranschaulichen die physikalische Bedeutung des Greenschen Tensors. Er repräsentiert das elektrische Feld, das von drei orthogonalen Dipolen in der geschichteten Struktur erzeugt wird. Der Vorteil dieser Methode für Streurechnungen beruht darauf, dass nur die Streukörper selbst diskretisiert werden müssen, der geschichtete Hintergrund dagegen vom Greenschen Tensor berücksichtigt wird. Weiterhin sind die Randbedingungen sowohl an den einzelnen Materialgrenzen als auch an den Rändern des Berechnungsfensters exakt und automatisch erfüllt.

Die vorgestellte Methode wird dann auf mehrere Streuprobleme in komplexen Strukturen angewandt. Zuerst wenden wir uns den sogenannten “light–coupling masks” zu. Diese Masken für hochauflösende optische Kontaktlithographie werden auf ihr Potential und ihre

Beschränkungen hin untersucht, indem elektrische Feldverteilungen im Photoresist berechnet werden. Wir betrachten den Einfluss der Polarisierung der Belichtung und bestimmen die maximale, mit einer 248 nm Belichtung erreichbare Auflösung sowohl für einzelne als auch für benachbarte Strukturen. Im letzteren Fall können sich die Strukturen gegenseitig beeinflussen und so die maximal erreichbare Packungsdichte begrenzen. Weiterhin zeigen wir, dass man mit einer geeigneten Beschichtung Rückreflexionen vom Substrat effizient unterdrücken kann. Die “light-coupling masks” werden dann mit einem weiteren Maskentyp für Kontaktlithographie verglichen und die Masse der Maske werden so optimiert, dass der Kontrast und die Tiefenschärfe maximal sind. In einer zweiten Anwendung betrachten wir, wie eine elektromagnetische Welle, die sich in einem planaren Wellenleiter ausbreitet, mit einem dreidimensionalen Defekt in der Struktur oder mit einem zweidimensionalen Gitter auf der Struktur wechselwirkt. Die Streuung an dem Defekt stört die Ausbreitung der Welle und optische Energie wird aus dem Wellenleiter ausgekoppelt. Ebenfalls untersuchen wir Oberflächenplasmonen, die sich entlang einer Metall/Vakuum-Grenzschicht ausbreiten und mit einem dielektrischen Defekt wechselwirken. Das veranschaulicht den Nutzen des Greenschen Tensors für die Untersuchung der optischen Eigenschaften von Metallen. Unsere Methode wird weiterhin eingesetzt, um optische Nahfeldmikroskopie zu simulieren. Es stellt sich heraus, dass die Rauhigkeit der metallischen Öffnung einen dramatischen Einfluss auf die Emissionscharakteristik einer Nahfeldsonde besitzt. Betroffen ist dabei insbesondere die Polarisationsempfindlichkeit. Schliesslich führen wir numerische Streuexperimente an einem dielektrischen radial-symmetrischen Zylinder durch, der sich in einem geschichteten Hintergrund befindet. Besondere Aufmerksamkeit gilt dabei der Abhängigkeit vom Einfallswinkel der Beleuchtung.

Contents

| | | |
|----------|--|-----------|
| 1 | Introduction | 1 |
| 1.1 | Motivation and objective of this thesis | 1 |
| 1.2 | Outline | 3 |
| 2 | Scattering calculations with the Green's tensor technique | 5 |
| 2.1 | Electric field integral equation | 6 |
| 2.2 | Discretized equation | 9 |
| 2.3 | Specialization to 2D structures | 11 |
| 3 | The Green's tensor for stratified media | 15 |
| 3.1 | Derivation by plane wave expansion | 15 |
| 3.1.1 | The 3D Green's tensor | 20 |
| 3.1.2 | The 2D Green's tensor | 21 |
| 3.2 | Numerical implementation | 22 |
| 3.2.1 | 3D implementation | 22 |
| | A. Singularities of the integrand | 22 |
| | B. Quadrature of the Sommerfeld type integrals . | 24 |
| 3.2.2 | 2D implementation | 27 |
| 3.3 | Illustrative examples | 28 |
| 3.3.1 | Singularities of the integrand | 28 |
| 3.3.2 | The Green's tensor as a dipole field | 31 |
| 4 | Applications | 35 |
| 4.1 | Light-coupling masks | 35 |
| 4.1.1 | Principle of LCMs | 36 |
| 4.1.2 | Simulation with the Green's tensor technique . . | 38 |
| 4.1.3 | Numerical results | 38 |
| | A. Polarization effects | 39 |
| | B. Resolution limits | 40 |
| | C. Bottom antireflection coating | 42 |
| | D. Contrast mechanisms | 44 |

| | | |
|----------|---|-----------|
| 4.2 | Planar waveguides | 47 |
| 4.2.1 | 3D defect | 47 |
| 4.2.2 | 2D grating coupler | 53 |
| 4.3 | Scattering of surface plasmons | 56 |
| 4.4 | Roughness in SNOM tips | 59 |
| 4.5 | Scattering by a dielectric cylinder | 63 |
| 5 | Conclusion and outlook | 67 |
| | Bibliography | 71 |
| | Acknowledgment | 79 |
| | Résumé | 81 |

Publications

- P1** “Accurate and efficient computation of the Green’s tensor for stratified media,” M. Paulus, P. Gay-Balmaz, and O. J. F. Martin, Phys. Rev. E **62**, 5797–5807 (2000).
- P2** “Light propagation and scattering in stratified media: a Green’s tensor approach,” M. Paulus and O. J. F. Martin, J. Opt. Soc. Am. A **18**, 854–861 (2001).
- P3** “Green’s tensor technique for scattering in 2D stratified media,” M. Paulus and O. J. F. Martin, Phys. Rev. E **63**, 066615 (2001).
- P4** “Near-field distribution in light-coupling masks for contact lithography,” M. Paulus, B. Michel, and O. J. F. Martin, J. Vac. Sci. Technol. B **17**, 3314–3317 (1999).
- P5** “Contrast mechanisms in high-resolution contact lithography: A comparative study,” M. Paulus, H. Schmid, B. Michel, and O. J. F. Martin, Microelectron. Eng. **57–58**, 109–116 (2001).
- P6** “A fully vectorial technique for scattering and propagation in three-dimensional stratified photonic structures,” M. Paulus and O. J. F. Martin, Opt. Quant. Electron. **33**, 315–325 (2001).
- P7** “How to tap an innocent waveguide,” M. Paulus and O. J. F. Martin, Opt. Express **8**, 644–648 (2001).
- P8** “Scattering experiments with a diving cylinder,” M. Paulus and O. J. F. Martin, Opt. Express **9**, 303–311 (2001).

Chapter 1

Introduction

1.1 Motivation and objective of this thesis

According to Moore’s Law the functionalities per chip (bits, transistors) double every 1.5–2 years. Since at the same time the chip size grows only with less than half this speed, the features must shrink tremendously. According to the “International Technology Roadmap for Semiconductors” the DRAM half-pitch will decrease from 150 nm today to 50 nm in 2011 [1].

Because the structures to be printed become smaller than the wavelength of common light sources, this development is a difficult challenge for the lithography process and requires significant technology progresses. Until now, the size reduction has mostly been achieved through the shortening of the wavelength and resolution enhancement technologies like projection lenses with increasing numerical aperture or phase-shifting masks [2]. Currently, the 157 nm technology is being developed using F₂ laser [3], and a strong effort is made for research on “next-generation lithography” (NGL) technologies using extreme ultraviolet light [4], X-rays [5], electron beams [6], or ion beams [7]. All these NGLs are still in the research phase and are expected to incur tremendous development costs. They generally employ principles beyond those currently used in optical lithography and innovations will be required in almost all technology domains (light sources, lenses, masks, resists, …). Hence, the development of low-cost alternatives, which can at least bridge the gap until these NGLs are available for commercial manufacturing, is desirable.

Contact lithography techniques are a very promising approach to high-resolution patterning. In theory, arbitrary small structures can be optically replicated with the evanescent near-field created by apertures in the mask [8, 9]. (The optical replication is even completely avoided with

imprint lithography, where the mask pattern is mechanically transferred to the substrate [10, 11].)

For the design and optimization of a contact mask, a detailed understanding of light propagation in the mask is essential. Geometrically, the mask, the photoresist and the substrate build a stack of planar material layers while openings in the mask define the features to be replicated. However, the interaction of light with subwavelength structures in the presence of a multilayer environment is a very complex topic which is far from being understood for most realistic applications.

There are several further examples where the accurate computation of light scattering from particles embedded in a stratified background is extremely important. Ridges on a multilayered waveguide [12], polarization gratings on a transparent backplane [13], and nanowires deposited on a substrate for surface-enhanced Raman scattering [14] all have in common that dielectric or metallic scatterers are distributed in a medium consisting of several layers with different permittivities.

Analytical solutions of such scattering problems only exist for special configurations. For example, if the system is a bare stratified structure formed only by different material layers stacked together, the light propagation is determined by the transmission matrix [15]. Further analytical or semi-analytical expressions can be derived for very large or very small particles [16]. In the limit $\lambda = 0$, if the characteristic dimensions of the scattering structure are much larger than the illumination wavelength, the interaction with light can be formulated with the laws of geometrical optics. For finite wavelengths, however, simple solutions can only be obtained for the far field, the near-field close to the scattering structure being much more complicated. For large structures, the Kirchhoff approximation provides an integral expression for the far field, whereas small structures are described by the Rayleigh formulas assuming that their response to an incident field is basically dipolar.

However, for the above mentioned structures these approximations are often not practical, because either the dimensions are in the range of the wavelength or the information about the near-field close to the structures is required. In these cases Maxwell's equations must be solved rigorously, taking into account the boundary conditions associated with the geometry. Many useful numerical techniques have already been developed for this task. They include, for example, methods based on beam propagation [17, 18], discrete sources [19, 20], eigenmode expansions [21, 22], finite differences [23], finite elements [24, 25], finite difference time domain [26, 27], ray-tracing [28, 29], transfer matrices [30] or the method of lines [31, 32]. However, most of them strongly depend

on the particular geometry under study. They cannot handle accurately the hybrid geometries encountered in many experimentally relevant situations, where strongly localized structures are combined with semi-infinite substrates.

The objective of this thesis is to present a very general frequency domain technique for scattering calculations where the scatterers are embedded in a background formed by an arbitrary number of layers. It is based on the electric field integral equation, which provides a solution to the vectorial wave equation for the total electric field. The advantage of this approach lies in the fact that only the scatterers must be discretized, the stratified background being accounted for in the corresponding Green's tensor. Further, the boundary conditions at the different material interfaces as well as at the edges of the computation window are perfectly and automatically fulfilled. To make use of these advantages, first the Green's tensor associated with the stratified background must be derived and its numerical computation must be implemented efficiently.

1.2 Outline

This thesis consists basically of two parts. The first part describes in detail the Green's tensor technique for scattering calculations in stratified media and discusses several application examples of this technique. The second part contains a series of publications that were written during this thesis.

In chapter 2 we introduce our formalism for the solution of scattering problems using the Green's tensor. We start with the general three-dimensional case and then particularize the formalism for two-dimensional geometries.

The detailed derivation of the Green's tensor both for two-dimensional and three-dimensional systems is presented in chapter 3. It is obtained by means of a numerical quadrature of so-called Sommerfeld integrals, which represents the core of the computation. We discuss the practical implementation and assess the accuracy of this approach. The physical properties of the Green's tensor are illustrated with several examples.

Having provided the theoretical background, we then apply our technique to the simulation of several scattering systems in chapter 4. The largest part deals with the simulation and optimization of light-coupling masks (LCMs) for optical contact lithography. We explain in section 4.1 the operation principle of LCMs and discuss their usability for high-

resolution subwavelength patterning. Section 4.2 treats the modeling of planar waveguides. The mode propagating in such a layered structure is scattered on a single defect or a grating edged into the waveguide and optical energy is coupled out. Similarly, a plasmon–polariton excited on a metal–dielectric interface strongly interacts with particles on the surface, as investigated in section 4.3. In section 4.4 we focus on the simulation of scanning near–field optical microscopy (SNOM). With an aperture SNOM the evanescent near–field is created by squeezing light through a subwavelength aperture of a metal tip. Modeling the tip as a metallic film with an opening, we investigate how surface roughness affects the performances of a SNOM. As concluding example for our technique, we study in section 4.5 the scattering on a circular dielectric cylinder in a two–layer medium. Interesting effects occur when the cylinder is illuminated with a stationary wave resulting from the reflection of the incident plane wave on the interface.

Finally, we conclude our work in chapter 5 and give an outlook on topics which should be tackled in future work.

Throughout this thesis SI units are used in all formulas. The permittivity and permeability functions ε and μ always refer to the relative values factorizing out the vacuum constants ε_0 and μ_0 . Non–magnetic materials are considered, except in chapter 3, where the formalism is developed for arbitrary permeabilities. Further, harmonic fields with an $\exp(-i\omega t)$ time dependence are assumed throughout.

Chapter 2

Scattering calculations with the Green's tensor technique

As already detailed in the introduction, the accurate computation of the electromagnetic field that propagates and is scattered by bodies distributed in a non-homogeneous background cannot be accomplished with conventional numerical methods. The presence of both infinitely extending interfaces and bodies with a size in the range of the wavelength renders the solution very difficult. We tackle this problem with the Green's tensor technique which provides a general framework for electromagnetic scattering calculations in the frequency domain. It is based on the decomposition of the entire geometry into a background plus embedded scatterers. The Green's tensor associated with this background contains the entire response of the background and assures that the radiation conditions at infinity and the boundary conditions at the interfaces are fulfilled. However, an analytical expression for the Green's tensor exists only for an infinite homogeneous background [33]. For several other configurations the Green's tensor can be found by eigenfunction expansion requiring a numerical computation. For example, one can construct solutions for rectangular or cylindrical waveguides and cavities [34] or for periodic structures [35, 36].

In this work we focus on the case of a planar stratified background. A typical system is shown in figure 2.1. Several scatterers described by the permittivity $\varepsilon(\mathbf{r})$ are embedded in a stratified background composed of L layers with permittivity ε_l , $l = 1, \dots, L$. The scatterers can extend over several layers and need not be homogeneous: $\varepsilon(\mathbf{r})$ can vary inside each scatterer. Further, they can be three-dimensional (3D) with finite extension in all three directions or two-dimensional (2D) extending infinitely in y direction. For convenience, we choose our coordinate system such that the layers are parallel to the xy plane.

In this chapter we study the solution of the scattering problem using

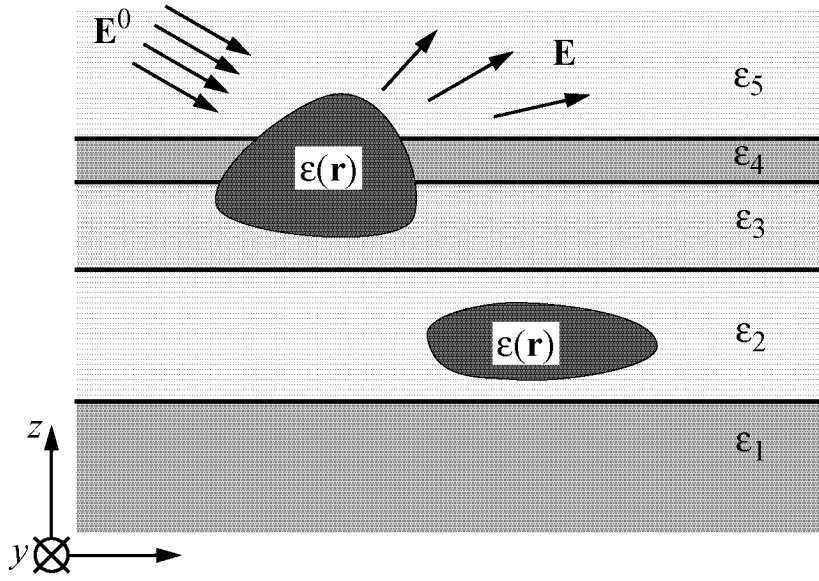


Figure 2.1. Typical geometry under study. Several scatterers with permittivity $\varepsilon(\mathbf{r})$ are embedded in a stratified background composed of L layers with respective permittivity ε_l , $l = 1, \dots, L$. Note that the first and last layers are semi-infinite media.

the Green's tensor. We start with the general 3D case and then particularize the formalism for 2D geometries. The detailed derivation of the Green's tensors associated with a stratified medium (3D and 2D) will be presented in chapter 3.

2.1 Electric field integral equation

When a scattering system is illuminated with an incident electric field $\mathbf{E}^0(\mathbf{r})$ propagating in the background, the total field $\mathbf{E}(\mathbf{r})$ is a solution of the vectorial wave equation [37]:

$$\nabla \times \nabla \times \mathbf{E}(\mathbf{r}) - k_0^2 \varepsilon(\mathbf{r}) \mathbf{E}(\mathbf{r}) = \mathbf{0}, \quad (2.1)$$

where $k_0^2 = \omega^2 \varepsilon_0 \mu_0$ is the vacuum wave number. The incident field $\mathbf{E}^0(\mathbf{r})$ must fulfill the vectorial wave equation for the bare stratified background:

$$\nabla \times \nabla \times \mathbf{E}^0(\mathbf{r}) - k_0^2 \varepsilon_\kappa \mathbf{E}^0(\mathbf{r}) = \mathbf{0}, \quad \mathbf{r} \in \text{layer } \kappa. \quad (2.2)$$

Introducing the dielectric contrast

$$\Delta \varepsilon(\mathbf{r}) = \varepsilon(\mathbf{r}) - \varepsilon_\kappa, \quad \mathbf{r} \in \text{layer } \kappa, \quad (2.3)$$

we can rewrite equation (2.1) as an inhomogeneous equation,

$$\nabla \times \nabla \times \mathbf{E}(\mathbf{r}) - k_0^2 \varepsilon_\kappa \mathbf{E}(\mathbf{r}) = k_0^2 \Delta \varepsilon(\mathbf{r}) \mathbf{E}(\mathbf{r}). \quad (2.4)$$

A solution to equation (2.4) is given by the electric field integral equation [34, 38]:

$$\mathbf{E}(\mathbf{r}) = \mathbf{E}^0(\mathbf{r}) + \int_V d\mathbf{r}' \mathbf{G}(\mathbf{r}, \mathbf{r}') \cdot k_0^2 \Delta \varepsilon(\mathbf{r}') \mathbf{E}(\mathbf{r}'), \quad (2.5)$$

where $\mathbf{G}(\mathbf{r}, \mathbf{r}')$ is the Green's tensor associated with the background. The integration in equation (2.5) runs over the volume V of all the different scatterers in the structure.

Physically, the Green's tensor $\mathbf{G}(\mathbf{r}, \mathbf{r}')$ represents the response of a point source in the stratified background. In chapter 3 we will see that this dyad diverges for $\mathbf{r} \rightarrow \mathbf{r}'$. Then, the principal value must be used for the integral and the singularity must be treated separately [39]. We will also see in chapter 3 that in the case of a stratified background $\mathbf{G}(\mathbf{r}, \mathbf{r}')$ can be split into two parts (see section 3.1):

$$\mathbf{G}(\mathbf{r}, \mathbf{r}') = \delta_{\kappa\kappa'} \mathbf{G}^D(\mathbf{r}, \mathbf{r}') + \mathbf{G}^I(\mathbf{r}, \mathbf{r}'), \quad \mathbf{r} \in \text{layer } \kappa, \mathbf{r}' \in \text{layer } \kappa'. \quad (2.6)$$

$\mathbf{G}^D(\mathbf{r}, \mathbf{r}')$ corresponds to the field radiated directly from \mathbf{r}' to \mathbf{r} and is given in closed form by the Green's tensor for an infinite homogeneous material with permittivity ε_κ [38]. The indirect part $\mathbf{G}^I(\mathbf{r}, \mathbf{r}')$ accounts for all the reflections and refractions at the interfaces and must be calculated numerically. With this decomposition of the Green's tensor, the divergence is completely included in $\mathbf{G}^D(\mathbf{r}, \mathbf{r}')$ (see section 3.1) and we can rewrite equation (2.5) using equation (2.6) as

$$\begin{aligned} \mathbf{E}(\mathbf{r}) &= \mathbf{E}^0(\mathbf{r}) + \int_V d\mathbf{r}' \mathbf{G}^I(\mathbf{r}, \mathbf{r}') \cdot k_0^2 \Delta \varepsilon(\mathbf{r}') \mathbf{E}(\mathbf{r}') \\ &\quad + \lim_{\delta V \rightarrow 0} \int_{V-\delta V} d\mathbf{r}' \delta_{\kappa\kappa'} \mathbf{G}^D(\mathbf{r}, \mathbf{r}') \cdot k_0^2 \Delta \varepsilon(\mathbf{r}') \mathbf{E}(\mathbf{r}') \\ &\quad - \mathbf{L} \cdot \frac{\Delta \varepsilon(\mathbf{r})}{\varepsilon_\kappa} \mathbf{E}(\mathbf{r}), \end{aligned} \quad (2.7)$$

where the infinitesimal volume δV centered at \mathbf{r} is used to exclude the singularity. The source dyadic \mathbf{L} depends on the shape of δV and is given in detail by Yaghjian [39].

The incident field $\mathbf{E}^0(\mathbf{r})$ in equation (2.5) must be a solution of the vector wave equation (2.2) in the stratified background. For a given geometry, this solution is not unique. Figure 2.2 shows three different excitations for the same three-layer structure. The incident field can be

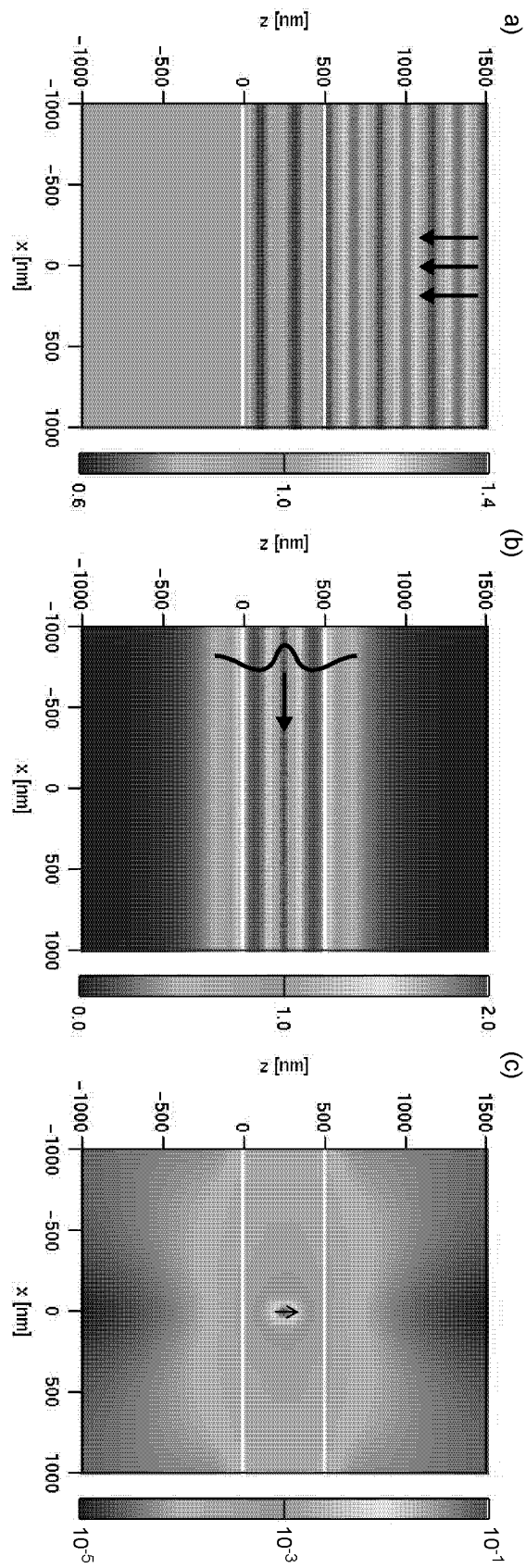


Figure 2.2. Examples of different excitations for the same three-layer system with $\varepsilon_1 = 1, \varepsilon_2 = 2.25, \varepsilon_3 = 1$ at a $\lambda = 633$ nm wavelength. The electric field amplitude $|E^0| = (E^0 \cdot E^{0*})^{1/2}$ is shown. (a) Plane wave illuminating from the top, (b) TE_1 mode propagating in the middle layer, and (c) z -oriented dipole.

a plane wave impinging on the stratified system [figure 2.2(a)]. In that case it must include all the multiple reflections inside the different layers. The incident field can also be a waveguide mode propagating inside the structure [figure 2.2(b)] or even the field of a dipolar source embedded in the system [figure 2.2(c)].

2.2 Discretized equation

For the numerical solution of the volume integral equation (2.7) we use a technique similar to the coupled-dipole approximation (CDA, also known as the discrete-dipole approximation, DDA). With the CDA, a common approach to scattering calculations in vacuum, the field is approximated with piecewise constant functions. This type of discretization is well suited when the dielectric contrast is not too large [40]. However, also more sophisticated techniques such as finite elements can be used to solve equation (2.7) numerically [41].

We define a grid with N meshes centered at $\mathbf{r}_i \in \text{layer } \kappa_i$ with volume V_i , $i = 1, \dots, N$, and dielectric contrast $\Delta\epsilon_i = \Delta\epsilon(\mathbf{r}_i)$. The only constraint for this discretization is that a given mesh must be entirely inside a layer and cannot sit astride a boundary between two layers, as illustrated in figure 2.3(a). The discretization needs not be regular but can vary locally to enhance the required accuracy, with a smaller mesh where the dielectric contrast $\Delta\epsilon(\mathbf{r})$ is large [42]. Introducing the discretized field $\mathbf{E}_i = \mathbf{E}(\mathbf{r}_i)$ and the discretized Green's tensors $\mathbf{G}_{i,j}^D = \mathbf{G}^D(\mathbf{r}_i, \mathbf{r}_j)$

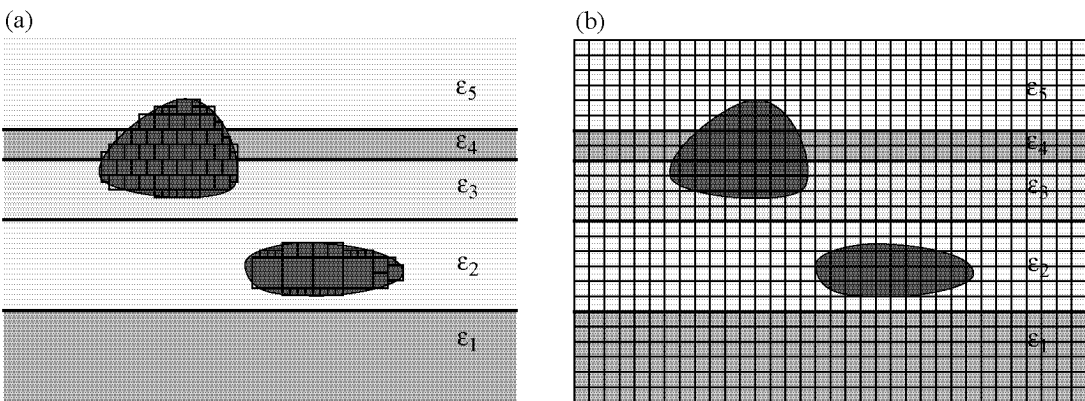


Figure 2.3. (a) Using the Green's tensor technique only the scatterers must be discretized to solve the scattering problem numerically. (b) A “standard” technique requires the discretization of the entire computation window.

and $\mathbf{G}_{i,j}^I = \mathbf{G}^I(\mathbf{r}_i, \mathbf{r}_j)$, the discretized form of equation (2.7) reads

$$\begin{aligned}\mathbf{E}_i &= \mathbf{E}_i^0 + \sum_{j=1}^N \mathbf{G}_{i,j}^I \cdot k_0^2 \Delta \varepsilon_j \mathbf{E}_j \mathbf{V}_j + \sum_{\substack{j=1 \\ j \neq i}}^N \delta_{\kappa_i \kappa_j} \mathbf{G}_{i,j}^D \cdot k_0^2 \Delta \varepsilon_j \mathbf{E}_j \mathbf{V}_j \\ &\quad + \mathbf{M}_i \cdot k_0^2 \Delta \varepsilon_i \mathbf{E}_i - \mathbf{L} \cdot \frac{\Delta \varepsilon_i}{\varepsilon_\kappa} \mathbf{E}_i, \quad i = 1, \dots, N,\end{aligned}\quad (2.8)$$

with the self-term \mathbf{M}_i defined as

$$\mathbf{M}_i = \lim_{\delta V \rightarrow 0} \int_{V_i - \delta V} d\mathbf{r}' \mathbf{G}^D(\mathbf{r}_i, \mathbf{r}'). \quad (2.9)$$

Since the tensors \mathbf{L} and \mathbf{M}_i come from the direct contribution, we can use their analytic form for a homogeneous polarizable background with permittivity ε_κ , as given in [38, 39].

The system of equations (2.8) is best solved numerically with an iterative solver such as conjugate gradients [43, 44]. We found that a stabilized version of the biconjugate gradients algorithm is the most efficient and stable solver [45]. Note that in a stratified medium, the Green's tensor does not have the same symmetry properties as in an infinite homogeneous background. In particular,

$$\mathbf{G}(\mathbf{r}, \mathbf{r}') \neq \mathbf{G}(\mathbf{r} - \mathbf{r}'). \quad (2.10)$$

It is therefore not possible to rewrite equation (2.5) as a convolution and to use a 3D fast Fourier transform to perform the integration [46]. It is however possible to use reduced symmetry properties in the xy plane to expedite the computation [47].

One of the important advantages of this technique lies in the fact that only the scatterers must be discretized, the background being accounted for in the Green's tensor [figure 2.3(a)]. In contrast, a “standard” technique like a finite difference or finite element solution of the Maxwell's equations would require the discretization of the entire window [figure 2.3(b)]. Further, the boundary conditions at the different material interfaces as well as at the edges of the computation window are perfectly and automatically fulfilled using the Green's tensor technique. There is no need for a special treatment with artificial absorbing boundary conditions like perfectly matched layers which are often difficult to implement [48].

2.3 Specialization to 2D structures

The formalism presented above is in principle valid for any shape of the scatterers. However, for two-dimensional (2D) geometries, i.e., systems where the scatterers extend infinitely in one direction, the integration volume in equation (2.5) becomes infinite. This configuration needs a special treatment.

From a practical point of view, in addition to truly two-dimensional geometries, 3D structures can often be considered as 2D when the extension of the scatterers in one particular direction is very large and the electromagnetic field is so well localized that edge effects in that direction become negligible. It is then justified to assume that the structures extend to infinity in that particular direction.

A typical 2D system is shown in figure 2.4. The scatterers extend infinitely along the y axis so that the material system is invariant in that direction. If also the excitation has such a translation symmetry, we can restrict the study of the 3D system [figure 2.4(a)] to a 2D cross section in the xz plane [figure 2.4(b)]. We then define the coordinate \mathbf{r}_{\parallel} parallel to this plane,

$$\mathbf{r} = (\mathbf{r}_{\parallel}, r_y) = (r_x, r_z, r_y), \quad (2.11)$$

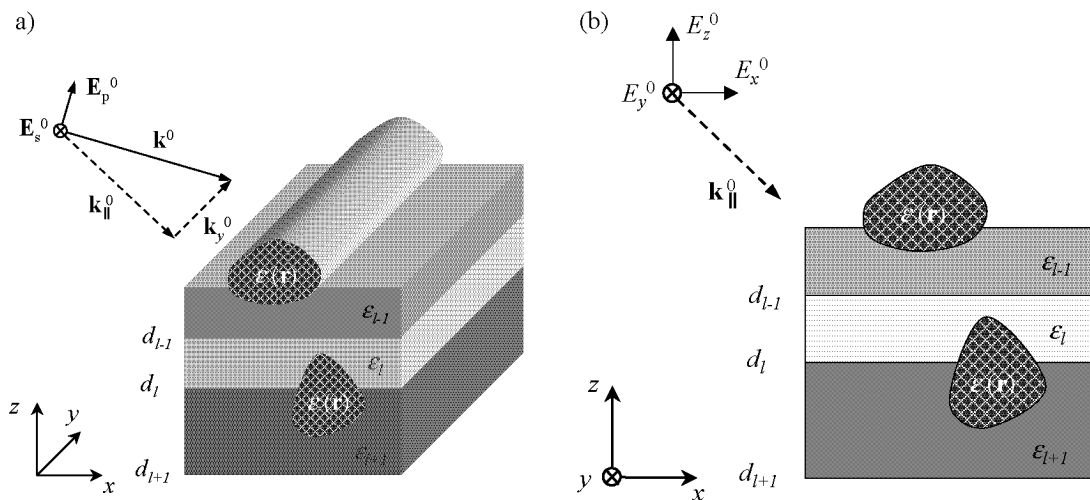


Figure 2.4. Schematic view of a 2D scattering system. (a) The electric field can be split into two contributions: the p-polarized part \mathbf{E}_p^0 lying within the plane of incidence formed by \mathbf{k}^0 and the z axis, and the s-polarized part \mathbf{E}_s^0 standing perpendicularly to this plane. (b) Projection on the xz plane. Note that in general all three components of the incident electric field are nonzero.

and the parallel wave vector \mathbf{k}_{\parallel} ,

$$\mathbf{k} = (\mathbf{k}_{\parallel}, k_y) = (k_x, k_z, k_y). \quad (2.12)$$

Let us emphasize that it is not necessary that also the incident field \mathbf{E}^0 propagates in the xz plane [figure 2.4(a)]. The sole constraint is that \mathbf{E}^0 has an $\exp(ik_y^0 y)$ dependence in the symmetry direction y . For example, a plane wave with wave vector $\mathbf{k}^0 = (\mathbf{k}_{\parallel}^0, k_y^0)$,

$$\mathbf{E}^0(\mathbf{r}) = \mathbf{E}^0 \exp(i\mathbf{k}^0 \cdot \mathbf{r}) = \mathbf{E}^0 \exp(i\mathbf{k}_{\parallel}^0 \cdot \mathbf{r}_{\parallel}) \exp(ik_y^0 y), \quad (2.13)$$

at oblique incidence on the structure fulfills this condition (figure 2.4). On the other hand, a point dipole is not a valid 2D excitation, because it breaks the symmetry of the system.

However, if \mathbf{E}^0 propagates in the xz plane ($k_y^0 = 0$) it is possible to decompose the total field into a transverse electric (TE) part with the electric field in the xz plane, and a transverse magnetic (TM) part with the electric field parallel to the y direction. These two polarizations are then decoupled and the scattered field conserves the polarization of the incident field, i.e., the x and z field components are independent of the y component. This is not the case for oblique incidence ($k_y^0 \neq 0$): All three field components are coupled together and new components that were not present in the incident field can be created during the scattering process [38].

Since we assume that all the fields have a plane wave dependence in y direction, the electric field can be written as

$$\mathbf{E}(\mathbf{r}) = \mathbf{E}(\mathbf{r}_{\parallel}) \exp(ik_y^0 y). \quad (2.14)$$

Let us note that the wave vector component k_y^0 which is tangential to the different material interfaces is constant throughout the entire stratified background. It is therefore solely determined by the illumination field and remains conserved in the scattered field. Further, the dielectric contrast being constant in y direction, equation (2.5) can be rewritten as

$$\mathbf{E}(\mathbf{r}_{\parallel}) = \mathbf{E}^0(\mathbf{r}_{\parallel}) + \int_A d\mathbf{r}'_{\parallel} \mathbf{G}_{2D}(\mathbf{r}_{\parallel}, \mathbf{r}'_{\parallel}) \cdot k_0^2 \Delta \varepsilon(\mathbf{r}'_{\parallel}) \mathbf{E}(\mathbf{r}'_{\parallel}), \quad (2.15)$$

where we introduced

$$\mathbf{G}_{2D}(\mathbf{r}_{\parallel}, \mathbf{r}'_{\parallel}) = \int_{-\infty}^{\infty} dy' \mathbf{G}(\mathbf{r}, \mathbf{r}') \exp[ik_y^0(y' - y)]. \quad (2.16)$$

Note that the integration in equation (2.15) runs only over the scatterer section A.

Recalling that $\mathbf{G}(\mathbf{r}, \mathbf{r}')$ corresponds to a point source, $\mathbf{G}_{2D}(\mathbf{r}_\parallel, \mathbf{r}'_\parallel)$ gives the field generated by an infinite line source extending in the y direction and represents the 2D Green's tensor associated with the stratified background. Again, we postpone the detailed discussion of this dyad to chapter 3.

From equation (2.15) we see that the results developed for the 3D case [equations (2.7) and (2.8)] can directly be used for 2D geometries. For example, equation (2.7) becomes

$$\begin{aligned}\mathbf{E}(\mathbf{r}_\parallel) = & \mathbf{E}^0(\mathbf{r}_\parallel) + \int_A d\mathbf{r}'_\parallel \mathbf{G}_{2D}^I(\mathbf{r}_\parallel, \mathbf{r}'_\parallel) \cdot k_0^2 \Delta\epsilon(\mathbf{r}'_\parallel) \mathbf{E}(\mathbf{r}'_\parallel) \\ & + \lim_{\delta A \rightarrow 0} \int_{A-\delta A} d\mathbf{r}'_\parallel \delta_{\kappa\kappa'} \mathbf{G}_{2D}^D(\mathbf{r}_\parallel, \mathbf{r}'_\parallel) \cdot k_0^2 \Delta\epsilon(\mathbf{r}'_\parallel) \mathbf{E}(\mathbf{r}'_\parallel) \\ & - \mathbf{L}_{2D} \cdot \frac{\Delta\epsilon(\mathbf{r}_\parallel)}{\varepsilon_\kappa} \mathbf{E}(\mathbf{r}_\parallel),\end{aligned}\quad (2.17)$$

The tensor \mathbf{L}_{2D} is the source dyad for a 2D system and is given for different exclusion sections δA in [39].

Chapter 3

The Green's tensor for stratified media

The Green's tensor $\mathbf{G}(\mathbf{r}, \mathbf{r}')$ plays a key role in our approach to scattering calculations. It represents the electric field radiated at \mathbf{r} by three orthogonal dipoles located at \mathbf{r}' . Whereas $\mathbf{G}(\mathbf{r}, \mathbf{r}')$ can be expressed analytically for an infinite homogeneous background, the situation is much more complex in a stratified medium, where the Green's tensor must take into account all the reflections and refractions that occur at the different interfaces. However, in that case a numerical solution for $\mathbf{G}(\mathbf{r}, \mathbf{r}')$ can be found by eigenmode expansion in plane waves. The continuous spectrum of these eigenfunctions leads to so-called Sommerfeld integrals. Sommerfeld found this type of integrals first when he treated the simplest stratified geometry, a dipolar source over a single interface [49]. Since the quadrature of these integrals is intricate, different methods have been proposed, such as integration along the steepest descent path [50], extrapolation methods [51], or the approximation with complex images [52]. However, these techniques are often limited to special configurations of \mathbf{r} and \mathbf{r}' or must be adapted to each particular geometry under study.

Our approach provides a general, accurate and efficient computation of the Green's tensor for stratified media by a direct calculation of Sommerfeld integrals. It is not restricted by the number of layers or the location of \mathbf{r} and \mathbf{r}' . The geometry under study and the corresponding notation is shown in figure 3.1. In this chapter we explicitly include magnetic materials with a permeability μ .

3.1 Derivation by plane wave expansion

The Green's tensor $\mathbf{G}(\mathbf{r}, \mathbf{r}')$ for an arbitrary scattering system described by the dielectric permittivity $\varepsilon(\mathbf{r})$ and the magnetic permeability $\mu(\mathbf{r})$ is

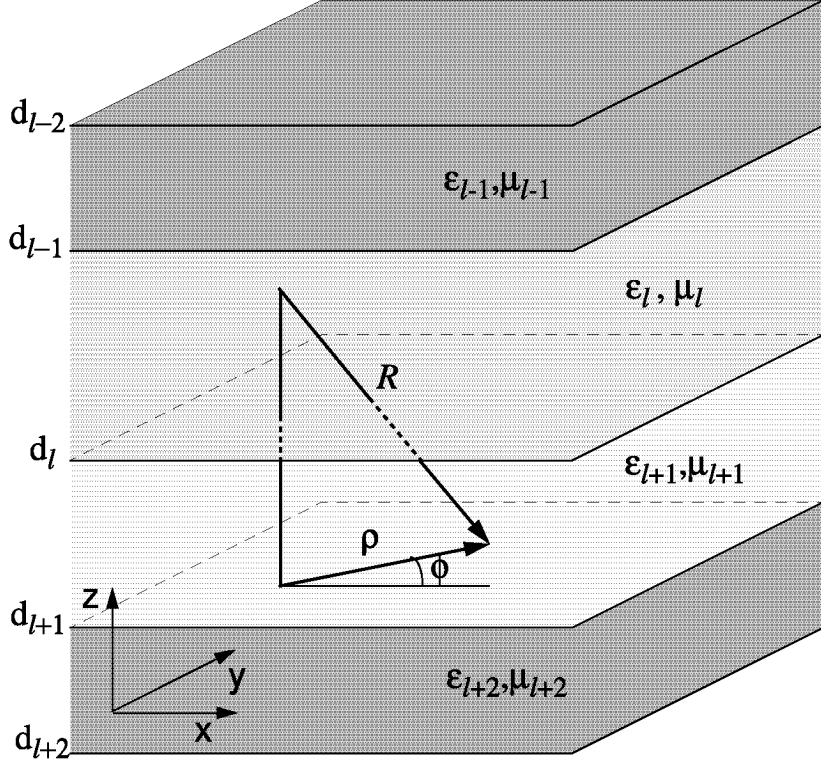


Figure 3.1. Stratified medium consisting of L layers with permittivity and permeability $(\varepsilon_1, \mu_1), \dots, (\varepsilon_L, \mu_L)$ separated by interfaces at $z = d_1, \dots, d_{L-1}$. The vector $\mathbf{R} = \mathbf{r} - \mathbf{r}'$ defines the relative distance between \mathbf{r} and \mathbf{r}' and $\boldsymbol{\rho} = (x - x', y - y') = (\rho \cos \phi, \rho \sin \phi)$ is the projection of \mathbf{R} onto the xy plane.

the solution of the vector wave equation with a point source term [33]:

$$\nabla \times \mu^{-1}(\mathbf{r}) \nabla \times \mathbf{G}(\mathbf{r}, \mathbf{r}') - k_0^2 \varepsilon(\mathbf{r}) \mathbf{G}(\mathbf{r}, \mathbf{r}') = \mu^{-1}(\mathbf{r}) \mathbf{1} \delta(\mathbf{r} - \mathbf{r}'), \quad (3.1)$$

where $k_0^2 = \omega^2 \varepsilon_0 \mu_0$ is the vacuum wave number. For a given $(\mathbf{r}, \mathbf{r}')$ pair, each column $\beta = x, y, z$ of the 3×3 matrix representing the Green's tensor,

$$\mathbf{G}(\mathbf{r}, \mathbf{r}') = \begin{pmatrix} G_{xx} & G_{xy} & G_{xz} \\ G_{yx} & G_{yy} & G_{yz} \\ G_{zx} & G_{zy} & G_{zz} \end{pmatrix}, \quad (3.2)$$

gives the three components $\alpha = x, y, z$ of the electric field radiated at position \mathbf{r} by a dipole at position \mathbf{r}' and oriented in β direction.

For the derivation of $\mathbf{G}(\mathbf{r}, \mathbf{r}')$ associated with a stratified background we start with the expression for the Green's tensor $\mathbf{G}_H(\mathbf{r}, \mathbf{r}')$ associated

with a homogeneous system ε_B, μ_B . It is given by [33]

$$\mathbf{G}_H(\mathbf{r}, \mathbf{r}') = \left(\mathbf{1} + \frac{\nabla \nabla}{k_B^2} \right) \frac{\exp(ik_B R)}{4\pi R} \quad (3.3)$$

$$= \left(\mathbf{1} + \frac{ik_B R - 1}{k_B^2 R^2} \mathbf{1} + \frac{3 - 3ik_B R - k_B^2 R^2}{k_B^2 R^4} \mathbf{R} \mathbf{R} \right) \times \frac{\exp(ik_B R)}{4\pi R}, \quad (3.4)$$

where $R = |\mathbf{R}| = |\mathbf{r} - \mathbf{r}'|$ is the relative distance and $k_B^2 = \omega^2 \varepsilon_B \mu_B$ corresponds to the wave number in the background medium.

To deduce $\mathbf{G}(\mathbf{r}, \mathbf{r}')$ for a stratified background it is more convenient to express $\mathbf{G}_H(\mathbf{r}, \mathbf{r}')$ in reciprocal space (\mathbf{k} space) where the boundary conditions at the stratification interfaces can be enforced more easily. Fourier transforming equation (3.3) leads to

$$\mathbf{G}_H(\mathbf{r}, \mathbf{r}') = \frac{1}{8\pi^3 k_B^2} \iiint d\mathbf{k} \left(\frac{\mathbf{1} k_B^2 - \mathbf{k} \mathbf{k}}{k^2 - k_B^2} \right) \exp(i\mathbf{k} \cdot \mathbf{R}). \quad (3.5)$$

Since we assume that the layers, which will be added later, are perpendicular to the z axis, we first perform the integration over k_z using calculus of residues. Hence, we must ensure that the integrand vanishes for $k_z \rightarrow \infty$ and rewrite equation (3.5) as

$$\begin{aligned} \mathbf{G}_H(\mathbf{r}, \mathbf{r}') &= \frac{1}{8\pi^3 k_B^2} \iiint d\mathbf{k} \left(\frac{\mathbf{1} k_B^2 - \mathbf{k} \mathbf{k}}{k^2 - k_B^2} + \hat{\mathbf{z}} \hat{\mathbf{z}} \right) \exp(i\mathbf{k} \cdot \mathbf{R}) \\ &\quad - \frac{\hat{\mathbf{z}} \hat{\mathbf{z}}}{8\pi^3 k_B^2} \iiint d\mathbf{k} \exp(i\mathbf{k} \cdot \mathbf{R}) \\ &= \frac{i}{8\pi^2 k_B^2} \iint dk_x dk_y \left(\frac{\mathbf{1} k_B^2 - \mathbf{k}_B}{k_{Bz}} \right) \exp(i\mathbf{k}_B \cdot \mathbf{R}) \\ &\quad - \frac{\hat{\mathbf{z}} \hat{\mathbf{z}}}{k_B^2} \delta(\mathbf{R}), \end{aligned} \quad (3.6)$$

where $k_{Bz} = (k_B^2 - k_x^2 - k_y^2)^{1/2}$ is the z component of the wave vector and

$$\mathbf{k}_B(k_{Bz}) = \begin{cases} k_x \hat{\mathbf{x}} + k_y \hat{\mathbf{y}} + k_{Bz} \hat{\mathbf{z}} & \text{for } z > z', \\ k_x \hat{\mathbf{x}} + k_y \hat{\mathbf{y}} - k_{Bz} \hat{\mathbf{z}} & \text{for } z < z'. \end{cases} \quad (3.7)$$

Note that in equation (3.6) the singularity of the Green's tensor for $\mathbf{R} = 0$ manifests in a δ function. Introducing this expression of the Green's tensor in the electric field integral equation (2.5) leads to an \mathbf{L} term for a pillbox shaped exclusion volume [39]. This is the natural

exclusion volume corresponding to the way we expanded $\mathbf{G}_H(\mathbf{r}, \mathbf{r}')$ with $\hat{\mathbf{z}}$ as preferred direction.

Now that we have the plane wave expansion of the Green's tensor for an infinite homogeneous background ϵ_B, μ_B , it is a simple matter to include additional layers. As a matter of fact, the effect of these layers will be to add two plane waves, one propagating upward and one downward, to each Fourier component, as illustrated in figure 3.2 (note that the propagation vector (k_x, k_y, k_z) is similar for the three plane waves, only the sign of k_z changes). The amplitudes of these additional components are determined by the boundary conditions at the different interfaces. Indeed, each plane wave is reflected and refracted according to the corresponding Fresnel reflection coefficient [15]. Since these coefficients depend on the polarization of the plane wave with respect to the stratification it is advantageous to introduce the new orthonormal system $\hat{\mathbf{k}}(k_{Bz}), \hat{\mathbf{l}}(k_{Bz}), \hat{\mathbf{m}}(k_{Bz})$ [53]

$$\hat{\mathbf{k}}(k_{Bz}) = \frac{\mathbf{k}_B(k_{Bz})}{k_B}, \quad (3.8a)$$

$$\hat{\mathbf{l}}(k_{Bz}) = \frac{\hat{\mathbf{k}}(k_{Bz}) \times \hat{\mathbf{z}}}{|\hat{\mathbf{k}}(k_{Bz}) \times \hat{\mathbf{z}}|}, \quad (3.8b)$$

$$\hat{\mathbf{m}}(k_{Bz}) = \hat{\mathbf{k}}(k_{Bz}) \times \hat{\mathbf{l}}(k_{Bz}). \quad (3.8c)$$

Equivalently, another orthonormal system is formed by $\hat{\mathbf{k}}(-k_{Bz}), \hat{\mathbf{l}}(-k_{Bz}), \hat{\mathbf{m}}(-k_{Bz})$. Remark that $\hat{\mathbf{l}}$ is perpendicular to the plane defined by $\hat{\mathbf{k}}$ and $\hat{\mathbf{z}}$, whereas $\hat{\mathbf{m}}$ lies within this plane. For a given k_B , the electric field component parallel to $\hat{\mathbf{l}}$ corresponds therefore to s polarization and that parallel to $\hat{\mathbf{m}}$ corresponds to p polarization. Using the fact

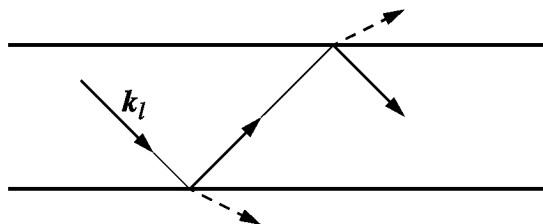


Figure 3.2. The effect of the surrounding layers on a given Fourier component \mathbf{k}_l in layer l is to add an upgoing and a downgoing plane wave with similar \mathbf{k} vectors.

that $\hat{\mathbf{k}}\hat{\mathbf{k}} + \hat{\mathbf{l}}\hat{\mathbf{l}} + \hat{\mathbf{m}}\hat{\mathbf{m}} = \mathbf{1}$, equation (3.6) can be rewritten as

$$\mathbf{G}_H(\mathbf{r}, \mathbf{r}') = -\frac{\hat{\mathbf{z}}\hat{\mathbf{z}}}{k_B^2} \delta(\mathbf{R}) + \frac{i}{8\pi^2} \iint dk_x dk_y \left(\frac{\hat{\mathbf{l}}\hat{\mathbf{l}} + \hat{\mathbf{m}}\hat{\mathbf{m}}}{k_{Bz}} \right) \exp(i\mathbf{k}_B \cdot \mathbf{R}). \quad (3.9)$$

To obtain the Green's tensor $\mathbf{G}(\mathbf{r}, \mathbf{r}')$ for a stratified medium, we can now superpose to the Green's tensor of a homogeneous medium $\varepsilon_\kappa, \mu_\kappa$ the additional terms by formally writing

$$\begin{aligned} \mathbf{G}(\mathbf{r}, \mathbf{r}') &= -\frac{\hat{\mathbf{z}}\hat{\mathbf{z}}}{k_\kappa^2} \delta(\mathbf{R}) + \frac{i}{8\pi^2} \iint dk_x dk_y \\ &\quad \times \exp\{i[k_x(x - x') + k_y(y - y')]\} \frac{1}{k_{\kappa z}} \\ &\quad \times [\hat{\mathbf{l}}\hat{\mathbf{l}} \exp[\pm i(k_{\kappa z}z - k_{\kappa' z}z')] \\ &\quad + \mathbf{R}^{s\uparrow} \exp(ik_{\kappa z}z) + \mathbf{R}^{s\downarrow} \exp(-ik_{\kappa z}z) \\ &\quad + \hat{\mathbf{m}}\hat{\mathbf{m}} \exp[\pm i(k_{\kappa z}z - k_{\kappa' z}z')] \\ &\quad + \mathbf{R}^{p\uparrow} \exp(ik_{\kappa z}z) + \mathbf{R}^{p\downarrow} \exp(-ik_{\kappa z}z)], \\ &\quad \mathbf{r} \in \text{layer } \kappa, \mathbf{r}' \in \text{layer } \kappa', \end{aligned} \quad (3.10)$$

where $k_l^2 = \omega^2 \varepsilon_l \mu_l$ and $k_{lz} = (k_l^2 - k_x^2 - k_y^2)^{1/2}$, $l = \kappa, \kappa'$. The upper sign in equation (3.10) refers to $z > z'$ and the lower sign to $z < z'$. The tensors $\mathbf{R}^{s\uparrow}$, $\mathbf{R}^{s\downarrow}$, $\mathbf{R}^{p\uparrow}$ and $\mathbf{R}^{p\downarrow}$ can obviously be interpreted as generalized reflection coefficients that take into account reflections from all existing surfaces. They are functions of $(k_x, k_y; \mathbf{r}, \mathbf{r}')$ and are explicitly derived in **P1** [equations (9), (10), appendix A].

If \mathbf{r} and \mathbf{r}' are inside the same layer, $\kappa = \kappa'$, we can still identify the Green's tensor for a homogeneous background in equation (3.10) [compare with equation (3.9)]. Hence, once we have determined $\mathbf{R}^{s\uparrow}$, $\mathbf{R}^{s\downarrow}$, $\mathbf{R}^{p\uparrow}$, and $\mathbf{R}^{p\downarrow}$, we can extract again $\mathbf{G}_H(\mathbf{r}, \mathbf{r}')$, and use its closed form [see equation (3.4)]. These terms define a direct field Green's tensor $\mathbf{G}^D(\mathbf{r}, \mathbf{r}')$, whereas the remaining integral constitutes an indirect field Green's tensor $\mathbf{G}^I(\mathbf{r}, \mathbf{r}')$ accounting for the reflections and refractions at the interfaces. This separation is not possible if \mathbf{r} and \mathbf{r}' are in different layers, $\kappa \neq \kappa'$, since then all plane waves are refracted and reflected by at least one interface. Hence, the total Green's tensor $\mathbf{G}(\mathbf{r}, \mathbf{r}')$ for a stratified medium can be written as

$$\mathbf{G}(\mathbf{r}, \mathbf{r}') = \delta_{\kappa\kappa'} \mathbf{G}^D(\mathbf{r}, \mathbf{r}') + \mathbf{G}^I(\mathbf{r}, \mathbf{r}'), \quad \mathbf{r} \in \text{layer } \kappa, \mathbf{r}' \in \text{layer } \kappa'. \quad (3.11)$$

This decomposition allows us to treat the singularity in the Green's tensor for $\mathbf{R} = 0$ in the same way as for a homogeneous background, since

it is completely included in $\mathbf{G}^D(\mathbf{r}, \mathbf{r}')$. Further, the choice of the exclusion volume determining the \mathbf{L} term in equation (2.7) is not restricted to the pillbox naturally arising in the plane wave expansion (3.6), but an arbitrary shape, for example a sphere, can be chosen.

Finally, for further discussions, we rewrite the Green's tensor in equation (3.10) condensing the terms associated with each polarization into the tensors \mathbf{h}^s and \mathbf{h}^p .

$$\begin{aligned}\mathbf{G}(\mathbf{r}, \mathbf{r}') = & -\frac{\hat{\mathbf{z}}\hat{\mathbf{z}}}{k_\kappa^2} \delta(\mathbf{R}) + \frac{i}{8\pi^2} \iint dk_x dk_y \\ & \times \exp\{i[k_x(x-x') + k_y(y-y')]\} \\ & \times [\mathbf{h}^s(k_x, k_y; \mathbf{r}, \mathbf{r}') + \mathbf{h}^p(k_x, k_y; \mathbf{r}, \mathbf{r}')].\end{aligned}\quad (3.12)$$

Now we have collected all necessary expressions and could, in principle, proceed with the solution of the two-dimensional Fourier integral (3.12). However, for the numerical implementation it is worth developing the calculation analytically.

3.1.1 The 3D Green's tensor

For 3D scatterers, equation (3.12) can be further simplified by introducing a cylindrical coordinate system. In the xy and $k_x k_y$ plane we introduce the transverse coordinate ρ

$$\mathbf{R} = (\rho, z - z') = (x - x', y - y', z - z'), \quad (3.13)$$

$$\rho = (\rho \cos \phi, \rho \sin \phi), \quad (3.14)$$

and the transverse wave vector \mathbf{k}_ρ

$$\mathbf{k} = (\mathbf{k}_\rho, k_z) = (k_x, k_y, k_z), \quad (3.15)$$

$$\mathbf{k}_\rho = (k_\rho \cos k_\phi, k_\rho \sin k_\phi). \quad (3.16)$$

The integration over k_ϕ in equation (3.10) is then performed analytically with the help of Bessel functions [54]:

$$J_n(k_\rho \rho) = \frac{i^{-n}}{2\pi} \int_0^{2\pi} dk_\phi \exp(ik_\rho \rho \cos k_\phi) \cos(nk_\phi). \quad (3.17)$$

For the computation of the Bessel functions we can rely on numerical standard libraries where efficient algorithms are already implemented.

Thus, only a one-dimensional integral over the radial component k_ρ must be calculated numerically:

$$\mathbf{G}_{3D}(\mathbf{r}, \mathbf{r}') = -\frac{\hat{\mathbf{z}}\hat{\mathbf{z}}}{k_\kappa^2} \delta(\mathbf{R}) + \frac{i}{4\pi} \int_0^\infty dk_\rho [\mathbf{f}_{3D}^s(k_\rho; \mathbf{r}, \mathbf{r}') + \mathbf{f}_{3D}^p(k_\rho; \mathbf{r}, \mathbf{r}')]. \quad (3.18)$$

The components of the tensors \mathbf{f}_{3D}^s and \mathbf{f}_{3D}^p are obtained after careful evaluation of equation (3.10). Note that in the case $\rho = 0$ no Bessel functions are necessary. All components are explicitly given in appendix B of **P1**.

3.1.2 The 2D Green's tensor

Equation (2.16) shows that the Green's tensor for a 2D system can be directly obtained from $\mathbf{G}(\mathbf{r}, \mathbf{r}')$ by integration along the translation axis y . For a stratified medium we perform this integration expressing the Green's tensor in cartesian coordinates rather than in cylindrical coordinates. Inserting equation (3.12) in equation (2.16), the integral over y' can be identified with a δ function:

$$\begin{aligned} \mathbf{G}_{2D}(\mathbf{r}_\parallel, \mathbf{r}'_\parallel) &= -\frac{\hat{\mathbf{z}}\hat{\mathbf{z}}}{k_\kappa^2} \delta(\mathbf{R}_\parallel) + \frac{i}{4\pi} \iint dk_x dk_y \\ &\quad \times \exp[ik_x(x - x')] \exp[i(k_y - k_y^0)y] \delta(k_y - k_y^0) \\ &\quad \times [\mathbf{h}^s(k_x, k_y; \mathbf{r}_\parallel, \mathbf{r}'_\parallel) + \mathbf{h}^p(k_x, k_y; \mathbf{r}_\parallel, \mathbf{r}'_\parallel)] \\ &= -\frac{\hat{\mathbf{z}}\hat{\mathbf{z}}}{k_\kappa^2} \delta(\mathbf{R}_\parallel) + \frac{i}{4\pi} \int_{-\infty}^\infty dk_x \exp[ik_x(x - x')] \\ &\quad \times [\mathbf{h}^s(k_x, k_y^0; \mathbf{r}_\parallel, \mathbf{r}'_\parallel) + \mathbf{h}^p(k_x, k_y^0; \mathbf{r}_\parallel, \mathbf{r}'_\parallel)], \end{aligned} \quad (3.19)$$

where $\mathbf{R}_\parallel = \mathbf{r}_\parallel - \mathbf{r}'_\parallel$.

Thus, to obtain the 2D Green's tensor, only a one-dimensional integral over the transverse component k_x must be calculated numerically. The explicit components of the tensors \mathbf{h}^s and \mathbf{h}^p are explicitly given in the appendix of **P3**.

Since the component functions of \mathbf{h}^s and \mathbf{h}^p are either even or odd symmetrical with respect to the integration variable k_x , it is further possible to reduce the integration to the semi-infinite positive k_x axis. Hence, in analogy to equation (3.18) we can rewrite equation (3.19) as

$$\mathbf{G}_{2D}(\mathbf{r}_\parallel, \mathbf{r}'_\parallel) = -\frac{\hat{\mathbf{z}}\hat{\mathbf{z}}}{k_\kappa^2} \delta(\mathbf{R}_\parallel) + \frac{i}{4\pi} \int_0^\infty dk_x [\mathbf{f}_{2D}^s(k_x; \mathbf{r}_\parallel, \mathbf{r}'_\parallel) + \mathbf{f}_{2D}^p(k_x; \mathbf{r}_\parallel, \mathbf{r}'_\parallel)], \quad (3.20)$$

where the tensors \mathbf{f}_{2D}^p and \mathbf{f}_{2D}^s contain only the even symmetric contributions to the integrand, the odd symmetric ones canceling out.

3.2 Numerical implementation

In the last section the Green's tensor for stratified media was expressed as a set of semi-infinite one-dimensional Sommerfeld type integrals [equations (3.18) and (3.20)]. The form of a typical integrand is for a 3D geometry

$$\begin{aligned} G_{3D}(k_\rho; \mathbf{r}, \mathbf{r}') &= g_{3D}(k_\rho; \mathbf{r}, \mathbf{r}') J_n(k_\rho \rho) \\ &\times [\mathcal{A}_{3D}(k_\rho) \exp(ik_{\kappa z} z) + \mathcal{B}_{3D}(k_\rho) \exp(-ik_{\kappa z} z)], \end{aligned} \quad (3.21)$$

and for a 2D geometry

$$\begin{aligned} G_{2D}(k_x; \mathbf{r}_\parallel, \mathbf{r}'_\parallel) &= g_{2D}(k_x; \mathbf{r}_\parallel, \mathbf{r}'_\parallel) \exp[ik_x(x - x')] \\ &\times [\mathcal{A}_{2D}(k_x) \exp(ik_{\kappa z} z) + \mathcal{B}_{2D}(k_x) \exp(-ik_{\kappa z} z)]. \end{aligned} \quad (3.22)$$

Note the basic difference between the 3D and 2D integrands: In 3D the angular integration of exponential functions in \mathbf{k} space leads to Bessel functions, whereas in 2D the bare exponential functions remain.

Integrals of this kind cannot be performed analytically, but have to be evaluated numerically. However, a straightforward implementation would fail because of the mathematically awkward behavior of the integrand: It involves several singularities (see section 3.2.1) and is strongly oscillating due to the $J_n(k_\rho \rho)$ terms in the 3D case and the $\exp[ik_x(x - x')]$ terms in the 2D case. To avoid these difficulties we use Cauchy's integral theorem and deform the integration path in the complex integration plane [33]. The objective of this section is to determine such an optimum path. We will first study the 3D case and then discuss the differences for 2D integrands.

3.2.1 3D implementation

A. Singularities of the integrand

The singularities of $G_{3D}(k_\rho; \mathbf{r}, \mathbf{r}')$ can be classified in two types: branch point singularities and pole singularities. Branch point singularities are related to the $k_{lz} = (k_l^2 - k_\rho^2)^{1/2}$ dependence of the integrands. Since k_{lz} is the square root of a complex number, it is double valued and branch cuts defined by $\text{Im}(k_{lz}) = 0$ intersect the plane of integration [33]. Each branch cut ends in a branch point at $k_\rho = \pm k_l$ (figure 3.3).

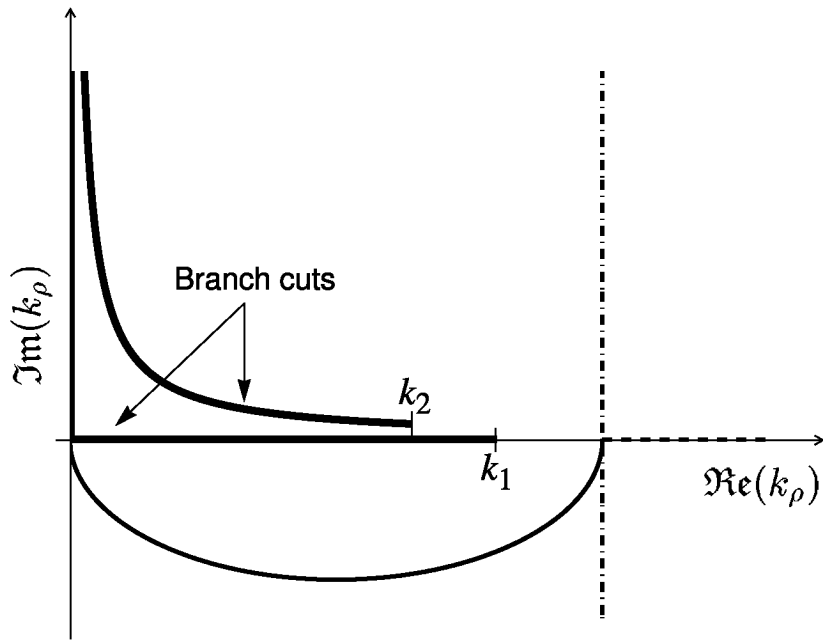


Figure 3.3. Plane of integration: The singularities are avoided by an elliptical path (solid line). At $k_\rho = 2k^{\text{maj}}$ the integration is resumed along the real k_ρ axis using Bessel functions (dashed line) or parallel to the imaginary k_ρ axis using Hankel functions (dash-dotted line).

One could expect that a branch cut exists for each layer, i.e., for each k_l . However it can be shown that the functional dependence of $G_{3D}(k_\rho; \mathbf{r}, \mathbf{r}')$ on k_{lz} is even for all l except the two outermost regions [55, 56]. Therefore branch cuts and branch points appear only for $k_\rho = \pm k_1, \pm k_L$. Since the integral runs from zero to infinity, we can further restrict our discussion to singularities with a non-negative real part.

To choose now the appropriate value for k_{1z} and k_{Lz} , thereby ensuring that the integration is performed on the correct Riemann sheet defined by the branch cut $\text{Im}(k_{lz}) = 0$, we simply apply the radiation conditions: We must use the value with $\text{Im}(k_{lz}) > 0$ to make the integrands vanish for $z \rightarrow \pm\infty$.

The second class of singularities, pole singularities, are due to vanishing denominators of $G_{3D}(k_\rho; \mathbf{r}, \mathbf{r}')$. These poles correspond physically to modes guided by the layered structure, as will be illustrated in section 3.3.1. For dielectric media with $\Re(\varepsilon) > 0$, such modes propagate between the interfaces (slab modes) with constants k_ρ smaller than $k_l^{\max} = \max_l \Re(k_l)$ [57]. For metals with $\Re(\varepsilon) < 0$ a different type of modes can be excited: surface modes that are bound to the interfaces between the material layers and decay exponentially in both directions

away from the interface (surface plasmon–polaritons) [58]. These modes can have propagation constants $k_\rho > k_l^{\max}$ and no upper limit can be found a priori without an explicit calculation of the pole locations.

For lossy materials with $\Im(\epsilon) > 0$ it can be shown that both branch points and pole singularities are shifted into the first quadrant of the complex k_ρ plane (see figure 3.3) [56].

B. Quadrature of the Sommerfeld type integrals

For lossless media both branch point singularities and poles are located on the original integration path along the real k_ρ axis. For media with small losses, the singularities remain close enough to this axis and can still cause serious problems. Hence, our integration path should be deformed into the fourth quadrant of the complex k_ρ plane with Cauchy's integral theorem. A possible choice would be to leave the real axis only in close vicinity of the singularities, for example by a semi-circle around each singularity. This requires to precisely determine the location of each pole, which is a tedious and time consuming task [59].

In our implementation we use an easier way of surrounding the singularities: an elliptical path starting at $k_\rho = 0$ with the major semi-axis k_ρ^{maj} and the minor semi-axis k_ρ^{min} (figure 3.3). From the discussion in the previous section we take $2k_\rho^{\text{maj}} = k_l^{\max} + k_0$, where the vacuum wave number k_0 is added as safety margin. For dielectric media k_ρ^{maj} is chosen large enough to enclose all the singularities. However, we must still ensure that also all poles corresponding to surface modes are included. A check for this case will be presented below.

The parameter k_ρ^{min} is empirically chosen such that the integration path is sufficiently far away from the singularities without extending too much in negative imaginary k_ρ direction, because the Bessel function $J_n(k_\rho \rho)$ increases then very rapidly. We have observed that $k_\rho^{\text{min}} = 10^{-3} k_\rho^{\text{maj}}$ was a good choice for this parameter. A typical integrand is shown in figure 3.4, together with the deformed integration path.

For the remaining integration, we usually follow the real k_ρ axis. The convergence of the integrand in this direction is mainly governed by an exponential damping

$$\exp[\pm i(k_{\kappa z} z - k_{\kappa' z'} z')] \rightarrow \exp(-k_\rho |z - z'|) \quad \text{for } k_\rho \rightarrow \infty, \quad (3.23)$$

corresponding to the dipole field radiated through the stratified structure [see equation (3.10)]. Hence, when $|z - z'|$ is small, the quadrature taken along the real axis converges only slowly. In that case, it is more

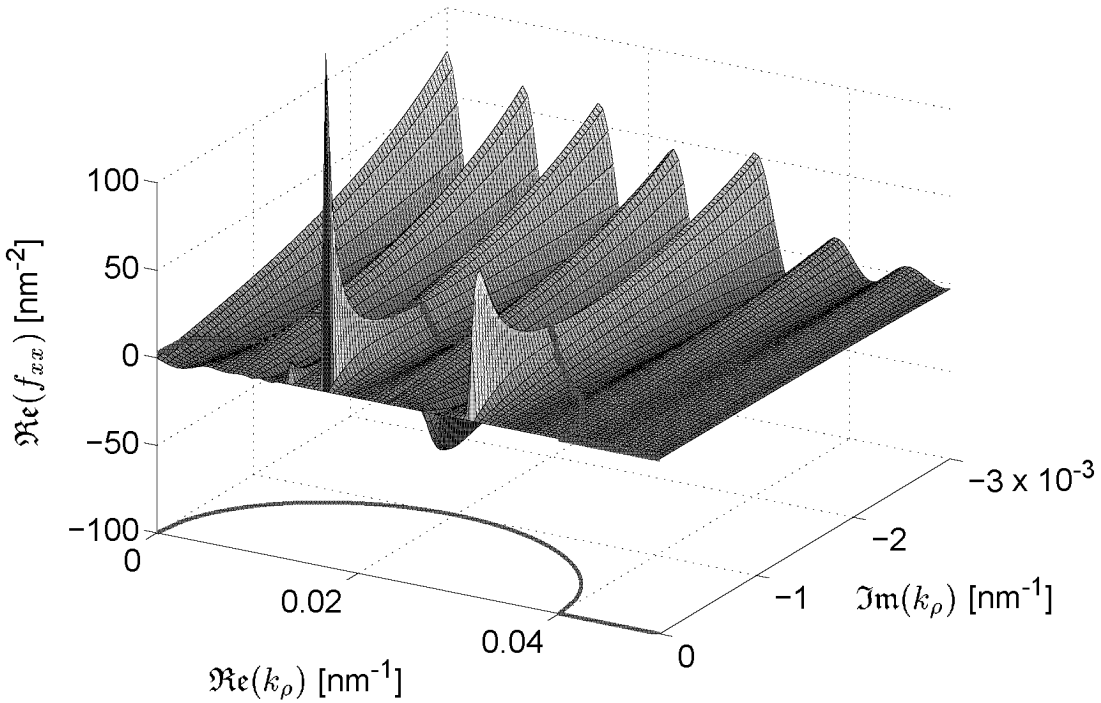


Figure 3.4. Real part of the integrand $f_{xx} = f_{xx}^s + f_{xx}^p$ as a function of the complex integration variable k_ρ [equation (3.18)]. In this example a non-magnetic three layer system with $\varepsilon_1 = 1$, $\varepsilon_2 = 4$ and $\varepsilon_3 = 2$ is used. The elliptical integration path used to avoid the singularities is shown on the integrand (red line) and on the projection plane.

advantageous to transform the integral using Hankel functions (for $\rho \neq 0$):

$$\begin{aligned} J_n(k_\rho \rho) &= \frac{1}{2}(H_n^{(1)}(k_\rho \rho) + H_n^{(2)}(k_\rho \rho)) \\ &= \frac{1}{2}[H_n^{(1)}(k_\rho \rho) + (H_n^{(1)}((k_\rho \rho)^*))^*]. \end{aligned} \quad (3.24)$$

Because of the asymptotic behavior of the Hankel functions for large values of $k_\rho \rho$ [60],

$$\lim_{|k_\rho \rho| \rightarrow \infty} H_n^{(1)}(k_\rho \rho) = \sqrt{\frac{2}{\pi k_\rho \rho}} \exp[i k_\rho \rho - \frac{1}{2} i \pi(n + \frac{1}{2})], \quad (3.25)$$

we can deflect the integration path from the real axis to a path parallel to the imaginary axis: for the first term of the right-hand side in equation (3.24) in positive imaginary direction, for the second term in negative imaginary direction (figure 3.3). Thus, it is ensured that the

integral along the closing path vanishes at infinity and Cauchy's integral theorem can be used. Note that for each $|k_\rho\rho|$ the Hankel function must only be calculated for the argument with the positive imaginary part [complex conjugate in the argument of the right-hand side's second term in equation (3.24)].

From equations (3.23) and (3.25) the path which provides fastest convergence is determined by a comparison between $|z - z'|$ and ρ : If $|z - z'| > \alpha\rho$ we proceed along the real axis, otherwise we follow the path parallel to the imaginary axis. The empirically determined parameter $\alpha = 10$ shows that the deflection of the integration path strongly facilitates the integration.

The comparison between the results of both integration paths offers now a possibility to check if all poles have been avoided by the elliptical path discussed above. Following Cauchy's integral theorem, the results are identical only if no singularity is enclosed [33]. Since the singularities of the integrals are determined only by the stratified system (and not by \mathbf{r} and \mathbf{r}'), it is enough to verify the validity of the elliptical path once at the beginning of a simulation.

From a practical point of view, we use Gauss-Kronrod quadrature to evaluate the integrals along the deformed path [61]. This efficient algorithm can accurately handle the oscillating behavior of the Bessel and Hankel functions. We are using 15 point Gauss-Kronrod quadrature and stop the integration when a relative accuracy of 10^{-9} is achieved. The application of a much more costly 64 point Gauss-Kronrod quadrature would roughly double the computation time without an appreciable gain in precision. Decreasing the desired relative accuracy to 10^{-6} typically speeds up the computation by a factor 1.5.

A very useful trick to expedite the computation of the Green's tensor for a stratified medium is to integrate simultaneously the different components of $\mathbf{G}_{3D}(\mathbf{r}, \mathbf{r}')$. However, we do not evaluate directly the individual components but rather choose a numerically more appropriate decomposition: The integrands in equation (3.18) can be ordered in s- and p-polarized terms with first and second order Bessel or Hankel functions. Thus, 7 independent terms can be defined. We have observed that for a given $(\mathbf{r}, \mathbf{r}')$ pair these terms have a similar behavior in the \mathbf{k}_ρ plane, which makes possible their simultaneous integration. In our practical implementation, we integrate in parallel 14 real functions that correspond to the real and imaginary parts of these independent contributions to the Green's tensor. As measure for the Gauss-Kronrod quadrature (stop criterion) we simply use the sum of these 14 functions.

To demonstrate the accuracy of our integration scheme we first per-

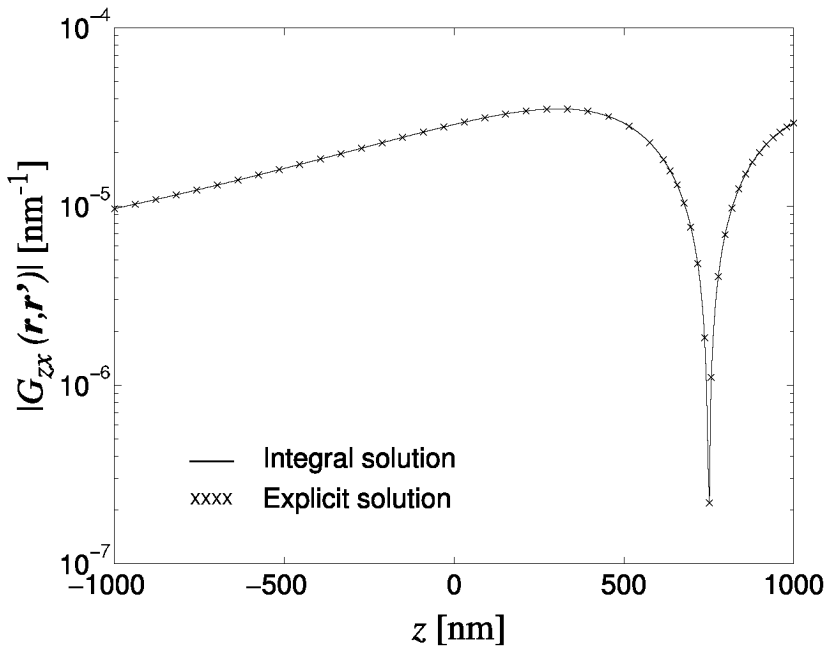


Figure 3.5. Accuracy of the method: comparison of the Green's tensor for a homogeneous medium obtained by numerical quadrature assuming four layers with identical permittivity (solid line) with that obtained from the explicit free space solution (equation (3.4), crosses). The zx component of $|G_{3D}|$ is shown.

form calculations for a system consisting of virtual layers, i.e., layers with identical permittivity and permeability. The results must be identical to the explicit solution given by the free space Green's tensor of a homogeneous medium, equation (3.4). Figure 3.5 shows the comparison for a virtual four-layer medium. Obviously, the agreement between the two calculations is perfect.

The presented integration procedure provides an accurate, stable and, in particular, generally applicable computation of the Green's tensor. The routine does not have to be adapted to the geometry under study and avoids a time consuming analysis of the integrands as necessary for calculating the residues [62] or integrating along the steepest descent path [50].

3.2.2 2D implementation

The mathematical structure of $G_{2D}(k_x; \mathbf{r}, \mathbf{r}')$ is similar to that of $G_{3D}(k_\rho; \mathbf{r}, \mathbf{r}')$: strongly oscillating and with the two above mentioned types of singularities. Hence, exactly the same integration technique as

in 3D can be applied if we take into account the following differences. Since in 2D the integration is performed in the complex k_x space and k_y^0 is constant throughout the entire stratified structure, the branch point singularities are at $k_x = k_{1,\parallel}, k_{L,\parallel}$ with $k_{l,\parallel} = (k_l^2 - k_y^0)^{1/2}$ and the upper limit for the pole singularities is given by $k_{l,\parallel}^{\max} = \max_l \Re(k_{l,\parallel})$. After avoiding these singularities in the forth quadrant we have again two possibilities to resume the integration: Either we follow the real k_x axis or (for $x \neq x'$) we deflect the integration path parallel to the imaginary axis with the correct direction chosen according to the sign of $x - x'$. In both cases the integrands converge exponentially [see equations (3.22) and (3.23)] and a comparison between $|z - z'|$ and $|x - x'|$ gives the path which provides fastest convergence. In contrast to 3D, in 2D both integration paths are equivalent with respect to their convergence and the deciding factor is $|z - z'| \leq \alpha|x - x'|$ with $\alpha = 1$.

Since the assumption of a translation invariance in one direction breaks the three-dimensional symmetry, we cannot reduce the number of independent terms as for $\mathbf{G}_{3D}(\mathbf{r}, \mathbf{r}')$. In general, 8 components must be calculated (note that $h_{xy} = h_{yx}$). Only when the incident field propagates in the xz plane ($k_y^0 = 0$) TE and TM polarization decouple and only 5 independent components remain (compare discussion in section 2.3).

3.3 Illustrative examples

In this section the physical substance of our mathematical formalism is illustrated with different examples. First, we discuss the physical meaning of the singularities in the 3D Green's tensor integrands and, then, the interpretation of the 2D Green's tensor as a field created by a line source.

3.3.1 Singularities of the integrand

Let us consider the most simple case of a stratified medium, a non-magnetic two-layer system $\varepsilon_1, \varepsilon_2$ separated by a single interface at $d = 0$. Assuming that \mathbf{r}' lies within layer 1 and \mathbf{r} within layer 2, the integrand $G_{zz}(k_\rho; \mathbf{r}, \mathbf{r}')$ reduces to

$$G_{zz}(k_\rho; \mathbf{r}, \mathbf{r}') = \frac{k_\rho^3}{k_2^2 k_{1z}} J_0(k_\rho \rho) T_{12}^P \exp[i(k_{1z} z' - k_{2z} z)], \quad (3.26)$$

where $T_{12}^P = 1 + \mathcal{F}_{12}^P = 2\varepsilon_2 k_{1z}/(\varepsilon_2 k_{1z} + \varepsilon_1 k_{2z})$ is the Fresnel transmission coefficient of the interface.

As already mentioned, branch point singularities exist for $k_\rho = \pm k_1, \pm k_2$. By definition, for any k_ρ lying on one of these branch cuts k_z is purely real, forming a wave propagating in $z \rightarrow \pm\infty$ direction. These waves define a continuum of modes called radiation modes.

In addition, pole singularities appear when the denominator of T_{12}^P vanishes, i.e., for k_ρ such that

$$\varepsilon_2 \sqrt{k_1^2 - k_\rho^2} + \varepsilon_1 \sqrt{k_2^2 - k_\rho^2} = 0. \quad (3.27)$$

The solutions of equation (3.27) are formally given by

$$k_\rho = \pm \sqrt{\frac{\varepsilon_1 \varepsilon_2}{\varepsilon_1 + \varepsilon_2}} k_0. \quad (3.28)$$

However, one has to verify if this solution is physically meaningful. If we choose ε_1 and ε_2 purely real and positive, obviously $k_\rho < k_1, k_2$. Hence, the square roots being also purely real and positive, equation (3.27) is not fulfilled. If we now assume that $\varepsilon_2 < 0$ and $\varepsilon_1 < |\varepsilon_2|$, a solution does exist. For such a plasma medium, the wave vectors in z direction k_{1z} and k_{2z} at the location of the pole k_ρ become

$$\begin{aligned} k_{lz} &= \pm \sqrt{k_l^2 - k_\rho^2} = \pm \sqrt{\varepsilon_l - \frac{\varepsilon_1 \varepsilon_2}{\varepsilon_1 + \varepsilon_2}} k_0 = \pm \sqrt{\frac{\varepsilon_l^2}{\varepsilon_1 + \varepsilon_2}} k_0 \\ &= i \sqrt{\frac{\varepsilon_l^2}{|\varepsilon_2| - \varepsilon_1}} k_0, \quad l = 1, 2. \end{aligned} \quad (3.29)$$

Referring to the discussion in section 3.2.1, the sign of the square root in equation (3.29) has been chosen such that the imaginary part is non-negative. Hence, k_{1z} and k_{2z} are pure imaginary and the field decays exponentially from the interface. The pole constitutes a surface plasmon mode. Similarly, for an appropriate choice of the material properties other surface modes can be found by analyzing the pole locations [58].

In a three-layer structure, in addition to the branch point singularities at $k_\rho = \pm k_1, \pm k_3$, poles singularities associated with guided modes can occur. If $k_\rho^2 > k_1^2$ and $k_\rho^2 > k_3^2$, the wave vectors in z direction $k_{1z} = (k_1^2 - k_\rho^2)^{1/2}$ and $k_{3z} = (k_3^2 - k_\rho^2)^{1/2}$ are imaginary and the field decreases exponentially in these outermost layers. Hence, k_ρ corresponds to the modes guided by the slab. Their number, i.e., the number of poles, depends on the wavelength and the thickness of the intermediate layer [63].

As an illustration, figure 3.6(a) shows the s-polarized contribution of the integrand along the real k_ρ axis for a symmetric planar GaAs/Al_{0.15}Ga_{0.85}As/GaAs waveguide structure at a $\lambda = 1.5 \mu\text{m}$ wavelength. According to a guided mode analysis, a similar structure with a $\Delta = 0.5 \mu\text{m}$ thick AlGaAs layer has one single s-polarized mode with $k_\rho = 14.6 \mu\text{m}^{-1}$. For a thicker AlGaAs layer, $\Delta = 2 \mu\text{m}$, three s-polarized modes exist with respectively $k_\rho = 14.9 \mu\text{m}^{-1}, 14.7 \mu\text{m}^{-1}, 14.5 \mu\text{m}^{-1}$. In figure 3.6(a) we observe that the integrands' divergences coincide perfectly with these eigenmodes.

We can also investigate more complicated structures, such as a planar waveguide coupler: We consider a symmetric GaAs/AlGaAs/GaAs/AlGaAs/GaAs system with the two guiding Al_{0.15}Ga_{0.85}As layers having identical thicknesses $\Delta = 0.5 \mu\text{m}$. The s-polarized contribution of the integrand along the real axis is plotted in figure 3.6(b). For a thick separating GaAs layer, $\Delta' = 2 \mu\text{m}$, the AlGaAs slabs are decoupled: Only one s-polarized mode can be excited at $k_\rho = 14.6 \mu\text{m}^{-1}$, like in the previous example. However, with decreasing separating layer thickness, the modes of the two waveguides can couple via their evanescent tails. The mode is split and the behavior of the structure develops towards that of a single layer waveguide. For a thin separating GaAs layer, $\Delta' = 0.05 \mu\text{m}$, the poles are located at $k_\rho = 14.8 \mu\text{m}^{-1}, 14.4 \mu\text{m}^{-1}$, corresponding to the modes of a single layer waveguide with $\Delta = 0.5 \mu\text{m} + 0.5 \mu\text{m} = 1 \mu\text{m}$.

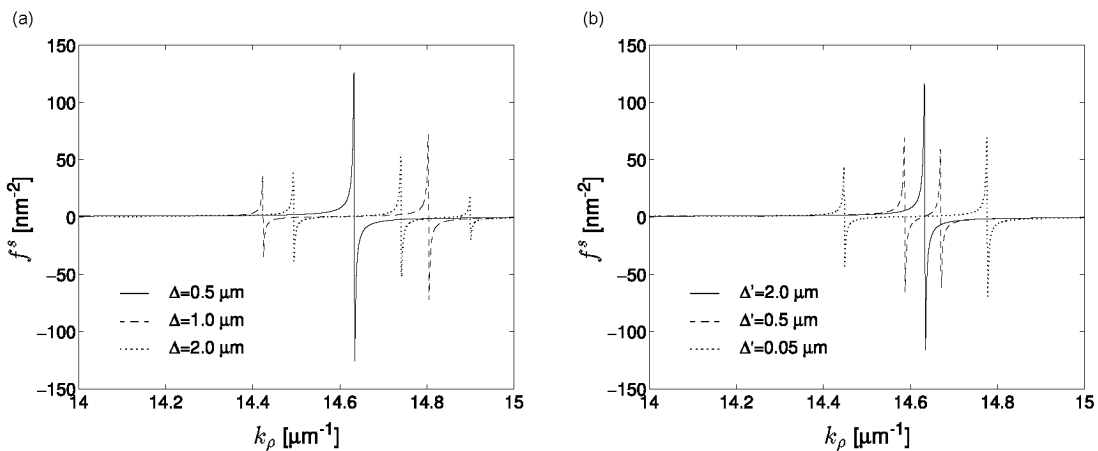


Figure 3.6. Integrand (s-polarization) for multilayer structures at a wavelength $\lambda = 1.5 \mu\text{m}$. (a) GaAs/Al_{0.15}Ga_{0.85}As/GaAs waveguide with three different widths Δ of the AlGaAs layer. (b) GaAs/AlGaAs/GaAs/AlGaAs/GaAs multilayer structure with three different widths Δ' of the separating GaAs layer.

3.3.2 The Green's tensor as a dipole field

To assess the physical substance of the 2D Green's tensor we consider a simple three layers system $\varepsilon_1 = 1$, $\varepsilon_2 = 9$, $\varepsilon_3 = 1$ with varying thickness h of the high permittivity slab, and study two components of the Green's tensor, G_{yz} and G_{zy} , as a function of the z coordinate of the observation point, $\mathbf{r}_\parallel = (\lambda, z)$. The source point $\mathbf{r}'_\parallel = (0, 1 \mu\text{m})$ is held fixed in the top layer. The vacuum illumination wavelength is $\lambda = 633 \text{ nm}$.

Let us first mention that both components vanish if the incident field does not have a component k_y^0 in y direction. (In that case TE and TM waves are decoupled and $G_{yx} = G_{xy} = G_{yz} = G_{zy} = 0$.) In our example, we use an illumination with a $11\bar{1}$ orientation, so that $k_y^0 = k_1/\sqrt{3}$. Figure 3.7 shows G_{yz} and G_{zy} when the high permittivity layer extends from $z = 0$ to $z = 430 \text{ nm}$. Since the Green's tensor represents the electric field radiated at \mathbf{r} by three orthogonal unit dipoles at \mathbf{r}' , its components must fulfill the respective boundary conditions at the interfaces [37]. Correspondingly, G_{yz} (the y component of a z -oriented dipole) is continuous across the interfaces, whereas G_{zy} (the z component of a y -oriented dipole) jumps by a factor $\varepsilon_2/\varepsilon_1 = 9$ and $\varepsilon_3/\varepsilon_2 = 1/9$, respectively.

It is quite surprising that in the lower layer ($z < 0$) both components are identical (figure 3.7). However, it can be shown that for \mathbf{r}' and \mathbf{r} in the two outermost layers 1 and L the components of the Greens tensor

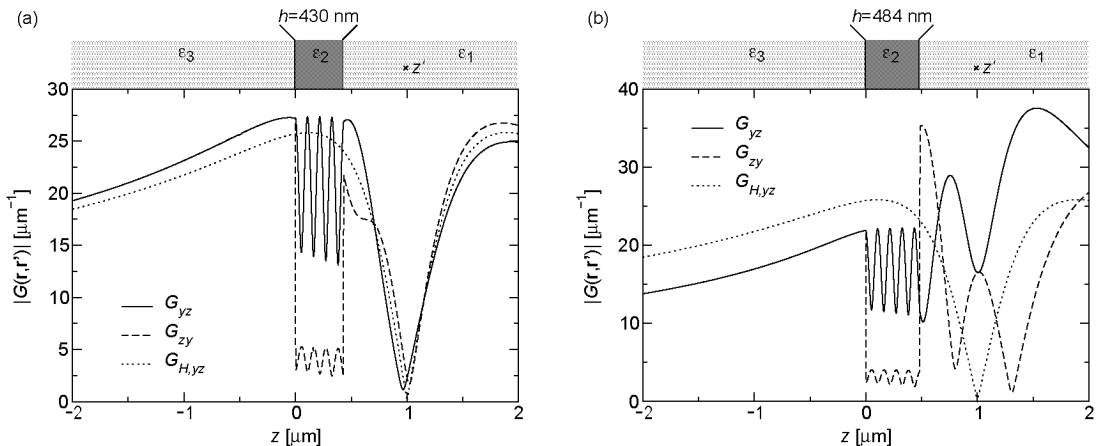


Figure 3.7. Green's tensor components for a stratified background ($|G_{yz}|$ and $|G_{zy}|$) and a homogeneous background ($|G_{H,yz}| = |G_{H,zy}|$) at a wavelength $\lambda = 633 \text{ nm}$. The permittivity of the homogeneous medium is $\varepsilon_H = 1$. The line source at $z' = 1 \mu\text{m}$ is located in the top layer and held fixed. Two different thicknesses of the high permittivity layer are considered: (a) $h = 430 \text{ nm}$ and (b) $h = 484 \text{ nm}$.

are coupled (see **P1** and **P3**):

$$\frac{G_{\alpha z}}{k_{1z}} = \frac{G_{z\alpha}}{k_{Lz}}, \quad \alpha = x, y, \quad (3.30)$$

where $k_{lz} = (k_l^2 - k_x^2 - k_y^{02})^{1/2}$, $l = 1, L$. Since in our example \mathbf{r}' is located in the top layer and $k_{1z} = k_{3z}$, the components coincide for $z < 0$ (figure 3.7).

Let us now discuss the asymptotic relation between the Green's tensor for a stratified medium and that associated with a homogeneous background ε_H . When $\mathbf{r}_\parallel - \mathbf{r}'_\parallel$ becomes large, the plane wave expansion of the Green's tensor is mainly governed by the plane wave which propagates in radial direction, $\mathbf{k}_\parallel / |\mathbf{k}_\parallel| = (\mathbf{r}_\parallel - \mathbf{r}'_\parallel) / |\mathbf{r}_\parallel - \mathbf{r}'_\parallel|$. Hence, with x fixed and $z \rightarrow \pm\infty$, the integrals in equation (3.19) are dominated by the $k_x = 0$ terms. In this limit, the ratio between the free space component and the component with stratification is given by the reflection and transmission coefficients of the stratified structure corresponding to this single plane wave. For a three-layer structure the transmission coefficient \mathcal{T} for G_{yz} and G_{zy} reads [15]:

$$\mathcal{T} = \frac{\mathcal{T}_{12}\mathcal{T}_{23} \exp(ihk_{2z})}{1 + \mathcal{R}_{12}\mathcal{R}_{23} \exp(2ihk_{2z})}, \quad (3.31)$$

where $\mathcal{R}_{l,l+1}$ and $\mathcal{T}_{l,l+1}$ are the Fresnel reflection and transmission coefficients:

$$\mathcal{R}_{l,l+1} = \frac{\varepsilon_{l+1}k_{lz} - \varepsilon_l k_{l+1z}}{\varepsilon_{l+1}k_{lz} + \varepsilon_l k_{l+1z}}, \quad (3.32a)$$

$$\mathcal{T}_{l,l+1} = \frac{2\varepsilon_{l+1}k_{lz}}{\varepsilon_{l+1}k_{lz} + \varepsilon_l k_{l+1z}}. \quad (3.32b)$$

Note that equations (3.32a) and (3.32b) give the coefficients for a p-polarized plane wave which corresponds to the polarization of G_{yz} and G_{zy} (see appendix of **P1**).

An analysis of equation (3.31) yields as condition for maximal transmission through the slab with thickness h

$$h_{\max} k_{2z} = n\pi, \quad (3.33a)$$

and for minimal transmission

$$h_{\min} k_{2z} = (n + \frac{1}{2})\pi, \quad (3.33b)$$

where $n = 1, 2, 3, \dots$. Since $k_{2z} = \sqrt{k_2^2 - k_y^{02}}$, maximal and minimal transmission through the slab in our example are obtained when

$h_{\max} \approx n \cdot 107.5 \text{ nm}$ and $h_{\min} \approx (n + 1/2) \cdot 107.5 \text{ nm}$, respectively. The corresponding coefficient of maximal and minimal transmission is $|\mathcal{T}_{\max}| = 1$ and $|\mathcal{T}_{\min}| \approx 0.69$, respectively [equation (3.31)]. Hence, the plane wave is completely transmitted without any reflection through a slab with thickness h_{\max} .

In figure 3.7(a) [$h = 430 \text{ nm} = 4 \cdot 107.5 \text{ nm}$, maximal transmission, see equation (3.33a)], we also report the component $G_{H,yz} = G_{H,zy}$ of the Green's tensor associated with a homogeneous background $\epsilon_H = 1$. In the far field limit $z \rightarrow \pm\infty$ we observe that indeed the components for the stratified structure converge to the free space solution. At $z = \pm 2 \mu\text{m}$ the difference is less than 5% and at $z = \pm 10 \mu\text{m}$ it is $\approx 1\%$ (not shown). For comparison, we also study a second structure with $h = 484 \text{ nm} \approx (4 + 1/2) \cdot 107.5 \text{ nm}$. Figure 3.7(b) shows G_{yz} , G_{zy} and $G_{H,yz}$ for this geometry with minimal transmission [see equation (3.33b)]. At $z = -2 \mu\text{m}$ the ratio $|G_{yz}/G_{H,yz}| \approx 0.75$ and at $z = -10 \mu\text{m}$ $|G_{yz}/G_{H,yz}| \approx 0.70$ (not shown) is close to 0.69, as expected from the above calculation.

Chapter 4

Applications

In this chapter we apply the formalism developed in the previous chapters to a broad spectrum of scattering problems. The first and most extensive part is devoted to the study of light–coupling masks for optical contact lithography. Then we investigate integrated optical waveguides, surface plasmon–polaritons, scanning near–field optical microscopy and, finally, in a more academic study, light scattering by a cylinder in the presence of a surface. The Green’s tensor technique is very well adapted for the simulation of these geometries because it is possible to decompose them into a stratified background with embedded scatterers.

4.1 Light–coupling masks

Following the laws of image formation in a lens system, the ultimate resolution Δ for pattern replication with optical lithography is given by the diffraction limit [15]:

$$\Delta \approx a \frac{\lambda}{NA}, \quad (4.1)$$

where a is a process parameter, λ is the vacuum wavelength and NA is the numerical aperture. Whereas for projection lithography this relation restricts the ultimate resolution to $\Delta \approx \lambda/2$, for contact lithography this limit is further reduced. Since the refractive index n of the mask lowers the effective wavelength λ_{eff} , structures with a size $\Delta \approx \lambda_{\text{eff}}/2 = \lambda/(2n)$ can be realized with this technique. For example, with a conventional glass mask ($n \approx 1.5$) the resolution is enhanced to $\Delta \approx 248/(2 \cdot 1.5) \text{ nm} = 80 \text{ nm}$. Even smaller structures can be replicated using the evanescent near field created by each opening in the mask [64]. Hence, contact lithography can, in theory, replicate features below the wavelength of the incident light. Moreover, the required illumination sources are simple,

no sophisticated imaging optics are necessary and large fields can be exposed in one step.

However, substrate topography and ubiquitous dust particles prevent the conventional hard chrome-on-glass mask from establishing a close contact with the substrate, thus limiting the maximal resolution by the minimally attainable gap size. On the other hand, excellent optics in conjunction with step and repeat exposure provide the projection of mask patterns on slightly uneven resist surfaces with an accuracy close to the diffraction limit [2]. Nowadays, manufacturing processes are usually rather based on projection lithographies than on contact lithographies.

In the recent years, with the development of new innovative mask concepts, research interest has been revived in utilizing the advantages of optical contact lithography for replicating structures in the subwavelength regime. There are several approaches to this task: high-resolution contact masks with protruding metal absorbers (metal-protruding masks) [8, 65], masks where the absorbers are embedded in the transparent background material (metal-embedded masks) [66, 67], topographically patterned masks with air gaps and recessed absorbers (light-coupling masks) [68], and structured masks where no absorbers are used (phase masks) [69]. Whereas the latter approach is based on interferences between light passing through materials with different optical thicknesses, the first three techniques use an amplitude contrast between transparent and opaque parts of the mask. With all of these techniques the formation of features in the 100 nm range was successfully demonstrated. The mask concepts have in common that they rely on a flexible glass or polymer, which allows the mask to be placed in contact with the entire substrate (“soft lithography”). This is the most important requirement for reliable subwavelength contact lithography.

In this section we focus on the performances of light-coupling masks (LCMs) for optical lithography, we test the limits of this approach and study the dependence of the near-field distribution in LCMs on typical experimental parameters. We further compare this technique to a related amplitude mask concept (metal-embedded masks) and investigate the contrast mechanisms with emphasis to their usability for subwavelength patterning.

4.1.1 Principle of LCMs

LCMs are siloxane polymer masks for optical contact lithography. Figure 4.1(a) shows a schematic view of an LCM and its operation. The surface of the mask is topographically patterned such that the areas

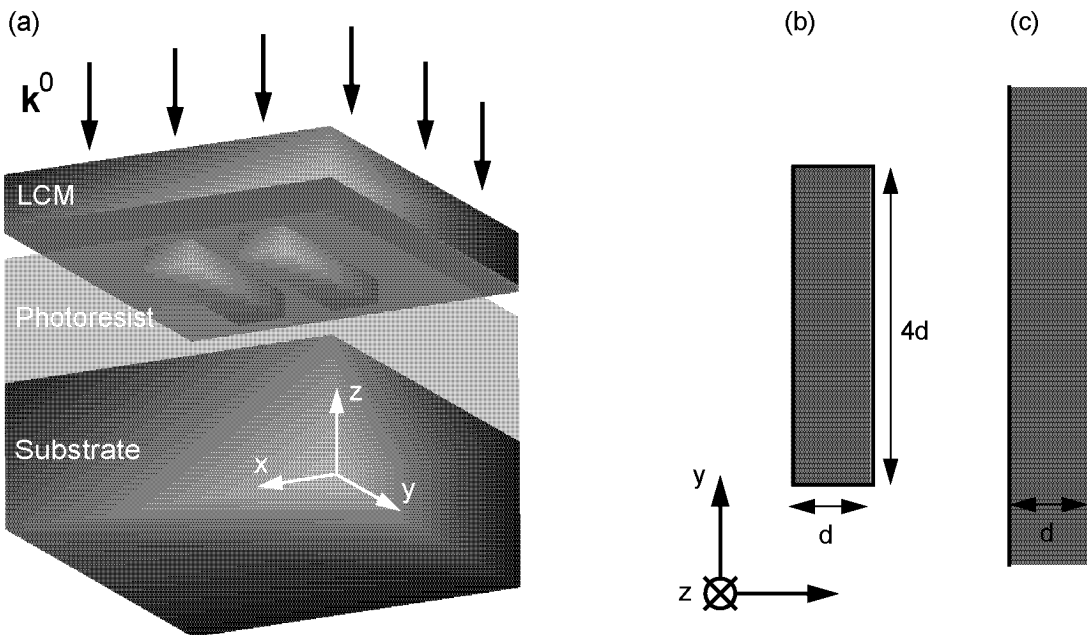


Figure 4.1. (a) Schematic view of an LCM and its operation using a normal incident field \mathbf{E}^0 through the backside of the LCM. The structures to be replicated are formed by protrusions at the bottom side of the polymer mask. For the simulation, we use either (b) 3D “linelets” with a width d and a length $4d$ or (c) 2D lines extending infinitely in y direction with a line width d .

to be exposed in the photoresist form protrusions on the mask surface. Placing such a “light stamp” in intimate contact with a resist-coated substrate, mechanical contact between mask and resist layer occurs only in the region to be exposed. The ability of a rubber elastic polymer to adapt to the substrate topography allows the formation of a uniform “conformal” contact with the photoresist over large areas [70]. When the LCM is illuminated through its backside, the light is differentially guided by the structure and coupled into the photoresist. In order to suppress the leaking of light through the non-contacting areas of the mask, a thin metal absorber is added in the recessed parts. It was demonstrated experimentally [71] and by simulations [72] that such a metallic layer considerably improves the contrast compared to an LCM without additional absorbers.

The mechanical stability of the protrusions limit the achievable resolution of LCMs, especially as lateral dimensions shrink and the ratio of lateral to vertical dimensions (aspect ratio) becomes large [70, 73]. Using this approach, Schmid *et al.* demonstrated the formation of features in the 100 nm range with a wavelength of 256 nm [71].

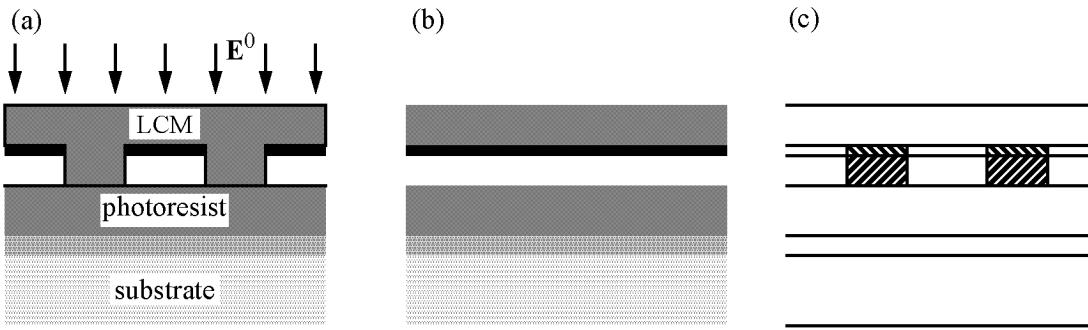


Figure 4.2. Cross sectional view of an LCM. (a) The structures to be written in the photoresist are defined as protrusions on a soft polymer substrate. This structure can be decomposed into a stratified background (b) with embedded scatterers of various permittivities (c). In this example, a bottom antireflection coating is deposited between the substrate and the photoresist (see section 4.1.3 D).

4.1.2 Simulation with the Green's tensor technique

Since the entire lithography structure is planar [figures 4.1, 4.2(a)], it can be decomposed into several layers: the polymer layer on top, a thin gold absorber, an air gap, the photoresist, potentially a bottom antireflection layer between resist and substrate (see section 4.1.3 C), and the substrate at the bottom. The light-guiding protrusions define variations of this stratified background and are obviously identical to the embedded scatterers from chapter 2. Hence, with our approach only the protrusions must be discretized, the stratified background being accounted for by the Green's tensor [figures 4.2(b) and (c)].

Note that, although the protrusions are made entirely of polymer, the discretized dielectric contrast $\Delta\epsilon_i$ that enters in the system of equations (2.8) is different for the meshes located in the gold absorber and those in the air layer [figure 4.2(c)].

4.1.3 Numerical results

For our simulations we consider different structures, depending on the effect we want to investigate. To study the impact of the polarization of the illumination light (subsection A below), the resolution limit of LCMs (subsection B below), and the reflection on the substrate (subsection C below) we consider short, densely packed lines of width d and length $4d$ [see figure 4.1(b)]. These “linelets” are known to be difficult to replicate optically owing to line shortening effects and crosstalks [2]. Since these structures are finite in all three directions, the 3D Green's tensor must be

used for the calculations. On the other hand, to compare the performance of LCMs with a different approach to high-resolution contact lithography (subsection D below), we consider isolated lines with a line width $d = 100\text{ nm}$ [see figure 4.1(c)]. These lines extend infinitely in one direction and require the 2D Green's tensor.

The determinant parameter to characterize a given exposure is the intensity $I = \mathbf{E} \cdot \mathbf{E}^*$ in the photoresist. The results presented here refer to a plane wave illumination normal to the mask surface with a vacuum wavelength $\lambda = 248\text{ nm}$ (the intensity of the incident field is normalized to unity). The polarization of the incident light is circular except in subsection A where we show that this polarization provides a homogeneous illumination for arbitrarily shaped features. The optical properties of the simulated material systems are assumed to be linear and isotropic. The relative permittivities at $\lambda = 248\text{ nm}$ are $\varepsilon = 2.25$ for the polymer mask background, $\varepsilon = 2.5$ for the photoresist, $\varepsilon = -3.4 + i3.6$ for chrome, $\varepsilon = -0.9 + i4.3$ for gold, and $\varepsilon = -9 + i11$ for the silicon substrate [74]. If not stated otherwise, the total height of the protrusions is 60 nm and the thickness of the metal absorber is 15 nm.

For the 3D structures we use a $\Delta_x = \Delta_y = \Delta_z = 15\text{ nm}$ discretization mesh and for the cross sections of the 2D lines a $\Delta_x = \Delta_z = 5\text{ nm}$ discretization mesh.

A. Polarization effects

The polarization of the illuminating light has a strong impact on the near-field close to the structure, because the continuity equations at the material boundaries determine the field distribution. This effect is particularly important for structures smaller than the wavelength. Since in the experiment the incident polarization can be chosen in a controlled manner, we want to investigate to what extent this parameter can be used to improve the replication of a subwavelength structure.

In figure 4.3 we show isosurfaces of the field intensity distribution in the photoresist, created by an isolated linelet with $d = 120\text{ nm}$, for three incident polarizations. The best results are achieved with a polarization in y direction, i.e., parallel to the linelet. In that case, the structure shape is reproduced accurately, steep edges providing approximately a 1:1 image of the linelet in the resist layer [figure 4.3(a)]. On the other hand, using a polarization in x direction leads to an irregular field distribution with intensity variations along the feature sides as well as in the depth [figure 4.3(b)]. As a complete mask possesses structures in both directions, circular polarization provides a homogeneous illumina-

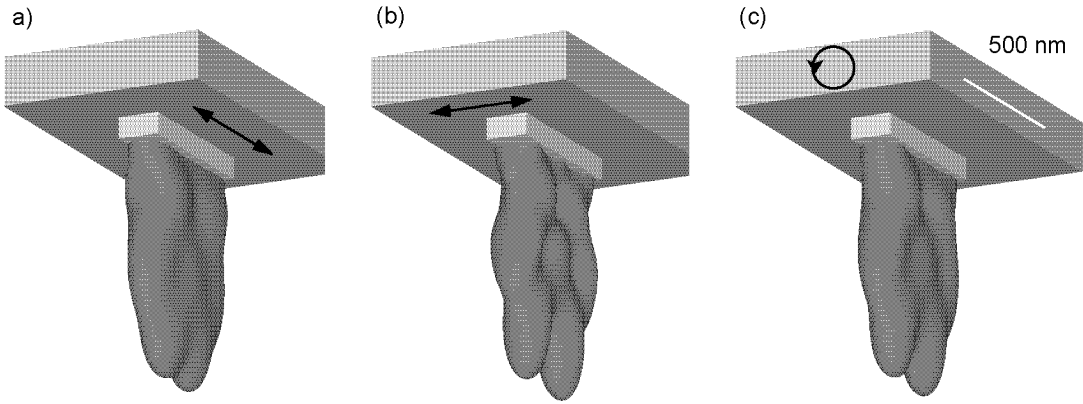


Figure 4.3. Illumination of an isolated linelet with $d = 120 \text{ nm}$. The isosurface representing 75% of the incident light intensity is shown in the photoresist. The polarization of the incident light is (a) linear in the y direction, (b) linear in the x direction and (c) circular. The extension of the isosurface in the photoresist is approximately 650 nm.

tion. Indeed, the field distribution for circular polarization turns out to be close to the ideal parallel polarization case, independent of the linelets' orientation [compare figures 4.3(a) and (c)].

B. Resolution limits

Let us now study the minimal size of structures replicated with LCMs at a $\lambda = 248 \text{ nm}$ illumination wavelength. Figure 4.4 shows isosurfaces of the field intensity distribution in the photoresist created by an isolated linelet, but with smaller extensions than in figure 4.3: $d = 90 \text{ nm}$ and $d = 60 \text{ nm}$. In both cases it is still possible to reproduce the struc-

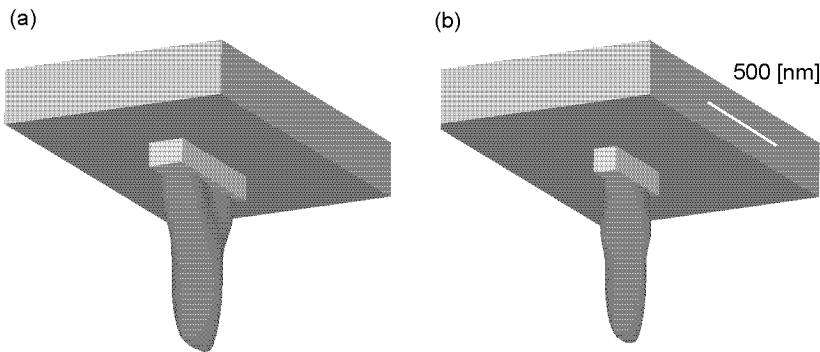


Figure 4.4. Isosurfaces of the electric field intensity (75%) in the photoresist using isolated linelets with (a) $d = 90 \text{ nm}$ and (b) $d = 60 \text{ nm}$. The extension of the isosurface in the photoresist is approximately 400 nm.

ture shape in the photoresist, even for features smaller than 1/4 of the vacuum wavelength of the illuminating light [figure 4.4(b)]. Note however, that deeper in the photoresist the aspect ratio of the isosurfaces (width:length) no longer corresponds to the aspect ratio of the original linelet (1:4). This deformation of the isosurface increases with the depth in the photoresist, so that 100 nm below the mask the aspect ratio for $d = 90$ nm is reduced to 1:3 and for $d = 60$ nm even to 1:2. The field distribution in the photoresist is more constrained leading to a strong line shortening of the replicated structure. However, figure 4.4 also shows that structures in the 50 nm range are amenable to this technique but imply a replication within a very thin layer of photoresist.

A realistic mask is not composed of isolated structures but contains a high pattern density. For increasing density, the crosstalks between neighboring structures become more and more important. Figures 4.5(a)–(c) show isosurfaces of the field intensity distribution in the photoresist for two linelets with $d = 120$ nm. The separation between the linelets is $2d$, $1.5d$, and d . In all cases, crosstalks between neighboring features are relatively small, especially within the relevant resist depth, where the field distribution replicates the mask structure accurately. However, for small separations, the distance between the isosurfaces of the two field distributions increases as light propagates into the

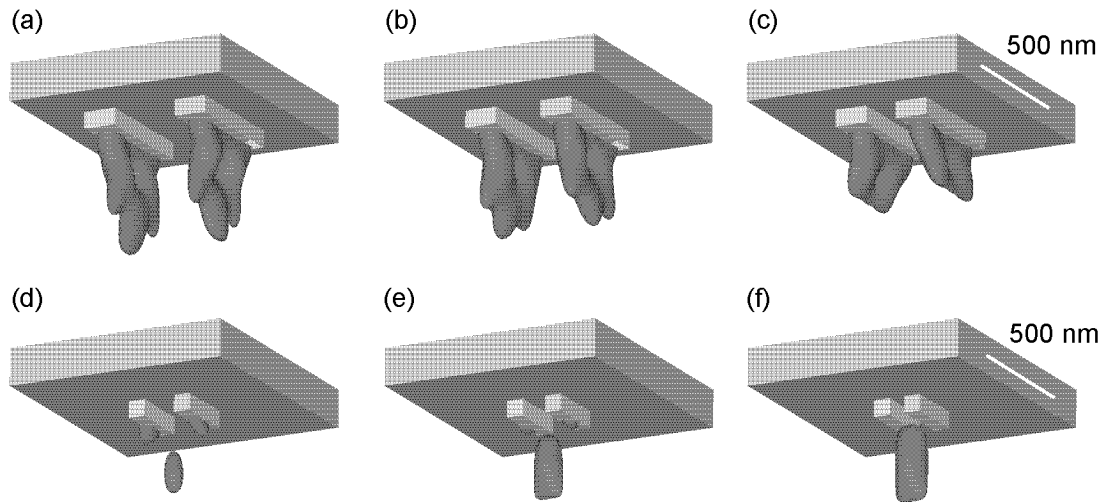


Figure 4.5. Isosurfaces of the electric field intensity (75%) in the photoresist using two linelets. The top row shows structures with $d = 120$ nm and separations of (a) $2d$, (b) $1.5d$, and (c) d , the bottom row shows structures with $d = 60$ nm and separations of (d) $2d$, (e) $1.5d$, and (f) d . The extension of the isosurface in the photoresist is approximately 400 nm in (a), 65 nm in (d), and 35 nm in (e).

photoresist [figure 4.5(c)].

In figures 4.5(d)–(f) the extension of the linelets is reduced to $d = 60\text{ nm}$. For such small structures, crosstalks turns out to be much more important. In the case of a separation equal to d the field distribution no longer reproduces the individual mask features, and a collective scattering behavior is observed: The incident light is focused by the structure such that a single spot appears between the linelets [figure 4.5(f)]. Note however that an isolated structure with $d = 60\text{ nm}$ can be replicated satisfactorily [figure 4.4(b)]. By increasing the separation to $1.5d$ [figure 4.5(e)] and $2d$ [figure 4.5(d)] one recovers the individual features in the near field. With a separation of $1.5d$ the isosurface has a length of 100 nm and a width of 40 nm , whereas for a separation of $2d$ the isosurface length is 140 nm and the width 60 nm . This corresponds to the same line shortening as for the isolated linelet.

Working with such small structures, therefore, requires special care to suppress crosstalks. Furthermore, the resist thickness appears to be crucial in that case.

C. Bottom antireflection coating

Since the absorption in a real photoresist is limited, quite some light travels through the resist layer, impinges on the substrate and is reflected back. With a strongly reflecting substrate, this can lead to a disturbing interference pattern in the photoresist. Figure 4.6(a) shows such a situation in a practical lithography experiment using a silicon substrate.

To avoid reflections at the resist–substrate interface, usually an absorbing layer is added on top of the substrate before spinning the photoresist (figure 4.2) [75]. The optimal height Δ_{BARC} of such a bottom antireflection coating (BARC) is given by the minimum of the reflected amplitude A_{refl} . Figure 4.7 shows A_{refl} as a function of Δ_{BARC} for a normally incident plane wave and a BARC with relative permittivity $\varepsilon = 1.98 + i1.23$. For $\Delta_{\text{BARC}} = 0$, i.e., without the BARC, the electric field is strongly reflected, $A_{\text{refl}} \approx 0.73$. With increasing Δ_{BARC} the reflection is reduced reaching a minimum for 60 nm with $A_{\text{refl}} \approx 0.04$. Note that this minimum is not simply given by $\lambda/4$ as for non-absorbing media [15]. For large Δ_{BARC} the entire energy is absorbed in the BARC and only the first interface between resist and BARC determines the reflected amplitude, $A_{\text{refl}} \approx 0.14$.

The influence of a BARC with this optimal thickness $\Delta_{\text{BARC}} = 60\text{ nm}$ is shown in figure 4.6(b). We observe that the BARC efficiently suppresses the interferences, although the field in the photoresist, created

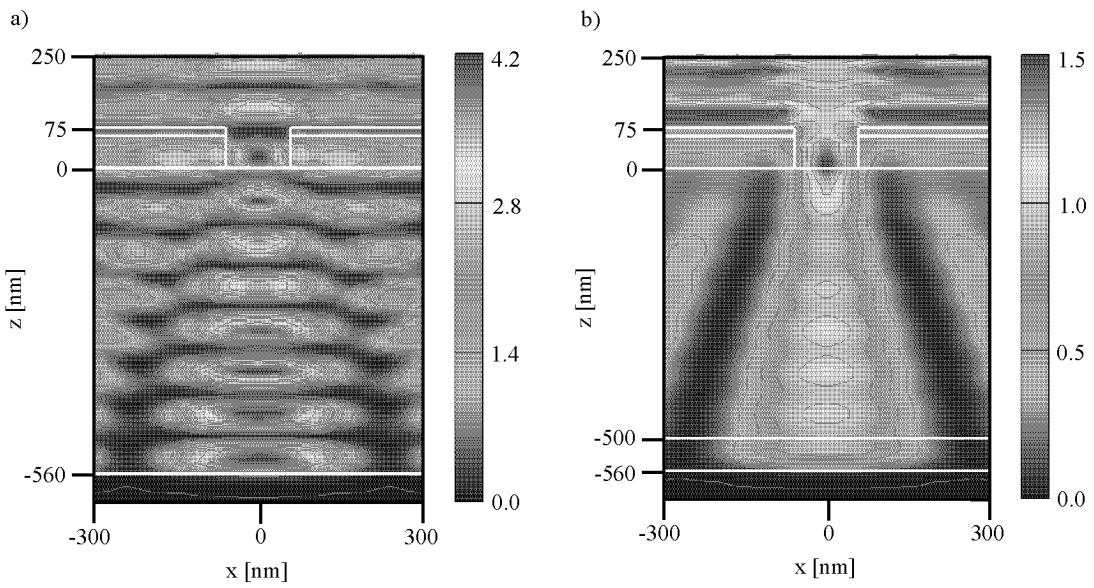


Figure 4.6. Electric field intensity for an isolated linelet with $d = 120 \text{ nm}$. Cross sectional views through the center of the structure. (a) Reflections at the photoresist–substrate interface lead to a disturbing interference pattern in the photoresist. (b) To suppress this effect a 60 nm thick bottom antireflection coating (BARC) is deposited on the substrate.

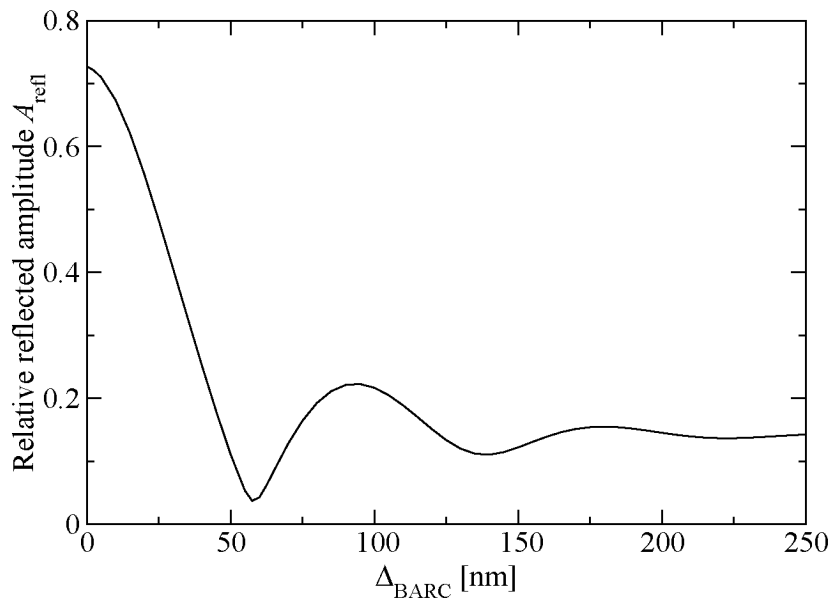


Figure 4.7. Relative reflected amplitude A_{refl} for the layered structure consisting of resist, bottom antireflection coating (BARC) and silicon substrate as a function of the BARC thickness Δ_{BARC} . The structure is illuminated with a normally incident plane wave.

by the propagation and scattering at the mask protrusion, is not a simple plane wave.

D. Contrast mechanisms

To assess the performances of LCMs for subwavelength lithography we now compare this technique with a related one based on masks where the absorbers are embedded in the transparent polymer background (metal-embedded masks, MEMs) [66, 67]. In both cases the light travels through the homogeneous transparent background material into the photoresist. Figure 4.8 shows a schematic view of these two mask types. Obviously, an MEM is equivalent to an LCM with completely metal-filled air gaps.

For this study we consider isolated lines extending infinitely in one direction [see figure 4.1(c)] and use therefore the 2D model. We first compare the contrast that can be achieved by the different techniques. For this purpose we define the contrast C as

$$C = \frac{I_{\max} - I_0}{I_{\max} + I_0}, \quad (4.2)$$

where I_{\max} is the maximal intensity of the transmitted light and I_0 is the intensity of the light that leaks through the absorbers and forms the background for the exposure.

If the air gaps of an LCM with a fixed total protrusion height h are filled with metal, the contrast increases, because the additional absorber significantly lowers the background I_0 . However, as a thicker metal also lowers the intensity transmitted into the resist, there is a tradeoff between good contrast and enough light passing through the mask. In the following we shall consider an LCM with a constant metal thickness of $a = 20$ nm and study the influence of the lateral air gaps. (In **P5** we

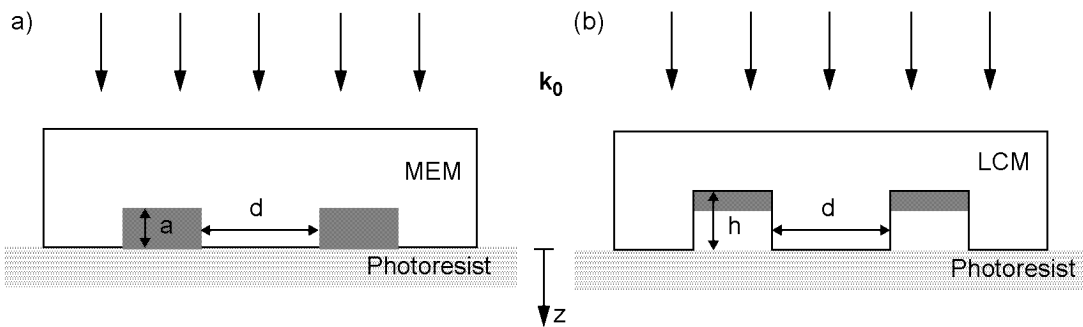


Figure 4.8. Schematic view of the two compared masks for contact lithography:
(a) metal-embedded mask (MEM) and (b) light-coupling mask (LCM).

find this thickness being optimal for the transmitted intensity.) Figure 4.9 reports the contrast of LCMs with chrome or gold absorbers as a function of the total protrusion height h . Note that h includes both the absorber thickness a and the remaining air gap. Chrome proves to be the metal that produces highest contrast because of its greater reflectivity and absorption. We further notice that C reaches a maximum at $h = 75$ nm. This maximum corresponds to the maximal reflectivity of the metal-air slab, leading to a minimum of I_0 . Thus, by choosing the appropriate total protrusion height, the contrast can be increased by 15% for a gold absorber and by 10% for a chrome absorber. As this effect is solely related to the air gap of the LCM, it is independent of the absorber thickness a . For a thicker absorber (leading to a reduction of the background), a similar effect is observed and an optimal total protrusion height h can be found.

The intensity distribution should ideally show not only a large difference between the regions to be illuminated and the shadowed regions, but also a shape that accurately replicates the pattern in the resist. To

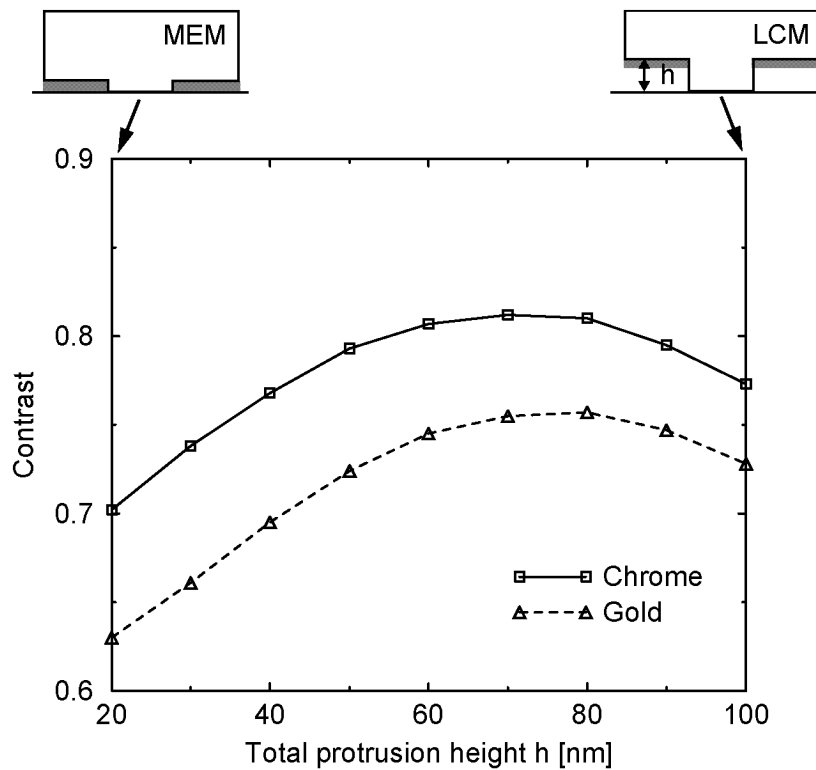


Figure 4.9. Contrast of LCMs as a function of the total protrusion height h at $z = 10$ nm. All masks have a 20-nm-thick chrome or gold absorber. The leftmost values correspond to an MEM with $a = 20$ nm.

assess this requirement as a function of the additional air gap we computed the electric field at different depths in the photoresist, $z = 10 \text{ nm}$, $z = 100 \text{ nm}$ and $z = 250 \text{ nm}$, and determined the full width at half maximum (FWHM) of the intensity distribution. Figure 4.10(a) presents line cuts through the intensity distribution close to the mask ($z = 10 \text{ nm}$) for an LCM and an MEM. The masks have a 20-nm-thick gold absorber, the total protrusion height h of the LCM is 80 nm, which is close to the optimum in figure 4.9. The FWHM of both line cuts is approximately 90 nm, and the intensity at the edges of the mask has dropped to $I = 0.6$ (recall that the intensity of the illumination is normalized, $I = 1$). With the additional air gap of the LCM, however, the confinement of the transmitted light is improved, leading to a slightly greater maximal intensity. This effect is even more pronounced for the intensity distribution deeper in the photoresist. Figure 4.10(b) shows line cuts of 100 nm and 250 nm depth in the photoresist. The shape of the intensity distributions becomes substantially more narrow and higher for the LCM. The FWHM decreases by approximately 10% at $z = 100 \text{ nm}$ and even by approximately 20% at $z = 250 \text{ nm}$, compared to MEM. Concurrently, at both depths the peak intensity is 10% greater for LCM than for MEM. The air gap in the LCM improves the guiding of the light into the resist, resulting in greater directionality without the loss of intensity that would occur with thick full-metal absorbers. At the corners of the targeted line, 100 nm deep in the photoresist, the relative intensity is

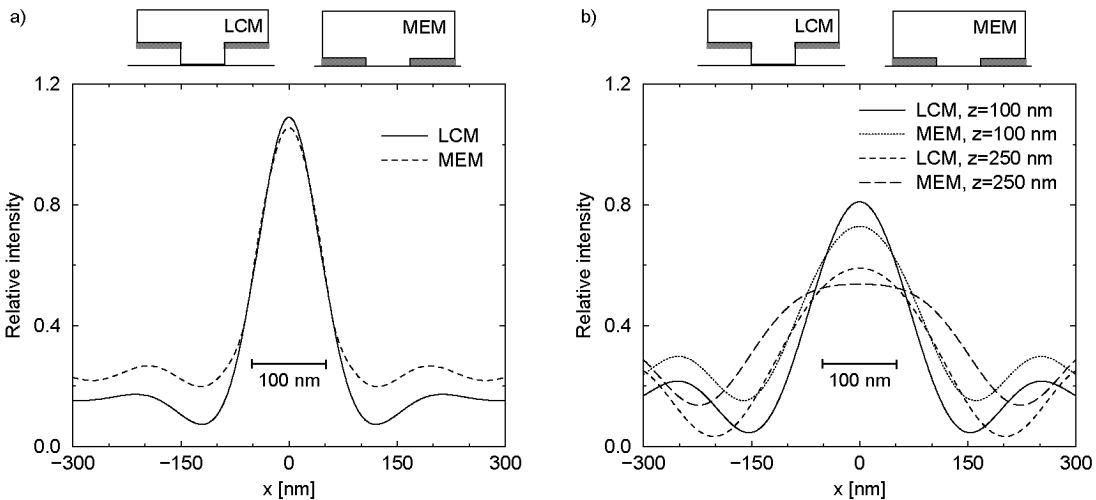


Figure 4.10. Relative intensity distributions for an MEM and an LCM at (a) $z = 10 \text{ nm}$ and (b) $z = 100 \text{ nm}$ and 250 nm . Both masks have a 20-nm-thick gold absorber; the total protrusion height of the LCM is $h = 80 \text{ nm}$. The bar represents the original line width.

$I = 0.6$ for both masks. This is still close to the value at $z = 10$ nm [figure 4.10(a)], thereby providing steep edges in the developed resist. At $z = 250$ nm the targeted line is defined only by the $I = 0.5$ isointensity lines for both masks. Hence, this corresponds to the bottom region of the developed photoresist.

In **P5** we further extend the comparison to masks with protruding metal absorbers (MPMs). We find that these masks, from an optical point of view, are inferior to MEMs and LCMs, because reflections at the two interfaces mask–air and air–photoresist lower the transmitted intensity and the achievable contrast.

In principle, all three amplitude mask types are capable of subwavelength resolution. However, the different contrast mechanisms imply different intensity distributions in the photoresist during exposure. For MEMs and MPMs a thicker metal absorber leads to an enhanced contrast but also lowers the intensity in the photoresist and, consequently, requires a more costly experimental setup. Especially with MPMs the amount of transmitted light is strongly reduced (see **P5**). The contrast can be further increased by an additional air gap below the metal absorbers [LCMs, figure 4.10(a)]. Since these air gaps improve the directional guiding of light, the intensity distribution remains better confined even deeper inside the photoresist.

4.2 Planar waveguides

In many applications the coupling of optical energy out of or into a waveguide is obtained by a grating deposited on top of the structure [57]. The properties of such a grating, like the coupling efficiency and the angular distribution of the radiated electric field, strongly depend on the shape, the size and the periodicity of the individual elements forming the grating [76]. For a quantitative analysis the collective behavior of these elements must be taken into account. However, from a physical point of view, much can be learned from the reduced problem of a “grating” composed of a single element. Hence, we start in section 4.2.1 with a study of the scattering by a single 3D defect on top of a planar waveguide. Then, in section 4.2.2 we investigate the effects due the coupling between such elements for a 2D grating coupler.

4.2.1 3D defect

In this section we focus on the scattering by a 3D rectangular notch in the planar InP/InGaAsP waveguide structure depicted in figure 4.11.

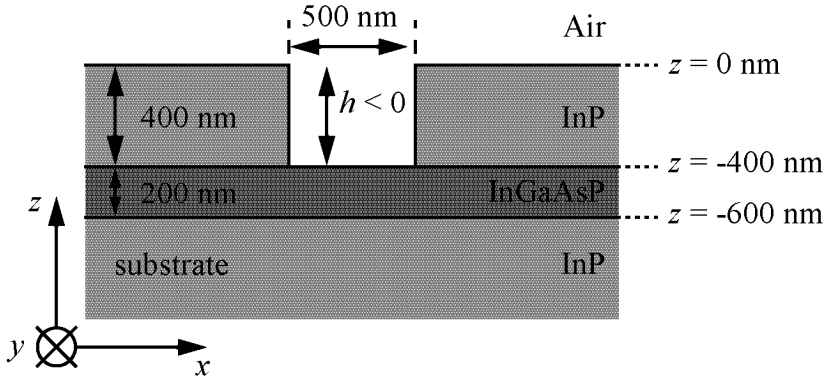


Figure 4.11. Geometry of the investigated InP/InGaAsP planar waveguide structure (permittivities: $\epsilon_{\text{InP}} = 10.05$, $\epsilon_{\text{InGaAsP}} = 11.42$, wavelength $\lambda = 1.55 \mu\text{m}$). A notch with depth $h = -500 \text{ nm}$ and finite lateral extension (500 nm) in both the x and the y directions is etched through the structure.

The notch with a negative height $h = -400 \text{ nm}$ is etched in z direction through the waveguide cladding and has an extension of $0.5 \times 0.5 \mu\text{m}^2$ in the x and y directions. Note that the dielectric contrast $\Delta\epsilon$ associated with this scatterer is negative, since its permittivity (air, $\epsilon = 1$) is lower than the permittivity of the surrounding medium [see equation (2.3)]. For the results presented in this section we use a $\Delta_x = \Delta_y = \Delta_z = 50 \text{ nm}$ discretization mesh.

At a wavelength $\lambda = 1.55 \mu\text{m}$ the planar InP/InGaAsP waveguide supports a transverse electric mode (TE_0 , electric field polarized in y direction) and a transverse magnetic mode (TM_0 , electric field polarized in the xz plane). The corresponding propagation constants are $\beta_{\text{TE}_0} = 12.96 \mu\text{m}^{-1}$ and $\beta_{\text{TM}_0} = 12.92 \mu\text{m}^{-1}$ [77].

Figure 4.12 shows cross sectional views of the electric field amplitude $|\mathbf{E}| = \sqrt{\mathbf{E} \cdot \mathbf{E}^*}$, when a TE_0 mode is used as excitation (we assume that the incident mode propagates in positive x direction). The incident mode is reflected at the waveguide-air interface and an interference pattern caused by the interaction of the incident field with the reflected one appears on the left-hand side of the notch [figure 4.12(a)]. In the forward direction the propagation of the mode is disrupted and the field amplitude is depleted just behind the defect. However, because of the defect's finite lateral extension, this depletion remains localized and the mode re-establishes after $2 \mu\text{m} \approx 4\lambda_{\text{InGaAsP}} = 4\lambda/\sqrt{\epsilon_{\text{InGaAsP}}}$. Further, the scattering by the notch leads to a deflection of the incident mode towards the substrate.

Some light is also coupled out upwards into the air, which is empha-

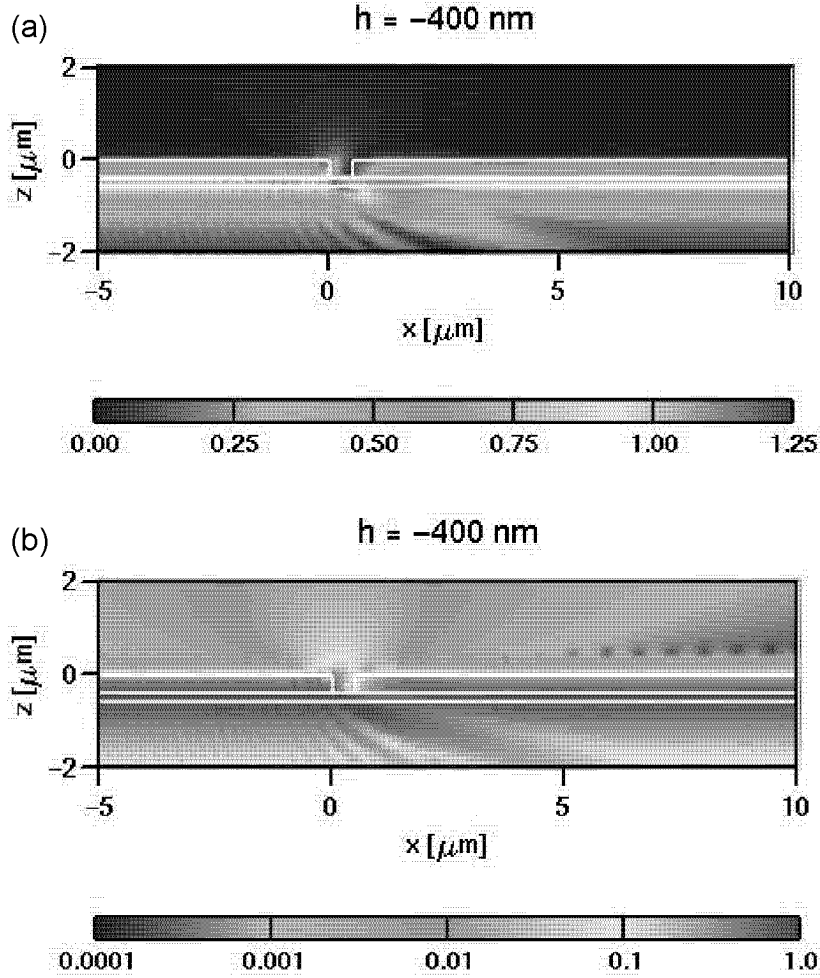


Figure 4.12. Electric field amplitude for the investigated waveguide structure (figure 4.11). A TE₀ mode propagating in x direction is used as illumination. Cross sectional view through the center of the structure ($y = 0$) with a (a) linear and (b) logarithmic color scale.

sized in figure 4.12(b), where we use a logarithmic color scale. This field is the forerunner of the field that would be coupled out of the structure if a long grating formed by many such elements was used (see section 4.2.2).

With the logarithmic scale we can also observe remarkable interference patterns in air at a distance $z \approx 500$ nm above the InP layer. These patterns arise on both sides of the scattering element with different periodicities. They originate from the interaction between the exponentially decaying electric field of the initial mode and the wave radiated in the air by the scattering element. For a quantitative analysis of this interference pattern we report in figure 4.13 the electric field computed along a

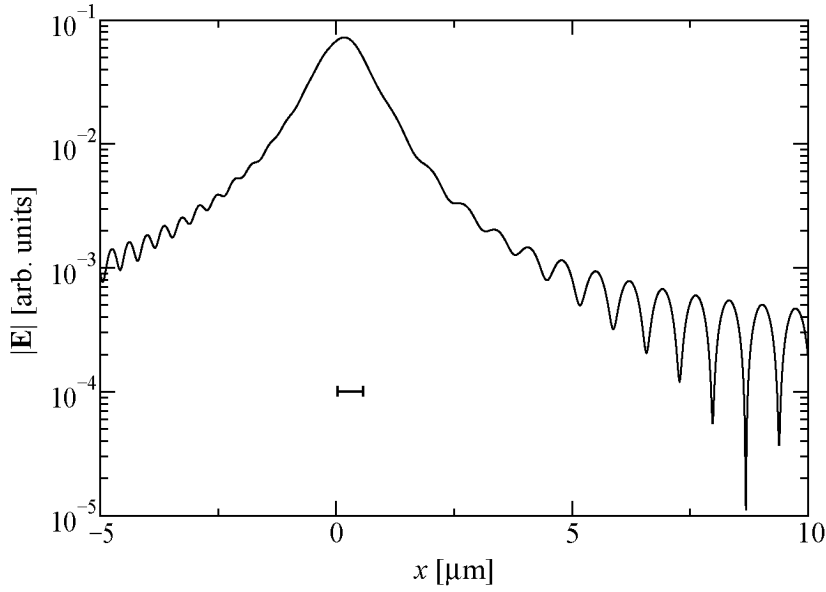


Figure 4.13. Electric field amplitude in the symmetry plane ($y = 0$), 500 nm above the InP–air interface (see figure 4.11). The bar represents the extension of the notch in x direction.

line 500 nm above the InP–air interface ($z = 500$ nm). Corresponding to the different propagation constants ($k_{\text{air}} = 2\pi/\lambda$ for the radiated wave and β_{TE_0} for the mode) the electric field amplitude should be modulated with the periodicities $\Delta_{\text{fw}} = 2\pi/(\beta_{\text{TE}_0} - k_{\text{air}}) \approx 705$ nm in the forward direction and $\Delta_{\text{bw}} = 2\pi/(\beta_{\text{TE}_0} + k_{\text{air}}) \approx 369$ nm in the backward direction [15]. Our numerical results agree perfectly with these predicted numbers.

Let us now study in greater detail the processes taking place inside the waveguide itself. Figure 4.14(a) shows a top view of the electric field amplitude at $z = -525$ nm, i.e., inside the guiding InGaAsP layer. The mode is scattered strongly by the notch, the region behind the defect becomes depleted and a complex interference pattern arises: The interaction of the incident field and the scattered field creates in backward direction a dense system of fringes and in forward direction a field distribution which can be interpreted as the diffraction pattern of the defect.

As last example, we would like to briefly discuss the cross-polarization coupling that can occur in this waveguide structure. Since our approach is fully vectorial, the computed electric field includes all three components, even when the excitation \mathbf{E}^0 is only a scalar field. For example, the TE_0 incident field has only a y component. However, during the scattering process, a TM electric field, with x and z com-

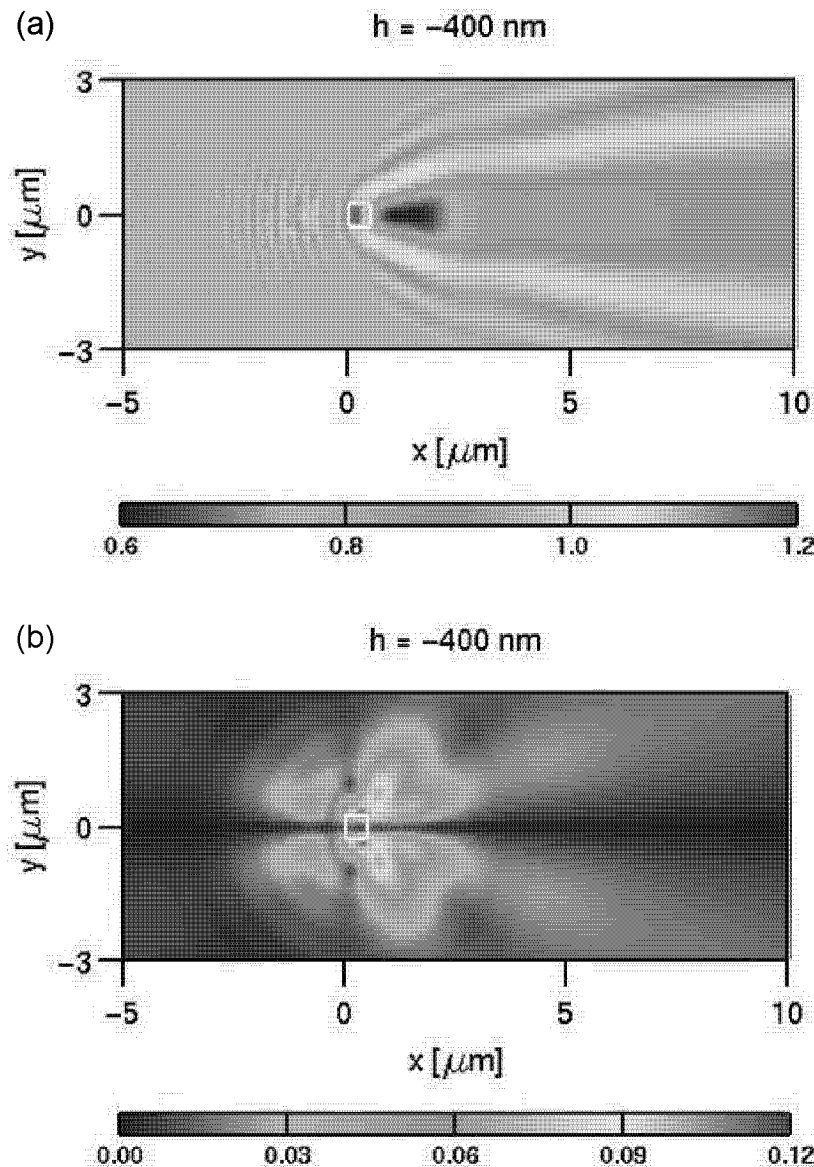


Figure 4.14. Top view of the electric field amplitude in the InGaAsP layer ($z = -525 \text{ nm}$). The white box represents the extension of the notch in the xy plane. (a) Total electric field and (b) cross-polarized TM field; this polarization, which was not present in the excitation, is created during the scattering process.

ponents, is generated. Its amplitude is represented in figure 4.14(b) for the notch. Note the perfect symmetry of this field with respect to the y direction. This is related to the fact that the scatterer is symmetrical and the incident field propagates along one of its symmetry axis. The diffraction pattern in figure 4.14(b) originates from the finite extension of the scatterer (in the order of one wavelength). It is similar in the for-

ward and backward directions because no TM components were present in the incident field. Therefore no interferences between incident and reflected fields can occur for this polarization component [compare with figure 4.14(a)].

Figure 4.15 reports the real part of the electric field component E_z created during the scattering process: This new field component corresponds to a field generated at the location of the notch and propagating in both directions in the waveguide. A mode cross-polarized to the incident field can therefore establish in the waveguide. As a matter of fact, an analysis of the periodicity of the generated field shows that its propagation constant is identical to the propagation constant expected for the TM_0 mode ($\beta_{\text{TM}_0} = 12.92 \mu\text{m}^{-1}$). Note however that the amplitude of this cross-polarized TM mode is much smaller than the amplitude of the original incident field.

The amplitude distributions for different heights of the defect (including positive heights corresponding to a protrusion deposited on top of the structure) are presented as movies in **P7**. In this paper, we also investigate the scattering when a TM_0 mode is used as excitation. In this case, the field distributions far away from the defect are similar to those for a TE_0 excitation. However, in the near field close to the defect,

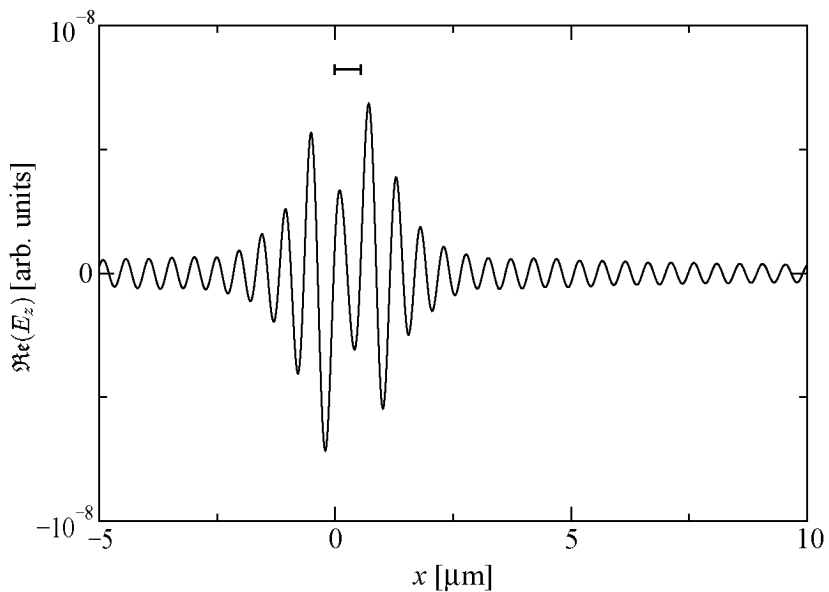


Figure 4.15. Real part of the electric field component E_z created during the scattering process depicted in figure 4.14(b). This new field component, that is not present in the TE_0 excitation, is calculated along the center of the structure in the InGaAsP layer [$z = -525 \text{ nm}$, $y = 0$ in figure 4.14(b)]. The bar represents the extension of the notch in x direction.

the different polarizations lead to different field distributions.

Since our approach is fully 3D, we can position protrusions on the structure arbitrarily, as illustrated in **P6**. In particular, we study for both TE_0 and TM_0 excitation the interaction between two protrusions deposited on the structure with a lateral offset.

4.2.2 2D grating coupler

To study the collective behavior of a larger number of scattering elements we consider a silicon-on-insulator (SOI) planar waveguide with a finite rectangular grating on top, as shown in figure 4.16 [78, 79]. If a mode propagates in the waveguide and scatters on the grating, light is coupled out of the guiding layer and is transmitted into the air and/or towards the substrate.

In figure 4.17 we report the electric field amplitude $|\mathbf{E}|$ when a grating consisting of 20 protrusions is illuminated with the TE_0 mode propagating in x direction at a wavelength $\lambda = 1.3 \mu\text{m}$. The maximum amplitude of the incident mode is normalized to unity, the discretization mesh for the calculations is $\Delta_x = \Delta_z = 25 \text{ nm}$.

Four periodicities, $d = 300 \text{ nm}$, $d = 350 \text{ nm}$, $d = 400 \text{ nm}$, and $d = 600 \text{ nm}$ are considered at a fixed filling factor 0.5. On the left side of all four geometries a standing wave occurs because of the reflection of the incoming mode by the grating. On the right side, beyond the grating, similar to the 3D case we can observe an interference pattern created by the interaction between the field of the mode and the scattered field (see section 4.2.1). However, the electric field distributions strongly differ in the four cases. For $d = 300 \text{ nm}$ most of the outcoupled light is

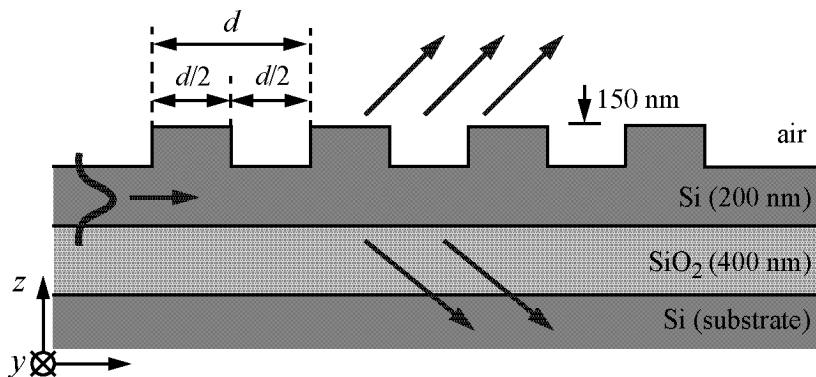


Figure 4.16. Geometry of the SOI planar waveguide (permittivities: $\epsilon_{\text{Si}} = 12.3$, $\epsilon_{\text{SiO}_2} = 2.1$; wavelength $\lambda = 1.3 \mu\text{m}$). A Si grating with 150 nm height and a 0.5 filling factor is etched on top of the waveguide.

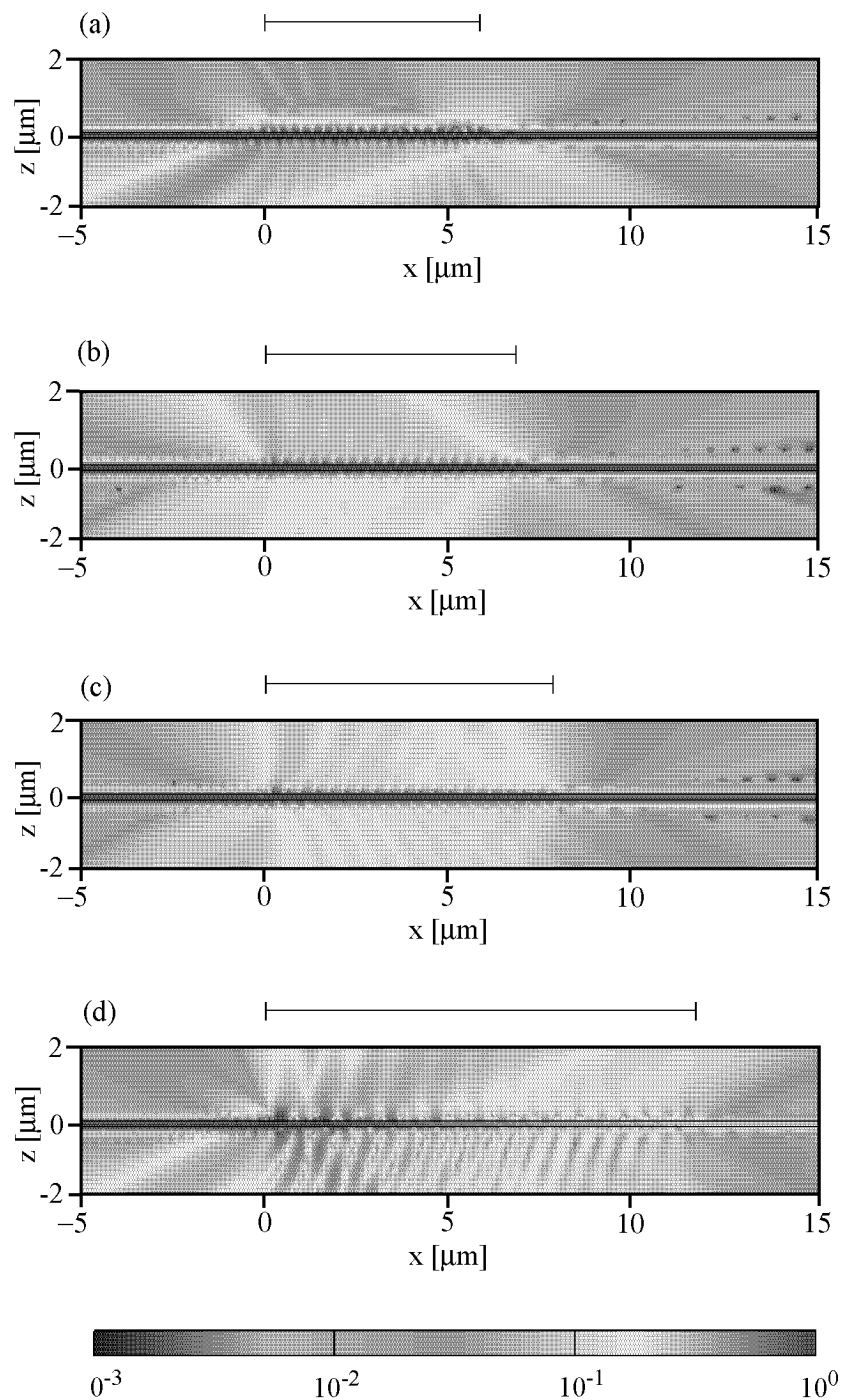


Figure 4.17. Electric field amplitude in the structure of figure 4.16 with four different grating periodicities: (a) $d = 300\text{ nm}$, (b) $d = 350\text{ nm}$, (c) $d = 400\text{ nm}$, and (d) $d = 600\text{ nm}$. The bars represent the total length of each grating. The systems are illuminated with a TE_0 mode propagating in x direction. For clarity, the guiding silicon layer is marked with two lines. A logarithmic color scale is used.

scattered towards the substrate and nearly no light is scattered upwards [figure 4.17(a)]. With increasing periodicity the main beam of the out-coupled light rotates, so that for $d = 350 \text{ nm}$ and $d = 400 \text{ nm}$ a larger fraction of the scattered field is transmitted into the air [figures 4.17(b) and 4.17(c)]. For $d = 600 \text{ nm}$ most of the incident mode is scattered out of the waveguide, strongly reducing the transmission through the grating [figure 4.17(d)].

For a more quantitative comparison we report in figure 4.18 the angular distribution of the electric field amplitude $|\mathbf{E}|$ far away from the grating ($50 \mu\text{m}$). Note first that the central peak at $\phi = 180^\circ$ represents the mode in the guiding layer. Of course, the same peak occurs at $\phi = 0^\circ$ and 360° (not shown). Whereas for $d = 300 \text{ nm}$ we can observe a single output beam with an angle $\phi \approx 205^\circ$ (backward direction in the substrate), two beams appear for $d = 350 \text{ nm}$ respectively $d = 400 \text{ nm}$: a major one into the air with $\phi \approx 133^\circ$ (backward direction in the air) respectively $\phi \approx 101^\circ$ (approximately normal to the waveguide surface) and a minor one towards the substrate with $\phi \approx 244^\circ$ respectively $\phi \approx 264^\circ$. With a larger grating periodicity, the angles of the output beams rotate both in the air and in the substrate towards the forward direction. For $d = 600 \text{ nm}$, in addition to these two peaks at $\phi \approx 33^\circ$ and $\phi \approx 308^\circ$ (forward direction both in air and substrate)

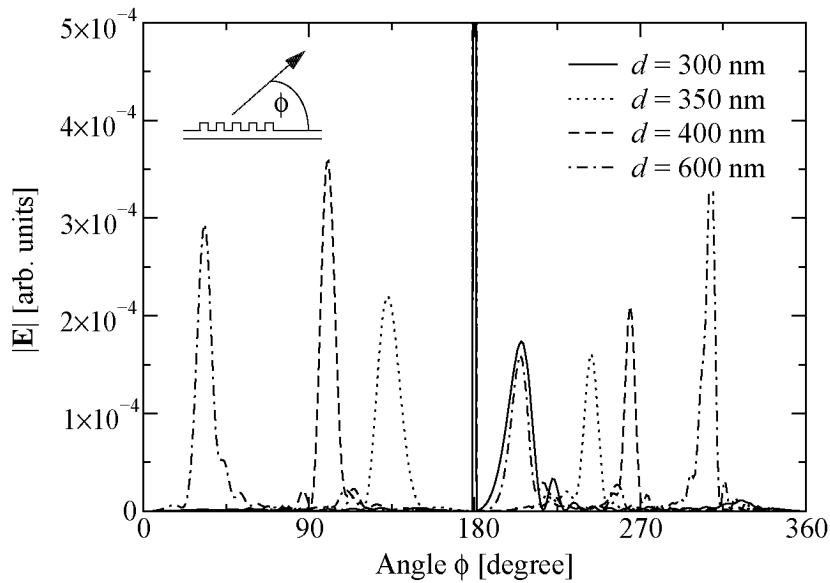


Figure 4.18. Angular distribution of the electric field amplitude $50 \mu\text{m}$ away from the center of the four gratings in figure 4.17. The central peak at $\phi = 180^\circ$ is caused by the mode in the guiding Si layer and appears also at $\phi = 0^\circ$ and 360° (not shown).

a third peak occurs at $\phi \approx 205^\circ$. This additional beam, similar to that for $d = 300\text{ nm}$, is created by the strong scattering at the front edge of the grating [compare figures 4.17(a) and (d)].

4.3 Scattering of surface plasmons

If one of the layers defining the background is a metal, a surface plasmon–polariton can be excited [58]. Such a surface mode propagates along a material interface and decays exponentially from the interface.

To excite a surface plasmon in a planar glass/metal/vacuum structure the method of attenuated total reflection (ATR) can be used [80]. A p-polarized plane wave is incident on the glass–metal interface with an angle larger than the critical angle of total internal reflection. Hence, an exponentially decaying evanescent field is created in the metal layer. When the component of the wave vector parallel to the interface fulfills the eigenvalue equation for the surface mode, a plasmon is excited at the metal–vacuum interface.

To determine the plasmon resonance angle for a silver film on a glass substrate (permittivities $\varepsilon_{\text{Glass}} = 2.25$, $\varepsilon_{\text{Ag}} = -18.32 + i 0.5$) at a wavelength $\lambda = 633\text{ nm}$ we show in figure 4.19 the relative reflected amplitude A_{refl} in the glass layer as a function of the angle of incidence ϕ . Indeed, at

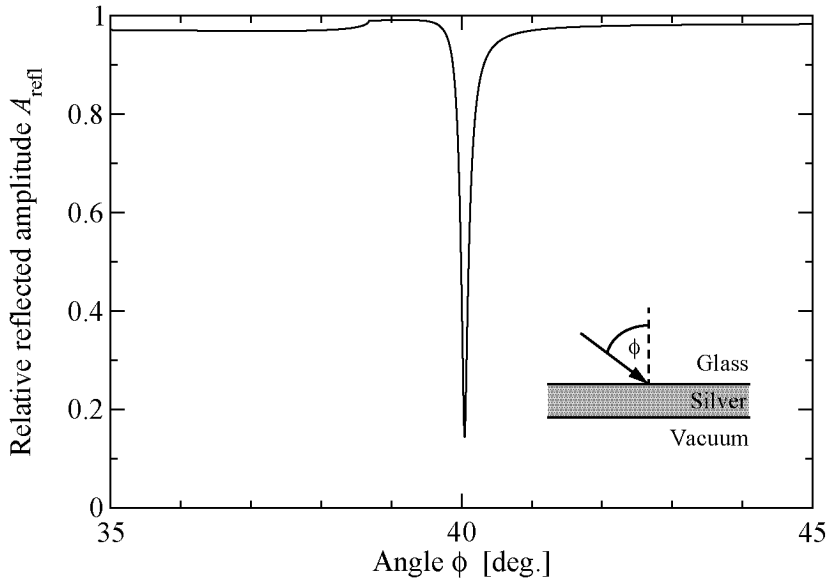


Figure 4.19. Plane wave impinging on a silver film on top of a glass substrate.

The relative reflected amplitude A_{refl} in the glass substrate is shown as a function of the angle of incidence. Both the angle of total internal reflection and the plasmon resonance angle are visible.

$\phi = 40.0^\circ$ the reflectivity drops strongly due to the excitation of the surface plasmon. Note further the critical angle of total internal reflection at $\phi = 38.7^\circ$.

This plasmon propagates along the metal surface and interacts with any defect on it. As an example, we investigate the scattering by a $100 \times 100 \times 50 \text{ nm}^3$ dielectric protrusion (glass, $\epsilon = 2.25$) deposited on a 100 nm thick silver film. For the simulations, this protrusion is discretized with $\Delta_x = \Delta_y = \Delta_z = 10 \text{ nm}$.

The resulting field amplitude is reported in figure 4.20. A stationary wave is visible on the left side of the protrusion. It results from the interaction of the plasmon propagating in positive x direction with the plasmon reflected by the protrusion. Inside the metal the electric field appears to vanish. Actually, the field amplitude profiles reported in figure 4.21 show that the electric field is strongly localized at the surface of the metal, characteristic of a plasmon. The stationary wave in the glass substrate resulting from the interaction of the incident field with the reflected one is also visible in this figure.

Notice in figure 4.21 that, due to the higher index, the field decays more rapidly in the glass than in vacuum [80]. The second peak that appears at the glass–vacuum interface is merely related to the continuity of the displacement field $\mathbf{D} = \epsilon \mathbf{E}$. As a matter of fact, the field associated

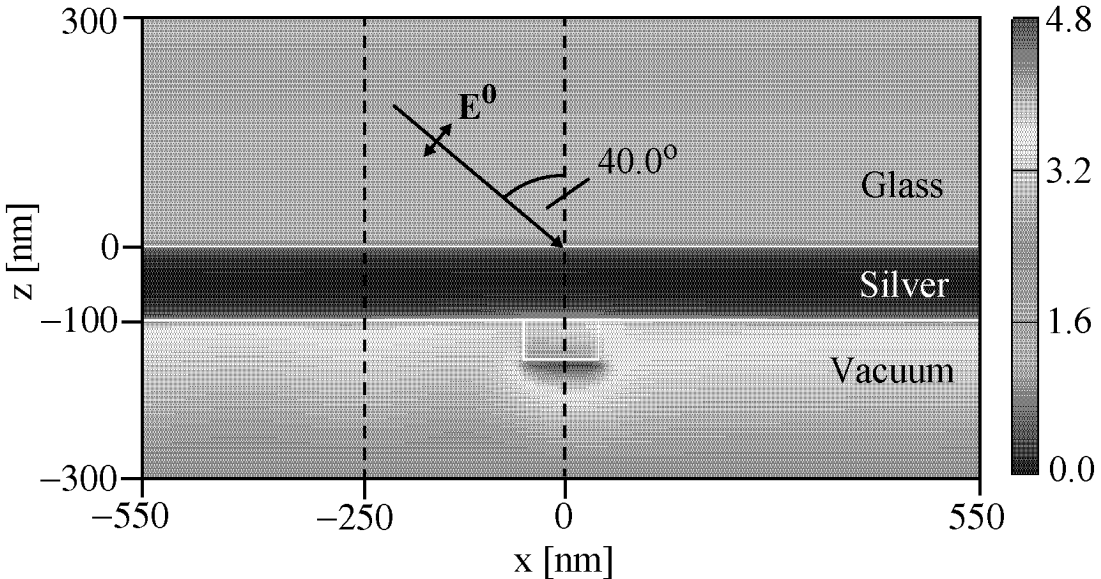


Figure 4.20. Attenuated total reflection (ATR) excitation of a surface plasmon propagating along the metal–vacuum interface. Cross sectional view of the electric field amplitude. Note the scattering of the surface plasmon by the protrusion.

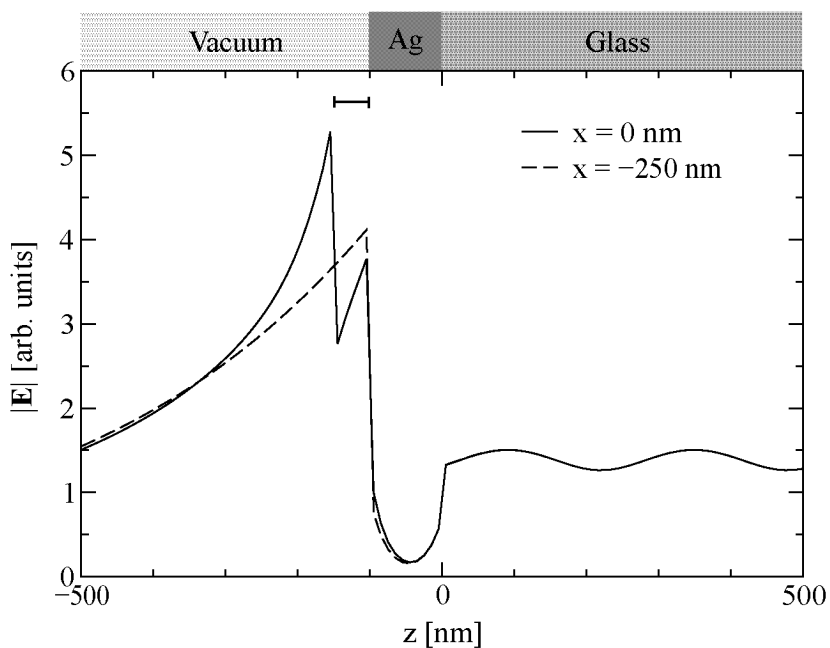


Figure 4.21. Field amplitude along the two dashed lines in figure 4.20 ($y = 0$).

The bar represents the extension of the defect in z direction. Remark the standing wave in the glass substrate and the localized plasmon field at the metal–vacuum, metal–glass and glass–vacuum interfaces.

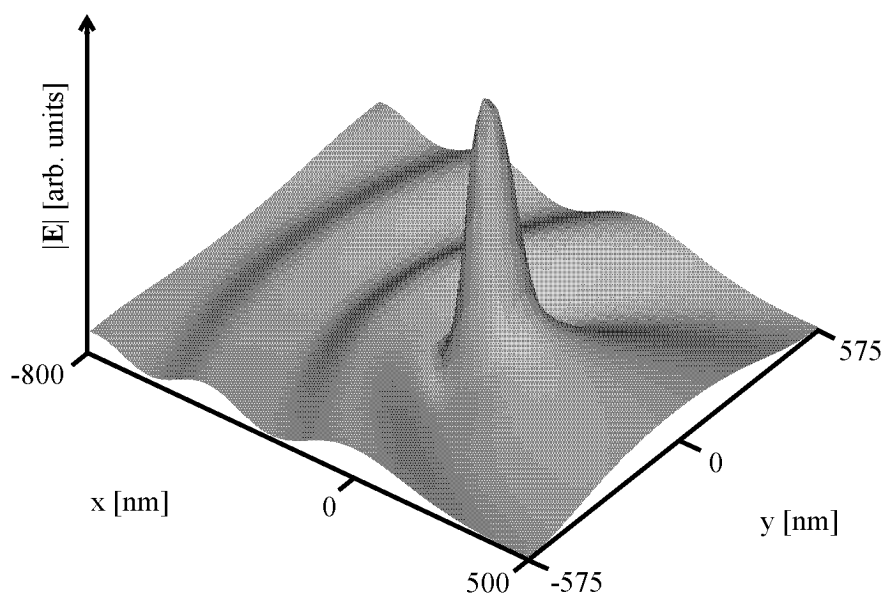


Figure 4.22. Field amplitude in a constant height plane in vacuum below the glass protrusion ($z = -155$ nm, see figure 4.20). Both the scattering and the confinement of the surface plasmon by the protrusion are visible.

with the plasmon being dominantly polarized in z direction, i.e., normal to the glass–vacuum interface, it is the displacement field (not the electric field) that must be continuous [37]. The amplitude difference observed in figure 4.21 actually corresponds to the dielectric contrast between glass and vacuum.

The strong field enhancement is evidenced in figure 4.22, where we report the field distribution in a plane parallel to the surface immediately below the protrusion. This figure clearly illustrates how the surface plasmon interacts with the glass protrusion.

Note that the study of such a complex system depends essentially on an accurate treatment of the singularities, as presented in chapter 3.2. It must be guaranteed that all the modes of the structure are correctly taken into account.

4.4 Roughness in SNOM tips

Whereas the resolution of a classical optical microscope is diffraction-limited to approximately half of the effective wavelength, scanning near-field optical microscope (SNOM) techniques overcome this restriction by using evanescent light [81]. With an aperture probe an evanescent near-field is created by squeezing light through a subwavelength aperture of a tip with a metallic cladding. Since this metallic opening determines the near-field distribution of the probe, surface roughness or small shape deviations can strongly affect the maximal resolution. In this section the influence of such a non-ideal aperture on the emission characteristics is investigated with emphasis on the polarization sensitivity of the probe.

To simulate an aperture SNOM tip with the Green's tensor technique we model the metallic cladding as an infinitely extending metal layer and the aperture as a three-dimensional glass-filled hole in this screen (figure 4.23). Illuminating the structure from above, only an evanescent field is detected below the opening if the metal layer is thick enough to prevent direct transmission.

We consider an aperture with a 100 nm nominal diameter, defined in aluminum with a 30 nm metal thickness at the aperture rim. The permittivity of aluminum at the considered vacuum illumination wavelength of 633 nm is $\varepsilon = -54.2 + i19.5$ [82]. We will concentrate our attention on the influence of a rough aperture and shall not consider the effect of metallic particles deposited further away from the aperture, since such a particle primarily influences the tip motion rather than the light scattered at the aperture [83].

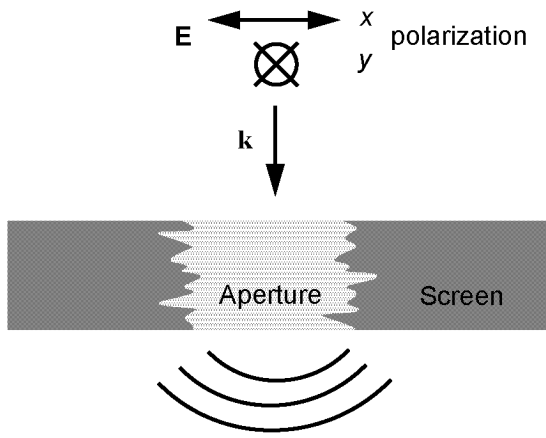


Figure 4.23. 2 Model of a rough SNOM aperture, cross-sectional view (the aperture has finite dimensions in all directions). When the structure is illuminated from above with x - or y -polarized light the transmission through the glass-filled subwavelength aperture creates an evanescent field directly below the opening.

The near-field distributions are computed in an xy plane 5 nm behind the aperture and the field intensity is normalized to the illumination intensity just before the aperture. To model the different roughnesses, the aperture is discretized with meshes between $\Delta_x = \Delta_y = \Delta_z = 1$ nm and 5 nm. To ease comparison a similar scale is used for the z axis (intensity axis) throughout the section [except in figure 4.24(f)] and the colorscale is adapted to emphasize the details of each field distribution. For each aperture we consider separately two orthogonal linear illumination polarizations (figure 4.23).

In figure 4.24 we illustrate the influence of the roughness on the near-field distribution. Let us first consider the perfectly smooth aperture in figure 4.24(a). The field distribution is dominated by two peaks located in the regions where the incident field is normal to the metallic surface. They correspond to the depolarization field created during the scattering process to fulfill Maxwell's equations: The illumination electric field \mathbf{E} in the tip being continuous, it does not fulfill Maxwell's equations when it is normal to the core-coating interface. As a matter of fact, it is the electric displacement $\mathbf{D} = \epsilon \mathbf{E}$ that must be continuous in that case [37]. Since the permittivity of the aluminum coating is much larger than that of the glass core, a strong depolarization field is created in the aperture at the core-coating interface (figure 4.25). On the other hand, when the incident field is parallel to the metallic interface, it already fulfills Maxwell's equations and no depolarization field is created (figure 4.25). If the incident polarization is rotated, the position of the peaks rotates

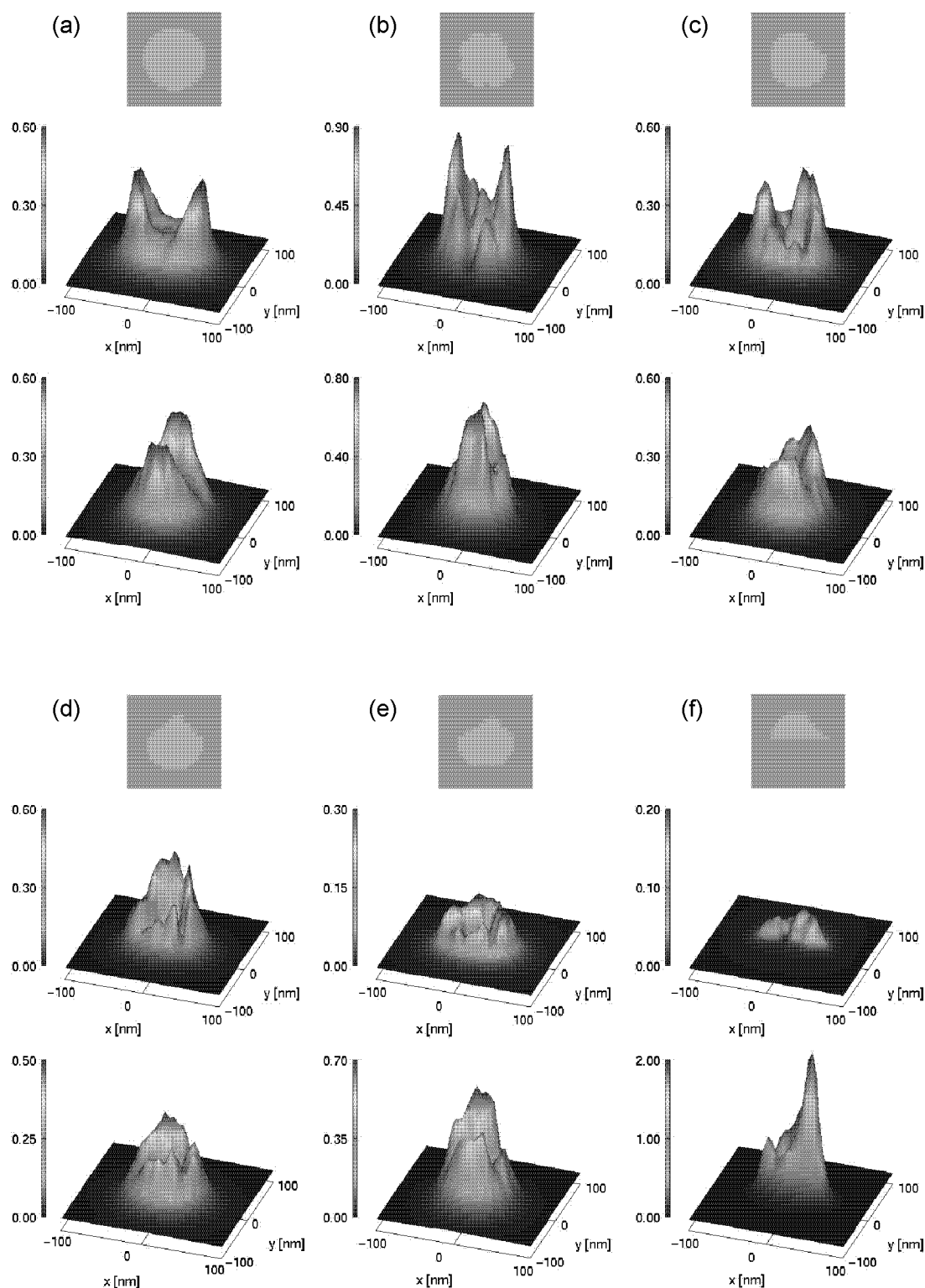


Figure 4.24. Relative electric field intensity transmitted through a nominally 100 nm aperture in aluminum with different roughnesses (shown in the insets). Two orthogonal incident polarizations are calculated: x polarization (top row) and y polarization (bottom row). The same z axis scaling is used for the intensity, except in (f) where it is scaled by a factor of 0.5.

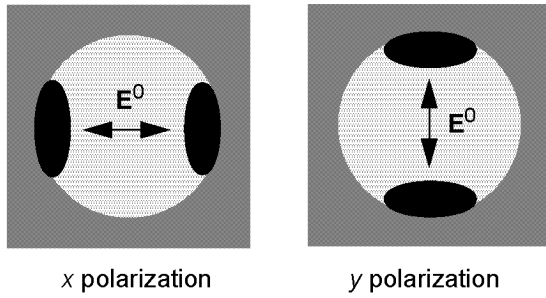


Figure 4.25. Top view of an illumination SNOM aperture. To fulfill Maxwell's equations in the aperture, strong depolarization fields are generated in the regions where the incident field is normal to the core-coating interface (black areas). When the incident polarization direction is changed, these depolarization regions move [compare figures 4.24(a) top and bottom].

as well [figure 4.24(a), bottom].

A small variation in the roughness and symmetry already distorts the field significantly and additional peaks appear in the field distribution [figure 4.24(b)]. When the roughness increases, the original field distribution with two well defined peaks progressively disappears. In figures 4.24(c)–(e) the field distribution occupies a large portion of the aperture rim. Further, when the illumination field rotates, the field distribution does not follow the incident polarization anymore and some regions remain lit up independently of the illumination. For example in figure 4.24(c) only the peak visible on the left for x polarization (top) is displaced for y polarization (bottom), the other peaks remaining mainly unchanged.

The overall intensity transmitted through a rough aperture also strongly depends on the incident polarization: In figure 4.24(e) there is a factor of 2 between the maximum intensity for both polarizations and in the more pathological case of 4.24(f) there is an order of magnitude between the intensity of the x - and y -polarized fields. The importance of the depolarization fields in that last case is quite striking. The strong depolarization fields occurring when the incident field is normal to that slit, together with the field enhancement due to the lightning rod effect at the sharp corner, dominate the near-field (figure 4.24(f), bottom).

Such strongly disturbed and non-symmetrical field distributions will produce near-field images that are quite difficult to interpret and reflect more the topology of the aperture than that of the sample under study. However, this polarization sensitivity, although very disruptive for practical measurements, could be used to assess the probe roughness by simply measuring its field throughput as a function of the incident

polarization.

In [84] this study is extended to apertureless probes, where the evanescent field is created by scattering by a metal tip. The results show that these probes are less sensitive to surface roughness providing a well-defined field, even with a defective tip.

4.5 Scattering by a dielectric cylinder

The optical properties of cylindrical particles have generated a lot of interest, as they provide a simple model for specific physical systems such as atmospheric particles or interstellar dust. The scattering by a cylinder situated in an infinite homogeneous background was for example already treated by Lord Rayleigh in 1881 [85].

However, most real situations are more complex, the particles are located on a substrate or embedded in an even more complicated stratified background. In this section we apply our approach to study the light scattered by a dielectric circular cylinder with radius $r = 150$ nm and permittivity $\varepsilon_{\text{Cyl}} = 2$, embedded in a two-layer background. The cylinder is located in the top layer with a distance $h = 615$ nm between the cylinder center and the interface [see figure 4.26(b)]. This system is illuminated from the top with a plane wave under different angles of incidence Θ . The illumination wavelength is $\lambda = 633$ nm and we focus on s polarization, with the electric field \mathbf{E}^0 in y direction. Since the scattering geometry under study is translation invariant in y direction we can restrict the investigation to a cross section in the xz plane and use the 2D formulation developed in sections 2.3, 3.1.2, and 3.2.2. For the simulation, the cross section of the cylinder is discretized with a $\Delta_x = \Delta_z = 30$ nm mesh.

Before studying complex effects that can arise when the cylinder is placed in a stratified background, it is educational to review the simpler case of the scattering by a cylinder in an infinite homogeneous space $\varepsilon_H = 1$. Figure 4.26(a) shows the total electric field amplitude in such a system, when the cylinder is illuminated with an s-polarized incident electric field \mathbf{E}^0 propagating in $-z$ direction:

$$\mathbf{E}^0(x, z) = \mathbf{A}^0 \exp(i\mathbf{k}\mathbf{r}) = \mathbf{A}^0 \exp(ik_z z), \quad (4.3)$$

where $\mathbf{A}^0 = (0, 1, 0)$ is the amplitude vector and $\mathbf{k} = (k_x, k_z) = (0, -|\mathbf{k}|)$ is the wave vector of the incident wave. (For all calculations we normalize the electric field amplitude of the incident field $|\mathbf{A}^0| = (\mathbf{E}^0 \cdot \mathbf{E}^{0*})^{1/2} = 1$.)

The field distribution in figure 4.26(a) shows in backward direction a stationary wave due to the interference of the incident and reflected

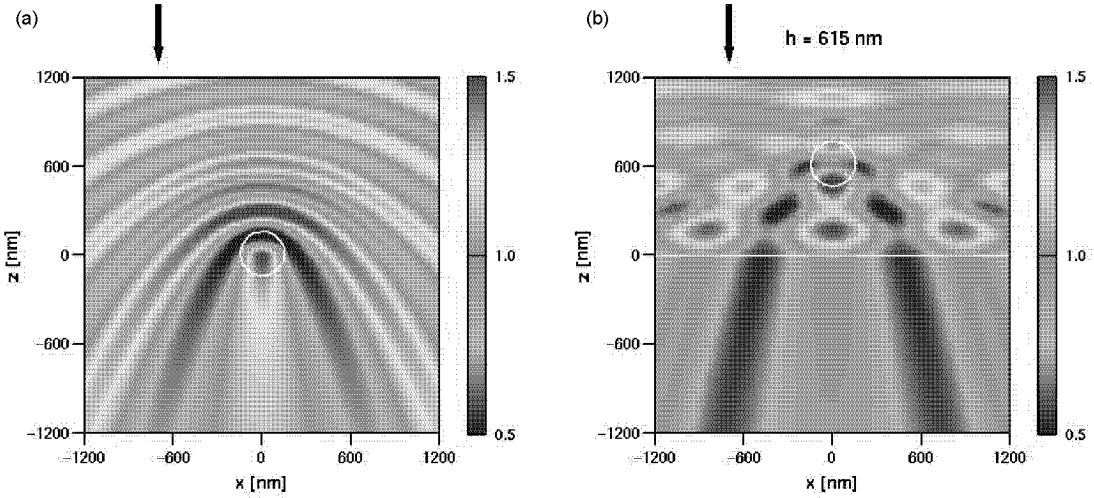


Figure 4.26. Electric field amplitude distribution for the scattering by a cylinder (a) in an infinite homogeneous background and (b) above a dielectric surface (distance between the cylinder center and the interface $h = 615$ nm). Illumination with an s-polarized plane wave under normal incidence ($\Theta = 0^\circ$, the arrow represents the propagation direction of the illumination wave).

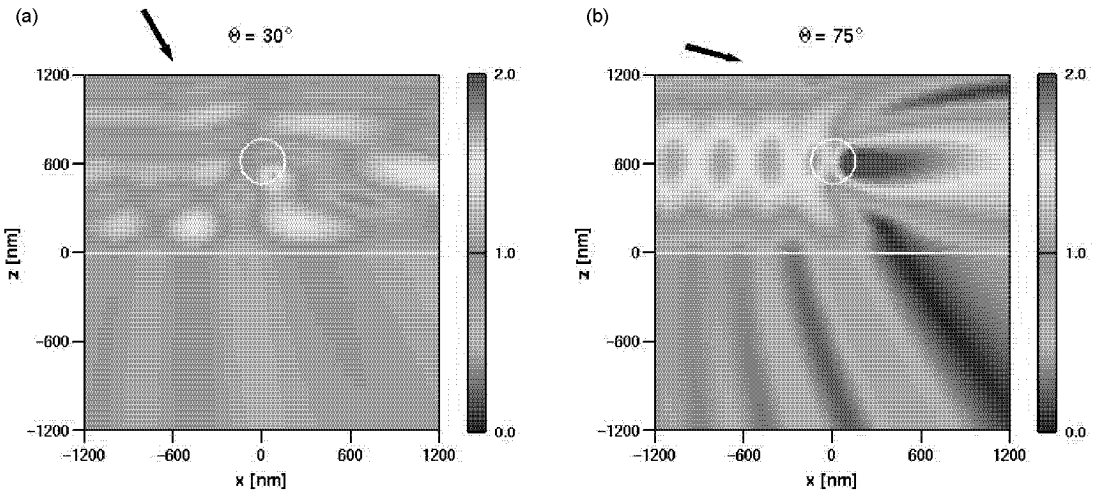


Figure 4.27. Same situation as in figure 4.26, but now the illumination field is incident at (a) $\Theta = 30^\circ$ and (b) $\Theta = 75^\circ$ (the arrow indicates the propagation direction of the illumination field).

waves. In the forward direction we recognize the diffraction pattern of the cylinder. Further, a maximum of the intensity can be observed inside the cylinder.

Now we divide the background into two half spaces $\varepsilon_1 = 1$ ($z \geq 0$) and $\varepsilon_2 = 2$ ($z < 0$), in such a way that the lower layer has the same permittivity as the cylindrical scatterer, $\varepsilon_2 = \varepsilon_{\text{Cyl}}$. Figure 4.26(b) shows

the response of the system under normal incidence ($\Theta = 0^\circ$).

Since the incident wave is now reflected back at the plane interface, the illumination electric field becomes in the top layer

$$\mathbf{E}^0(x, z) = \mathbf{A}^0 [\exp(ik_{1z}z) + R \exp(-ik_{1z}z)], \quad z \geq 0, \quad (4.4)$$

and in the bottom layer

$$\mathbf{E}^0(x, z) = \mathbf{A}^0 T \exp(ik_{2z}z), \quad z < 0, \quad (4.5)$$

where k_{lz} , $l = 1, 2$, is the z component of the wave vector in layer l , R is the Fresnel reflection coefficient and T is the corresponding transmission coefficient for normal incidence [15]:

$$R = \frac{\sqrt{\varepsilon_1} - \sqrt{\varepsilon_2}}{\sqrt{\varepsilon_1} + \sqrt{\varepsilon_2}}, \quad (4.6)$$

$$T = \frac{2\sqrt{\varepsilon_1}}{\sqrt{\varepsilon_1} + \sqrt{\varepsilon_2}}. \quad (4.7)$$

Note that R and T are real for absorptionless media. The negative reflection coefficient obtained in our system leads to a phase shift of 180° for the reflected field.

The illumination amplitude reads now in the upper half space

$$A = (\mathbf{E}^0 \cdot \mathbf{E}^{0*})^{\frac{1}{2}} = |\mathbf{A}^0| [1 + R^2 + 2R \cos(2k_{1z}z)]^{\frac{1}{2}}, \quad z \geq 0, \quad (4.8)$$

and a stationary wave with period $\Delta = \pi/k_{1z} = \lambda/2$ is created in the top layer [figure 4.26(b)]. Because of $R < 0$ the amplitude is minimal directly at the interface.

The cylinder is not anymore illuminated with a homogeneous plane wave but moves in the field of the stationary wave. Hence, in the top layer the total field distribution is a superposition of the stationary wave and a diffraction pattern similar to that in figure 4.26(a). This pattern determines also the field distribution in the bottom layer, depending on the transmittance of the interface.

The stationary wave itself is further amplified in the region between the cylinder and the interface. This is caused both by the focusing provided by the cylinder and by multiple reflections between the surface and the cylinder. Note also that the interaction between the excitation and the field scattered by the cylinder creates an interference pattern in x direction.

Let us now rotate the angle of incidence Θ with respect to the surface normal. Figure 4.27 shows the scattering for $\Theta = 30^\circ$ and for $\Theta = 75^\circ$.

In this case of non-normal illumination, the Fresnel reflection coefficient depends on the polarization of the incident wave and reads for s polarization [15]:

$$R^s = \frac{k_{1z} - k_{2z}}{k_{1z} + k_{2z}}. \quad (4.9)$$

Again, a stationary wave excites the cylinder, but the period is now increased to $\Delta = \pi/k_z = \lambda/(2 \cos \Theta)$. The diffraction patterns and the positions of the near field maxima rotate accordingly to the change of the incidence angle (compare figures 4.26 and 4.27).

Since the reflection coefficient of the interface R^s approaches 1 in the limit $\Theta = 90^\circ$, the field transmitted into the lower half space vanishes for larger angles and the amplitude maxima of the stationary wave converge towards their upper value for total reflection $A = 2$ (see equation (4.8) with $k_z \rightarrow 0$ and $R \rightarrow 1$). This produces a strong scattering both in forward and backward directions when a maximum of the stationary wave coincides with the cylinder altitude [$\Theta = 75^\circ$, figure 4.27(b)].

Note finally that corresponding to the boundary conditions for s polarization the electric field must be continuous across the interface between the two layers.

Movies of the electric field distribution as a function of the relative cylinder position with respect to the background interface as well as of the illumination direction are presented in **P8**. In this paper, we also investigate a p-polarized plane wave illumination. Depolarization effects corresponding to the boundary conditions at the material interfaces lead in this case to a strongly different near-field distribution at close vicinity of the cylinder. Finally, in **P8** we study a three-layer system, where the intermediate slab acts as antireflection layer, i.e., there is no stationary wave in the top layer due to reflections of the illuminating field by the slab (compare with the discussion in section 4.1.3 C). We observe that the antireflection layer remains very efficient, even in the presence of the cylinder.

Chapter 5

Conclusion and outlook

Many experimentally relevant structures consist of dielectric or metallic scatterers distributed in a stack of material layers with different permittivities. In this thesis, a Green's tensor approach for the computation of light scattering in such geometries has successfully been developed. Based on the electric field integral equation, it requires the calculation of the Green's tensor associated with the multilayered background. This dyad is known analytically only for a homogeneous background and must be computed numerically when the background is stratified. This is best done in reciprocal space, where the boundary conditions at the material interfaces can be enforced most easily. The backtransformation in direct space leads to Sommerfeld type integrals with a strongly oscillating behavior and singularities in the integration domain. The quadrature of these integrals is a key issue for our approach. We have found an accurate and stable integration scheme which is generally applicable and not restricted to a limited set of geometrical configurations. By an elliptical deformation of the integration path in the complex plane, the singularities occurring in the integrands are avoided without locating them individually. The remaining integration is then performed on a path providing fast convergence.

An important advantage of the Green's tensor technique lies in the fact that only the scatterers must be discretized, the stratified background being accounted for by the Green's tensor. Further, the boundary conditions at the different material interfaces as well as at the edges of the computation window are perfectly and automatically fulfilled. The development and implementation of this technique should be a step towards the accurate modeling of real structures without the restriction to special configurations or excessive simplifications as required by other numerical methods.

In this work, we have successfully applied our approach to the study

of several optical structures. We have investigated light–coupling masks (LCMs) for optical contact lithography and demonstrated the feasibility of subwavelength resolution. In principle, features smaller than 1/4 of the illumination wavelength can be replicated with LCMs, but crosstalks limit the minimal distance between individual structures for high–density patterning. The contrast mechanism of an LCM has been compared with that of alternative mask concepts and optimized mask dimensions have been found. If the mask structures are not aligned along one direction, circular polarized light provides the most homogeneous illumination. Further, interfering backreflections at the substrate can be efficiently suppressed with a bottom antireflection coating between substrate and photoresist. Examples of mode scattering in planar waveguides demonstrate that with our fully vectorial approach subtle cross–polarization effects can be studied. Since the Maxwell’s equations are solved rigorously, both the near–field and the far–field patterns of a grating coupler can be accurately computed. For those geometries, it is particularly valuable that our approach applies “open” boundaries at the edges of the computation window, because the mode propagation in an integrated optics structure can be very sensitive to inappropriate boundary conditions [86]. Even the optics of metals can be investigated since the material permittivities can be chosen arbitrarily, including negative real parts and imaginary parts to account for absorption. This allows the study of surface plasmon–polaritons and the influence of surface roughness on a scanning near–field optical microscopy tip. We have demonstrated the dramatic influence of the aperture shape on the homogeneity of the field distribution and on the polarization sensitivity of the probe, with the maximum field intensity varying in extreme cases by an order of magnitude when the polarization changes by 90°.

In all these examples our method provides accurate results, the assumption of a piecewise constant discretized field distribution in section 2.2 turning out to be an appropriate approximation. However, if the dielectric contrast becomes very large leading to extremely strong field gradients, more sophisticated methods must be used to solve the volume integral equation (2.7). Recently, a finite element approach for the solution has been developed in our group [41]. A set of basis functions is defined on each discretization element and the fields are expanded in terms of these basis functions. A regularization scheme helps then to accurately handle the strong singularity of the Green’s tensor. Since triangular and tetrahedral elements can be used as discretization elements, the shape of non–regular scatterers can be modeled very smoothly. With this approach, Kottmann *et al.* studied successfully plasmon resonances

of silver particles [87–92]. For two-dimensional geometries, this finite element solution has already been combined with the Green’s tensor for stratified media developed in the present thesis and gave very promising first results. However, some work is still needed to derive a general regularization scheme to handle the large values of the reflected and transmitted parts of the Green’s tensor for discretization elements at close vicinity of the interfaces.

Although our technique provides a very efficient discretization, limited only to the scatterers, the size of these scatterers is restricted by the tolerable computation time. If for a large optimization problem many geometrical parameters must be varied, a typical simulation can become quite time-consuming. For a homogeneous background, the conjugate gradient algorithm (see section 2.2) is often coupled with a fast Fourier transform (FFT) since it uses extensively the symmetry properties of a regular cubic discretization grid [46]. Its importance lies in the drastic reduction of both the computation time and memory requirements. However, for a stratified background the FFT cannot significantly improve the performance. The bottleneck is the computation of the Sommerfeld integrals and all symmetry properties of the structure which effectively reduce the numerical effort with FFT are already used in our implementation. Hence, an acceleration could only be provided by faster quadrature routines. However, the awkward behavior of the integrands prohibits any generally applicable treatment. All fast integral approximations available in the literature have a very limited validity domain with respect to the location of \mathbf{r} and \mathbf{r}' and often the surface wave contributions are neglected. Including these methods in the implementation would require a very careful inspection, so that the gain in time does not result in an intolerable loss of accuracy. More promising seems to apply interpolation methods for the field calculation in the solution domain [93]. Green’s tensors could be precomputed on a grid of points and stored in a look-up table. All further Green’s tensor coefficients are then derived by an appropriate interpolation between these tabulated values. However, care must be taken that the precomputed grid is not too coarse, thus neglecting effects like interferences appearing on a shorter length scale. On the other hand, the mesh should be coarse enough to provide a reasonable reduction of the simulation time.

Note further that the volume integral equation (2.7) can be reformulated as a surface integral equation using the vector Green’s theorem [15]. Hence, the unknowns of the problem lie on the surface of the scatterer rather than in the volume. Being mathematically equivalent, at first view this formulation is advantageous since it reduces the dimensional-

ity of the problem by one, and only the boundaries of the scatterers must be discretized for the numerical solution. However, this formulation has intrinsic limitations since it yields incorrect and non-unique solutions at discrete frequencies associated with eigenmodes of the structure [56]. To overcome this limitation several remedies have been proposed requiring either significant modifications to the formulation or a substantial additional computational effort [94]. Since the volume integral equation does not suffer from this internal resonance problem, it seems to be more appropriate for the investigation of resonant structures like cavities and metals.

Let us finally mention that the scattering calculations with surface plasmons in section 4.3 gave us the idea to use LCMs alternatively to the way discussed in section 4.1. The strongly localized fields as shown in figures 4.20 and 4.21 could provide a replication of subwavelength patterns with high contrast in the photoresist. Note that in figure 4.20 we have “reproduced” a 100 nm structure with a 633 nm illumination. The technological realization of such a “plasmon-based light stamp” is possible, although the roughness of the metalization could lead to unexpected effects. Obviously, the exponential decay of the plasmon field in the photoresist (see figure 4.21) requires an ultrathin resist layer. The coupling of the field in the photoresist, however, is still an open question, since the presence of this additional material layer strongly disrupts the plasmon excitation.

Bibliography

- [1] *The International Technology Roadmap for Semiconductors: 1999*, Semiconductor Industry Association, <http://public.itrs.net> (1999).
- [2] “Special Issue on Optical Lithography,” IBM J. Res. Dev. **41**, No. 1/2 (1997).
- [3] M. Rothschild *et al.*, “157 nm: Deepest deep-ultraviolet yet,” J. Vac. Sci. Technol. B **17**, 3262–3266 (1999).
- [4] *Extreme Ultraviolet Lithography*, Vol. 4 of *OSA Trends in Optics and Photonics*, G. D. Kubiak and D. R. Kania, eds. (Optical Society of America, Washington, DC, 1996).
- [5] M. Khan, G. Han, S. B. Bollepalli, and F. Cerrina, “Extension of x-ray lithography to 50 nm with a harder spectrum,” J. Vac. Sci. Technol. B **17**, 3426–3432 (1999).
- [6] H. C. Pfeiffer and W. Stickel, “PREVAIL – An e-beam stepper with variable axis immersion lenses,” Microelectron. Eng. **27**, 143–146 (1995).
- [7] R. Kaesmaier, A. Ehrmann, and H. Löschner, “Ion projection lithography: status of tool and mask developments,” Microelectron. Eng. **57-58**, 145–153 (2001).
- [8] H. I. Smith, “Method for fabricating high frequency surface wave transducers,” Rev. Sci. Instrum. **40**, 729–730 (1969).
- [9] E. Cullmann, “Excimer laser applications in contact printing,” Semicond. Int. **8**, 332–334 (1985).
- [10] S. Y. Chou, P. R. Krauss, and P. J. Renstrom, “Imprint lithography with 25-nanometer resolution,” Science **272**, 85–87 (1996).
- [11] H. A. Biebuyck, N. B. Larsen, E. Delamarche, and B. Michel, “Lithography beyond light: Microcontact printing with monolayer resist,” IBM J. Res. Develop. **41**, 159–170 (1997).

- [12] R. März, *Integrated Optics Design and Modeling* (Artech House, Boston, 1994).
- [13] B. Schnabel, E. B. Kley, and F. Wyrowski, “Study on polarizing visible light by subwavelength-period metal–stripe gratings,” *Opt. Eng.* **38**, 220–226 (1999).
- [14] M. Kahl and E. Voges, “Analysis of plasmon resonance and surface-enhanced Raman scattering on periodic silver structures,” *Phys. Rev. B* **61**, 14078–14088 (2000).
- [15] M. Born and E. Wolf, *Principles of Optics*, 6th. ed. (Pergamon Press, Oxford, 1987).
- [16] H. C. van de Hulst, *Light Scattering by Small Particles* (Dover, New York, 1981).
- [17] Y. Hsueh, M. Yang, and H. Chang, “Three-dimensional noniterative full–vectorial beam propagation method based on the alternating direction implicit method,” *J. Lightwave Technol.* **17**, 2389–2397 (1999).
- [18] H. El-Refaei, D. Yevick, and I. Betty, “Stable and noniterative bidirectional beam propagation method,” *IEEE Photonic. Tech. L.* **12**, 389–391 (2000).
- [19] Y. A. Eremin and V. I. Ivakhnenko, “Modeling of light scattering by non–spherical inhomogeneous particles,” *J. Quant. Spectrosc. Radiat. Transfer* **60**, 475–482 (1998).
- [20] C. Hafner, *Post–Modern Electromagnetics: Using Intelligent MaXwell Solvers* (Wiley, Chichester, 1999).
- [21] J. Willems, J. Haes, and R. Baets, “The bidirectional mode expansion method for two–dimensional waveguides: the TM case,” *Opt. Quant. Electron.* **27**, 995–1007 (1995).
- [22] H. Derudder, D. De Zutter, and F. Olyslager, “Analysis of waveguide discontinuities using perfectly matched layers,” *Electron. Letters* **34**, 2138–2140 (1998).
- [23] G. R. Hadley, “Low–truncation–error finite difference equations for photonics simulation II: Vertical–cavity surface–emitting lasers,” *J. Lightwave Technol.* **16**, 142–151 (1998).

- [24] J. B. Davies, “Finite element analysis of waveguides and cavities – a review,” *IEEE Trans. Magn.* **29**, 1578–1583 (1993).
- [25] M. J. Noble, J. A. Lott, and J. P. Loehr, “Quasi-exact optical analysis of oxide-apertured microcavity VCSEL’s using vector finite elements,” *IEEE J. Quantum Electron.* **34**, 2327–2339 (1998).
- [26] P. R. Hayes, M. T. O’Keefe, P. R. Woodward, and A. Gopinath, “High-order-compact time-domain numerical simulation of optical waveguides,” *Opt. Quant. Electron.* **31**, 813–826 (1999).
- [27] A. Taflove and S. C. Hagness, *Computational Electrodynamics: The Finite-Difference Time-Domain Method*, 2nd. ed. (Artech House, Boston, 2000).
- [28] E. Hasman, N. Davidson, Y. Danziger, and A. A. Friesem, “Diffractive optics: Design, realization, and applications,” *Fiber Integrated Opt.* **16**, 1–25 (1997).
- [29] D. R. Beltrami, J. D. Love, and F. Ladouceur, “Multimode planar devices,” *Opt. Quant. Electron.* **31**, 307–326 (1999).
- [30] J. B. Pendry and P. M. Bell, “Transfer matrix techniques for electromagnetic waves,” in *Photonic Band Gap Materials*, Vol. 315 of *NATO ASI Series*, C. M. Soukoulis, ed., pp. 203–228 (Kluwer, Dordrecht, 1996).
- [31] S. F. Helfert and R. Pregla, “Analysis of thin layers and discontinuities,” *Opt. Quant. Electron.* **31**, 721–732 (1999).
- [32] W. Huang and R. R. A. Syms, “Analysis of folded erbium-doped planar waveguide amplifiers by the method of lines,” *J. Lightwave Technol.* **17**, 2658–2664 (1999).
- [33] P. M. Morse and H. Feshbach, *Methods of Theoretical Physics* (McGraw-Hill, New York, 1953).
- [34] C.-T. Tai, *Dyadic Green Function in Electromagnetic Theory* (IEEE Press, New York, 1994).
- [35] T. Suzuki and P. K. L. Yu, “Emission power of an electric dipole in the photonic band structure of the fcc lattice,” *J. Opt. Soc. Am. B* **12**, 570–582 (1995).

- [36] C. Caloz, “Green’s functions in a PC–PPWG structure,” *Microwave Opt. Technol. Lett.* **29**, 405–408 (2001).
- [37] J. D. Jackson, *Classical Electrodynamics*, 3rd ed. (Wiley, New York, 1999).
- [38] O. J. F. Martin and N. B. Piller, “Electromagnetic scattering in polarizable backgrounds,” *Phys. Rev. E* **58**, 3909–3915 (1998).
- [39] A. D. Yaghjian, “Electric dyadic Green’s functions in the source region,” *Proc. IEEE* **68**, 248–263 (1980).
- [40] B. T. Draine and P. J. Flatau, “Discrete–dipole approximation for scattering calculations,” *J. Opt. Soc. Am. A* **11**, 1491–1499 (1994).
- [41] J. P. Kottmann and O. J. F. Martin, “Accurate solution of the volume integral equation for high permittivity scatterers,” *IEEE Trans. Antennas Propag.* **48**, 1719–1726 (2000).
- [42] N. B. Piller and O. J. F. Martin, “Extension of the generalized multipole technique to anisotropic media,” *Opt. Comm.* **150**, 1–6 (1998).
- [43] P. J. Flatau, “Improvements in the discrete–dipole approximation method of computing scattering and absorption,” *Opt. Lett.* **22**, 1205–1207 (1997).
- [44] B. M. Nebeker, G. W. Starr, and E. D. Hirleman, “Evaluation of iteration methods used when modeling scattering from features on surfaces using the discrete–dipole approximation,” *J. Quant. Spectrosc. Radiat. Transfer* **60**, 493–500 (1998).
- [45] H. A. Van Der Vorst, “Bi–CGSTAB: A fast and smoothly converging variant of Bi–CG for the solution of nonsymmetric linear systems,” *SIAM J. Sci. Stat. Comput.* **13**, 631–644 (1992).
- [46] M. F. Cátedra, R. P. Torres, J. Basterrechea, and E. Gago, *The CG–FFT Method* (Artech House, Boston, 1995).
- [47] R. Schmehl, B. M. Nebeker, and E. D. Hirleman, “Discrete–dipole approximation for scattering by features on surfaces by means of a two–dimensional fast Fourier transform technique,” *J. Opt. Soc. Am. A* **14**, 3026–3036 (1997).

- [48] J.-P. Bérenger, “Evanescent waves in PML’s: Origin of the numerical reflections in wave–structure interaction problems,” *IEEE Trans. Antennas Propag.* **47**, 1497–1503 (1999).
- [49] A. Sommerfeld, “Über die Ausbreitung der Wellen in der drahtlosen Telegraphie,” *Ann. Physik* **28**, 665 (1909).
- [50] T. J. Cui and W. C. Chew, “Fast evaluation of Sommerfeld integrals for EM scattering and radiation by three-dimensional buried objects,” *IEEE Trans. Geosci. Remote Sensing* **37**, 887–899 (1999).
- [51] K. A. Michalski, “Extrapolation methods for Sommerfeld integral tails,” *IEEE Trans. Antennas Propag.* **46**, 1405–1418 (1998).
- [52] Y. L. Chow, J. J. Yang, D. G. Fang, and G. E. Howard, “A closed-form spatial Green’s function for the thick microstrip substrate,” *IEEE Trans. Microwave Theory Tech.* **39**, 588–592 (1991).
- [53] J. A. Kong, *Electromagnetic Wave Theory* (Wiley, New York, 1986).
- [54] M. Abramowitz and I. A. Stegun, *Handbook of Mathematical Functions* (Dover, New York, 1972).
- [55] L. B. Felsen and N. Marcuvitz, *Radiation and Scattering of Waves* (IEEE Press, New York, 1994).
- [56] W. C. Chew, *Waves and Fields in Inhomogeneous Media* (IEEE Press, New York, 1995).
- [57] R. G. Hunsperger, *Integrated Optics: Theory and Technology*, 3rd ed. (Springer, Berlin, 1991).
- [58] *Electromagnetic Surface Modes*, A. D. Boardman, ed. (Wiley, New York, 1982).
- [59] L. Barlatey, J. R. Mosig, and T. Sphicopoulos, “Analysis of stacked microstrip patches with mixed potential integral equation,” *IEEE Trans. Antennas Propag.* **38**, 608–15 (1990).
- [60] G. N. Watson, *A Treatise on the Theory of Bessel Functions*, 2nd ed. (Cambridge University Press, Cambridge, 1944).
- [61] W. Gautschi, “Gauss–Kronrod quadrature – a survey,” in *Numerical Methods and Approximation Theory, III (Niš, 1987)*, G. V. Milovanović, ed., pp. 39–66 (Univ. Niš, Niš, 1988).

- [62] J. R. Mosig and F. E. Gardiol, "Analytical and numerical techniques in the Green's function treatment of microstrip antennas and scattereres," IEE Proc. Pt. H Microwaves, Optics and Antennas **130**, 175–82 (1983).
- [63] D. Marcuse, *Theory of Dielectric Optical Waveguides* (Academic Press, San Diego, 1974).
- [64] S. J. McNab and R. J. Blaikie, "Contrast in the evanescent near field of $\lambda/20$ period gratings for photolithography," Appl. Opt. **39**, 20–25 (2000).
- [65] M. M. Alkaisi, R. J. Blaikie, S. J. McNab, R. Cheung, and D. R. S. Cumming, "Sub-diffraction-limited patterning using evanescent near-field optical lithography," Appl. Phys. Lett. **75**, 3560–3562 (1999).
- [66] U. C. Fischer and H. P. Zingsheim, "Submicroscopic pattern replication with visible light," J. Vac. Sci. Technol. **19**, 881–885 (1981).
- [67] J. G. Goodberlet, "Patterning 100 nm features using deep-ultraviolet contact photolithography," Appl. Phys. Lett. **76**, 667–669 (2000).
- [68] H. Schmid, H. Biebuyck, B. Michel, and O. J. F. Martin, "Light-coupling masks for lensless, sub-wavelength optical lithography," Appl. Phys. Lett. **72**, 2379–2381 (1998).
- [69] J. A. Rodgers, K. E. Paul, R. J. Jackman, and G. M. Whitesides, "Using an elastomeric phase mask for sub-100 nm photolithography in the optical near field," Appl. Phys. Lett. **70**, 2658–2660 (1997).
- [70] A. Bietsch and B. Michel, "Conformal contact and pattern stability of stamps used for soft lithography," J. Appl. Phys. **88**, 4310–4318 (2001).
- [71] H. Schmid, H. Biebuyck, B. Michel, O. J. F. Martin, and N. B. Piller, "Light-coupling masks: an alternative, lensless approach to high-resolution optical contact lithography," J. Vac. Sci. Technol. B **16**, 3422–3425 (1998).
- [72] O. J. F. Martin, N. B. Piller, H. Schmid, H. Biebuyck, and B. Michel, "Energy flow in light-coupling masks for lensless optical lithography," Optics Express **3**, 280–285 (1998).

- [73] H. Schmid and B. Michel, "Siloxane polymers for high-resolution, high-accuracy soft lithography," *Macromolecules* **33**, 3042–3049 (2000).
- [74] *Handbook of Optics*, 2nd ed., M. Bass, ed., Vol. II (McGraw-Hill, New York, 1995).
- [75] H. A. Macleod, *Thin-Film Optical Filters*, 2nd. ed. (Adam Hilger, Bristol, 1986).
- [76] T. Tamir and S. T. Peng, "Analysis and design of grating couplers," *Appl. Phys.* **14**, 235–254 (1977).
- [77] D. Marcuse, *Light Transmission Optics*, 2nd ed. (Krieger, Malabar, 1989).
- [78] T. W. Ang, G. T. Reed, A. Vonsovici, A. G. R. Evans, P. R. Routley, and M. R. Josey, "Effects of grating heights on highly efficient unibond SOI waveguide grating couplers," *IEEE Photonics Tech. L.* **12**, 59–61 (2000).
- [79] R. Orobctchouk, A. Layadi, H. Gualous, D. Pascal, A. Koster, and S. Laval, "High-efficiency light coupling in a submicrometric silicon-on-insulator waveguide," *Appl. Opt.* **39**, 5773–5777 (2000).
- [80] K. Welford, in *Surface Plasmon-Polaritons*, No. 9 in *IOP Short Meetings Series*, pp. 25–78 (IOP, Bristol, 1988).
- [81] N. F. van Hulst, J.-A. Veerman, M. F. Garcia-Parajó, and L. K. Kuipers, "Analysis of individual (macro)molecules and proteins using near-field optics," *J. Chem. Phys.* **112**, 7799–7810 (2000).
- [82] J. H. Weaver, C. Krafska, D. W. Lynch, and E. E. Koch, *Optical Properties of Metal*, No. I and II in *Physics Data* (Fachinformationzentrum Karlsruhe, 1981).
- [83] O. J. F. Martin, "3D simulations of the experimental signal measured in near-field optical microscopy," *J. Microscopy* **194**, 235–239 (1999).
- [84] O. J. F. Martin and M. Paulus, "Influence of the metal roughness on the near-field generated by an aperture/apertureless probe," *J. Microscopy*, in press (2001).

- [85] Lord Rayleigh, “On the electromagnetic theory of light,” *Philos. Mag.* **12**, 81–101 (1881).
- [86] S. Selleri, L. Vincetti, A. Cucinotta, and M. Zoboli, “Complex FEM modal solver of optical waveguides with PML boundary conditions,” *Opt. Quant. Electron.* **33**, 359–371 (2001).
- [87] J. P. Kottmann, O. J. F. Martin, D. R. Smith, and S. Schultz, “Spectral response of Silver nanoparticles,” *Optics Express* **6**, 213–219 (2000).
- [88] J. P. Kottmann, O. J. F. Martin, D. R. Smith, and S. Schultz, “Dramatic localized electromagnetic enhancement in plasmon resonant nanowires,” *Chem. Phys. Lett.* **341**, 1–6 (2001).
- [89] J. P. Kottmann, O. J. F. Martin, D. R. Smith, and S. Schultz, “Field polarization and polarization charge distributions in plasmon resonant particles,” *New J. Phys.* **2**, 27.1–27.9 (2000).
- [90] J. P. Kottmann, O. J. F. Martin, D. R. Smith, and S. Schultz, “Non-regularly shaped plasmon resonant nanoparticle as localized light source for near-field microscopy,” *J. Microscopy* **202**, 60–65 (2001).
- [91] J. P. Kottmann and O. J. F. Martin, “Retardation-induced plasmon resonances in coupled nanoparticles,” *Opt. Lett.* **26**, 1096–1098 (2001).
- [92] J. P. Kottmann and O. J. F. Martin, “Plasmon resonant coupling in metallic nanowires,” *Optics Express* **8**, 655–663 (2001).
- [93] P. Gay-Balmaz and J. R. Mosig, “Three-dimensional planar radiating structures in stratified media,” *Int. J. Microwave and Millimeter wave CAE* **3**, 330–343 (1997).
- [94] A. F. Peterson, “The interior resonance problem associated with surface integral equations of electromagnetics: Numerical consequences and a survey of remedies,” *Electromagnetics* **10**, 293–312 (1990).

Acknowledgment

The work for this thesis was carried out both at the Electromagnetic Fields and Microwave Electronics Laboratory at the Swiss Federal Institute of Technology (ETH) in Zurich and at the IBM Zurich Research Laboratories in Rüschlikon. At both locations I have been fortunate to meet outstanding people, who helped me considerably and inspired me in my research activities. I feel honored to mention the following in particular:

I am very much obliged to Prof. Rüdiger Vahldieck, the head of the field theory group. Not only did he grant me the freedom to do my research, but he has also been an example with his positive attitude and the supremely good management of our lab. With his generous support I could attend several international conferences and introduce myself to the scientific community.

It is considerably due to Prof. Olivier J. F. Martin that I have accomplished this work. Being my thesis supervisor he taught me computational optics, encouraged me to treat the Green's tensor as a good friend, and, above all, he introduced me to the wonderful world of nano-optics. He has strongly motivated me with his enthusiasm and impressed me with his open mind and his creativity. I would like to sincerely thank him for the numerous discussions, his guidance and his personal commitment.

I also feel greatly indebted to Dr. Bruno Michel at the IBM Zurich Research Laboratories. He has continuously supported my project and has always welcomed me in the IBM labs. Meeting the brilliant people there and benefiting from their creativity and expertise has been a great experience. In particular, I have been lucky to work with Heinz Schmid who often confronted me with the experimentalist's point of view and the real practical issues. Thank you, Heinz, for many discussions and for your inspiring ideas. I would also like to thank the other members of the microcontact processing group at IBM for showing interest in my work and supporting my project.

Whenever I felt lost within the mysteries of optics, a talk with my

colleague Jörg Kottmann helped to set me straight again. Thank you, Jörg, for many scientific discussions about singularities and soccer. I would also like to thank Philippe Gay-Balmaz for the friendly atmosphere in our office and for plenty of diversion.

Thanks to Ray Ballisti I could smoothly work with our computer infrastructure. He has managed our system so well that problems came up only very rarely. Ray, you really do a great job! I am also very grateful to Annemarie Pfenninger and Verena Hofer for their administrative support.

I have truly enjoyed working at the field theory lab. Thanks to all colleagues who shared with me the good times and the not-so-good times, the days and some nights, the fun of skiing and mountaineering, and, above all, the unconditional dedication to electromagnetics. Gentlemen, it has been a pleasure to meet you. But eventually you failed to teach me thinking in terms of dB.

Zurich, October 2001

Michael Paulus

Résumé

Name: Michael PAULUS

Birth: October 23, 1971 in Landshut, Germany

Citizenship: German

Education:

PhD Student and Research Assistant, 1998-2001.

Electromagnetic Fields and Microwave Electronics
Laboratory, Swiss Federal Institute of Technology
Zurich, Switzerland.

Diplom–Physiker, 1998.

University of Augsburg, Germany.
Diploma Thesis: Modeling and simulation of
plasma immersion ion implantation.

Allgemeine Hochschulreife, 1991.

Hans–Leinberger–Gymnasium in Landshut, Germany.

Primary School, 1978–1982.

Carl–Orff–Grundschule in Landshut, Germany.

Publications

P1

**Accurate and efficient computation of the
Green's tensor for stratified media**

Michael Paulus, Phillippe Gay-Balmaz, and Olivier J. F. Martin
Phys. Rev. E **62**, 5797–5807 (2000)

Accurate and efficient computation of the Green's tensor for stratified media

Michael Paulus,^{1,2} Phillippe Gay-Balmaz,¹ and Olivier J. F. Martin^{1,*}

¹*Electromagnetic Fields and Microwave Electronics Laboratory, Swiss Federal Institute of Technology, ETH-Zentrum ETZ, CH-8092 Zurich, Switzerland*

²*IBM Research Division, Zurich Research Laboratory, CH-8803 Rüschlikon, Switzerland*

(Received 28 April 2000)

We present a technique for the computation of the Green's tensor in three-dimensional stratified media composed of an arbitrary number of layers with different permittivities and permeabilities (including metals with a complex permittivity). The practical implementation of this technique is discussed in detail. In particular, we show how to efficiently handle the singularities occurring in Sommerfeld integrals, by deforming the integration path in the complex plane. Examples assess the accuracy of this approach and illustrate the physical properties of the Green's tensor, which represents the field radiated by three orthogonal dipoles embedded in the multilayered medium.

PACS number(s): 42.25.Bs, 42.25.Fx, 42.25.Gy, 42.68.Mj

I. INTRODUCTION

The Green's tensor $\mathbf{G}(\mathbf{r}, \mathbf{r}')$ represents the electric field radiated at position \mathbf{r} by three orthogonal dipoles located at \mathbf{r}' . For an infinite homogeneous background, this dyadic can be computed analytically [1,2]. The situation is much more complex in a stratified medium, where the Green's tensor must take into account all the reflections and refractions that occur at the different interfaces.

The simplest geometry of interest here is that of a dipolar source above a surface. This problem was first treated by Sommerfeld [3] and then extensively studied in connection with antennae radiation [4–7].

In this context of a single interface, the intrinsic properties of the Green's tensor were also used to investigate the variation of spontaneous emission for a dipolar transition in the presence of a surface [8–11]. Similar properties were also utilized to determine the polariton spectrum in semiconductor superlattices [12].

The Green's tensor plays a key role in scattering calculations. As a matter of fact, when a scatterer is discretized into small enough elements, the response of each element to an external field is essentially dipolar [13] and the Green's tensor gives the interaction between these discretized elements. This technique, known also as the coupled dipole approximation, has been successfully applied to many scattering problems in infinite homogeneous backgrounds [14–16]. Using the Green's tensor associated with a surface, it was also used to investigate scattering on a surface [17–21].

In this paper we present an efficient technique for the accurate computation of the Green's tensor for arbitrarily layered media (i.e., not limited to a single interface). The formalism is derived in Sec. II. It leads to so-called Sommerfeld integrals that must be performed numerically in the complex plane. Our numerical implementation is described in Sec. III. In Sec. IV we illustrate the physical properties of the Green's tensor and summarize our work in Sec. V. Ap-

pendixes A and B give the detailed formulas for the practical implementation of this technique.

II. FORMALISM

The Green's tensor $\mathbf{G}(\mathbf{r}, \mathbf{r}')$ for an arbitrary scattering system described by the dielectric permittivity $\epsilon(\mathbf{r})$ and the magnetic permeability $\mu(\mathbf{r})$ is the solution of the vector wave equation with a point source term [1]:

$$\nabla \times \mu^{-1}(\mathbf{r}) \nabla \times \mathbf{G}(\mathbf{r}, \mathbf{r}') - k_0^2 \epsilon(\mathbf{r}) \nabla \times \mathbf{G}(\mathbf{r}, \mathbf{r}') = \mu^{-1}(\mathbf{r}) \mathbf{1} \delta(\mathbf{r} - \mathbf{r}'), \quad (1)$$

where $k_0^2 = \omega^2 \epsilon_0 \mu_0$ is the vacuum wave number [throughout the paper we assume time harmonic fields with an $\exp(-i\omega t)$ dependence].

In this paper we specifically consider planar stratified systems, where each layer $l = 1, \dots, N$ can be characterized by the permittivity ϵ_l and the permeability μ_l as illustrated in Fig. 1. For convenience, we chose our coordinate system such that the layers are parallel to the xy plane.

For the derivation of $\mathbf{G}(\mathbf{r}, \mathbf{r}')$ associated with a stratified background, we start with the expression for the free-space Green's tensor $\mathbf{G}_H(\mathbf{r}, \mathbf{r}')$ of a homogeneous system $\epsilon_B = \epsilon_0 \epsilon_r$, $\mu_B = \mu_0 \mu_r$. It is given by [16]

$$\mathbf{G}_H(\mathbf{r}, \mathbf{r}') = \left(\mathbf{1} + \frac{\nabla \nabla}{k_B^2} \right) \frac{\exp(ik_B R)}{4\pi R} \quad (2)$$

$$= \left(\mathbf{1} + \frac{ik_B R - 1}{k_B^2 R^2} \mathbf{1} + \frac{3 - 3ik_B R - k_B^2 R^2}{k_B^2 R^4} \mathbf{R} \mathbf{R} \right) \times \frac{\exp(ik_B R)}{4\pi R}, \quad (3)$$

where $R = |\mathbf{R}| = |\mathbf{r} - \mathbf{r}'|$ is the relative distance and $k_B^2 = \omega^2 \epsilon_B \mu_B$ corresponds to the wave number in the background medium.

*Correspondence author. Email address: martin@ifh.ee.ethz.ch

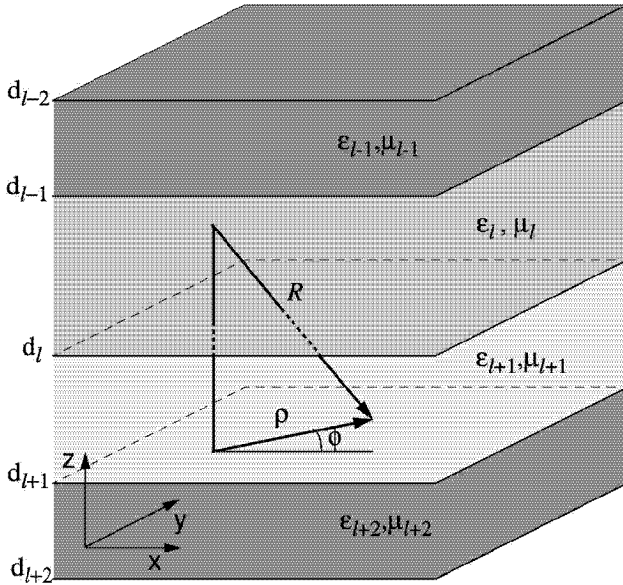


FIG. 1. Stratified medium consisting of N layers with $(\epsilon_1, \mu_1), \dots, (\epsilon_N, \mu_N)$ separated by interfaces at $z = d_1, \dots, d_{N-1}$. The vector $\mathbf{R} = \mathbf{r} - \mathbf{r}'$ defines the relative distance between \mathbf{r} and \mathbf{r}' and $\mathbf{p} = (x - x', y - y') = (\rho \cos \phi, \rho \sin \phi)$ is the projection of \mathbf{R} onto the xy plane.

To deduce $\mathbf{G}(\mathbf{r}, \mathbf{r}')$ for a stratified background, it is more convenient to use an integral representation of $\mathbf{G}_H(\mathbf{r}, \mathbf{r}')$. Fourier transforming Eq. (2) leads to

$$\mathbf{G}_H(\mathbf{r}, \mathbf{r}') = \frac{1}{8\pi^3 k_B^2} \int \int \int d\mathbf{k} \left(\frac{\mathbf{1}k_B^2 - \mathbf{k}\mathbf{k}}{k^2 - k_B^2} \right) \exp(i\mathbf{k} \cdot \mathbf{R}). \quad (4)$$

Since we assume that the layers, which will be added later, are perpendicular to the z axis, we first perform the integration over k_z using calculus of residues. Hence, we must ensure that the integrand vanishes for $k_z \rightarrow \infty$ and rewrite Eq. (4) as

$$\begin{aligned} \mathbf{G}_H(\mathbf{r}, \mathbf{r}') &= \frac{1}{8\pi^3 k_B^2} \int \int \int d\mathbf{k} \left(\frac{\mathbf{1}k_B^2 - \mathbf{k}\mathbf{k}}{k^2 - k_B^2} + \hat{\mathbf{z}}\hat{\mathbf{z}} \right) \exp(i\mathbf{k} \cdot \mathbf{R}) \\ &\quad - \frac{\hat{\mathbf{z}}\hat{\mathbf{z}}}{8\pi^3 k_B^2} \int \int \int d\mathbf{k} \exp(i\mathbf{k} \cdot \mathbf{R}) \\ &= \frac{i}{8\pi^2 k_B^2} \int \int dk_x dk_y \left(\frac{\mathbf{1}k_B^2 - \mathbf{k}_B}{k_{Bz}} \right) \\ &\quad \times \exp(i\mathbf{k}_B \cdot \mathbf{R}) - \frac{\hat{\mathbf{z}}\hat{\mathbf{z}}}{k_B^2} \delta(\mathbf{R}), \end{aligned} \quad (5)$$

where $k_{Bz} = (k_B^2 - k_x^2 - k_y^2)^{1/2}$ is the z component of the wave vector and

$$\mathbf{k}_B(k_{Bz}) = \begin{cases} k_x \hat{\mathbf{x}} + k_y \hat{\mathbf{y}} + k_{Bz} \hat{\mathbf{z}} & \text{for } z > z', \\ k_x \hat{\mathbf{x}} + k_y \hat{\mathbf{y}} - k_{Bz} \hat{\mathbf{z}} & \text{for } z < z' \end{cases} \quad (6)$$

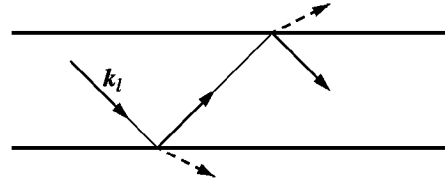


FIG. 2. The effect of the surrounding layers on a given Fourier component \mathbf{k}_l in layer l is to add an upgoing and a downgoing plane wave with similar \mathbf{k} vectors.

Now that we have the plane-wave expansion of the Green's tensor for an infinite homogeneous background ϵ_B, μ_B , it is a simple matter to include additional layers. Indeed, the effect of these layers will be to add two plane waves, one propagating upward and one downward, to each Fourier component, as illustrated in Fig. 2 [note that the propagation vector (k_x, k_y, k_z) is similar for the three plane waves, only the sign of k_z changes]. The amplitudes of these additional components are determined by the boundary conditions at the different interfaces. Since the Green's tensor represents the electric field radiated at \mathbf{r} by three orthogonal point sources at \mathbf{r}' , the boundary conditions depend on the polarization of the corresponding Fourier component. It is therefore advantageous to introduce a new orthonormal system $\hat{\mathbf{k}}(k_{Bz})$, $\hat{\mathbf{l}}(k_{Bz})$, and $\hat{\mathbf{m}}(k_{Bz})$ [22],

$$\hat{\mathbf{k}}(k_{Bz}) = \frac{\mathbf{k}_B(k_{Bz})}{k_B}, \quad (7a)$$

$$\hat{\mathbf{l}}(k_{Bz}) = \frac{\hat{\mathbf{k}}(k_{Bz}) \times \hat{\mathbf{z}}}{|\hat{\mathbf{k}}(k_{Bz}) \times \hat{\mathbf{z}}|}, \quad (7b)$$

$$\hat{\mathbf{m}}(k_{Bz}) = \hat{\mathbf{k}}(k_{Bz}) \times \hat{\mathbf{l}}(k_{Bz}). \quad (7c)$$

Equivalently, another orthonormal system is formed by $\hat{\mathbf{k}}(-k_{Bz})$, $\hat{\mathbf{l}}(-k_{Bz})$, and $\hat{\mathbf{m}}(-k_{Bz})$. Remark that $\hat{\mathbf{l}}$ is perpendicular to the plane defined by $\hat{\mathbf{k}}$ and $\hat{\mathbf{z}}$, whereas $\hat{\mathbf{m}}$ lies within this plane. For a given k_B , the electric-field component parallel to $\hat{\mathbf{l}}$ corresponds, therefore, to s polarization and that parallel to $\hat{\mathbf{m}}$ corresponds to p polarization. Using the fact that $\hat{\mathbf{k}}\hat{\mathbf{k}} + \hat{\mathbf{l}}\hat{\mathbf{l}} + \hat{\mathbf{m}}\hat{\mathbf{m}} = \mathbf{1}$, Eq. (5) can be rewritten as

$$\begin{aligned} \mathbf{G}_H(\mathbf{r}, \mathbf{r}') &= -\frac{\hat{\mathbf{z}}\hat{\mathbf{z}}}{k_B^2} \delta(\mathbf{R}) + \frac{i}{8\pi^2} \int \int dk_x dk_y \left(\frac{\hat{\mathbf{l}}\hat{\mathbf{l}} + \hat{\mathbf{m}}\hat{\mathbf{m}}}{k_{Bz}} \right) \\ &\quad \times \exp(i\mathbf{k}_B \cdot \mathbf{R}). \end{aligned} \quad (8)$$

To obtain the Green's tensor $\mathbf{G}(\mathbf{r}, \mathbf{r}')$ for a stratified medium, we can now superpose to the free-space Green's tensor of a homogeneous medium ϵ_l, μ_l the additional terms by formally writing

$$\begin{aligned} \mathbf{G}(\mathbf{r}, \mathbf{r}') &= -\frac{\hat{\mathbf{z}}\hat{\mathbf{z}}}{k_l^2} \delta(\mathbf{R}) + \frac{i}{8\pi^2} \int \int dk_x dk_y \exp\{i[k_x(x - x')] \\ &\quad + k_y(y - y')]\} \frac{1}{k_{lz}} [\hat{\mathbf{l}} \exp(ik_{lz}|z - z'|) \\ &\quad + \mathbf{R}^{s\dagger} \exp(ik_{lz}z) + \mathbf{R}^{s\perp} \exp(-ik_{lz}z)] \end{aligned}$$

$$+ \hat{\mathbf{m}}\hat{\mathbf{m}} \exp(ik_{lz}|z-z'|) + \mathbf{R}^{p\uparrow} \exp(ik_{lz}z) \\ + \mathbf{R}^{p\downarrow} \exp(-ik_{lz}z), \quad (9)$$

where $k_l^2 = \omega^2 \epsilon_l \mu_l$ and $k_{lz} = (k_l^2 - k_x^2 - k_y^2)^{1/2}$. The tensors $\mathbf{R}^{s\uparrow}$, $\mathbf{R}^{s\downarrow}$, $\mathbf{R}^{p\uparrow}$, and $\mathbf{R}^{p\downarrow}$ can obviously be interpreted as generalized reflection coefficients that take into account reflections from all existing surfaces.

For the explicit calculation of $\mathbf{G}(\mathbf{r}, \mathbf{r}')$ it is necessary to consider separately the two cases $z > z'$ and $z < z'$. In Eq. (9) each component of the Green's tensor is expressed in terms of s - and p -polarized upgoing and downgoing plane waves with amplitude coefficients $A_{l,\alpha\beta}^s$, $B_{l,\alpha\beta}^s$, $A_{l,\alpha\beta}^p$, and $B_{l,\alpha\beta}^p$:

$$G_{\alpha\beta}(\mathbf{r}, \mathbf{r}') = \frac{i}{8\pi^2} \int \int dk_x dk_y \exp\{i[k_x(x-x') \\ + k_y(y-y')]\} \frac{1}{k_{lz}} \{ [\hat{l}_\alpha(\pm k_{lz}) A_{l,\alpha\beta}^s \exp(ik_{lz}z) \\ + \hat{l}_\alpha(\mp k_{lz}) B_{l,\alpha\beta}^s \exp(-ik_{lz}z)] \hat{l}_\beta(k_{lz}) \\ + [\hat{m}_\alpha(\pm k_{lz}) A_{l,\alpha\beta}^p \exp(ik_{lz}z) \\ + \hat{m}_\alpha(\mp k_{lz}) B_{l,\alpha\beta}^p \exp(-ik_{lz}z)] \hat{m}_\beta(k_{lz}) \}, \quad (10)$$

where the upper sign refers to the case $z > z'$ and the lower sign to $z < z'$. For simplicity, the contribution of the δ function is omitted in Eq. (10). The amplitude coefficients $A_{l,\alpha\beta}^s$, $B_{l,\alpha\beta}^s$, $A_{l,\alpha\beta}^p$, and $B_{l,\alpha\beta}^p$ are functions of $(k_{lz}; \mathbf{r}, \mathbf{r}')$ and are derived in Appendix A.

Equation (10) can be further simplified by introducing a cylindrical coordinate system. In the xy and $k_x k_y$ plane we introduce the transverse coordinate ρ ,

$$\mathbf{R} = (\rho, z - z') = (x - x', y - y', z - z'), \quad (11)$$

$$\rho = (\rho \cos \phi, \rho \sin \phi), \quad (12)$$

and the transverse wave vector \mathbf{k}_ρ ,

$$\mathbf{k} = (\mathbf{k}_\rho, k_z) = (k_x, k_y, k_z), \quad (13)$$

$$\mathbf{k}_\rho = (k_\rho \cos k_\phi, k_\rho \sin k_\phi). \quad (14)$$

The integration over k_ϕ in Eq. (10) is then performed analytically with the help of Bessel functions [23]:

$$J_n(k_\rho \rho) = \frac{i^{-n}}{2\pi} \int_0^{2\pi} dk_\phi \exp(ik_\rho \rho \cos k_\phi) \cos(nk_\phi). \quad (15)$$

Thus, only a one-dimensional integral over the radial component k_ρ must be calculated numerically:

$$\mathbf{G}(\mathbf{r}, \mathbf{r}') = -\frac{\hat{\mathbf{z}}\hat{\mathbf{z}}}{k_l^2} \delta(\mathbf{R}) \\ + \frac{i}{4\pi} \int_0^\infty dk_\rho [\mathbf{f}^s(k_\rho; \mathbf{r}, \mathbf{r}') + \mathbf{f}^p(k_\rho; \mathbf{r}, \mathbf{r}')]. \quad (16)$$

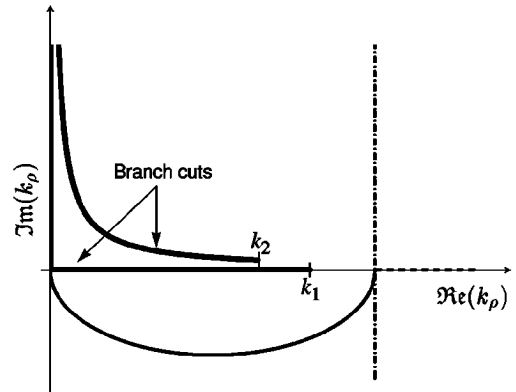


FIG. 3. Plane of integration: The singularities are surrounded by an elliptical path (solid line). At $k_\rho = 2k^{\text{maj}}$ the integration is resumed along the real k_ρ axis using Bessel functions (dashed line) or parallel to the imaginary k_ρ axis using Hankel functions (dash-dotted line).

The components of the tensors \mathbf{f}^s and \mathbf{f}^p , obtained after careful evaluation of Eq. (10), are given in Appendix B.

III. PRACTICAL IMPLEMENTATION

The objective of this paper being to provide a useful framework for the computation of the Green's tensor for stratified media, we discuss in this section the practical details related to the numerical evaluation of Eq. (16).

A. Singularities

In the preceding section the Green's tensor for stratified media was expressed as a set of one-dimensional semi-infinite integrals, so-called Sommerfeld integrals [Eqs. (16) and (B1)–(B18)]. A typical integrand has the form

$$G(k_\rho; \mathbf{r}, \mathbf{r}') = g(k_\rho; \mathbf{r}, \mathbf{r}') J_n(k_\rho \rho) [\mathcal{A}(k_\rho, z') \\ \times \exp(ik_{lz}z) + \mathcal{B}(k_\rho, z') \exp(-ik_{lz}z)]. \quad (17)$$

An integral of this kind cannot be performed analytically, but has to be evaluated numerically. However, a straightforward implementation would fail because of the mathematically awkward behavior of the integrand. To avoid these difficulties we use Cauchy's integral theorem and deform the integration path in the complex k_ρ plane. The objective of this section is to determine such an optimum path.

The singularities of $G(k_\rho; \mathbf{r}, \mathbf{r}')$ can be classified in two types: branch point singularities and pole singularities. Branch point singularities are related to the $k_{lz} = (k_l^2 - k_\rho^2)^{1/2}$ dependence of the integrands. Since k_{lz} is the square root of a complex number, it is double valued and branch cuts defined by $\text{Im}(k_{lz}) = 0$ intersect the plane of integration [1]. Each branch cut ends in a branch point at $k_\rho = \pm k_l$. If the medium is lossless, these singularities are located on the real k_ρ axis, i.e., on the integration path (Fig. 3).

One could expect that a branch cut exists for each layer, i.e., for each k_l . However, it can be shown that the functional dependence of $G(k_\rho; \mathbf{r}, \mathbf{r}')$ on k_{lz} is even for all l except the two outermost regions [24,25]. Therefore, branch cuts and branch points appear only for $k_\rho = \pm k_1, \pm k_N$.

Since the integral runs from zero to infinity, we can further restrict our discussion to singularities with a non-negative real part.

To choose now the appropriate value for k_{1z} and k_{Nz} , thereby ensuring that the integration is performed on the correct Riemann sheet defined by the branch cut $\text{Im}(k_{lz})=0$, we simply apply the radiation conditions: We must use the value with $\text{Im}(k_{lz})>0$ to make the integrands vanish for $z\rightarrow\pm\infty$.

The second class of singularities, pole singularities, is due to vanishing denominators of $G(k_\rho; \mathbf{r}, \mathbf{r}')$. These poles correspond physically to modes guided by the layered structure, as will be illustrated in Sec. IV. For dielectric media, such modes have propagation vectors k_ρ smaller than $k_l^{\max} = \max_i \text{Re}(k_l)$ [26].

For lossy materials with $\text{Im}(\epsilon)>0$, it can be shown that both branch points and pole singularities are shifted into the first quadrant of the complex k_ρ plane. However, if the losses are small, the singularities remain close enough to the $\text{Re}(k_\rho)$ axis and can still cause serious problems.

B. Numerical quadrature

To avoid singularities, our integration path must therefore run inside the fourth quadrant in the complex k_ρ plane. A possible choice would be to leave the real axis only in close vicinity of the singularities, e.g., by a semicircle around each singularity. This requires us to precisely determine the location of each pole, which is a tedious and time-consuming task [27].

In our implementation we use an easier way of surrounding the singularities: an elliptical path starting at $k_\rho=0$ with the major semiaxis k_ρ^{\max} and the minor semiaxis k_ρ^{\min} (Fig. 3). Of course, we must ensure that k_ρ^{\max} is chosen large enough to enclose all the singularities. From the discussion in the preceding section we take $2k_\rho^{\max}=k_l^{\max}+k_0$, where the vacuum wave number k_0 is added as a safety margin.

The parameter k_ρ^{\min} is empirically chosen such that the integration path is sufficiently far away from the singularities without extending too much in negative imaginary k_ρ direction, because the Bessel function $J_n(k_\rho\rho)$ increases then very rapidly. We have observed that $k_\rho^{\min}=10^{-3}k_\rho^{\max}$ was a good choice for this parameter. A typical integrand is shown in Fig. 4, together with the deformed integration path.

For the remaining integration, we usually follow the real k_ρ axis. However, when $z-z'$ is small, the exponential damping in Eq. (17) becomes weak and the quadrature taken along the real axis converges very slowly. In that case, it is more advantageous to transform the integral using Hankel functions:

$$\begin{aligned} J_n(k_\rho\rho) &= \frac{1}{2}[H_n^{(1)}(k_\rho\rho) + H_n^{(2)}(k_\rho\rho)] \\ &= \frac{1}{2}\{H_n^{(1)}(k_\rho\rho) + [H_n^{(1)}((k_\rho\rho)^*)]^*\}. \end{aligned} \quad (18)$$

Because of the asymptotic behavior of the Hankel functions for large values of $k_\rho\rho$,

$$\lim_{|k_\rho\rho|\rightarrow\infty} H_n^{(1)}(k_\rho\rho) = \sqrt{\frac{2}{\pi k_\rho\rho}} \exp[ik_\rho\rho - \frac{1}{2}i\pi(n+\frac{1}{2})], \quad (19)$$

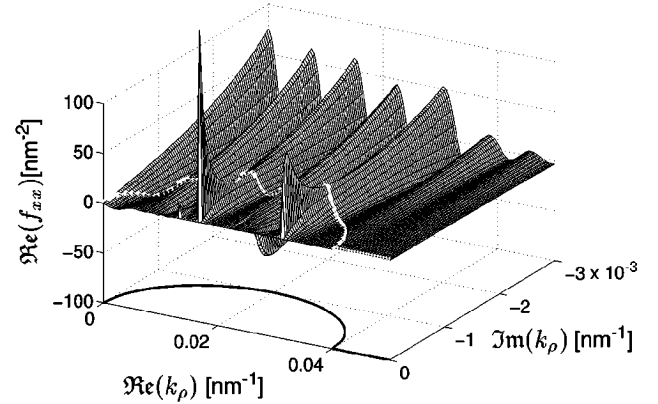


FIG. 4. Real part of the integrand $f_{xx}(k_\rho)$ [Eqs. (B1) and (B2)]. In this example, a nonmagnetic three-layer system with $\epsilon_1=1$, $\epsilon_2=4$, and $\epsilon_3=2$ is used. The elliptical integration path used to avoid the singularities is shown on the integrand (white line) and on the projection plane.

we can deflect the integration path from the real axis to a path parallel to the imaginary axis: for the first term in Eq. (18) in the positive imaginary direction, for the second term in the negative imaginary direction (Fig. 3). Thus, for each $|k_\rho\rho|$ the Hankel function must only be calculated for the argument with the positive imaginary part. The exponential term in Eq. (19) ensures then a much faster convergence of the integrand. This is illustrated in Fig. 5, where we compare the integrand using Bessel functions along the real k_ρ axis with that corresponding to Hankel functions parallel to the imaginary k_ρ axis. Evidently, the integration using Hankel functions converges much faster.

From a practical point of view, we use the Gauss-Kronrod quadrature to evaluate the integrals along the deformed path [28]. This efficient algorithm can easily handle the oscillating behavior of the Bessel and Hankel functions for large $k_\rho\rho$. We are using the 15-point Gauss-Kronrod quadrature and stop the integration when a relative accuracy of 10^{-9} is

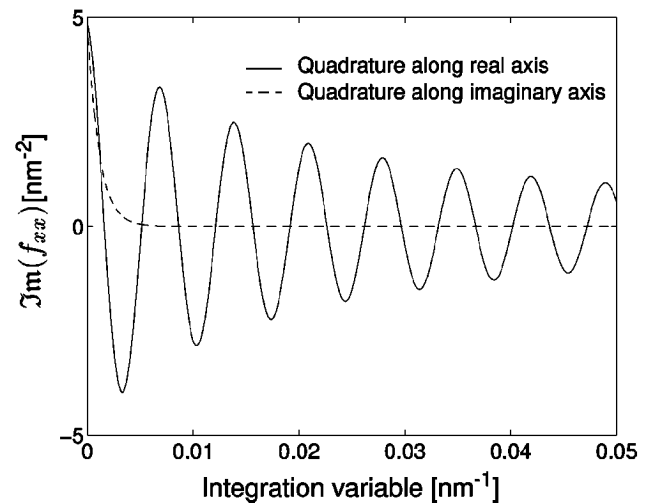


FIG. 5. Comparison of the imaginary part of the integrand $f_{xx}(k_\rho)$ along the real axis and the imaginary axis, respectively, using a formulation in terms of Bessel (solid line) and Hankel functions (dashed line), respectively. The system is identical to that used in Fig. 4.

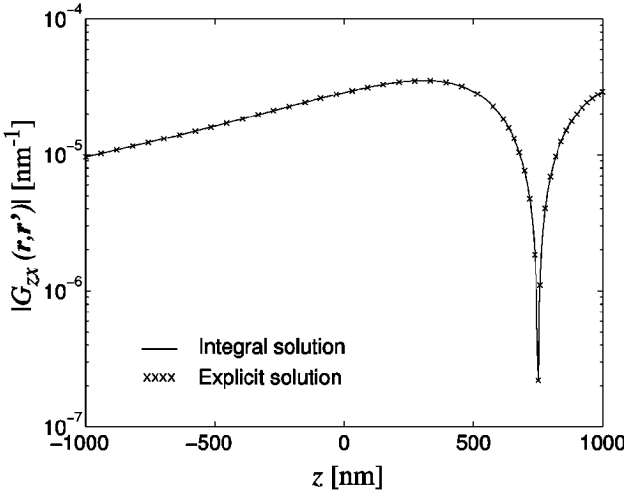


FIG. 6. Accuracy of the method: Comparison of the Green's tensor for a homogeneous medium obtained by numerical quadrature assuming four layers with identical permittivity (solid line) with that obtained from the explicit free-space solution [Eq. (3), crosses]. The $|G_{zx}|$ component is shown.

achieved. The application of a much more costly 64-point Gauss-Kronrod quadrature would roughly double the computation time without an appreciable gain in precision. Decreasing the desired relative accuracy to 10^{-6} typically speeds up the computation by a factor 1.5.

A very useful trick to expedite the computation of the Green's tensor for a stratified medium is to integrate simultaneously the different components of $\mathbf{G}(\mathbf{r}, \mathbf{r}')$. However, we do not evaluate directly the individual components but rather choose a numerically more appropriate decomposition: The integrands in Eqs. (B1)–(B18) can be ordered in *s*- and *p*-polarized terms with first- and second-order Bessel or Hankel functions. Thus, seven independent terms can be defined. We have observed that for a given $(\mathbf{r}, \mathbf{r}')$ pair these terms have a similar behavior in the \mathbf{k}_p plane, which makes possible their simultaneous integration. In our practical implementation, we integrate in parallel 14 real functions that correspond to the real and imaginary parts of these independent contributions to the Green's tensor. As a measure for the Gauss-Kronrod quadrature (stop criterion), we simply use the sum of these 14 functions.

On our system (IBM PS/6000 7012-397, 160 MHz) the calculation of the complete Green's tensor for 1000 $(\mathbf{r}, \mathbf{r}')$ pairs takes for the example shown in Fig. 9 approximately 380 s of CPU time. Note, however, that this calculation time strongly depends on the relative position of \mathbf{r} and \mathbf{r}' .

To demonstrate the accuracy of our integration scheme, we first perform calculations for a system consisting of virtual layers, i.e., layers with identical permittivity and permeability. These results must be identical to the explicit solution given by the free-space Green's tensor of a homogeneous medium, Eq. (3). Figure 6 shows a comparison for a virtual four-layer medium. Obviously, the agreement between the two calculations is perfect.

IV. ILLUSTRATIVE EXAMPLES

To illustrate the physical substance of our mathematical formalism, let us consider the most simple case of a nonmag-

netic two-layer system ϵ_1, ϵ_2 separated by a single interface at $d=0$. Assuming that \mathbf{r}' lies within layer 1 and \mathbf{r} within layer 2, the integrand $G_{zz}(k_p; \rho, \phi)$ reduces to

$$G_{zz}(k_p; \mathbf{r}, \mathbf{r}') = \frac{k_p^3}{k_2^2 k_{1z}} J_0(k_p \rho) T_{12}^p \exp[i(k_{1z} z' - k_{2z} z)], \quad (20)$$

where $T_{12}^p = 1 + \mathcal{F}_{12}^p = \epsilon_2 k_{1z} / (\epsilon_2 k_{1z} + \epsilon_1 k_{2z})$ is the transmission coefficient of the surface.

As already mentioned, branch point singularities exist for $k_p = \pm k_1, \pm k_2$. By definition, for any k_p lying on one of these branch cuts k_z is pure real, forming a wave propagating in $z \rightarrow \pm \infty$ direction. These waves form a continuum of modes called radiation modes.

In addition, pole singularities appear when the denominator of T_{12}^p vanishes, i.e., for k_p such that

$$\epsilon_2 \sqrt{k_1^2 - k_p^2} + \epsilon_1 \sqrt{k_2^2 - k_p^2} = 0. \quad (21)$$

The solutions of Eq. (21) are formally given by

$$k_p = \pm \sqrt{\frac{\epsilon_1 \epsilon_2}{\epsilon_1 + \epsilon_2}} k_0. \quad (22)$$

However, one has to verify if this solution is physically meaningful. If we choose ϵ_1 and ϵ_2 purely real and positive, obviously $k_p < k_1, k_2$. Hence, the square roots being also purely real and positive, Eq. (21) is not fulfilled. If we now assume that $\epsilon_2 < 0$ and $\epsilon_1 < |\epsilon_2|$, a solution does exist. For such a plasma medium, the wave vectors in the z direction k_{1z} and k_{2z} at the location of the pole k_p become

$$k_{iz} = \sqrt{k_i^2 - k_p^2} = \sqrt{\epsilon_i - \frac{\epsilon_1 \epsilon_2}{\epsilon_1 + \epsilon_2}} k_0 = \sqrt{\frac{\epsilon_i^2}{\epsilon_1 + \epsilon_2}} k_0 \quad \text{for } i=1,2. \quad (23)$$

Referring to the discussion in Sec. III A, the sign of the square root in Eq. (23) has to be chosen such that the imaginary part is non-negative. Hence, k_{1z} and k_{2z} are pure imaginary and the field decays exponentially from the interface. The pole constitutes a surface-plasmon mode. Similarly, for an appropriate choice of the material properties other surface modes can be found by analyzing the pole locations [29].

In a three-layer structure, in addition to the branch point singularities at $k_p = \pm k_1, \pm k_3$, pole singularities associated with guided modes can occur. If $k_p^2 > k_1^2$ and $k_p^2 > k_3^2$, the wave vectors in the z direction $k_{1z} = (k_1^2 - k_p^2)^{1/2}$ and $k_{3z} = (k_3^2 - k_p^2)^{1/2}$ are imaginary and the field decreases exponentially in these outermost layers. Hence, k_p corresponds to the modes guided by the slab. Their number, i.e., the number of poles, depends on the wavelength and the thickness of the intermediate layer [30].

As an illustration, Fig. 7 shows the *s*-polarized contribution of the integrand along the real axis for a symmetric planar GaAs/Al_{0.15}Ga_{0.85}As/GaAs waveguide structure at a $\lambda = 1.5 \mu\text{m}$ wavelength. According to a guided mode analysis, a similar structure with a $\Delta = 0.5 \mu\text{m}$ thick AlGaAs layer has one single *s*-polarized mode, located at $k_p = 14.6 \mu\text{m}^{-1}$. For a thicker AlGaAs layer, $\Delta = 2 \mu\text{m}$, three *s*-polarized modes exist with, respectively, k_p

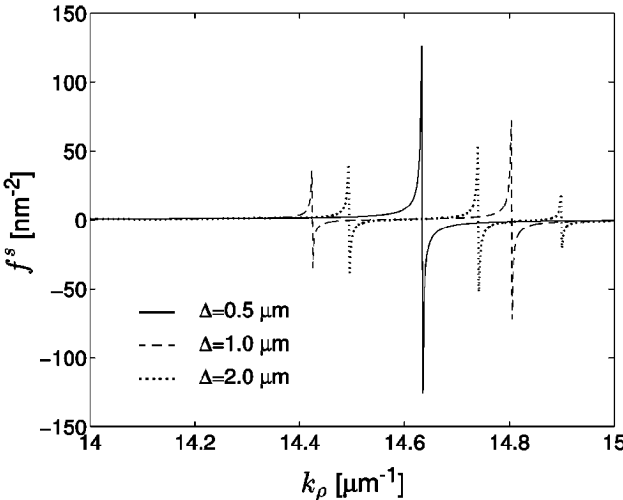


FIG. 7. Integrand (s polarization) for a symmetric GaAs/Al_{0.15}Ga_{0.85}As/GaAs planar waveguide, for three different widths Δ of the AlGaAs layer. The wavelength is $\lambda = 1.5 \mu\text{m}$.

$=14.9 \mu\text{m}^{-1}$, $14.7 \mu\text{m}^{-1}$, and $14.5 \mu\text{m}^{-1}$. In Fig. 7 we observe that the integrands' divergences coincide perfectly with these eigenmodes.

We can also investigate more complicated structures, such as a planar waveguide coupler: We consider a symmetric GaAs/AlGaAs/GaAs/AlGaAs/GaAs system with the two guiding Al_{0.15}Ga_{0.85}As layers having identical thicknesses $\Delta=0.5 \mu\text{m}$. The s -polarized contribution of the integrand along the real axis is plotted in Fig. 8. For a thick separating GaAs layer, $\Delta'=2 \mu\text{m}$, the AlGaAs slabs are decoupled: only one s -polarized mode can be excited at $k_\rho = 14.6 \mu\text{m}^{-1}$, as in the previous example. However, with decreasing separating layer thickness, the modes of the two waveguides can couple via their evanescent tails. The mode is split and the behavior of the structure develops towards that of a single-layer waveguide. For a thin separating GaAs layer, $\Delta'=0.05 \mu\text{m}$, the poles are located at k_ρ

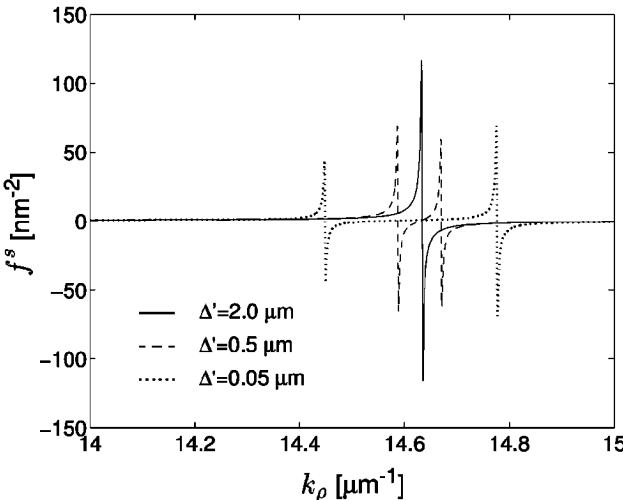


FIG. 8. Integrand (s polarization) for a GaAs/AlGaAs/GaAs/AlGaAs/GaAs multilayer structure, for three different widths Δ' of the separating GaAs layer. The wavelength is $\lambda = 1.5 \mu\text{m}$.

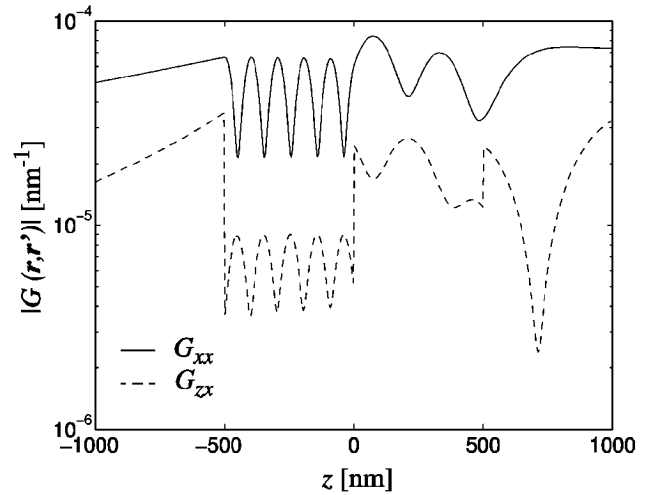


FIG. 9. $|G_{xx}|$ and $|G_{zx}|$ components of the Green's tensor for a four-layer structure with $\epsilon_1=1$, $\epsilon_2=2$, $\epsilon_3=10$, and $\epsilon_4=1$. The second layer extends from $z=0$ nm to $z=-500$ nm, the third layer to $z=-1000$ nm. $z'=750$ nm is located in the top layer and held fixed.

$=14.8 \mu\text{m}^{-1}$ and $14.4 \mu\text{m}^{-1}$, which corresponds to the modes of a single-layer waveguide with $\Delta=0.5 \mu\text{m} + 0.5 \mu\text{m}=1 \mu\text{m}$.

As the last example, we consider a four-layer medium with $\epsilon_1=1$, $\epsilon_2=2$, $\epsilon_3=10$, and $\epsilon_4=1$ at a $\lambda=633$ nm wavelength. The thickness of each inner layer is 500 nm. Two components of the Green's tensor, $G_{xx}(\mathbf{r}, \mathbf{r}')$ and $G_{zx}(\mathbf{r}, \mathbf{r}')$, are given as a function of the altitude z of the observation point $\mathbf{r}=(\rho, \Phi, z)=(\lambda, \pi/4, z)$, whereas the source point $\mathbf{r}'=(0, 0, 750 \text{ nm})$ is held constant in the top layer. Physically, these functions represent the x and z components of the electric field radiated by an x -oriented electric dipole. In the slab regions the dipole source excites standing waves with a period $\Lambda_2=224 \text{ nm}$ and $\Lambda_3=100 \text{ nm}$, which correspond to the half-effective wavelength in the according layer. (Note, however, that our source is a dipole, not a plane wave.) Figure 9 also illustrates the continuity properties across the interfaces. The tangential component of the electric field is continuous across all interfaces [Eq. (A1a)], whereas the normal component of the electric displacement is continuous [Eq. (A1b)]. Hence, $G_{zx}(\mathbf{r}, \mathbf{r}')$ jumps at the interfaces by a factor $\epsilon_3/\epsilon_2=5$ and $\epsilon_3/\epsilon_4=10$, respectively.

V. SUMMARY

We have presented a technique for the computation of the Green's tensor in stratified media. The computation details have been extensively discussed, which should make the practical implementation of this technique on a computer straightforward.

Several examples demonstrated the accuracy of this approach and illustrated the intrinsic physical properties of the Green's tensor in a stratified medium. This dyadic can also be used in conjunction with the Green's tensor technique for efficient scattering calculations in media composed of an arbitrary number of layers [16].

ACKNOWLEDGMENTS

The authors thank B. Michel for his support of the project and gratefully acknowledge the funding of the Swiss National Science Foundation.

APPENDIX A

In this appendix we compute the amplitude coefficients $A_{l,\alpha\beta}^{s/p}$ and $B_{l,\alpha\beta}^{s/p}$, respectively, for s/p -polarized upgoing and downgoing waves in the different layers forming the structure [see Eqs. (10) and (B1)–(B18)]. These coefficients can be summarized in the matrices \mathbf{A}_l^s , \mathbf{B}_l^s , \mathbf{A}_l^p , and \mathbf{B}_l^p .

At each interface the Green's tensor must fulfill the continuity equations resulting from Maxwell's equations:

$$\hat{\mathbf{z}} \times (\mathbf{G}^+ - \mathbf{G}^-) = \mathbf{0}, \quad (\text{A1a})$$

$$\hat{\mathbf{z}} \cdot (\epsilon^+ \mathbf{G}^+ - \epsilon^- \mathbf{G}^-) = \mathbf{0}, \quad (\text{A1b})$$

$$\hat{\mathbf{z}} \times \nabla \times \left(\frac{\mathbf{G}^+}{\mu^+} - \frac{\mathbf{G}^-}{\mu^-} \right) = \mathbf{0}, \quad (\text{A1c})$$

$$\hat{\mathbf{z}} \cdot \nabla \times (\mathbf{G}^+ - \mathbf{G}^-) = \mathbf{0}, \quad (\text{A1d})$$

where \mathbf{G}^+ , ϵ^+ , and μ^+ denote the quantities just above and \mathbf{G}^- , ϵ^- , and μ^- just below the interface. Equations (A1a) and (A1b) are the boundary conditions for the electric field, whereas Eqs. (A1c) and (A1d) are the boundary conditions for the magnetic field.

Using Eqs. (A1a)–(A1d), we can deduce iteratively the amplitude ratios of upgoing and downgoing waves in each layer l . For that purpose, we consider separately the case when \mathbf{r} is above \mathbf{r}' and that when it is below.

When $z > z'$, we use the fact that no field is reflected from infinity ($z \rightarrow +\infty$), so that $B_{l,\alpha\beta} = 0$. Thus, we can iteratively determine the amplitude ratio of the downgoing/upgoing wave in each layer $l=2, \dots, l'$ using the relation

$$\left(\frac{B_l}{A_l} \right)_{z>z'}^{s/p} = \frac{\mathcal{F}_{l,l-1}^{s/p} \exp[i d_{l-1}(k_{l-1z} + k_{lz})] + \left(\frac{B_{l-1}}{A_{l-1}} \right)_{z>z'}^{s/p} \exp[-i d_{l-1}(k_{l-1z} - k_{lz})]}{\exp[i d_{l-1}(k_{l-1z} - k_{lz})] + \mathcal{F}_{l,l-1}^{s/p} \left(\frac{B_{l-1}}{A_{l-1}} \right)_{z>z'}^{s/p} \exp[-i d_{l-1}(k_{l-1z} + k_{lz})]}. \quad (\text{A2a})$$

In a similar way, for $z < z'$, we use the fact $A_{N,\alpha\beta} = 0$ (no field is reflected from $z \rightarrow -\infty$). Now we obtain for the amplitude ratio of the upgoing/downgoing wave in each layer $l=N-1, \dots, l'$,

$$\left(\frac{A_l}{B_l} \right)_{z<z'}^{s/p} = \frac{\mathcal{F}_{l,l+1}^{s/p} \exp[-i d_l(k_{l+1z} + k_{lz})] + \left(\frac{A_{l+1}}{B_{l+1}} \right)_{z<z'}^{s/p} \exp[i d_l(k_{l+1z} - k_{lz})]}{\exp[-i d_l(k_{l+1z} - k_{lz})] + \mathcal{F}_{l,l+1}^{s/p} \left(\frac{A_{l+1}}{B_{l+1}} \right)_{z<z'}^{s/p} \exp[i d_l(k_{l+1z} + k_{lz})]}. \quad (\text{A2b})$$

The coefficients $\mathcal{F}_{l,l-1}^{s/p}$ and $\mathcal{F}_{l,l+1}^{s/p}$ in Eqs. (A2a) and (A2b) are the Fresnel reflection coefficients:

$$\mathcal{F}_{l,l\pm 1}^s = \frac{\mu_{l\pm 1} k_{lz} - \mu_l k_{l\pm 1z}}{\mu_{l\pm 1} k_{lz} + \mu_l k_{l\pm 1z}}, \quad (\text{A3a})$$

$$\mathcal{F}_{l,l\pm 1}^p = \frac{\epsilon_{l\pm 1} k_{lz} - \epsilon_l k_{l\pm 1z}}{\epsilon_{l\pm 1} k_{lz} + \epsilon_l k_{l\pm 1z}}. \quad (\text{A3b})$$

We dropped the $\alpha\beta$ indices in Eqs. (A2a) and (A2b) because the ratio is the same for each component.

In the layer l' the amplitudes can be explicitly calculated. According to Eq. (9), the total field in this region can be written as a superposition of the direct nonreflected wave and the reflected upgoing and downgoing waves:

$$\mathcal{A}_{l',\alpha\beta}^{s/p} \exp(i k_{l'z} z) + \mathcal{B}_{l',\alpha\beta}^{s/p} \exp(-i k_{l'z} z)$$

$$= \mathcal{C}_{l',\alpha\beta}^{s/p} \exp(i k_{l'z} |z - z'|) + R_{l',\alpha\beta}^{s/p\uparrow} \exp(i k_{l'z} z) + R_{l',\alpha\beta}^{s/p\downarrow} \exp(-i k_{l'z} z), \quad (\text{A4})$$

where $\mathcal{A}_{l',\alpha\beta}^{s/p}$ is the amplitude of the upgoing wave, $\mathcal{B}_{l',\alpha\beta}^{s/p}$ the amplitude of the downgoing wave, and $\mathcal{C}_{l',\alpha\beta}^{s/p}$ the amplitude of the direct wave [see Eq. (9)]:

$$\mathcal{C}_{l',\alpha\beta}^s = \hat{l}_\alpha(k_{l'z}) \hat{l}_\beta(k_{l'z}), \quad (\text{A5a})$$

$$\mathcal{C}_{l',\alpha\beta}^p = \hat{m}_\alpha(k_{l'z}) \hat{m}_\beta(k_{l'z}). \quad (\text{A5b})$$

Evaluating the products in Eqs. (A5a) and (A5b) using Eqs. (6) and (7) shows immediately that $\mathcal{C}_{l',xz}^p$, $\mathcal{C}_{l',yz}^p$, $\mathcal{C}_{l',zx}^p$, and $\mathcal{C}_{l',zy}^p$ are odd about $z=z'$, whereas all the other amplitudes are even about $z=z'$. Note that the amplitudes $\mathcal{A}_{l',\alpha\beta}^{s/p}$ and $\mathcal{B}_{l',\alpha\beta}^{s/p}$ are not identical to the coefficients $A_{l',\alpha\beta}^{s/p}$ and $B_{l',\alpha\beta}^{s/p}$ used above. However, they can be connected by comparison

with the integrands given in Appendix B. For example, for the p -polarized part of the xx component, they are coupled via

$$\begin{aligned} \mathcal{A}_{l',xx}^p &= R_{l',xx}^{p\uparrow} + \Theta(z-z') \mathcal{C}_{l',xx}^p \exp(-ik_{l'z} z') \\ &= \pm \mathcal{C}_{l',xx}^p A_{l',xx}^p, \end{aligned} \quad (\text{A6a})$$

$$\begin{aligned} \mathcal{B}_{l',xx}^p &= R_{l',xx}^{p\downarrow} + \Theta(z'-z) \mathcal{C}_{l',xx}^p \exp(ik_{l'z} z') \\ &= \mp \mathcal{C}_{l',xx}^p B_{l',xx}^p, \end{aligned} \quad (\text{A6b})$$

where the upper sign refers to $z>z'$ and the lower sign to $z<z'$.

Using Eq. (A4), the amplitude ratio of the downgoing/upgoing wave reads for $z>z'$

$$\left(\frac{\mathcal{B}_{l',\alpha\beta}}{\mathcal{A}_{l',\alpha\beta}} \right)_{z>z'}^{s/p} = \frac{R_{l',\alpha\beta}^{s/p\downarrow}}{\mathcal{C}_{l',\alpha\beta}^{s/p} \exp(-ik_{l'z} z') + R_{l',\alpha\beta}^{s/p\uparrow}}, \quad (\text{A7a})$$

and the amplitude ratio of the upgoing/downgoing wave becomes for $z<z'$

$$\left(\frac{\mathcal{A}_{l',\alpha\beta}}{\mathcal{B}_{l',\alpha\beta}} \right)_{z<z'}^{s/p} = \frac{R_{l',\alpha\beta}^{s/p\uparrow}}{\mathcal{C}_{l',\alpha\beta}^{s/p} \exp(ik_{l'z} z') + R_{l',\alpha\beta}^{s/p\downarrow}}. \quad (\text{A7b})$$

Solving Eqs. (A7a) and (A7b) for $R_{l',\alpha\beta}^{s/p\downarrow}$ and $R_{l',\alpha\beta}^{s/p\uparrow}$ and substituting the result into the equations formed in analogy to Eqs. (A6a) and (A6b) gives the components of $\mathbf{A}_{l'}^{s/p}$ and $\mathbf{B}_{l'}^{s/p}$. One only has to replace the amplitude ratios formed by $\mathcal{A}_{l',\alpha\beta}^{s/p}$ and $\mathcal{B}_{l',\alpha\beta}^{s/p}$ with the ratios of the corresponding coefficients $A_{l',\alpha\beta}^{s/p}$ and $B_{l',\alpha\beta}^{s/p}$, keeping in mind the differences between $z>z'$ and $z<z'$. It turns out that for p polarization two cases must be distinguished. For $\beta\neq z$ the solution reads

$$\begin{aligned} A_{l',\alpha\beta}^p &= \pm \left(\frac{A_{l'}}{B_{l'}} \right)_{z<z'}^p \left[1 - \left(\frac{B_{l'}}{A_{l'}} \right)_{z>z'}^p \left(\frac{A_{l'}}{B_{l'}} \right)_{z<z'}^p \right]^{-1} \\ &\times \left[\left(\frac{B_{l'}}{A_{l'}} \right)_{z>z'}^p \exp(-ik_{l'z} z') - \exp(ik_{l'z} z') \right] \\ &\pm \Theta(z-z') \exp(-ik_{l'z} z'), \end{aligned} \quad (\text{A8a})$$

$$\begin{aligned} B_{l',\alpha\beta}^p &= \mp \left(\frac{B_{l'}}{A_{l'}} \right)_{z>z'}^p \left[1 - \left(\frac{B_{l'}}{A_{l'}} \right)_{z>z'}^p \left(\frac{A_{l'}}{B_{l'}} \right)_{z<z'}^p \right]^{-1} \\ &\times \left[\left(\frac{A_{l'}}{B_{l'}} \right)_{z<z'}^p \exp(ik_{l'z} z') - \exp(-ik_{l'z} z') \right] \\ &\mp \Theta(z'-z) \exp(ik_{l'z} z'), \end{aligned} \quad (\text{A8b})$$

whereas for $\beta=z$, $A_{l',\alpha\beta}^p$ and $B_{l',\alpha\beta}^p$ are given by

$$\begin{aligned} A_{l',\alpha z}^p &= \left(\frac{A_{l'}}{B_{l'}} \right)_{z<z'}^p \left[1 - \left(\frac{B_{l'}}{A_{l'}} \right)_{z>z'}^p \left(\frac{A_{l'}}{B_{l'}} \right)_{z<z'}^p \right]^{-1} \\ &\times \left[\left(\frac{B_{l'}}{A_{l'}} \right)_{z>z'}^p \exp(-ik_{l'z} z') + \exp(ik_{l'z} z') \right] \\ &+ \Theta(z-z') \exp(-ik_{l'z} z'), \end{aligned} \quad (\text{A8c})$$

$$\begin{aligned} B_{l',\alpha z}^p &= \left(\frac{B_{l'}}{A_{l'}} \right)_{z>z'}^p \left[1 - \left(\frac{B_{l'}}{A_{l'}} \right)_{z>z'}^p \left(\frac{A_{l'}}{B_{l'}} \right)_{z<z'}^p \right]^{-1} \\ &\times \left[\left(\frac{A_{l'}}{B_{l'}} \right)_{z<z'}^p \exp(ik_{l'z} z') + \exp(-ik_{l'z} z') \right] \\ &+ \Theta(z'-z) \exp(ik_{l'z} z'). \end{aligned} \quad (\text{A8d})$$

Physically, this difference is due to the fact that the components with $\beta=z$ represent the field of a vertical dipole whereas the other components come from a horizontal dipole.

Since an s -polarized wave is only generated by a horizontal dipole, such a distinction does not occur:

$$\begin{aligned} A_{l',\alpha\beta}^s &= \left(\frac{A_{l'}}{B_{l'}} \right)_{z>z'}^s \left[1 - \left(\frac{B_{l'}}{A_{l'}} \right)_{z>z'}^s \left(\frac{A_{l'}}{B_{l'}} \right)_{z<z'}^s \right]^{-1} \\ &\times \left[\left(\frac{B_{l'}}{A_{l'}} \right)_{z>z'}^s \exp(-ik_{l'z} z') + \exp(ik_{l'z} z') \right] \\ &+ \Theta(z-z') \exp(-ik_{l'z} z'), \end{aligned} \quad (\text{A9a})$$

$$\begin{aligned} B_{l',\alpha\beta}^s &= \left(\frac{B_{l'}}{A_{l'}} \right)_{z>z'}^s \left[1 - \left(\frac{B_{l'}}{A_{l'}} \right)_{z>z'}^s \left(\frac{A_{l'}}{B_{l'}} \right)_{z<z'}^s \right]^{-1} \\ &\times \left[\left(\frac{A_{l'}}{B_{l'}} \right)_{z<z'}^s \exp(ik_{l'z} z') + \exp(-ik_{l'z} z') \right] \\ &+ \Theta(z'-z) \exp(ik_{l'z} z'). \end{aligned} \quad (\text{A9b})$$

In this case, $A_{l',\alpha\beta}^s$ and $B_{l',\alpha\beta}^s$ are only defined for $\alpha=x,y$ and $\beta=x,y$, whereas the five other components are set to zero.

In Eqs. (A8) and (A9) the amplitude coefficients in layer l' are expressed in terms of amplitude ratios which we have already calculated in Eqs. (A2b) and (A2a). Since the amplitude coefficients of the upgoing and downgoing waves in the layer l are iteratively connected to the amplitude coefficients in l' via the boundary conditions (A1), we can explicitly calculate the components of $\mathbf{A}_l^{s/p}$ and $\mathbf{B}_l^{s/p}$, keeping in mind that the boundary conditions are different for the x,y , and for the z components (note, however, that the s -polarized wave has no z component). This relationship can be formulated using propagation matrices [31] with different factors γ . For $z>z'$ we have

$$\begin{pmatrix} A_{l,\alpha\beta}^{s/p} \\ B_{l,\alpha\beta}^{s/p} \end{pmatrix} = \gamma_{z>z'}^{s/p} \begin{pmatrix} \exp[id_l(k_{l+1z}-k_{lz})] & \mathcal{F}_{l,l+1}^{s/p} \exp[-id_l(k_{l+1z}+k_{lz})] \\ \mathcal{F}_{l,l+1}^{s/p} \exp[id_l(k_{l+1z}+k_{lz})] & \exp[-id_l(k_{l+1z}-k_{lz})] \end{pmatrix} \begin{pmatrix} A_{l+1,\alpha\beta}^{s/p} \\ B_{l+1,\alpha\beta}^{s/p} \end{pmatrix}, \quad (\text{A10})$$

where

$$\gamma_{z>z'}^s = \frac{1}{2} \frac{\mu_{l+1} k_{lz} + \mu_l k_{l+1z}}{\mu_{l+1} k_{l+1z}} \quad \text{for } \alpha=x,y, \beta=x,y, \quad (\text{A11a})$$

$$\gamma_{z>z'}^p = \begin{cases} \frac{1}{2} \frac{\mu_l}{\mu_{l+1}} \frac{k_{l+1z}}{k_{lz}} \frac{\epsilon_{l+1} k_{lz} + \epsilon_l k_{l+1z}}{\epsilon_{l+1} k_{l+1z}} & \text{for } \alpha=x,y, \beta=x,y,z, \\ \frac{1}{2} \frac{\mu_l}{\mu_{l+1}} \frac{\epsilon_{l+1} k_{lz} + \epsilon_l k_{l+1z}}{\epsilon_{l+1} k_{l+1z}} & \text{for } \alpha=z, \beta=x,y,z. \end{cases} \quad (\text{A11b})$$

Similarly, for $z < z'$ we obtain the following expressions:

$$\begin{pmatrix} A_{l,\alpha\beta}^{s/p} \\ B_{l,\alpha\beta}^{s/p} \end{pmatrix} = \gamma_{z<z'}^{s/p} \begin{pmatrix} \exp[id_{l-1}(k_{l-1z}-k_{lz})] & \mathcal{F}_{l,l-1}^{s/p} \exp[-id_{l-1}(k_{l-1z}+k_{lz})] \\ \mathcal{F}_{l,l-1}^{s/p} \exp[id_{l-1}(k_{l-1z}+k_{lz})] & \exp[-id_{l-1}(k_{l-1z}-k_{lz})] \end{pmatrix} \begin{pmatrix} A_{l-1,\alpha\beta}^{s/p} \\ B_{l-1,\alpha\beta}^{s/p} \end{pmatrix}, \quad (\text{A12})$$

where

$$\gamma_{z<z'}^s = \frac{1}{2} \frac{\mu_{l-1} k_{lz} + \mu_l k_{l-1z}}{\mu_{l-1} k_{l-1z}} \quad \text{for } \alpha=x,y, \beta=x,y, \quad (\text{A13a})$$

$$\gamma_{z<z'}^p = \begin{cases} \frac{1}{2} \frac{\mu_l}{\mu_{l-1}} \frac{k_{l-1z}}{k_{lz}} \frac{\epsilon_{l-1} k_{lz} + \epsilon_l k_{l-1z}}{\epsilon_{l-1} k_{l-1z}} & \text{for } \alpha=x,y, \beta=x,y,z, \\ \frac{1}{2} \frac{\mu_l}{\mu_{l-1}} \frac{\epsilon_{l-1} k_{lz} + \epsilon_l k_{l-1z}}{\epsilon_{l-1} k_{l-1z}} & \text{for } \alpha=z, \beta=x,y,z. \end{cases} \quad (\text{A13b})$$

Like this, we obtain the amplitude of s - and p -polarized upgoing/downgoing waves in each layer.

APPENDIX B

Using $\hat{\mathbf{l}}(-k_{lz}) = \hat{\mathbf{l}}(k_{lz})$ and $\hat{\mathbf{m}}(-k_{lz}) = (-\hat{m}_x(k_{lz}), -\hat{m}_y(k_{lz}), \hat{m}_z(k_{lz}))$ the components of the integrand for the Green's tensor (10) read, after evaluation of the angular integral,

$$f_{xx}^s(k_\rho; \rho, \phi) = \frac{1}{k_{lz}} \left(k_\rho J_0(k_\rho \rho) \sin^2 \phi + \frac{1}{\rho} J_1(k_\rho \rho) \cos 2\phi \right) [A_l^s \exp(ik_{lz}z) + B_l^s \exp(-ik_{lz}z)], \quad (\text{B1})$$

$$f_{xx}^p(k_\rho; \rho, \phi) = \pm \frac{k_{lz}}{k_l^2} \left(k_\rho J_0(k_\rho \rho) \cos^2 \phi - \frac{1}{\rho} J_1(k_\rho \rho) \cos 2\phi \right) [A_{l,xx}^p \exp(ik_{lz}z) - B_{l,xx}^p \exp(-ik_{lz}z)], \quad (\text{B2})$$

$$f_{xy}^s(k_\rho; \rho, \phi) = \frac{1}{k_{lz}} \left(-k_\rho J_0(k_\rho \rho) + \frac{2}{\rho} J_1(k_\rho \rho) \right) \sin \phi \cos \phi [A_l^s \exp(ik_{lz}z) + B_l^s \exp(-ik_{lz}z)], \quad (\text{B3})$$

$$f_{xy}^p(k_\rho; \rho, \phi) = \pm \frac{k_{lz}}{k_l^2} \left(k_\rho J_0(k_\rho \rho) - \frac{2}{\rho} J_1(k_\rho \rho) \right) \sin \phi \cos \phi [A_{l,xy}^p \exp(ik_{lz}z) - B_{l,xy}^p \exp(-ik_{lz}z)], \quad (\text{B4})$$

$$f_{xz}^s(k_\rho; \rho, \phi) = 0, \quad (\text{B5})$$

$$f_{xz}^p(k_\rho; \rho, \phi) = -\frac{i k_\rho^2}{k_l^2} J_1(k_\rho \rho) \cos \phi [A_{l,xz}^p \exp(ik_{lz}z) - B_{l,xz}^p \exp(-ik_{lz}z)], \quad (\text{B6})$$

$$f_{yx}^s(k_\rho; \rho, \phi) = f_{xy}^s, \quad (\text{B7})$$

$$f_{yx}^p(k_\rho; \rho, \phi) = f_{xy}^p, \quad (\text{B8})$$

$$f_{yy}^s(k_\rho; \rho, \phi) = \frac{1}{k_{lz}} \left(k_\rho J_0(k_\rho \rho) \cos^2 \phi - \frac{1}{\rho} J_1(k_\rho \rho) \cos 2\phi \right) [A_l^s \exp(ik_{lz}z) + B_l^s \exp(-ik_{lz}z)], \quad (\text{B9})$$

$$f_{yy}^p(k_\rho; \rho, \phi) = \pm \frac{k_{lz}}{k_l^2} \left(k_\rho J_0(k_\rho \rho) \sin^2 \phi + \frac{1}{\rho} J_1(k_\rho \rho) \cos 2\phi \right) [A_{l,yy}^p \exp(ik_{lz}z) - B_{l,yy}^p \exp(-ik_{lz}z)], \quad (\text{B10})$$

$$f_{yz}^s(k_\rho; \rho, \phi) = 0, \quad (\text{B11})$$

$$f_{yz}^p(k_\rho; \rho, \phi) = - \frac{ik_\rho^2}{k_l^2} J_1(k_\rho \rho) \sin \phi [A_{l,yz}^p \exp(ik_{lz}z) - B_{l,yz}^p \exp(-ik_{lz}z)], \quad (\text{B12})$$

$$f_{zx}^s(k_\rho; \rho, \phi) = 0, \quad (\text{B13})$$

$$f_{zx}^p(k_\rho; \rho, \phi) = \mp \frac{ik_\rho^2}{k_l^2} J_1(k_\rho \rho) \cos \phi [A_{l,zx}^p \exp(ik_{lz}z) + B_{l,zx}^p \exp(-ik_{lz}z)], \quad (\text{B14})$$

$$f_{zy}^s(k_\rho; \rho, \phi) = 0, \quad (\text{B15})$$

$$f_{zy}^p(k_\rho; \rho, \phi) = \mp \frac{ik_\rho^2}{k_l^2} J_1(k_\rho \rho) \sin \phi [A_{l,zy}^p \exp(ik_{lz}z) + B_{l,zy}^p \exp(-ik_{lz}z)], \quad (\text{B16})$$

$$f_{zz}^s(k_\rho; \rho, \phi) = 0, \quad (\text{B17})$$

$$f_{zz}^p(k_\rho; \rho, \phi) = \frac{k_\rho^3}{k_l^2 k_{lz}} J_0(k_\rho \rho) [A_{l,zz}^p \exp(ik_{lz}z) + B_{l,zz}^p \exp(-ik_{lz}z)]. \quad (\text{B18})$$

The upper sign in these equations refers to $z > z'$ and the lower sign to $z < z'$. As mentioned in Appendix A [Eqs. (A9), (A11a), and (A13a)], all nonvanishing amplitude coefficients of s -polarized waves are equal, as denoted by the scalar A_l^s and B_l^s . Note further that $A_{l,\alpha\beta}^{s/p}$ and $B_{l,\alpha\beta}^{s/p}$ are also functions of k_{lz} and hence, because of $k_{lz} = (k_l^2 - k_\rho^2)^{1/2}$, functions of k_ρ .

For $\rho = 0$, some of the integrands are no longer defined because the denominator ρ and the numerator $J_1(k_\rho \rho)$ van-

ish. Furthermore, ϕ is not defined for $\rho = 0$. However, explicit evaluation of Eq. (10) for $\rho = 0$ shows that the upper formulas are still valid if we take their value for $\phi = 0$ and make use of the limit

$$\lim_{\rho \rightarrow 0} \frac{J_1(k_\rho \rho)}{\rho} = \frac{1}{2} k_\rho. \quad (\text{B19})$$

-
- [1] P.M. Morse and H. Feshbach, *Methods of Theoretical Physics* (McGraw-Hill, New York, 1953).
 - [2] C.-T. Tai, *Dyadic Green Function in Electromagnetic Theory* (IEEE Press, New York, 1994).
 - [3] A. Sommerfeld, Ann. Phys. (Leipzig) **28**, 665 (1909).
 - [4] A. Baños, *Dipole Radiation in the Presence of a Conducting Half-Space* (Pergamon Press, Oxford, 1966).
 - [5] J.R. Mosig and F.E. Gardiol, IEE Proc. Pt.H: Microwaves. Opt. Antennas **130**, 175 (1983).
 - [6] J.R. Wait, *Electromagnetic Waves in Stratified Media* (IEEE Press, New York, 1996).
 - [7] P. Gay-Balmaz and J.R. Mosig, Int. J. Microwave and Millimeter wave CAE **3**, 330 (1997).
 - [8] G.S. Agarwal, Phys. Rev. A **11**, 253 (1975).
 - [9] H. Metiu, Prog. Surf. Sci. **17**, 153 (1984).
 - [10] G.W. Ford and W.H. Weber, Phys. Rep. **113**, 195 (1984).
 - [11] F. Wijnands *et al.*, Opt. Quantum Electron. **29**, 199 (1997).
 - [12] A. Dereux, J.P. Vigneron, P. Lambin, and A.A. Lucas, Superlattices Microstruct. **3**, 547 (1987).
 - [13] J. van Kranendonk and J. E. Sipe, in *Progress in Optics*, edited by E. Wolf (Elsevier, New York, 1977), Vol. 15.
 - [14] B.T. Draine and P.J. Flatau, J. Opt. Soc. Am. A **11**, 1491 (1994).
 - [15] P.J. Flatau, Opt. Lett. **22**, 1205 (1997).
 - [16] O.J.F. Martin and N.B. Piller, Phys. Rev. E **58**, 3909 (1998).
 - [17] A.A. Maradudin and D.L. Mills, Phys. Rev. B **11**, 1392 (1975).
 - [18] J.E. Sipe, J. Opt. Soc. Am. B **4**, 481 (1987).
 - [19] M.A. Taubenblatt and T.K. Tran, J. Opt. Soc. Am. A **10**, 912

- (1993).
- [20] C. Girard, A. Dereux, O.J.F. Martin, and M. Devel, Phys. Rev. B **52**, 2889 (1995).
- [21] O.J.F. Martin, J. Microsc. **194**, 235 (1999).
- [22] J. A. Kong, *Electromagnetic Wave Theory* (Wiley, New York, 1986).
- [23] *Handbook of Mathematical Functions*, edited by M. Abramowitz and I.A. Stegun (Dover, New York, 1972).
- [24] L.B. Felsen and N. Marcuvitz, *Radiation and Scattering of Waves* (IEEE Press, New York, 1994).
- [25] W.C. Chew, *Waves and Fields in Inhomogeneous Media* (IEEE Press, New York, 1995).
- [26] R.G. Hunsperger, *Integrated Optics: Theory and Technology*, 3rd ed. (Springer, Berlin, 1991).
- [27] L. Barlatey, J.R. Mosig, and T. Sphicopoulos, IEEE Trans. Antennas Propag. **38**, 608 (1990).
- [28] W. Gautschi, in *Numerical Methods and Approximation Theory III*, edited by G.V. Milovanović (Univ. Niš, Niš, 1988), pp. 39–66.
- [29] A.D. Boardman, *Electromagnetic Surface Modes* (Wiley, New York, 1982).
- [30] D. Marcuse, *Theory of Dielectric Optical Waveguides* (Academic Press, San Diego, 1974).
- [31] J.A. Kong, Geophysics **37**, 985 (1972).

P2

**Light propagation and scattering in stratified media:
a Green's tensor approach**

Michael Paulus and Olivier J. F. Martin
J. Opt. Soc. Am. A **18**, 854–861 (2001)

Light propagation and scattering in stratified media: a Green's tensor approach

Michael Paulus

Electromagnetic Fields and Microwave Electronics Laboratory, Swiss Federal Institute of Technology, ETH-Zentrum ETZ, CH-8092 Zurich, Switzerland, and IBM Research, Zurich Research Laboratory, CH-8803 Rüschlikon, Switzerland

Oliver J. F. Martin

Electromagnetic Fields and Microwave Electronics Laboratory, Swiss Federal Institute of Technology, ETH-Zentrum ETZ, CH-8092 Zurich, Switzerland

Received July 27, 2000; accepted October 26, 2000

We present a new technique for computing the electromagnetic field that propagates and is scattered in three-dimensional structures formed by bodies embedded in a stratified background. This fully vectorial technique is based on the Green's tensor associated with the stratified background. Its advantage lies in the fact that only the scatterers must be discretized, the stratified background being accounted for in the Green's tensor. Further, the boundary conditions at the different material interfaces as well as at the edges of the computation window are perfectly and automatically fulfilled. Several examples illustrate the utilization of the technique for the modeling of photonic circuits (integrated optical waveguides), the study of the optics of metal (surface plasmons), and the development of new optical lithography techniques. © 2001 Optical Society of America

OCIS codes: 220.3740, 230.0230, 240.0240, 240.6680, 290.0290, 310.0310.

1. INTRODUCTION

Vertical-cavity surface-emitting laser diodes with Bragg mirrors, complex lens systems with antireflecting coatings, optical amplifiers with multiple quantum wells, and structured masks for optical nanolithography are all examples of optical systems that rely on stratified media formed by stacks of material layers with different permittivities. Light propagation and scattering in stratified media therefore cover an extremely broad spectrum of applications.

When the system is a bare stratified structure formed only by different material layers stacked together, the propagation of light can be investigated by simple techniques such as the use of a transmission matrix.^{1–4} However, most practical applications do not rely on a bare, stratified medium but rather also incorporate active elements in the stratified background: for example, a Bragg grating on the top of a multilayered waveguide, a metallic profile on a glass mask for optical lithography, a ridge at the surface of a semiconductor laser, and a trench to define a cavity in a semiconductor substrate.

The objective of this paper is to present a general technique for light propagation and scattering in such a system formed by a stratified background with embedded elements. The techniques available for the study of these systems depend on the particular geometry under study.^{4–6} They include, for example, beam propagation methods,^{7–10} discrete sources,^{11,12} eigenmode expansions,^{13–15} finite differences,¹⁶ finite-difference time domain,^{17–19} finite elements,^{20,21} the method of lines,^{22,23} ray tracing,^{24,25} and transfer matrix.²⁶

Our approach is related to the coupled dipole approxi-

mation (also known as the discrete dipole approximation). This powerful technique has been used extensively for scattering calculations in systems in an infinite homogeneous background.^{27–30} It has also been applied to scatters on a surface, the simplest form of a stratified background.^{31–33}

In the present paper we introduce a technique that can accommodate scatterers in a stratified background formed by an arbitrary number of layers. This method is described in Section 2. In Section 3 we discuss several application examples that illustrate the utilization of the technique in different domains of modern optics. We summarize our results in Section 4.

2. FORMALISM

A. Electric Field Integral Equation

The typical system that we want to study is depicted in Fig. 1. Several three-dimensional (3D) scatterers described by the permittivity $\varepsilon(\mathbf{r})$ are distributed in a 3D stratified background composed of L layers with different relative permittivities ε_i , $i = 1, \dots, L$. Throughout the paper we consider nonmagnetic materials with relative permeability $\mu = 1$ and harmonic fields with time dependence $\exp(-i\omega t)$.

When this system is illuminated with an incident electric field $\mathbf{E}^0(\mathbf{r})$ propagating in the stratified background, the total field $\mathbf{E}(\mathbf{r})$ is given by the integral equation^{30,34}

$$\mathbf{E}(\mathbf{r}) = \mathbf{E}^{(0)}(\mathbf{r}) + \int_V d\mathbf{r}' \mathbf{G}(\mathbf{r}, \mathbf{r}') \cdot k_0^2 \Delta \varepsilon(\mathbf{r}') \mathbf{E}(\mathbf{r}'), \quad (1)$$

where $\mathbf{G}(\mathbf{r}, \mathbf{r}')$ is the Green's tensor associated with the stratified background, k_0 is the wave number in vacuum, and $\Delta \varepsilon(\mathbf{r})$ is the dielectric contrast:

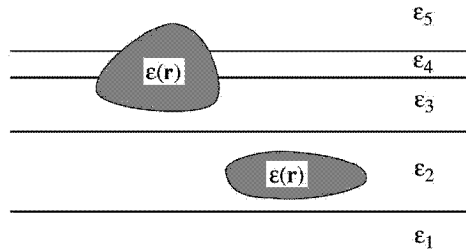


Fig. 1. Typical geometry under study: Several scatterers with permittivity $\epsilon(\mathbf{r})$ are embedded in a stratified background composed of L layers with respective permittivity ϵ_i . Note that the first and last layers are semi-infinite media.

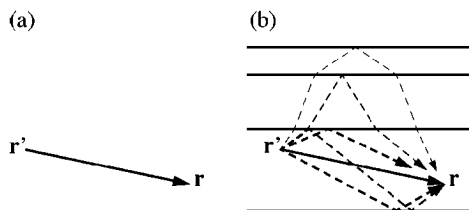


Fig. 2. The Green's tensor gives the electric field radiated at \mathbf{r} by a dipole located at \mathbf{r}' , which (a) corresponds in an infinite homogeneous background to only direct radiation from \mathbf{r}' to \mathbf{r} and (b) further includes in a stratified medium all possible reflections at the $L-1$ interfaces.

$$\Delta\epsilon(\mathbf{r}) = \epsilon(\mathbf{r}) - \epsilon_\kappa \quad \text{for } \mathbf{r} \in \text{layer } \kappa. \quad (2)$$

The integration in Eq. (1) runs on the volume of all the different scatterers $\epsilon(\mathbf{r})$ in the structure.

It is important to note that the scatterers do not have to be embedded inside a background layer but can extend over several layers (Fig. 1). Further, these scatterers need not be homogeneous: $\epsilon(\mathbf{r})$ can vary inside each scatterer. Finally, the permittivity of the scatterers does not necessarily have to be higher than that of their surroundings, and, for example, holes in a dielectric layer can be accounted for by use of a negative dielectric contrast $\Delta\epsilon(\mathbf{r})$.

B. Green's Tensor for a Stratified Medium

The Green's tensor represents the response of a point source in the background. More precisely, each column β of the 3×3 matrix $G_{\alpha\beta}(\mathbf{r}, \mathbf{r}')$ gives the three components $\alpha = x, y, z$ of the electric field radiated at position \mathbf{r} by a dipole located at position \mathbf{r}' and oriented in the β direction ($\beta = x, y, z$).

For an infinite homogeneous background, this dyadic is just the field radiated directly from \mathbf{r}' to \mathbf{r} [Fig. 2(a)] and has a simple analytical form [see, e.g., Eq. (15) in Ref. 30].

Such is not the case for a stratified background. As illustrated in Fig. 2(b), the field radiated at \mathbf{r} by a dipole located at \mathbf{r}' now also includes the field reflected and refracted at all the interfaces. No analytical expressions exist in this case, and the Green's tensor must be computed numerically. This is quite a complicated task, which is best achieved by expressing the Green's tensor in reciprocal space (Fourier space) and using the symmetry properties of the background in that space. The Green's tensor is then obtained in direct space by means of inverse Fourier transform, i.e., by means of a numerical

quadrature. This quadrature, which represents the core of the computation, is intricate because it involves several poles and branch cuts associated with the different electromagnetic modes that can be excited in the stratified background.

We recently developed an efficient computation technique for the evaluation of the Green's tensor in a stratified medium and refer the reader to Ref. 35, where the practical implementation of this technique is discussed in great detail. In the present paper we shall concentrate on the utilization of the Green's tensor for 3D scattering calculations in stratified media.

In that context, let us first discuss the evaluation of the integral in Eq. (1). For clarity, we use the following notation for the Green's tensor:

$$\mathbf{G}(\mathbf{r}, \mathbf{r}')$$

$$= \begin{cases} \mathbf{G}^D(\mathbf{r}, \mathbf{r}') + \mathbf{G}^I(\mathbf{r}, \mathbf{r}') & \mathbf{r}, \mathbf{r}' \text{ in same layer } \kappa \\ \mathbf{G}^I(\mathbf{r}, \mathbf{r}') & \mathbf{r}, \mathbf{r}' \text{ in different layers} \end{cases}, \quad (3)$$

where \mathbf{G}^D is the direct contribution and \mathbf{G}^I accounts for the field reflected and refracted by all the interfaces [Fig. 2(b)]. Note that the direct tensor \mathbf{G}^D is simply the Green's tensor associated with an infinite homogeneous polarizable background with permittivity ϵ_κ .³⁰

When $\mathbf{r} \rightarrow \mathbf{r}'$, only the direct contribution \mathbf{G}^D diverges because the direct interaction path vanishes while all the indirect interaction paths remain finite [the forthcoming discretization scheme will impose that the points where $\mathbf{G}(\mathbf{r}, \mathbf{r}')$ is computed are not on a boundary between two layers]. We can therefore handle the singularity of the Green's tensor in a similar manner as for an infinite homogeneous medium. Introducing Eq. (3) into Eq. (1) and taking the principal value as for Eq. (7) in Ref. 30, we obtain

$$\begin{aligned} \mathbf{E}(\mathbf{r}) = & \mathbf{E}^0(\mathbf{r}) + \int_V d\mathbf{r}' \mathbf{G}^I(\mathbf{r}, \mathbf{r}') \cdot k_0^2 \Delta\epsilon(\mathbf{r}') \mathbf{E}(\mathbf{r}') \\ & + \lim_{\delta V \rightarrow 0} \int_{V-\delta V}^{V+\delta V} d\mathbf{r}' \mathbf{G}^D(\mathbf{r}, \mathbf{r}') \cdot k_0^2 \Delta\epsilon(\mathbf{r}') \mathbf{E}(\mathbf{r}') \\ & - \mathbf{L} \cdot \frac{\Delta\epsilon(\mathbf{r})}{\epsilon_\kappa} \mathbf{E}(\mathbf{r}), \end{aligned} \quad (4)$$

where the infinitesimal volume δV centered at point \mathbf{r} is used to exclude the singularity. The source dyadic \mathbf{L} , which depends on the shape of this exclusion volume δV , was derived in detail by Yaghjian.³⁶ Note in the last term of Eq. (4) the permittivity ϵ_κ of the layer where \mathbf{r} is located. Note also that Eq. (4) is implicit for the unknown field $\mathbf{E}(\mathbf{r})$.

C. Discretized Equation

To solve Eq. (4) numerically, we define a mesh on the system with N discretized elements centered at \mathbf{r}_i with permittivity $\epsilon_i = \epsilon(\mathbf{r}_i)$ and volume V_i . The only constraint for this discretization is that a given mesh must be entirely inside a layer and cannot sit astride a boundary between two layers (Fig. 3). The discretization volume V_i need not be constant. To achieve a given accuracy, it is

actually necessary to use a smaller mesh when the dielectric contrast is larger. To that extent, one can expect that the convergence of this scheme will be similar to that observed for scattering calculations in a homogeneous background. We refer the reader to Ref. 37, where this point was discussed in detail.

Keeping in mind that the discrete dielectric contrast $\Delta\epsilon_i = \epsilon_i - \epsilon_\kappa$ depends on the permittivity of the layer κ where mesh i is located, we can write the discretized system of equations that correspond to Eq. (4):

$$\begin{aligned} \mathbf{E}_i &= \mathbf{E}_i^0 + \sum_{j=1}^N \mathbf{G}_{i,j}^I \cdot k_0^2 \Delta\epsilon_j \mathbf{E}_j V_j \\ &+ \sum_{\substack{j \in \text{layer } \kappa \\ j \neq i}} \mathbf{G}_{i,j}^D \cdot k_0^2 \Delta\epsilon_j \mathbf{E}_j V_j + \mathbf{M}_i \cdot k_0^2 \Delta\epsilon_i \mathbf{E}_i \\ &- \mathbf{L} \cdot \frac{\Delta\epsilon_i}{\epsilon_\kappa} \mathbf{E}_i, \quad i = 1, \dots, N. \end{aligned} \quad (5)$$

The self-term \mathbf{M}_i is obtained in a similar manner as for an infinite homogeneous background:³⁰

$$\begin{aligned} \mathbf{M}_i &= \lim_{\delta V \rightarrow 0} \int_{V_i - \delta V} d\mathbf{r}' \mathbf{G}^D(\mathbf{r}_i, \mathbf{r}') \\ &= \frac{2}{3k_\kappa^2} [(1 - ik_\kappa R_i^{\text{eff}}) \exp(ik_\kappa R_i^{\text{eff}}) - 1] \mathbf{1}, \end{aligned} \quad (6)$$

where R_i^{eff} is the effective radius of mesh i :

$$R_i^{\text{eff}} = \left(\frac{3}{4\pi} V_i \right)^{1/3}. \quad (7)$$

For the integration in Eq. (6) we assumed a spherical exclusion volume δV . The corresponding source dyadic is³⁶

$$\mathbf{L} = \frac{1}{3} \mathbf{1}. \quad (8)$$

Note in Eq. (6) the effective wave number $k_\kappa = k_0 \sqrt{\epsilon_\kappa}$ in layer κ .

The system of Eq. (5) represents the self-consistent interaction of N dipoles. Unlike for the coupled dipole approximation in vacuum, each dipole is now a dipole embedded in a stratified background, and the interaction includes all possible reflections and refractions at the $L - 1$ interfaces.

This system of equations is best solved numerically with an iterative solver.^{29,38} Let us mention that, in a stratified medium, the Green's tensor does not have the same symmetry properties as in an infinite homogeneous background. In particular,

$$\mathbf{G}(\mathbf{r}, \mathbf{r}') \neq \mathbf{G}(\mathbf{r} - \mathbf{r}'). \quad (9)$$

It is therefore not possible to rewrite Eq. (1) as a convolution and to use a 3D fast Fourier transform to perform the integration.³⁹ It is, however, possible to use reduced symmetry properties in the x, y plane to expedite the computation.³³

One of the advantages of the technique presented in this paper lies in the fact that only the scatterers must be discretized, the background being accounted for in the

Green's tensor. Similarly, the interaction of scatterers located at large distances from one another does not require the discretization of the stratified background between them. Further, the complex boundary conditions at the edges of the computational window are automatically fulfilled, since they are included in the Green's tensor.

We mentioned that Eq. (1) is an *implicit* equation for the field $\mathbf{E}(\mathbf{r})$. Actually, this is the case only when \mathbf{r} is located inside a scatterer. When \mathbf{r} is located in the stratified background, Eq. (1) gives the field *explicitly* by integration on the scatterers' volume [$\Delta\epsilon(\mathbf{r}') = 0$ when \mathbf{r}' is in the background]. From a physical point of view, this means that knowledge of the field inside all the scatterers allows one to compute the field at any point in the stratified background. This can be used to expedite the calculation by first computing and storing the solution of Eq. (5) only for the discretized points inside the scatterers and then using this solution at a later stage to obtain the field in the background. Note that the last step does not necessitate the solution of a system of equations but requires only simple vector matrix multiplications.

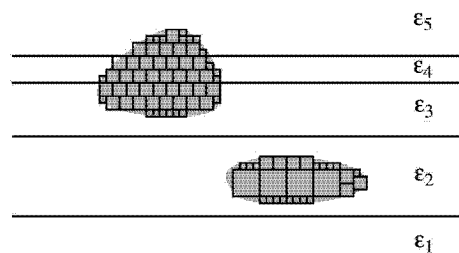


Fig. 3. Solving the scattering problem numerically requires that only the scatterers in the structure must be discretized. The sole constraint on the discretization is that a mesh cannot sit astride a boundary between two layers.

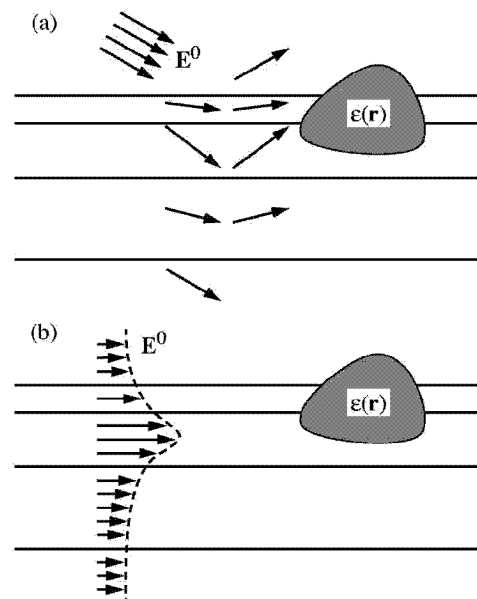


Fig. 4. The incident field must be a solution of the wave equation for the stratified background. It can correspond, for example, (a) to a plane wave impinging on the system or (b) to a waveguide mode propagating in the stratified background.

D. Incident Field

The incident field $\mathbf{E}^0(\mathbf{r})$ in Eq. (1) must be a solution of the wave equation in the stratified background. For a given geometry, this solution is not unique, as illustrated in Fig. 4. For example, the incident field can be a plane-wave excitation impinging on the stratified system [Fig. 4(a)]. In that case it must include all the multiple reflections inside the different layers. For the same geometry, $\mathbf{E}^0(\mathbf{r})$ could also be a waveguide mode propagating inside the structure [Fig. 4(b)] or even the field of a dipolar source embedded in the system. The latter can be used to investigate the radiation properties of a two-level molecule interacting with the system.⁴⁰

3. APPLICATION EXAMPLES

In this section we present several examples that illustrate the application of our technique in domains as diverse as integrated optics, surface plasmons, and optical lithography.

A. Three-Dimensional Notch on a Planar Waveguide

As a first example, we consider a 3D notch of varying depth δ in a planar InP/InGaAsP waveguide (Fig. 5).⁴¹ The notch has a finite extension ($1 \mu\text{m}$) in both the x and the y directions. For this geometry, only the air notch must be discretized, the associated polarizability $\Delta\epsilon$ being negative, since the scatterer permittivity (air; $\epsilon = 1$) is lower than the permittivity of the surrounding semiconductor. For the results presented in this section we use a $\Delta_x = \Delta_y = \Delta_z = 100 \text{ nm}$ discretization mesh.

At a wavelength $\lambda = 1.55 \mu\text{m}$, this waveguide supports a transverse electric mode (TE_0 , electric field polarized in the y direction) and a transverse magnetic mode (TM_0 , electric field polarized in the z direction).

We illustrate in Fig. 6 the electric field amplitude when this system is illuminated with a TE_0 mode propagating in the x direction (the mode is normalized so that the maximum electric field amplitude is unity). Some of the incident field is reflected by the notch, leading to an interference pattern caused by the interaction of the incident field with the reflected field. The incident mode is also scattered into the substrate and, to a lesser extent, into the air notch. These effects increase with the depth δ of the notch (note the different amplitude scales in Fig. 6). For the largest perturbation, the propagation of the mode in the forward direction is strongly disrupted [Fig. 6(c)].

In Fig. 7 we show the field amplitude distribution in the InGaAsP layer for the two mode excitations. Again the interference between incident and reflected fields is visible on the left-hand sides of the figures. The interaction of the incident field with the scatterer depends on the mode polarization. It is stronger for the TM_0 mode than for the TE_0 mode (note the different amplitude scales in Fig. 7). The disruption of the mode propagation in the forward direction, which leads to a dark shadow behind the notch, is clearly visible in Fig. 7. In spite of the finite lateral notch extension, it takes a large number of propagation wavelengths before the mode is reestablished in the waveguide (not shown).

Since our approach is fully vectorial and takes into ac-

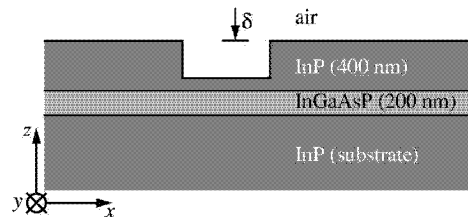


Fig. 5. A notch with a depth δ is etched in an InP/InGaAsP planar waveguide (permittivities $\epsilon_{\text{InP}} = 10.05$ and $\epsilon_{\text{InGaAsP}} = 11.42$; wavelength $\lambda = 1.55 \mu\text{m}$). The layer thicknesses are given in the figure. The notch has a finite extension ($1 \mu\text{m}$) in both the x and the y directions.

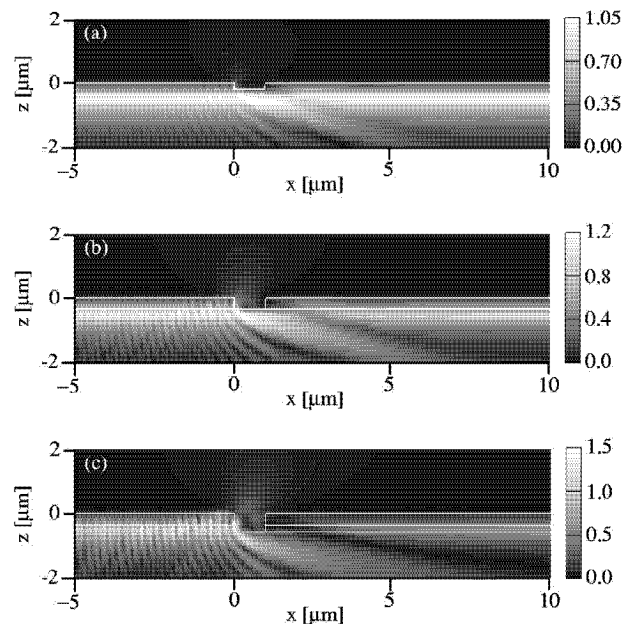


Fig. 6. Field amplitude at $y = 0$ in the structure depicted in Fig. 5 illuminated with a TE_0 mode propagating in the x direction. Three notch thicknesses are investigated: (a) $\delta = 200 \text{ nm}$, (b) $\delta = 400 \text{ nm}$, (c) $\delta = 600 \text{ nm}$.

count all the different field components, subtle effects such as polarization coupling can also be investigated.^{42,43}

Figures 6 and 7 also illustrate how perfectly the boundary conditions at the edges of the computational window and at the different material interfaces in the stratified background are fulfilled. In particular, Fig. 6 shows the field scattered into the substrate and reflected backward to the incident direction; in Fig. 7 some of the field is scattered from the notch and escapes on the lateral sides of the computational window. In every case, the edges of the computational window remain perfectly transparent. This does not require any special treatment since these boundary conditions are already included in the Green's tensor.

B. Scattering of Surface Plasmons

Since our technique is not restricted to dielectric materials with a positive real part of the dielectric constant, we can also investigate the scattering of surface plasmons propagating along a metal–vacuum interface.⁴⁴

In this example we excite a surface plasmon with the method of attenuated total reflection:⁴⁵ A *p*-polarized plane wave is incident on a planar glass–metal interface with an angle larger than the critical angle of total internal reflection (Fig. 8). Hence an exponentially decaying

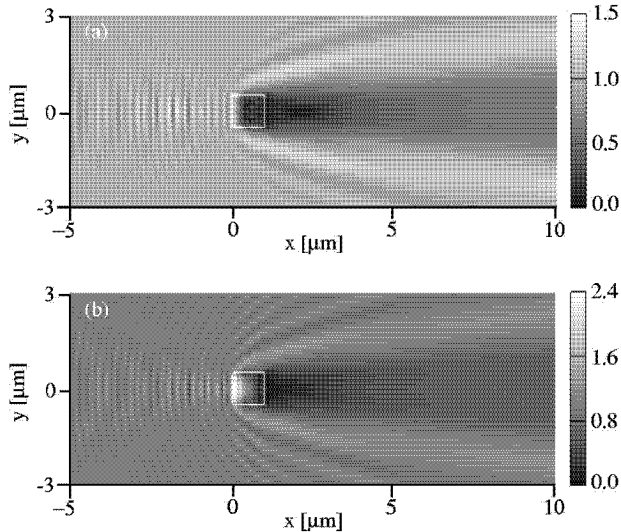


Fig. 7. Field amplitude in the InGaAsP layer ($z = -550$ nm) for the geometry depicted in Fig. 6(c) ($\delta = 600$ -nm notch). The system is illuminated with two different modes, (a) TE₀ and (b) TM₀, propagating in the x direction. The maximum amplitude of each incident mode is normalized to unity.

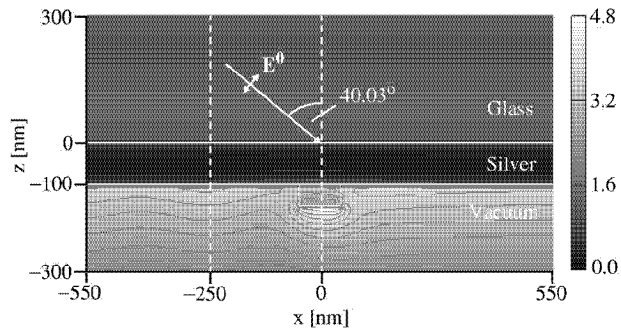


Fig. 8. Attenuated total reflection excitation of a surface plasmon. An incident field propagating in the glass substrate ($\epsilon = 2.25$, $\lambda = 633$ nm) impinges at a 40.03° angle onto a 100-nm-thick silver film ($\epsilon = -18.32 + i0.5$). This generates a surface plasmon propagating along the metal–vacuum interface. A $100 \times 100 \times 50$ -nm³ glass protrusion is deposited onto the silver surface. The electric field amplitude is shown. Note the scattering of the surface plasmon by the protrusion.

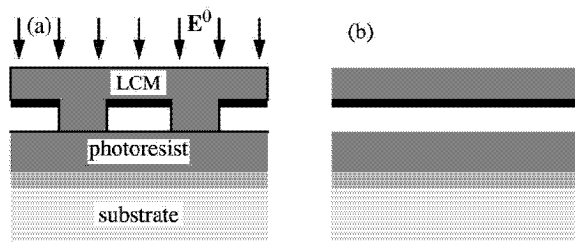


Fig. 11. LCM for optical nanolithography. (a) The structures to be written in the photoresist are defined as protrusions on a soft polymer substrate. This structure can easily be decomposed into (b) a stratified background with (c) embedded scatterers of various permittivities. A bottom antireflection coating (BARC) is deposited between the substrate and the photoresist.

evanescent field is created in the metal layer. When the component of the wave vector parallel to the interface fulfills the eigenvalue equation for the surface mode, a plasmon is excited at the metal–vacuum interface (Fig. 8).

This plasmon propagates along the metal surface and interacts with any defect on it. As an example, we use the technique presented in Section 2 to investigate the scattering of such a plasmon with a dielectric protrusion

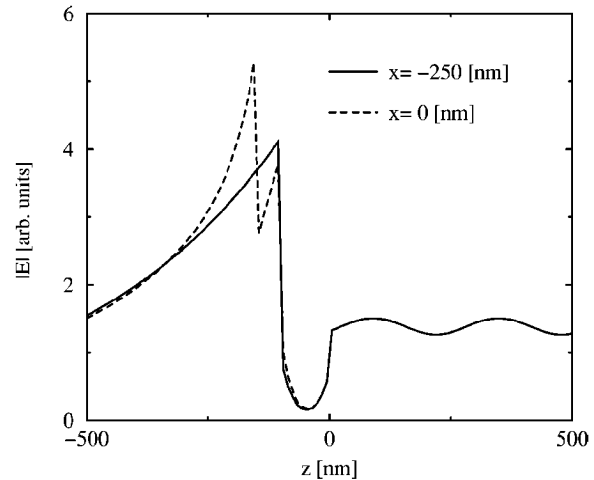


Fig. 9. Field amplitude along the two dashed lines in Fig. 8 ($y = 0$). Note the standing wave in the glass substrate and the localized plasmon field at the metal–vacuum, metal–glass, and glass–vacuum interfaces.

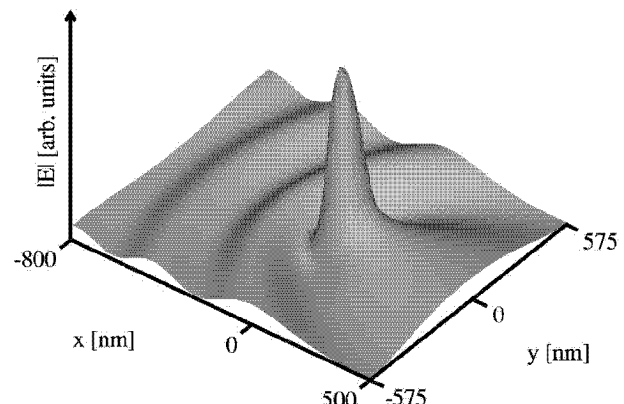


Fig. 10. Field amplitude in a constant-height plane in vacuum ($z = -155$ nm) below the glass protrusion (Fig. 8). Both the scattering and the confinement of the surface plasmon by the protrusion are visible.

deposited on the silver surface (the protrusion is discretized with $\Delta_x = \Delta_y = \Delta_z = 10 \text{ nm}$).

The resulting field amplitude is illustrated in Fig. 8. A stationary wave is visible on the left side of the protrusion. It results from the interaction of the plasmon propagating in the positive x direction with the plasmon reflected by the protrusion.

In Fig. 8 the electric field appears to vanish inside the metal. Actually, the field amplitude profiles in Fig. 9 show that the electric field is strongly localized at the surface of the metal, which is characteristic of a plasmon. The stationary wave in the glass substrate resulting from the interaction of the incident field with the reflected field is also visible in this figure.

Notice in Fig. 9 that, because of the higher index, the field decays more rapidly in the glass than in vacuum.⁴⁵ The second peak that appears at the glass–vacuum interface is merely related to the continuity of the displace-

ment field $\mathbf{D} = \epsilon \mathbf{E}$. As a matter of fact, because the field associated with the plasmon is predominantly polarized in the z direction, i.e., normal to the glass–vacuum interface, it is the displacement field (not the electric field) that must be continuous.⁴⁶ The amplitude difference observed in Fig. 9 actually corresponds to the dielectric contrast between glass and vacuum. This depolarization effect has been discussed in detail in Ref. 47.

The strong field enhancement is evidenced in Fig. 10, where we show the field distribution in a plane parallel to the surface immediately below the protrusion. This figure clearly illustrates how the surface plasmon interacts with the glass protrusion.

C. Optical Nanolithography

As last example, we consider a light-coupling mask (LCM) for optical lithography. This polymer mask has proved to be an efficient alternative for high-resolution lithography: Using 248-nm light, it allows one to define structures in the sub-100-nm range.^{48,49}

The structures to be written in the photoresist are defined as protrusions on the mask, which will guide and focus the light into the photoresist (Fig. 11). To increase contrast, a thin gold layer is deposited inside the mask. The mask is illuminated from the top by circularly polarized light [Fig. 11(a)].

With our approach, only the protrusions must be discretized, as illustrated in Figs. 11(b) and 11(c). Note that, although the protrusions are made entirely of polymer, the discretized polarizability $\Delta\epsilon_i$ that enters into the system of Eq. (5) is different for the meshes located in the gold absorber and those in the air layer [Fig. 11(c)]. For this example we use a $\Delta_x = \Delta_y = \Delta_z = 15 \text{ nm}$ mesh.

Typical structures to be written on an integrated circuit are formed by so-called linelets with width d and length $4d$. Figure 12 shows an isosurface of the electric

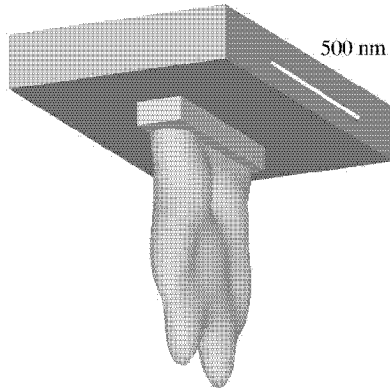


Fig. 12. LCM with a $120 \times 480 \times 75 \text{ nm}^3$ protrusion. An isosurface of the field intensity distribution transmitted in the photoresist is shown. Such an isosurface corresponds to the profile of the structure that will be developed in the photoresist.

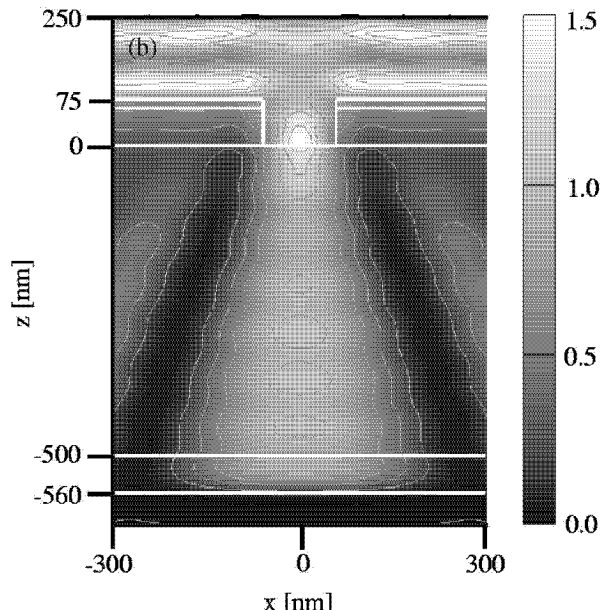
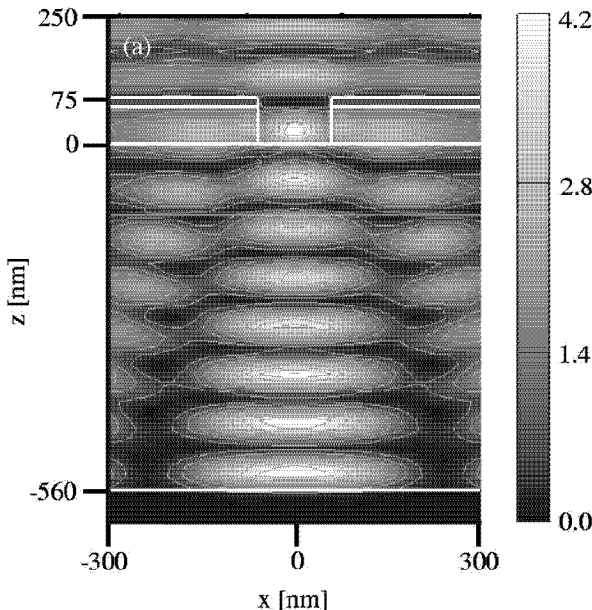


Fig. 13. (a) In a practical nanolithography experiment, reflections at the photoresist–substrate interface lead to a disturbing interference pattern in the photoresist. (b) To suppress this effect a 60-nm-thick BARC is deposited on the substrate. The electric field intensity is shown.

field intensity in the photoresist, below the LCM, for such an isolated linelet with $d = 120$ nm. This isosurface corresponds to the volume that will be exposed in the photoresist.⁴⁸ Such calculations are therefore useful for optimizing the exposition and assessing the ultimate resolution that can be achieved with this new lithography technique.

To avoid reflections at the resist–substrate interface, one usually includes an absorbing layer on top of the substrate before spinning the photoresist (Fig. 11).⁵⁰ The influence of such a 60-nm-thick bottom antireflection coating (BARC; $\epsilon = 1.98 + i1.23$) is investigated in Fig. 13. Without the BARC we observe strong reflections from the substrate, leading to an interference pattern in the photoresist [Fig. 13(a)]. These disturbing interferences are suppressed by adding the BARC [Fig. 13(b)]. Note again in this figure how perfectly the boundary conditions are fulfilled at each medium interface as well as at the edges of the computation window.

4. CONCLUSION

It should be straightforward to implement in a computer the technique described in Section 2, together with the computation of the Green's tensor for a stratified medium detailed in Ref. 35.

The different examples presented in Section 3 illustrate the versatility of this new approach for propagation and scattering calculations in stratified media. This technique can be applied to a broad spectrum of problems ranging from classical optics to integrated optics and nanotechnology. Further, it can also be used to study the optics of metals.

ACKNOWLEDGMENTS

It is a pleasure to acknowledge stimulating discussions with A. Dereux, P. Gay-Balmaz, J. P. Kottmann, and C. Girard and to thank B. Michel and R. Vahldieck for their support of the project. We gratefully acknowledge funding from the Swiss National Science Foundation.

Address correspondence to Oliver J. F. Martin at martin@ifh.ee.ethz.ch.

REFERENCES

- J. A. Kong, *Electromagnetic Wave Theory* (Wiley, New York, 1986).
- M. Born and E. Wolf, *Principles of Optics*, 6th. ed. (Pergamon, Oxford, 1987).
- L. B. Felsen and N. Marcuvitz, *Radiation and Scattering of Waves* (IEEE Press, Piscataway, N.J., 1994).
- W. C. Chew, *Waves and Fields in Inhomogeneous Media* (IEEE Press, Piscataway, N.J., 1995).
- R. März, *Integrated Optics Design and Modeling* (Artech House, Boston, Mass., 1994).
- R. Scarmozzino, A. Gopinath, R. Pregla, and S. Helfert, "Numerical techniques for modeling guided-wave photonic devices," *IEEE J. Sel. Top. Quantum Electron.* **6**, 150–162 (2000).
- W. P. Huang and C. L. Xu, "Simulation of three-dimensional optical waveguides by a full-vector beam propagation method," *IEEE J. Quantum Electron.* **29**, 2639–2646 (1993).
- G. R. Hadley, "Low-truncation-error finite difference equations for photonics simulation. I. Beam propagation," *J. Lightwave Technol.* **16**, 134–141 (1998).
- Y. Hsueh, M. Yang, and H. Chang, "Three-dimensional noniterative full-vectorial beam propagation method based on the alternating direction implicit method," *J. Lightwave Technol.* **17**, 2389–2397 (1999).
- H. El-Refaei, D. Yevick, and I. Betty, "Stable and noniterative bidirectional beam propagation method," *IEEE Photonics Technol. Lett.* **12**, 389–391 (2000).
- Y. A. Eremin and V. I. Ivakhnenko, "Modeling of light scattering by non-spherical inhomogeneous particles," *J. Quant. Spectrosc. Radiat. Transf.* **60**, 475–482 (1998).
- C. Hafner, *Post-Modern Electromagnetics: Using Intelligent Maxwell Solvers* (Wiley, Chichester, UK, 1999).
- C. M. Herzinger, C. C. Lu, T. A. DeTemple, and W. C. Chew, "The semiconductor waveguide facet reflectivity problem," *IEEE J. Quantum Electron.* **29**, 2273–2281 (1993).
- J. Willems, J. Haes, and R. Baets, "The bidirectional mode expansion method for two-dimensional waveguides: the TM case," *Opt. Quantum Electron.* **27**, 995–1007 (1995).
- H. Derudder, D. De Zutter, and F. Olyslager, "Analysis of waveguide discontinuities using perfectly matched layers," *Electron. Lett.* **34**, 2138–2140 (1998).
- G. R. Hadley, "Low-truncation-error finite difference equations for photonics simulation. II. Vertical-cavity surface-emitting lasers," *J. Lightwave Technol.* **16**, 142–151 (1998).
- J.-F. Lee, R. Palandech, and R. Mittra, "Modeling three-dimensional discontinuities in waveguides using nonorthogonal FDTD algorithm," *IEEE Trans. Microwave Theory Tech.* **40**, 346–352 (1992).
- P. R. Hayes, M. T. O'Keefe, P. R. Woodward, and A. Gopinath, "High-order-compact time-domain numerical simulation of optical waveguides," *Opt. Quantum Electron.* **31**, 813–826 (1999).
- A. Tafove and S. C. Hagness, *Computational Electrodynamics: The Finite-Difference Time-Domain Method*, 2nd ed. (Artech House, Boston, Mass., 2000).
- J. B. Davies, "Finite element analysis of waveguides and cavities—a review," *IEEE Trans. Magn.* **29**, 1578–1583 (1993).
- M. J. Noble, J. A. Lott, and J. P. Loehr, "Quasi-exact optical analysis of oxide-aperture microcavity VCSEL's using vector finite elements," *IEEE J. Quantum Electron.* **34**, 2327–2339 (1998).
- S. F. Helfert and R. Pregla, "Analysis of thin layers and discontinuities," *Opt. Quantum Electron.* **31**, 721–732 (1999).
- W. Huang and R. R. A. Syms, "Analysis of folded erbium-doped planar waveguide amplifiers by the method of lines," *J. Lightwave Technol.* **17**, 2658–2664 (1999).
- E. Hasman, N. Davidson, Y. Danziger, and A. A. Friesem, "Diffractive optics: design, realization, and applications," *Fiber Integr. Opt.* **16**, 1–25 (1997).
- D. R. Beltrami, J. D. Love, and F. Ladouceur, "Multimode planar devices," *Opt. Quantum Electron.* **31**, 307–326 (1999).
- J. B. Pendry and P. M. Bell, "Transfer matrix techniques for electromagnetic waves," in *Photonic Band Gap Materials*, Vol. 315 of *NATO ASI Series*, C. M. Soukoulis, ed. (Kluwer, Dordrecht, The Netherlands, 1996), pp. 203–228.
- G. H. Goedecke and S. G. O'Brien, "Scattering by irregular inhomogeneous particles via the digitized Green's function algorithm," *Appl. Opt.* **27**, 2431–2438 (1988).
- B. T. Draine and P. J. Flatau, "Discrete-dipole approximation for scattering calculations," *J. Opt. Soc. Am. A* **11**, 1491–1499 (1994).
- P. J. Flatau, "Improvements in the discrete-dipole approximation method of computing scattering and absorption," *Opt. Lett.* **22**, 1205–1207 (1997).
- O. J. F. Martin and N. B. Piller, "Electromagnetic scattering in polarizable backgrounds," *Phys. Rev. E* **58**, 3909–3915 (1998).
- M. A. Taubenblatt and T. K. Tran, "Calculation of light scattering from particles and structures on a surface by the

- coupled-dipole method," *J. Opt. Soc. Am. A* **10**, 912–919 (1993).
32. C. Girard, A. Dereux, O. J. F. Martin, and M. Devel, "Generation of optical standing waves around mesoscopic surface structures: scattering and light confinement," *Phys. Rev. B* **52**, 2889–2898 (1995).
 33. R. Schmehl, B. M. Nebeker, and E. D. Hirleman, "Discrete-dipole approximation for scattering by features on surfaces by means of a two-dimensional fast Fourier transform technique," *J. Opt. Soc. Am. A* **14**, 3026–3036 (1997).
 34. C.-T. Tai, *Dyadic Green Function in Electromagnetic Theory* (IEEE Press, Piscataway, N.J., 1994).
 35. M. Paulus, P. Gay-Balmaz, and O. J. F. Martin, "Accurate and efficient computation of the Green's tensor for stratified media," *Phys. Rev. E* **62**, 5797–5807 (2000).
 36. A. D. Yaghjian, "Electric dyadic Green's functions in the source region," *Proc. IEEE* **68**, 248–263 (1980).
 37. N. B. Piller and O. J. F. Martin, "Increasing the performances of the coupled-dipole approximation: a spectral approach," *IEEE Trans. Antennas Propag.* **46**, 1126–1137 (1998).
 38. B. M. Nebeker, G. W. Starr, and E. D. Hirleman, "Evaluation of iteration methods used when modeling scattering from features on surfaces using the discrete-dipole approximation," *J. Quant. Spectrosc. Radiat. Transf.* **60**, 493–500 (1998).
 39. M. F. Cátedra, R. P. Torres, J. Basterrechea, and E. Gago, *The CG-FFT Method* (Artech House, Boston, Mass., 1995).
 40. G. W. Ford and W. H. Weber, "Electromagnetic interactions of molecules with metal surfaces," *Phys. Rep.* **113**, 195–287 (1984).
 41. J.-J. He, B. Lamontagne, A. Delâge, L. Erickson, M. Davies, and E. S. Koteles, "Monolithic integrated wavelength demultiplexer based on a waveguide rowland circle grating in InGaAs/InP," *J. Lightwave Technol.* **16**, 631–638 (1998).
 42. O. J. F. Martin, A. Dereux, and C. Girard, "Iterative scheme for computing exactly the total field propagating in dielectric structures of arbitrary shape," *J. Opt. Soc. Am. A* **11**, 1073–1080 (1994).
 43. M. Paulus and O. J. F. Martin, "A fully vectorial technique for scattering and propagation in three-dimensional stratified photonic structures," *Opt. Quantum Electron.* (to be published).
 44. A. D. Boardman, ed., *Electromagnetic Surface Modes* (Wiley, New York, 1982).
 45. K. Welford, "The method of attenuated total reflections," in *Surface Plasmon-Polaritons* (Institute of Physics, Bristol, UK, 1988).
 46. J. D. Jackson, *Classical Electrodynamics*, 3rd ed. (Wiley, New York, 1999).
 47. O. J. F. Martin, C. Girard, and A. Dereux, "Dielectric vs. topographic contrast in near-field microscopy," *J. Opt. Soc. Am. A* **13**, 1801–1808 (1996).
 48. H. Schmid, H. Biebuyck, B. Michel, and O. J. F. Martin, "Light-coupling masks for lensless, sub-wavelength optical lithography," *Appl. Phys. Lett.* **72**, 2379–2381 (1998).
 49. H. Schmid, H. Biebuyck, B. Michel, O. J. F. Martin, and N. B. Piller, "Light-coupling masks: an alternative, lensless approach to high-resolution optical contact lithography," *J. Vac. Sci. Technol. B* **16**, 3422–3425 (1998).
 50. H. A. Macleod, *Thin-Film Optical Filters*, 2nd ed. (Adam Hilger, Bristol, UK, 1986).

P3

**Green's tensor technique for scattering
in 2D stratified media**

Michael Paulus and Olivier J. F. Martin

Phys. Rev. E **63**, 066615 (2001)

Green's tensor technique for scattering in two-dimensional stratified media

Michael Paulus^{1,2} and Olivier J. F. Martin^{1,*}

¹*Electromagnetic Fields and Microwave Electronics Laboratory, Swiss Federal Institute of Technology, ETH-Zentrum ETZ, CH-8092 Zurich, Switzerland*

²*IBM Research, Zurich Research Laboratory, CH-8803 Rüschlikon, Switzerland*

(Received 1 February 2001; published 29 May 2001)

We present an accurate and self-consistent technique for computing the electromagnetic field in scattering structures formed by bodies embedded in a stratified background and extending infinitely in one direction (two-dimensional geometry). With this fully vectorial approach based on the Green's tensor associated with the background, only the embedded scatterers must be discretized, the entire stratified background being accounted for by the Green's tensor. We first derive the formulas for the computation of this dyadic and discuss in detail its physical substance. The utilization of this technique for the solution of scattering problems in complex structures is then illustrated with examples from photonic integrated circuits (waveguide grating couplers with varying periodicity).

DOI: 10.1103/PhysRevE.63.066615

PACS number(s): 42.25.-p, 42.79.Gn, 42.82.Et, 02.60.Cb

I. INTRODUCTION

The accurate computation of light scattering from particles in the presence of a stratified background is extremely important for the understanding of realistic structures. Ridges on a multilayered waveguide [1], opaque regions on a contact lithography mask [2], polarization gratings on a transparent backplane [3], and nanowires deposited on a substrate for surface-enhanced Raman scattering [4] all have in common that dielectric or metallic scatterers are distributed in a medium consisting of several layers with different permittivities.

Recently, we presented a technique for computing the propagation and scattering of light in three-dimensional (3D) structures formed by a stratified background with embedded scatterers of finite extension in all three dimensions [5,6]. This approach is based on the Green's tensor associated with the stratified background. In this paper, we extend this technique to two-dimensional (2D) geometries, i.e., systems with a translation symmetry in one direction.

A typical 2D system that we want to study is shown in Fig. 1. Several scatterers described by the permittivity $\epsilon(\mathbf{r})$ are embedded in a stratified background and illuminated with an incident field \mathbf{E}^0 . The stratified background is composed of L layers with relative permittivity ϵ_l , $l=1, \dots, L$, and the scatterers extend infinitely along the y axis so that the material system is invariant in that direction. If also the excitation has such a translation symmetry, we can restrict the study of the 3D system (Fig. 1) to a 2D cross section in the xz plane (Fig. 2). We then define the coordinate \mathbf{r}_\parallel parallel to this plane,

$$\mathbf{r} = (\mathbf{r}_\parallel, r_y) = (r_x, r_z, r_y), \quad (1)$$

and the parallel wave vector \mathbf{k}_\parallel ,

$$\mathbf{k} = (\mathbf{k}_\parallel, k_y) = (k_x, k_z, k_y). \quad (2)$$

Let us emphasize that it is not necessary that also the incident field \mathbf{E}^0 propagates in the xz plane (Fig. 1). The sole constraint is that \mathbf{E}^0 has an $\exp(ik_y^0 y)$ dependence on the symmetry direction y . For example, a plane wave

$$\mathbf{E}^0(\mathbf{r}, t) = \mathbf{E}^0 \exp(i\mathbf{k}^0 \mathbf{r} - i\omega t) = \mathbf{E}^0 \exp(i\mathbf{k}_\parallel^0 \mathbf{r}_\parallel - i\omega t) \exp(ik_y^0 y) \quad (3)$$

at oblique incidence on the structure fulfills this condition (Figs. 1 and 2).

However, if \mathbf{E}^0 propagates in the xz plane ($k_y^0 = 0$), it is possible to decompose the total field into a transverse electric (TE) part with the electric field in the xz plane, and a transverse magnetic (TM) part with the electric field parallel to

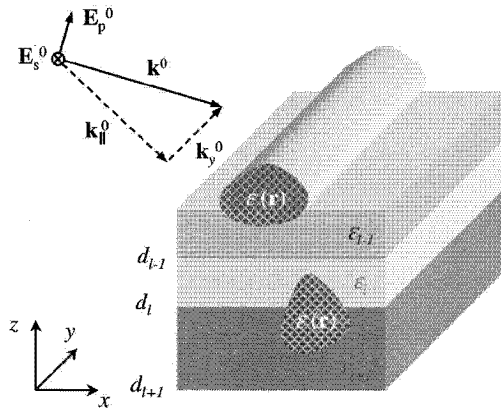


FIG. 1. Schematic view of a 2D scattering system. Several scatterers with permittivity $\epsilon(\mathbf{r})$ are embedded in a stratified background formed by L layers with permittivity ϵ_l , $l=1, \dots, L$. The scatterers are infinitely extended in the y direction. However, the propagation of the incident field is not restricted and its wave vector $\mathbf{k}^0 = \mathbf{k}_\parallel^0 + \mathbf{k}_y^0$ can have components parallel and perpendicular to the xz plane. Similarly, the electric field can be split into two contributions: the p -polarized part \mathbf{E}_p^0 lying within the plane of incidence formed by \mathbf{k}_\parallel^0 and the z axis, and the s -polarized part \mathbf{E}_s^0 standing perpendicularly to this plane. If $\mathbf{k}^0 = \mathbf{k}_\parallel^0$ ($\mathbf{k}_y^0 = 0$), p polarization is referred to as TE and s polarization as TM.

*Correspondence author. Email address: martin@ifh.ee.ethz.ch

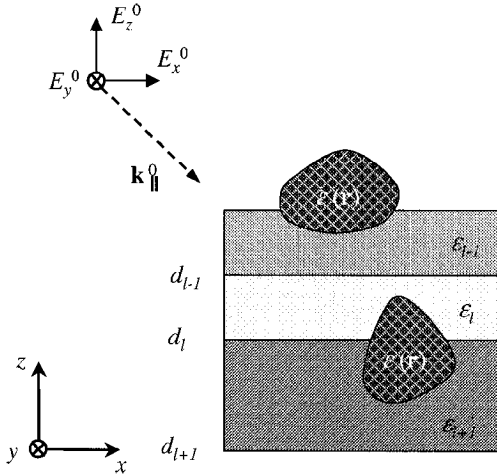


FIG. 2. Projection of Fig. 1 on the xz plane. This plane is normal to the direction of translation symmetry and the investigation of the system can be restricted to this plane. Note that only the projection \mathbf{k}_\parallel^0 of the incident wave vector \mathbf{k}^0 is shown and in general all three components of the incident electric field are nonzero.

the y direction. These two polarizations are then decoupled and the scattered field conserves the polarization of the incident field, i.e., the x and z field components are independent of the y component. This is not the case for oblique incidence ($k_y^0 \neq 0$): all three field components are coupled together and new components that were not present in the incident field can be created during the scattering process [7].

For the investigation of such 2D geometries, many useful techniques have already been developed [8–21]. However, most of them strongly depend on the particular geometry under study. The aim of this paper is to present a very general technique for scattering calculations in 2D systems where the scatterers are embedded in a background formed by an arbitrary number of layers. The description of our approach in Sec. II consists of two parts. First, we study the general solution of the scattering problem using the Green's tensor associated with the background of the system. We then derive this Green's tensor and discuss its numerical computation. In Sec. III, we illustrate the technique with two examples and summarize in Sec. IV. All the detailed formulas required for the practical implementation of this method are given in the Appendix.

II. FORMALISM

A. Solution of the 2D scattering problem

To obtain the solution of the 2D scattering problem depicted in Figs. 1 and 2, let us start with the more general solution of the corresponding 3D problem as developed in Refs. [5,6]. We consider nonmagnetic materials with relative permeability $\mu=1$ and harmonic fields with time dependence $\exp(-i\omega t)$.

When a system formed by a stratified background with embedded scatterers is illuminated with an incident electric field $\mathbf{E}^0(\mathbf{r})$, the total field $\mathbf{E}(\mathbf{r})$ is given by the volume integral equation:

$$\mathbf{E}(\mathbf{r}) = \mathbf{E}^0(\mathbf{r}) + \int_V d\mathbf{r}' \mathbf{G}_{3D}(\mathbf{r}, \mathbf{r}') \cdot k_0^2 \Delta \epsilon(\mathbf{r}') \mathbf{E}(\mathbf{r}'), \quad (4)$$

where $\mathbf{G}_{3D}(\mathbf{r}, \mathbf{r}')$ is the Green's tensor associated with the stratified background, $k_0^2 = \omega^2 \epsilon_0 \mu_0$ is the vacuum wave number, and $\Delta \epsilon(\mathbf{r})$ is the dielectric contrast:

$$\Delta \epsilon(\mathbf{r}) = \epsilon(\mathbf{r}) - \epsilon_\kappa, \quad \mathbf{r} \in \text{layer } \kappa. \quad (5)$$

The integration in Eq. (4) runs over the scatterer volume V . The Green's tensor $\mathbf{G}_{3D}(\mathbf{r}, \mathbf{r}')$ is the solution of the vector wave equation with a point source term [22],

$$\nabla \times \nabla \times \mathbf{G}_{3D}(\mathbf{r}, \mathbf{r}') - k_0^2 \epsilon_\kappa \mathbf{G}_{3D}(\mathbf{r}, \mathbf{r}') = \mathbf{1} \delta(\mathbf{r} - \mathbf{r}'),$$

$$\mathbf{r} \in \text{layer } \kappa, \quad (6)$$

and represents the electric field in the stratified background radiated at \mathbf{r} by three orthogonal unit dipoles located at \mathbf{r}' .

In a 2D system, where the scatterer volume extends infinitely in the y direction, the dielectric contrast does not depend on this coordinate. Since we assume, as discussed in the Introduction, that all the fields have a plane-wave dependence in the y direction, the electric field can be written as

$$\mathbf{E}(\mathbf{r}) = \mathbf{E}(\mathbf{r}_\parallel) \exp(ik_y^0 y). \quad (7)$$

Let us note that the wave-vector component k_y^0 , which is tangential to the different material interfaces, is constant throughout the entire stratified background. It is therefore solely determined by the illumination field and remains conserved in the scattered field. Hence, Eq. (4) can be rewritten as

$$\mathbf{E}(\mathbf{r}_\parallel) = \mathbf{E}^0(\mathbf{r}_\parallel) + \int_A d\mathbf{r}' \mathbf{G}_{2D}(\mathbf{r}_\parallel, \mathbf{r}') \cdot k_0^2 \Delta \epsilon(\mathbf{r}') \mathbf{E}(\mathbf{r}'), \quad (8)$$

where we introduced

$$\mathbf{G}_{2D}(\mathbf{r}_\parallel, \mathbf{r}') = \int_{-\infty}^{\infty} dy' \mathbf{G}_{3D}(\mathbf{r}, \mathbf{r}') \exp[i k_y^0 (y' - y)]. \quad (9)$$

Note that the integration in Eq. (8) runs only over the scatterers section A . Recalling that $\mathbf{G}_{3D}(\mathbf{r}, \mathbf{r}')$ corresponds to a point source, $\mathbf{G}_{2D}(\mathbf{r}_\parallel, \mathbf{r}')$ gives the field generated by an infinite line source extending in the y direction and represents the 2D Green's tensor associated with the stratified background.

As for 3D systems [6], the Green's tensor can be split into two parts:

$$\mathbf{G}_{2D}(\mathbf{r}_\parallel, \mathbf{r}') = \delta_{\kappa\kappa'} \mathbf{G}_{2D}^D(\mathbf{r}_\parallel, \mathbf{r}') + \mathbf{G}_{2D}^I(\mathbf{r}_\parallel, \mathbf{r}'),$$

$$\mathbf{r}_\parallel \in \text{layer } \kappa, \mathbf{r}' \in \text{layer } \kappa'. \quad (10)$$

\mathbf{G}_{2D}^D corresponds to the direct field from \mathbf{r}' to \mathbf{r}_\parallel and is given in closed form by the 2D Green's tensor for an infinite homogeneous material of permittivity ϵ_κ [7]. The indirect part \mathbf{G}_{2D}^I accounts for all the reflections and refractions at the interfaces and must be evaluated numerically. Since the di-

vergence of the Green's tensor for $\mathbf{r} \rightarrow \mathbf{r}'$ is completely included in \mathbf{G}_{2D}^D , it can be treated in a similar way to that for an infinite homogeneous medium. Taking the principal value as in Eq. (7) in Ref. [7], we rewrite Eq. (8) as

$$\begin{aligned} \mathbf{E}(\mathbf{r}_\parallel) = & \mathbf{E}^0(\mathbf{r}_\parallel) + \int_A d\mathbf{r}' \mathbf{G}_{2D}^I(\mathbf{r}_\parallel, \mathbf{r}') \cdot k_0^2 \Delta \varepsilon(\mathbf{r}') \mathbf{E}(\mathbf{r}') \\ & + \lim_{\delta A \rightarrow 0} \int_{A - \delta A} d\mathbf{r}' \delta_{\kappa\kappa'} \mathbf{G}_{2D}^D(\mathbf{r}_\parallel, \mathbf{r}') \cdot k_0^2 \Delta \varepsilon(\mathbf{r}') \mathbf{E}(\mathbf{r}') \\ & - \mathbf{L} \cdot \frac{\Delta \varepsilon(\mathbf{r}_\parallel)}{\varepsilon_\kappa} \mathbf{E}(\mathbf{r}_\parallel), \end{aligned} \quad (11)$$

where the infinitesimal area δA centered at \mathbf{r}_\parallel is used to exclude the singularity. The source dyadic \mathbf{L} depends on the shape of δA and is given in detail by Yaghjian [23].

B. Discretized 2D equation

The integral equation (11) is solved numerically on a two dimensional grid with N meshes centered at $\mathbf{r}_{\parallel,i} \in$ layer κ_i with area A_i , $i=1, \dots, N$, and dielectric contrast $\Delta \varepsilon_i = \Delta \varepsilon(\mathbf{r}_{\parallel,i})$. The discretization need not be regular but can vary locally to enhance the required accuracy, with a smaller mesh where the dielectric contrast $\Delta \varepsilon(\mathbf{r}_\parallel)$ is large. Introducing the discretized field $\mathbf{E}_i = \mathbf{E}(\mathbf{r}_{\parallel,i})$ and the discretized Green's tensors $\mathbf{G}_{i,j}^D = \mathbf{G}_{2D}^D(\mathbf{r}_{\parallel,i}, \mathbf{r}_{\parallel,j})$ and $\mathbf{G}_{i,j}^I = \mathbf{G}_{2D}^I(\mathbf{r}_{\parallel,i}, \mathbf{r}_{\parallel,j})$, the discretized version of Eq. (11) reads

$$\begin{aligned} \mathbf{E}_i = & \mathbf{E}_i^0 + \sum_{j=1}^N \mathbf{G}_{i,j}^I \cdot k_0^2 \Delta \varepsilon_j \mathbf{E}_j A_j \\ & + \sum_{j=1, j \neq i} \delta_{\kappa_i \kappa_j} \mathbf{G}_{i,j}^D \cdot k_0^2 \Delta \varepsilon_j \mathbf{E}_j A_j \\ & + \mathbf{M}_i \cdot k_0^2 \Delta \varepsilon_i \mathbf{E}_i - \mathbf{L} \cdot \frac{\Delta \varepsilon_i}{\varepsilon_{\kappa_i}} \mathbf{E}_i, \\ & i = 1, \dots, N, \end{aligned} \quad (12)$$

with the self-term \mathbf{M}_i defined as

$$\mathbf{M}_i = \lim_{\delta A \rightarrow 0} \int_{A_i - \delta A} d\mathbf{r}' \mathbf{G}_{2D}^D(\mathbf{r}_{\parallel,i}, \mathbf{r}'). \quad (13)$$

Since the tensors \mathbf{L} and \mathbf{M}_i come from the direct contribution, we can use their analytic form for a homogeneous polarizable background with permittivity ε_κ , as given in Ref. [7]. The system of equations (12) is best solved using an iterative solver such as conjugate gradients [24].

C. 2D Green's tensor for a stratified medium

Equation (9) shows that the Green's tensor for the 2D system can be directly obtained from $\mathbf{G}_{3D}(\mathbf{r}, \mathbf{r}')$ by integration along the translation axis y . Whereas $\mathbf{G}_{3D}(\mathbf{r}, \mathbf{r}')$ for an infinite homogeneous background can be expressed analytically [7], this is not possible when the background is stratified. However, a formulation can be found that provides a numerical solution for $\mathbf{G}_{3D}(\mathbf{r}, \mathbf{r}')$ in that case, as explained in detail in Ref. [5]. Let us briefly summarize this procedure:

The Green's tensor is expressed in reciprocal space (\mathbf{k} space), where the boundary conditions at the stratification interfaces can be enforced more easily. Since we need the Green's tensor in direct space, an inverse Fourier transform is performed and, after analytical integration over k_z (z is the stratification direction), we find the following expression for the Green's tensor associated with a stratified background [Eq. (10) in Ref. [5]]:

$$\begin{aligned} \mathbf{G}_{3D}(\mathbf{r}, \mathbf{r}') = & -\frac{\hat{\mathbf{z}}\hat{\mathbf{z}}}{k_\kappa^2} \delta(\mathbf{R}) + \frac{i}{8\pi^2} \int \int dk_x dk_y \\ & \times \exp\{i[k_x(x-x') + k_y(y-y')]\} \\ & \times [\mathbf{h}^s(k_x, k_y; z, z') + \mathbf{h}^p(k_x, k_y; z, z')], \end{aligned} \quad (14)$$

where $\mathbf{R} = (x-x', y-y', z-z')$ and $k_\kappa^2 = \omega^2 \varepsilon_\kappa \mu_\kappa$ with $\mathbf{r} \in$ layer κ . The tensors \mathbf{h}^s and \mathbf{h}^p take into account all the reflections and refractions at the different interfaces. They are determined by the boundary conditions for the electric and the magnetic fields and can be split into two parts corresponding to the s - and p -polarized waves, as indicated by the superscript.

Inserting Eq. (14) in Eq. (9), the integral over y' can be identified with a δ function:

$$\begin{aligned} \mathbf{G}_{2D}(\mathbf{r}, \mathbf{r}') = & -\frac{\hat{\mathbf{z}}\hat{\mathbf{z}}}{k_\kappa^2} \delta(\mathbf{R}) + \frac{i}{4\pi} \int \int dk_x dk_y \\ & \times \exp[i k_x(x-x')] \exp[i(k_y - k_y^0)y] \delta(k_y - k_y^0) \\ & \times [\mathbf{h}^s(k_x, k_y; z, z') + \mathbf{h}^p(k_x, k_y; z, z')] \\ = & -\frac{\hat{\mathbf{z}}\hat{\mathbf{z}}}{k_\kappa^2} \delta(\mathbf{R}) + \frac{i}{4\pi} \int_{-\infty}^{\infty} dk_x \exp[i k_x(x-x')] \\ & \times [\mathbf{h}^s(k_x, k_y^0; z, z') + \mathbf{h}^p(k_x, k_y^0; z, z')]. \end{aligned} \quad (15)$$

Thus, to obtain the 2D Green's tensor, only a one-dimensional integral over the transverse component k_x must be calculated numerically. The components of the tensors \mathbf{h}^s and \mathbf{h}^p can be derived from careful evaluation of Eq. (10) in Ref. [5] and are explicitly given in the Appendix.

The numerical evaluation of the remaining integrals [Eq. (15)] is intricate because it involves several poles and branch cuts corresponding to the different electromagnetic modes that can be excited in the stratified medium. However, the mathematical structure of the equations for the 2D case presented here is similar to that of the 3D case detailed in Ref. [5]. A difference at first view is that in 2D the integrals run along the entire k_x axis while for 3D the integration path is restricted to the semi-infinite positive k_ρ axis. However, in 2D the component functions of \mathbf{h}^s and \mathbf{h}^p are either even or odd symmetrical with respect to the integration variable k_x . It is therefore possible to reduce the quadrature to the semi-infinite positive k_x axis. Hence, exactly the same integration technique as proposed in 3D can be applied [5]: We first use an elliptical deformation of the integration path in the fourth

quadrant of the complex k_x plane to avoid the singularities. As in the 3D case, we then have two possibilities to resume the integration: Either we follow the real k_x axis or (for $x \neq x'$) we deflect the integration path parallel to the imaginary axis with the correct direction chosen in accordance to the sign of $x - x'$. In both cases the integrands converge exponentially because of their dependence on $\exp(ik_{xz}|z - z'|) = \exp[i(k_x^2 - k_y^2)^{1/2}|z - z'|] \rightarrow \exp(-k_x|z - z'|)$ when $k_x \rightarrow \infty$ for the real axis integration [see Eqs. (A1)–(A18)], and on $\exp(ik_x|x - x'|)$ [see Eq. (15)] for the deflected integration path. Hence, a comparison between $|z - z'|$ and $|x - x'|$ gives the path that provides fastest convergence. Let us finally note the basic difference between the 2D and 3D integrals: In 3D, the angular integration of exponential functions in \mathbf{k} space leads to Bessel/Hankel functions in the integrand, whereas in 2D, the bare exponential functions remain.

III. ILLUSTRATIVE EXAMPLES

A. The Green's tensor as a dipole field

To clarify the physical substance of the Green's tensor for stratified media, let us start by illustrating some of its basic properties. We consider a simple three-layer system $\epsilon_1 = 1$, $\epsilon_2 = 9$, $\epsilon_3 = 1$ with varying thickness h of the high permittivity slab, and we study two components of the Green's tensor, G_{yz} and G_{zy} , as a function of the z coordinate of the observation point, $\mathbf{r}_\parallel = (\lambda, z)$. The source point $\mathbf{r}'_\parallel = (0, 1 \mu\text{m})$ is held fixed in the top layer. The vacuum illumination wavelength is $\lambda = 633 \text{ nm}$.

Let us first mention that both components vanish if the incident field does not have a component k_y^0 in the y direction. (In that case, TE and TM waves are decoupled and $G_{yx} = G_{xy} = G_{yz} = G_{zy} = 0$.) In our example, we use an illumination with a [111] orientation, so that $k_y^0 = k_1 / \sqrt{3}$. Figure 3 shows G_{yz} and G_{zy} when the high permittivity layer extends from $z = 0$ to $z = 430 \text{ nm}$. Since the Green's tensor represents the electric field radiated at \mathbf{r} by three orthogonal unit dipoles at \mathbf{r}' , its components must fulfill the respective boundary conditions at the interfaces. Correspondingly, G_{yz} (the y component of a z -oriented dipole) is continuous across the interfaces, whereas G_{zy} (the z component of a y -oriented dipole) jumps by a factor $\epsilon_2 / \epsilon_1 = 9$ and $\epsilon_3 / \epsilon_2 = \frac{1}{9}$, respectively.

It is quite surprising that in the lower layer ($z < 0$) both components are identical (Fig. 3). Using the integrands given in the Appendix and the iterative derivation of the amplitude coefficients of Appendix A in Ref. [5], it can be shown that for \mathbf{r}' and \mathbf{r} in the two outermost layers 1 and L , the components of the Green's tensor are coupled:

$$\frac{G_{\alpha z}}{k_{1z}} = \frac{G_{z\alpha}}{k_{Lz}}, \quad \alpha = x, y, \quad (16)$$

where $k_{Iz} = [k_I^2 - k_x^2 - (k_y^0)^2]^{1/2}$, $I = 1, L$. Since in our example \mathbf{r}' is located in the top layer and $k_{1z} = k_{3z}$, the components coincide for $z < 0$ (Fig. 3).

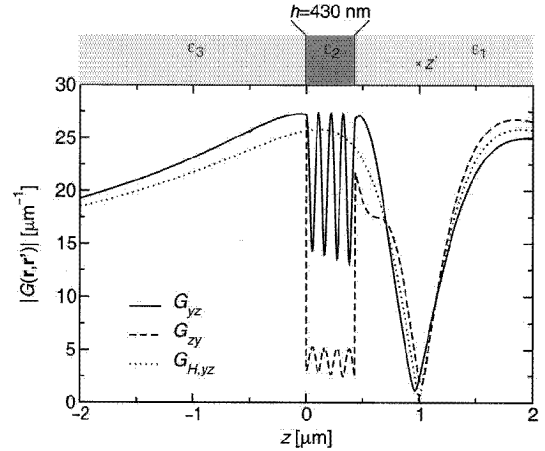


FIG. 3. Green's tensor components for a stratified background ($|G_{yz}|$ and $|G_{zy}|$) and a homogeneous background ($|G_{H,yz}| = |G_{H,zy}|$). The stratified structure consists of three layers with $\epsilon_1 = 1$, $\epsilon_2 = 9$, $\epsilon_3 = 1$. The high permittivity slab extends from $z = 0$ to $z = 430 \text{ nm}$ resulting in maximal transmission ($T_{\max} = 1$). The permittivity of the homogeneous medium is $\epsilon_H = 1$. The line source at $z' = 1 \mu\text{m}$ is located in the top layer and held fixed. The wavelength is $\lambda = 633 \text{ nm}$.

Let us now discuss the relation between the Green's tensor for a stratified medium and that associated with a homogeneous background ϵ_H . When $\mathbf{r}_\parallel - \mathbf{r}'_\parallel$ becomes large, the plane-wave expansion of the Green's tensor is mainly governed by the plane wave which propagates in radial direction, $\mathbf{k}_\parallel / |\mathbf{k}_\parallel| = (\mathbf{r}_\parallel - \mathbf{r}'_\parallel) / |\mathbf{r}_\parallel - \mathbf{r}'_\parallel|$. Hence, with x fixed and $z \rightarrow \pm\infty$, the integrals in Eq. (15) are dominated by the $k_x = 0$ terms. In this limit, the ratio between the free-space component and the component with stratification is given by the reflection and transmission coefficients of the stratified structure corresponding to this single plane wave. For a three-layer structure, the transmission coefficient T for G_{yz} and G_{zy} reads [25]

$$T = \frac{T_{12}T_{23}\exp(ihk_{2z})}{1 + \mathcal{R}_{12}\mathcal{R}_{23}\exp(2ihk_{2z})}, \quad (17)$$

where $\mathcal{R}_{l,l+1}$ and $T_{l,l+1}$ are the Fresnel reflection and transmission coefficients:

$$\mathcal{R}_{l,l+1} = \frac{\epsilon_{l+1}k_{lz} - \epsilon_l k_{l+1z}}{\epsilon_{l+1}k_{lz} + \epsilon_l k_{l+1z}}, \quad (18a)$$

$$T_{l,l+1} = \frac{2\epsilon_{l+1}k_{lz}}{\epsilon_{l+1}k_{lz} + \epsilon_l k_{l+1z}}. \quad (18b)$$

Note that Eqs. (18a) and (18b) give the coefficients for a p -polarized plane wave corresponding to the polarization of G_{yz} and G_{zy} [see Eqs. (A12) and (A16)].

An analysis of Eq. (17) yields a condition for maximal transmission through the slab with thickness h :

$$h_{\max}k_{2z} = n\pi, \quad (19a)$$

and for minimal transmission

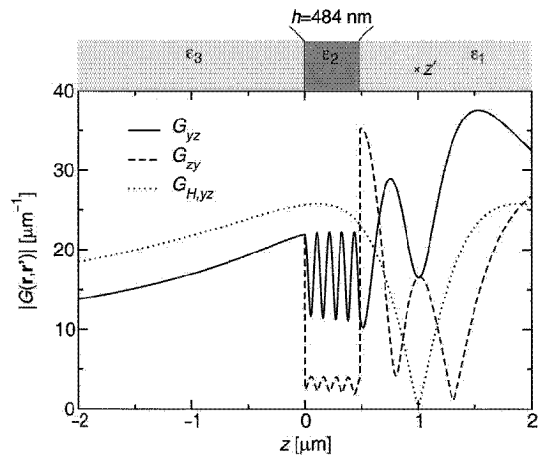


FIG. 4. Same situation as in Fig. 3, but with a high permittivity layer with thickness $h=484$ nm. This corresponds to minimal transmission through the slab ($T_{\min}\approx 0.69$).

$$h_{\min}k_{2z}=(n+\frac{1}{2})\pi, \quad (19b)$$

where $n=1,2,3,\dots$. Since for the $k_y=0$ terms $k_{2z}=\sqrt{k_2^2-(k_y^0)^2}$, maximal and minimal transmission through the slab of our example are obtained when $h_{\max}\approx n\times 107.5$ nm and $h_{\min}\approx(n+1/2)\times 107.5$ nm, respectively. The corresponding coefficient of maximal and minimal transmission is $|T_{\max}|=1$ and $|T_{\min}|\approx 0.69$, respectively [Eq. (17)]. Hence, the plane wave is completely transmitted through a slab with thickness h_{\max} without any reflection.

In Fig. 3 ($h=430$ nm = 4×107.5 nm, maximal transmission [see Eq. (19a)]), we also report the component $G_{H,yz}=G_{H,zy}$ of the Green's tensor associated with a homogeneous background $\epsilon_H=1$. In the far-field limit $z\rightarrow\pm\infty$, we observe that indeed the components for the stratified structure converge to the free-space solution. At $z=\pm 2$ μm, the difference is less than 5% and at $z=\pm 10$ μm it is $\approx 1\%$ (not shown). For comparison, we also study a second structure with $h=484$ nm $\approx(4+1/2)\times 107.5$ nm. Figure 4 shows G_{yz} , G_{zy} , and $G_{H,yz}$ for this geometry with minimal transmission. At $z=-2$ μm, the ratio $|G_{yz}/G_{H,yz}|\approx 0.75$ and at $z=-10$ μm $|G_{yz}/G_{H,yz}|\approx 0.70$ (not shown) it is close to 0.69, as expected from the above calculation.

B. Scattering on a planar waveguide grating coupler

We now use our formalism for a scattering calculation in an integrated optics structure. We consider a silicon-on-insulator (SOI) planar waveguide with a finite rectangular grating on top, as shown in Fig. 5 [26,27]. If a mode propagates in the waveguide and scatters on the grating, light is coupled out of the guiding layer and is transmitted into the air and/or towards the substrate. In Fig. 6, we report the electric-field amplitude $|\mathbf{E}|$ when a grating consisting of 20 protrusions is illuminated with the TE_0 mode (transverse electric mode with electric field polarized in the y direction) propagating in the x direction at a wavelength $\lambda=1.3$ μm. The maximum amplitude of the incident mode is normalized

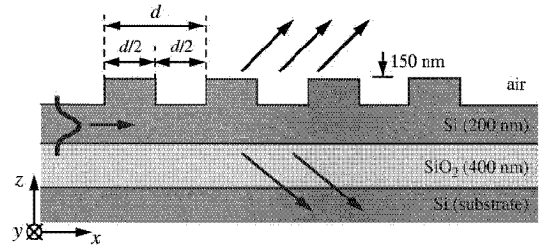


FIG. 5. Geometry of the SOI planar waveguide (permittivities $\epsilon_{\text{Si}}=12.3$, $\epsilon_{\text{SiO}_2}=2.1$; wavelength $\lambda=1.3$ μm). A Si grating with 150-nm height, periodicity d , and a 0.5 filling factor is etched on top of the waveguide.

to unity. Three periodicities— $d=300$ nm, $d=400$ nm, and $d=500$ nm—are considered at a fixed filling factor 0.5. At the left side of all three geometries, a standing wave occurs because of the reflection of the incoming mode by the grating. At the right side, beyond the grating, we can observe an interference pattern created by the interaction of the fields scattered in the forward direction by the different protrusions (and the waveguide mode). The electric-field distributions strongly differ in the three cases. For $d=300$ nm, most of the outcoupled light is scattered towards the substrate and almost no light is scattered upwards [Fig. 6(a)]. With increasing periodicity, the main beam of the outcoupled light rotates, so that for $d=400$ nm and $d=500$ nm a larger fraction of the scattered field is transmitted into the air [Figs. 6(b) and 6(c)].

For a more quantitative comparison, we report in Fig. 7 the angular distribution of the electric-field amplitude $|\mathbf{E}|$ far

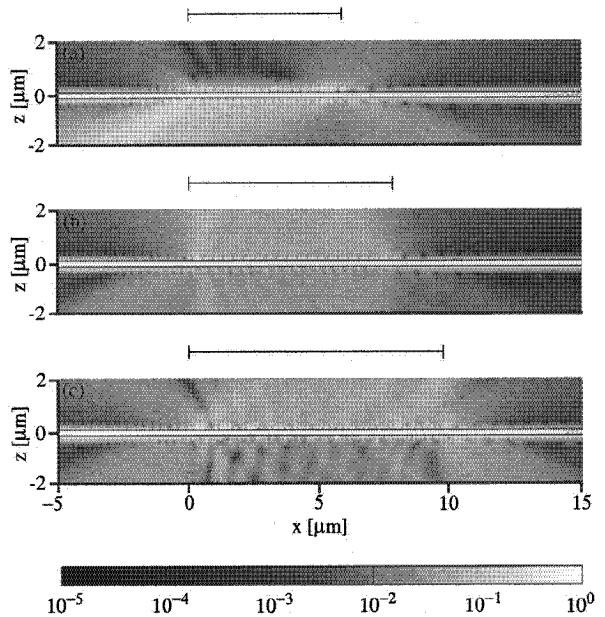


FIG. 6. Electric-field amplitude in the structure of Fig. 5 with three grating periodicities: (a) $d=300$ nm, (b) $d=400$ nm, and (c) $d=500$ nm. The bars represent the total length of each grating. The systems are illuminated with a TE_0 mode propagating in the x direction. For clarity, the guiding silicon layer is marked with two lines. A logarithmic color scale is used.

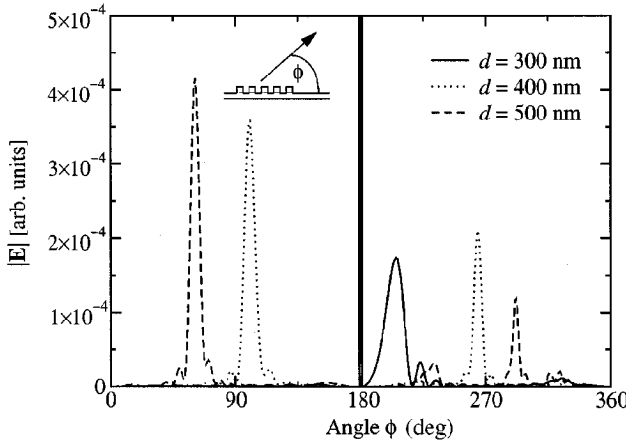


FIG. 7. Angular distribution of the electric-field amplitude 50 μm away from the center of the three gratings in Fig. 6. The central peak at $\phi=180^\circ$ is caused by the mode in the guiding Si layer and appears also at $\phi=0^\circ$ and $\phi=360^\circ$ (not shown).

away from the grating (50 μm). Note first that the central peak at $\phi=180^\circ$ represents the mode in the guiding layer. Of course, the same peak occurs at $\phi=0^\circ$ and $\phi=360^\circ$ (not shown). Whereas for $d=300$ nm, we can observe a single output beam with an angle $\phi=205^\circ$ (backward direction in the substrate), two beams appear for $d=400$ nm and $d=500$ nm, respectively: a major one into the air with $\phi=100^\circ$ (approximately normal to the waveguide surface) and $\phi=61^\circ$ (backward direction in the air), respectively, and a minor one towards the substrate with $\phi=264^\circ$ and $\phi=293^\circ$, respectively.

In the substrate region one observes for all three periodicities two additional, much broader and smaller peaks at $\phi \approx 225^\circ$ and $\phi \approx 325^\circ$. A comparison with the field distributions of Fig. 6 shows that these peaks correspond to edge effects at the beginning and at the end of the grating. At these interfaces between the planar geometry and the grating, the mode scatters strongly.

Figure 6 also illustrates that the boundary conditions both at the edges of the computation window and at the different material interfaces are perfectly fulfilled. These boundary conditions are already included in the Green's tensor so that there is no special treatment necessary to avoid unphysical reflections. Let us finally emphasize that the discretization of the geometry is restricted to the protrusions forming the grating. The optical processes in the stratified planar waveguide are completely accounted for in the Green's tensor associated with the background.

IV. SUMMARY

In this paper, we have presented a Green's tensor approach for the computation of scattering problems with 2D bodies embedded in a stratified background. We have first described in detail the numerical procedure required for the computation of the Green's tensor associated with a stratified background. We have then demonstrated the utilization of this dyadic to perform scattering calculations in complex 2D systems. From a practical point of view, in addition to truly

two-dimensional geometries, 3D structures can often be considered as 2D when the extension of the scatterers in one particular direction is very large and the electromagnetic field is so well localized that edge effects in that direction become negligible. It is then justified to assume that the system extends to infinity in that particular direction.

ACKNOWLEDGMENTS

It is a pleasure to acknowledge stimulating discussions with P. Gay-Balmaz, J. P. Kottmann, and E. Moreno and to thank B. Michel (IBM) and R. Vahldieck (ETH) for their support of the project. We gratefully acknowledge the funding from the Swiss National Science Foundation.

APPENDIX

In this appendix, we explicitly give the integrands of Eq. (15). To impose the boundary conditions at the different interfaces, the components of the tensors \mathbf{h}^s and \mathbf{h}^p are expressed in terms of upgoing and downgoing *s*-and *p*-polarized plane waves:

$$h_{xx}^s(k_x) = \frac{k_y^{0^2}}{k_{\kappa z} k_\rho^2} [A_\kappa^s \exp(i k_{\kappa z} z) + B_\kappa^s \exp(-i k_{\kappa z} z)], \quad (\text{A1})$$

$$h_{xx}^p(k_x) = \pm \frac{k_x^2 k_{\kappa z}}{k_\kappa^2 k_\rho^2} [A_{\kappa,xx}^p \exp(i k_{\kappa z} z) - B_{\kappa,xx}^p \exp(-i k_{\kappa z} z)], \quad (\text{A2})$$

$$h_{xy}^s(k_x) = -\frac{k_y^0 k_x}{k_{\kappa z} k_\rho^2} [A_\kappa^s \exp(i k_{\kappa z} z) + B_\kappa^s \exp(-i k_{\kappa z} z)], \quad (\text{A3})$$

$$h_{xy}^p(k_x) = \pm \frac{k_y^0 k_x k_{\kappa z}}{k_\kappa^2 k_\rho^2} [A_{\kappa,xy}^p \exp(i k_{\kappa z} z) - B_{\kappa,xy}^p \exp(-i k_{\kappa z} z)], \quad (\text{A4})$$

$$h_{xz}^s(k_x) = 0, \quad (\text{A5})$$

$$h_{xz}^p(k_x) = -\frac{k_x}{k_\kappa^2} [A_{\kappa,xz}^p \exp(i k_{\kappa z} z) - B_{\kappa,xz}^p \exp(-i k_{\kappa z} z)], \quad (\text{A6})$$

$$h_{yx}^s(k_x) = h_{xy}^s, \quad (\text{A7})$$

$$h_{yx}^p(k_x) = h_{xy}^p, \quad (\text{A8})$$

$$h_{yy}^s(k_x) = \frac{k_x^2}{k_{\kappa z} k_\rho^2} [A_\kappa^s \exp(i k_{\kappa z} z) + B_\kappa^s \exp(-i k_{\kappa z} z)], \quad (\text{A9})$$

$$h_{yy}^p(k_x) = \pm \frac{k_y^0 k_{\kappa z}}{k_\kappa^2 k_\rho^2} [A_{\kappa,yy}^p \exp(i k_{\kappa z} z) - B_{\kappa,yy}^p \exp(-i k_{\kappa z} z)], \quad (\text{A10})$$

$$h_{yz}^s(k_x) = 0, \quad (\text{A11})$$

$$h_{yz}^p(k_x) = -\frac{k_y^0}{k_\kappa^2} [A_{\kappa,yz}^p \exp(ik_{\kappa z} z) - B_{\kappa,yz}^p \exp(-ik_{\kappa z} z)], \quad (\text{A12})$$

$$h_{zx}^s(k_x) = 0, \quad (\text{A13})$$

$$h_{zx}^p(k_x) = \mp \frac{k_x}{k_\kappa^2} [A_{\kappa,zx}^p \exp(ik_{\kappa z} z) + B_{\kappa,zx}^p \exp(-ik_{\kappa z} z)], \quad (\text{A14})$$

$$h_{zy}^s(k_x) = 0, \quad (\text{A15})$$

$$h_{zy}^p(k_x) = \mp \frac{k_y^0}{k_\kappa^2} [A_{\kappa,zy}^p \exp(ik_{\kappa z} z) + B_{\kappa,zy}^p \exp(-ik_{\kappa z} z)], \quad (\text{A16})$$

$$h_{zz}^s(k_x) = 0, \quad (\text{A17})$$

$$h_{zz}^p(k_x) = \frac{k_\rho^2}{k_\kappa^2 k_{\kappa z}} [A_{\kappa,zz}^p \exp(ik_{\kappa z} z) + B_{\kappa,zz}^p \exp(-ik_{\kappa z} z)], \quad (\text{A18})$$

where $k_\rho^2 = k_x^2 + (k_y^0)^2$ and $k_{\kappa z} = (k_\kappa^2 - k_\rho^2)^{1/2}$ with \mathbf{r} in layer κ . The upper sign in these equations refers to $z > z'$ and the lower sign to $z < z'$. The amplitude coefficients A_κ^s , B_κ^s , A_κ^p , $A_{\kappa,\alpha\beta}^p$, and $B_{\kappa,\alpha\beta}^p$ must be calculated for the layer κ where \mathbf{r} is located and are functions of $(k_{\kappa z}; z, z')$. They are connected to the amplitudes in all other layers and can be found via an iterative scheme completely identical to that of the 3D case given in Appendix A of Ref. [5]. Note that $k_{\kappa z}$ is now only a function of k_x , since k_y is replaced by the constant parameter k_y^0 given by the incident field. Since all non-

vanishing amplitude coefficients of s -polarized waves are equal, we can suppress the indices α and β and simply write A_κ^s and B_κ^s .

Let us now consider the special case in which the incident field propagates in the xz plane. With $k_y^0 = 0$, the tensors \mathbf{h}^s and \mathbf{h}^p reduce to

$$h_{xx}^p(k_x) = \pm \frac{k_{\kappa z}}{k_\kappa^2} [A_{\kappa,xx}^p \exp(ik_{\kappa z} z) - B_{\kappa,xx}^p \exp(-ik_{\kappa z} z)], \quad (\text{A2}')$$

$$h_{xz}^p(k_x) = -\frac{k_x}{k_\kappa^2} [A_{\kappa,xz}^p \exp(ik_{\kappa z} z) - B_{\kappa,xz}^p \exp(-ik_{\kappa z} z)], \quad (\text{A6}')$$

$$h_{yy}^s(k_x) = \frac{1}{k_{\kappa z}} [A_\kappa^s \exp(ik_{\kappa z} z) + B_\kappa^s \exp(-ik_{\kappa z} z)], \quad (\text{A9}')$$

$$h_{zx}^p(k_x) = \mp \frac{k_x}{k_\kappa^2} [A_{\kappa,zx}^p \exp(ik_{\kappa z} z) + B_{\kappa,zx}^p \exp(-ik_{\kappa z} z)], \quad (\text{A14}')$$

$$h_{zz}^p(k_x) = \frac{k_x^2}{k_\kappa^2 k_{\kappa z}} [A_{\kappa,zz}^p \exp(ik_{\kappa z} z) + B_{\kappa,zz}^p \exp(-ik_{\kappa z} z)], \quad (\text{A18}')$$

and all other components vanish.

These equations clearly show the decoupling of the two polarizations that can be excited in that case. For the component of the illuminating electric field parallel to the translation symmetry axis y (TM polarization), \mathbf{G}_{2D} reduces to a scalar [Eq. (A9')]. For the components perpendicular to that axis, i.e., lying within the xz plane (TE polarization), \mathbf{G}_{2D} reduces to a (2×2) matrix [Eqs. (A2'), (A6'), (A14'), and (A18')].

-
- [1] R. März, *Integrated Optics Design and Modeling* (Artech House, Boston, 1994).
 - [2] H. Schmid, H. Biebuyck, B. Michel, and O. J. F. Martin, *Appl. Phys. Lett.* **72**, 2379 (1998).
 - [3] B. Schnabel, E. B. Kley, and F. Wyrowski, *Opt. Eng.* **38**, 220 (1999).
 - [4] M. Kahl and E. Voges, *Phys. Rev. B* **61**, 14 078 (2000).
 - [5] M. Paulus, P. Gay-Balmaz, and O. J. F. Martin, *Phys. Rev. E* **62**, 5797 (2000).
 - [6] M. Paulus and O. J. F. Martin, *J. Opt. Soc. Am. A* **18**, 854 (2001).
 - [7] O. J. F. Martin and N. B. Piller, *Phys. Rev. E* **58**, 3909 (1998).
 - [8] G. R. Hadley, *J. Lightwave Technol.* **16**, 134 (1998).
 - [9] H. El-Refaei, D. Yevick, and I. Betty, *IEEE Photonics Technol. Lett.* **12**, 389 (2000).
 - [10] C. M. Herzinger, C. C. Lu, T. A. DeTemple, and W. C. Chew, *IEEE J. Quantum Electron.* **29**, 2273 (1993).
 - [11] J. Willems, J. Haes, and R. Baets, *Opt. Quantum Electron.* **27**, 995 (1995).
 - [12] H. Derudder, D. De Zutter, and F. Olyslager, *Electron. Lett.* **34**, 2138 (1998).
 - [13] G. Videen and D. Ngo, *J. Opt. Soc. Am. A* **14**, 70 (1997).
 - [14] G. R. Hadley, *J. Lightwave Technol.* **16**, 142 (1998).
 - [15] A. Taflove and S. C. Hagness, *Computational Electrodynamics: The Finite Difference Time domain Method*, 2nd ed. (Artech House, Boston, 2000).
 - [16] S. F. Helfert and R. Pregla, *Opt. Quantum Electron.* **31**, 721 (1999).
 - [17] W. Huang and R. R. A. Syms, *J. Lightwave Technol.* **17**, 2658 (1999).
 - [18] D. R. Beltrami, J. D. Love, and F. Ladouceur, *Opt. Quantum Electron.* **31**, 307 (1999).
 - [19] J. B. Pendry and P. M. Bell, in *Photonic Band Gap Materials*, Vol. 315 of *NATO Advanced Study Institute Series*, edited by C. M. Soukoulis (Kluwer, Dordrecht, 1996), pp. 203–228.
 - [20] P. J. Valle, F. Moreno, and J. M. Saiz, *J. Opt. Soc. Am. A* **15**, 158 (1998).
 - [21] B. Hu and W. C. Chew, *Radio Sci.* **35**, 31 (2000).

- [22] P. M. Morse and H. Feshbach, *Methods of Theoretical Physics* (McGraw-Hill, New York, 1953).
- [23] A.D. Yaghjian, Proc. IEEE **68**, 248 (1980).
- [24] P. J. Flatau, Opt. Lett. **22**, 1205 (1997).
- [25] M. Born and E. Wolf, *Principles of Optics*, 6th ed. (Pergamon Press, Oxford, 1987).
- [26] T. W. Ang *et al.*, IEEE Photonics Technol. Lett. **12**, 59 (2000).
- [27] R. Orobchouk *et al.*, Appl. Opt. **39**, 5773 (2000).

P4

**Near-field distribution in light-coupling
masks for contact lithography**

Michael Paulus, Bruno Michel, and Olivier J. F. Martin
J. Vac. Sci. Technol. B **17**, 3314–3317 (1999)

Near-field distribution in light-coupling masks for contact lithography

Michael Paulus^{a)}

Electromagnetic Fields and Microwave Electronics Laboratory, Swiss Federal Institute of Technology,
ETH-Zentrum ETZ, CH-8092 Zurich, Switzerland and IBM Research Division, Zurich Research Laboratory,
CH-8803 Rüschlikon, Switzerland

Bruno Michel

IBM Research Division, Zurich Research Laboratory, CH-8803 Rüschlikon, Switzerland

Olivier J. F. Martin

Electromagnetic Fields and Microwave Electronics Laboratory, Swiss Federal Institute of Technology,
ETH-Zentrum ETZ, CH-8092 Zurich, Switzerland

(Received 2 June 1999; accepted 12 August 1999)

We discuss the potential and limitations of light-coupling masks for high-resolution subwavelength optical lithography. Using a three-dimensional fully vectorial numerical approach based on Green's tensor technique, the near-field distribution of the electric field in the photoresist is calculated. We study the dependence of the illuminating light and the angle of incidence on polarization. Furthermore, we investigate the replication of structures of various sizes and separations. It is predicted that the formation of features in the 60 nm range is possible using light with a 248 nm wavelength. However, with decreasing separation among the features, crosstalk limits the ultimate resolution. © 1999 American Vacuum Society. [S0734-211X(99)04606-5]

I. INTRODUCTION

Hard-contact lithographies can, in theory, replicate features below the wavelength of the incident light.¹ Substrate topography and ubiquitous dust particles prevent the hard chrome mask from establishing a close contact with the substrate, thus limiting the maximal resolution by the minimally attainable gap size. Projection lithographies have replaced hard-contact lithographies because excellent optics in conjunction with step and repeat exposure are able to direct and focus light with an accuracy close to its vacuum wavelength on slightly uneven resist surfaces.²

Recently a new approach to high-resolution optical lithography based on light-coupling masks (LCMs) was introduced.³ The surface of a polymer mask is topographically patterned such that the areas to be exposed in the photoresist form protrusions on the mask surface. The ability of a rubber elastic polymer to adapt to the substrate topography allows the formation of a uniform "conformal" contact with the photoresist over large areas. Placing the mask in intimate contact with a resist-coated substrate, mechanical contact between mask and resist layer occurs only in the region to be exposed (Fig. 1). When the LCM is illuminated through its backside, the light is differentially guided by the structure and coupled into the photoresist. This technique, called soft lithography, exploits the virtues of contact lithography and avoids its weaknesses. Soft lithography, on the other hand, is limited by the mechanical stability of protrusions—especially as lateral dimensions shrink and the ratio of lateral to vertical dimensions (aspect ratio) becomes large.⁴ Using this approach, Schmid *et al.* demonstrated the formation of features in the 100 nm range with a wavelength of 256 nm.⁵

Rodgers *et al.*⁶ focused on the effects of the phase delay

between the light beam crossing the air gap and the beam guided within the polymer. By means of this phase-shift lithography, Aizenberg *et al.*⁷ demonstrated the fabrication of line structures with a 50 nm linewidth. However, this approach is only suitable for the replication of low-density lines.

In this article we test the limits of the LCM approach when the protrusions guide light into the photoresist. We study numerically the dependence of the near-field distribution in LCMs on typical experimental parameters. The model for our calculations based on the solution of the vectorial wave equation is presented in Sec. II. In Sec. III the results of our simulations are shown. First, we investigate the effects

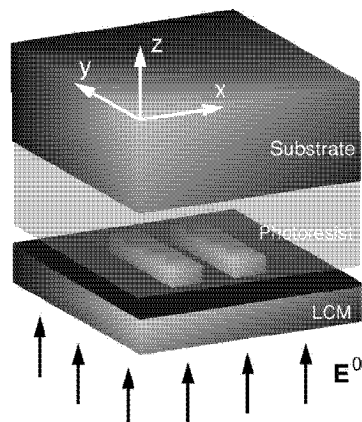


FIG. 1. Schematic view of a LCM and its operation using a normal incident field E^0 through the backside of the LCM. The simulated structures with a width d and a length $4d$ are identical and parallel. In the z direction a fixed protrusion height of 60 nm was chosen. In order to suppress light leaking through the noncontacting sections of the mask, a 15 nm gold absorber was added in recessed parts.

^{a)}Electronic mail: paulus@ifh.ee.ethz.ch

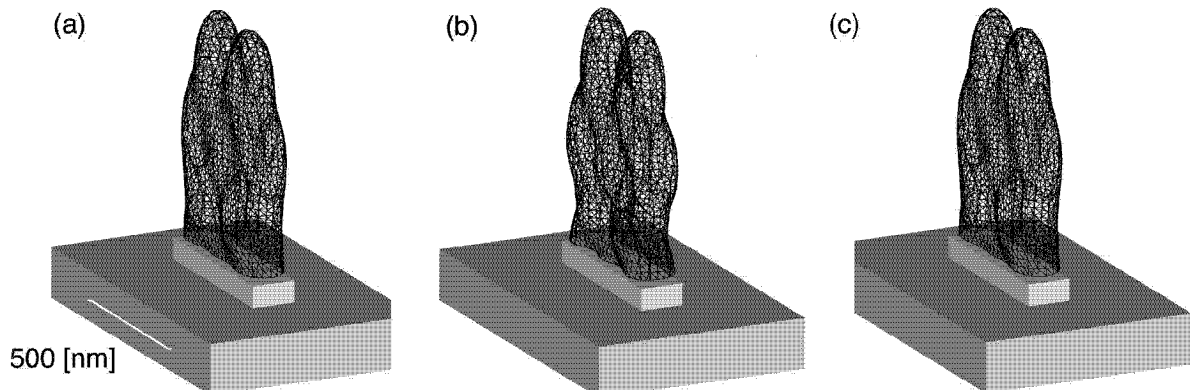


FIG. 2. Illumination of an isolated linelet with $d=120$ nm. The isosurface representing 75% of the incident light intensity is shown. The polarization of the incident light is (a) linear in the y direction, (b) linear in the x direction, and (c) circular. The extension of the isosurface in the photoresist is approximately 650 nm.

of the polarization of the incident field and discuss near-field distributions for various feature sizes. Then, we concentrate on the interaction between neighboring structures and, finally, we examine the consequences of oblique incidence on the resulting intensity profiles.

II. MODEL

We calculate the electric field distribution inside the resist layer caused by the guiding and scattering processes in a LCM illuminated by an incident field \mathbf{E}^0 . Our calculations are based on Green's tensor technique and take the vectorial character of the electromagnetic field into account. This approach delivers a three-dimensional, self-consistent, and accurate description of the optical processes in the LCM resist system. Thus, it even allows the simulation of structures with dimensions far smaller than the wavelength. For details about the formalism please refer to Ref. 8. It should be emphasized that our approach is different from the in depth projection of the aerial image on the resist surface, since it provides the electric field distribution in the entire structure. One could use our calculated three-dimensional intensity distribution in conjunction with a sophisticated resist model to exactly predict the profile of the developed photoresist.^{9,10} However, it has been previously shown that for this particular nanolithography technique, surfaces of constant intensity (or isosurfaces) of the electric field distribution do correspond to the resist profile that is measured experimentally.³

For our simulations we selected short, densely packed lines of width d and length $4d$ because these “linelets” are known to be difficult to replicate optically owing to line shortening effects and neighbor interference.² We use the term “design rule” for the width because in a technological environment the smallest replicable feature width determines the design of an electronic circuit based on this lithographic feature.

The results presented here refer to a vacuum wavelength of the incident light of 248 nm. The optical properties of the simulated resist are linear and isotropic, the refractive index of LCM and photoresist at this wavelength is assumed to be 1.6. Thus, we do not investigate possible reflections on the LCM/photoresist or photoresist/substrate interfaces due to a mismatch of the dielectric constants. In order to suppress the leaking of light through the noncontacting sections of the mask, a 15 nm gold absorber was added in the recessed parts.¹¹

III. RESULTS

A. Polarization effects

The direction of polarization of light strongly affects the replication by LCM of features elongated in one dimension.

In Fig. 2 we show isosurfaces of the field intensity distribution in the photoresist created by an isolated linelet for three incident polarizations. The design rule is $d=120$ nm. The best results are achieved with a polarization in the y direction, i.e., parallel to the linelet. In that case, the structure shape is reproduced accurately within the first 250 nm of photoresist, steep edges providing approximately a 1:1 image of the linelet in the resist layer [Fig. 2(a)]. On the other hand, using a polarization in the x direction leads to an irregular field distribution with intensity variations along the sides of the feature as well as in the depth [Fig. 2(b)]. As a complete mask possesses structures in both directions, circular polarization provides a homogeneous illumination. Actually, the field distribution for circular polarization turns out to be close to the ideal parallel polarization case, independent of

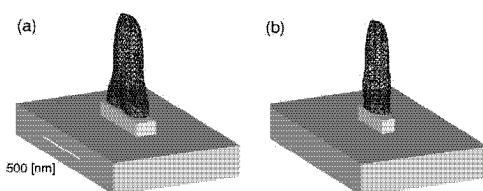


FIG. 3. Isosurfaces of the electric field intensity (75%) in the photoresist using isolated linelets with (a) $d=90$ nm and (b) $d=60$ nm. The incident light is circularly polarized. The extension of the isosurface in the photoresist is approximately 400 nm.

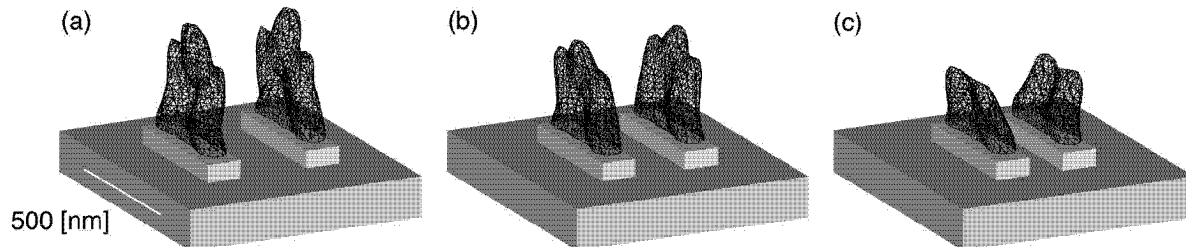


FIG. 4. Isosurfaces of the electric field intensity (75%) in the photoresist using two linelets with $d = 120$ nm and separations of (a) $2d$, (b) $1.5d$, and (c) d . The incident light is circularly polarized. The extension of the isosurface in the photoresist in (a) is approximately 400 nm.

the linelets' orientation [compare Figs. 2(a) and 2(c)]. The shape of the structure is well replicated within the first 250 nm of photoresist.

B. Resolution limit for isolated linelets

Figure 3 shows isosurfaces of the field intensity distribution in the photoresist created by an isolated linelet, but with smaller design rules, $d = 90$ and $d = 60$ nm. In both cases it is still possible to reproduce the structure shape in the photoresist, even for features smaller than 1/4 of the vacuum wavelength of the illuminating light [Fig. 3(b)]. Note that for $d = 60$ nm the aspect ratio of the isosurface no longer corresponds to the aspect ratio of the linelet, the field distribution being more constrained. The length of the isosurface $d = 15$ nm below the mask in the photoresist is 190 nm, the width 90 nm. This corresponds approximately to an aspect ratio of 1:2, leading to a strong line shortening. However, this figure also shows that structures in the 50 nm range are amenable to this technique. For $d = 90$ nm, line shortening increases with the depth in the photoresist, so that 100 nm below the mask the aspect ratio is reduced to 1:3.

C. Two linelets, variation of separation

A realistic mask is not composed of isolated structures but contains a high density of patterns. For increasing density the mutual interactions between neighboring structures become more and more important.

Figure 4 shows isosurfaces of the field intensity distribution in the photoresist for two linelets. The design rule is $d = 120$ nm, and the separation is $2d$, $1.5d$, and d . In all cases the crosstalk between neighboring features is relatively small, especially within the relevant resist depth, where the field distribution replicates the mask structure accurately.

However, for small separations, the distance between the isosurfaces of the two field distributions increases as light propagates into the photoresist [Fig. 4(c)].

In Fig. 5 the design rule is reduced to $d = 60$ nm. For such small structures, crosstalk turns out to be much more important. In the case of a separation equal to d the field distribution no longer reproduces the individual mask features, and a collective scattering behavior is observed: the incident light is focused by the structure such that a single spot appears between the linelets [Fig. 5(a)]. Note, however, that an isolated structure with a design rule of $d = 60$ nm can be replicated satisfactorily [Fig. 3(b)]. By increasing the separation to $1.5d$ and $2d$ one recovers the individual features in the near field [Figs. 5(b) and 5(c)]. With a separation of $1.5d$ the isosurface has a length of 100 nm and a width of 40 nm, whereas for a separation of $2d$ the isosurface length is 140 nm and the width 60 nm. This corresponds to the same line shortening as for the isolated linelet.

Working with such small structures, therefore, requires special care to suppress crosstalk. Furthermore, the resist depth seems to be a particularly important issue in that case.

D. Dependence on the angle of incidence

A further important experimental parameter is the dependence of the field intensity distribution on the angle of incidence. Therefore, we also performed calculations for oblique illuminations.

Figure 6 presents lines of equal field intensity for a cut in the x direction of the structure shown in Fig. 2(c). The angles of incidence are 0° , 5° , and 10° ; circularly polarized light is used. These graphs emphasize the steepness of the edges, which guarantees the accurate reproduction of the mask features in the photoresist. With increasing angle of incidence the orientation of the isolines follows the direction of the

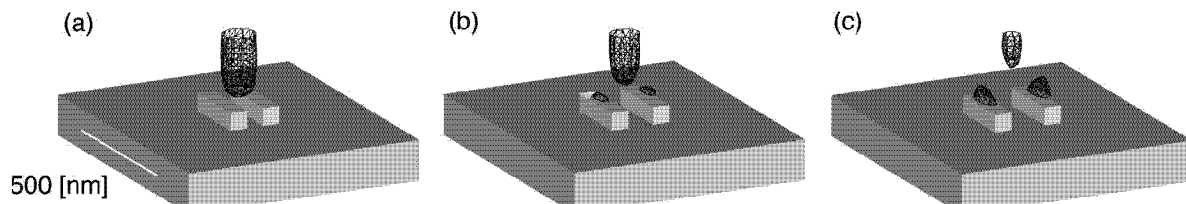


FIG. 5. Same situation as in Fig. 4, but with $d = 60$ nm linelets and separations of (a) d , (b) $1.5d$, and (c) $2d$. The extension of the isosurface in the photoresist is in (b) 35 and in (c) 65 nm.

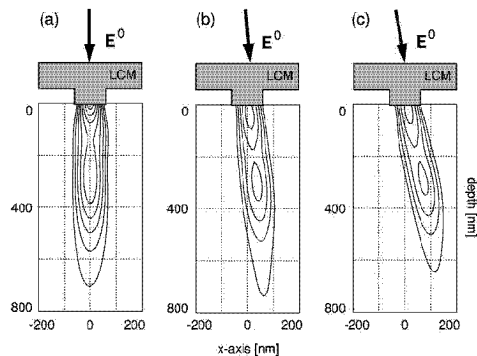


FIG. 6. Isointensity lines for a cross section in the x direction of the structure shown in Fig. 2(c), $d=120$ nm. The illumination directions investigated are: (a) normal incidence, (b) 5° tilt, and (c) 10° tilt. The line spacing corresponds to an intensity increment of 10%, where the outer isoline represents the value of 75% compared to the incident light intensity.

illuminating field. Furthermore, the entire image in the resist layer is slightly shifted in this direction [Figs. 6(a) and 6(b)]. However, for a thin resist layer, the field distribution within the photoresist does not differ much from that at normal incidence, so that a 5° tilt seems tolerable.

IV. SUMMARY

We presented three-dimensional calculations for the near-field distribution in light-coupling masks. It was shown that using an illumination with circularly polarized light, structures can be replicated accurately with steep edges in the photoresist, independent of their orientation on the mask.

Even features in the 60 nm range can be reproduced using a 248 nm wavelength. Although crosstalk between neighboring structures appears to be negligible for features of 120 nm, it can become dominant when the size shrinks to 60 nm. Finally, it was illustrated that the process is not very sensitive to small deviations of the angle of incidence.

The numerical results emphasize the suitability of light-coupling masks as a lensless alternative for high-density, high-resolution optical lithography in the subwavelength regime.

ACKNOWLEDGMENTS

It is a pleasure to acknowledge extremely stimulating discussions with H. Schmid. This work was supported by the Swiss National Science Foundation.

¹E. Cullmann, *Semicond. Int.* **8**, 332 (1985).

²Special issue on Optical Lithography, *IBM J. Res. Devel.* **41** (1997).

³H. Schmid, H. Biebuyck, B. Michel, and O. J. F. Martin, *Appl. Phys. Lett.* **72**, 2379 (1998).

⁴H. Schmid and B. Michel, *Macromolecules* (submitted).

⁵H. Schmid, H. Biebuyck, B. Michel, O. J. F. Martin, and N. B. Piller, *J. Vac. Sci. Technol. B* **16**, 3422 (1998).

⁶J. A. Rodgers, K. E. Paul, R. J. Jackman, and G. M. Whitesides, *Appl. Phys. Lett.* **70**, 2658 (1997).

⁷J. Aizenberg, J. A. Rodgers, K. E. Paul, and G. M. Whitesides, *Appl. Opt.* **37**, 2145 (1998).

⁸O. J. F. Martin and N. Piller, *Phys. Rev. E* **58**, 3909 (1998).

⁹J. Randall, H. Gangala, and A. Tritchko, *Microelectron. Eng.* **46**, 59 (1999).

¹⁰T. A. Brunner and R. A. Ferguson, *Solid State Technol.* **39**, 95 (1996).

¹¹O. J. F. Martin, N. B. Piller, H. Schmid, H. Biebuyck, and B. Michel, *Opt. Express* **3**, 280 (1998).

**Contrast mechanisms in high-resolution contact
lithography: A comparative study**

Michael Paulus, Heinz Schmid, Bruno Michel, and Olivier J. F. Martin
Microelectron. Eng. **57–58**, 109–116 (2001)



ELSEVIER

Microelectronic Engineering 57–58 (2001) 109–116

MICROELECTRONIC
ENGINEERING

www.elsevier.com/locate/mee

Contrast mechanisms in high-resolution contact lithography: A comparative study

Michael Paulus^{a,b,*}, Heinz Schmid^b, Bruno Michel^b, Olivier J.F. Martin^a

^a*Electromagnetic Fields and Microwave Electronics Laboratory, Swiss Federal Institute of Technology, ETH-Zentrum,
ETZ, CH-8092 Zurich, Switzerland*

^b*IBM Research, Zurich Research Laboratory, CH-8803 Rüschlikon, Switzerland*

Abstract

We compare three different approaches to high-resolution contact lithography with special emphasis on contrast mechanisms for subwavelength structures. Masks with protruding metal absorbers, masks with absorbers embedded in the transparent background, and masks with air gaps and recessed absorbers are studied. Using the Green's tensor technique we compute the light intensity distribution in the photoresist. The intensity and contrast functions are investigated for different mask geometries (absorber thickness, height of protruding elements), and the difference between chrome and gold as absorber material is discussed. Our results show that embedding the absorbers in a transparent mask material enhances the transmitted intensity and the contrast compared with a mask having protruding metal absorbers. A further improvement is achieved by a topographically patterned mask with air gaps and recessed absorbers. Optimized mask dimensions can be found for which the contrast and the depth of focus are increased. © 2001 Elsevier Science B.V. All rights reserved.

Keywords: Contact lithography; Contrast mechanism; Electric field distribution; Scattering calculation; Green's tensor technique

PACS: 07.05.Tp; 42.25.-p; 85.40.Hp

1. Introduction

In recent years, research interest has been revived in utilizing the advantages of optical contact lithography for replicating structures in the subwavelength regime. There are several approaches to this task: high-resolution contact masks with protruding metal absorbers (metal-protruding masks, MPM) [1,2], masks where the absorbers are embedded in the transparent background material (metal-embedded masks, MEM) [3,4], topographically patterned masks with air gaps and recessed absorbers (light-coupling masks, LCM) [5], and structured masks where no absorber is used (phase masks) [6]. Whereas the latter approach is based on interferences between light passing through

*Corresponding author.

E-mail address: paulus@ifh.ee.ethz.ch (M. Paulus).

materials with different optical thicknesses, the first three techniques use an amplitude contrast between transparent and opaque parts of the mask. These mask concepts have in common that they rely on a flexible glass or polymer, which allows the mask to be placed in contact with the entire substrate. This is the most important requirement for reliable subwavelength contact lithography.

With these techniques the formation of features in the 100-nm range was successfully demonstrated. Several theoretical studies have been published to investigate the potentials of these approaches for subwavelength patterning and to determine the corresponding optical interactions in the mask [7,8]. However, it has not yet been studied how these concepts compare to each other and whether one approach provides better performance. In this article we focus on the three types of amplitude masks (MPM, MEM, LCM) and investigate their optical properties. Fig. 1 shows a schematic view of these mask types. Whereas in an MEM and an LCM the light travels through the homogeneous transparent background material into the photoresist, in an MPM it has to cross the air gap between the mask substrate and the photoresist. It is assumed that further experimental parameters (e.g. contact with the photoresist surface, resist response, treatment after the exposure) are identical for all three systems.

2. Model

For the calculation of the electric field distribution E we used a two-dimensional, self-consistent numerical approach based on the Green's tensor technique [9]. This fully vectorial technique is based on the electric field integral equation and enables the investigation of the scattering and propagation of light through the mask/photoresist system. The advantage of this approach lies in the fact that the

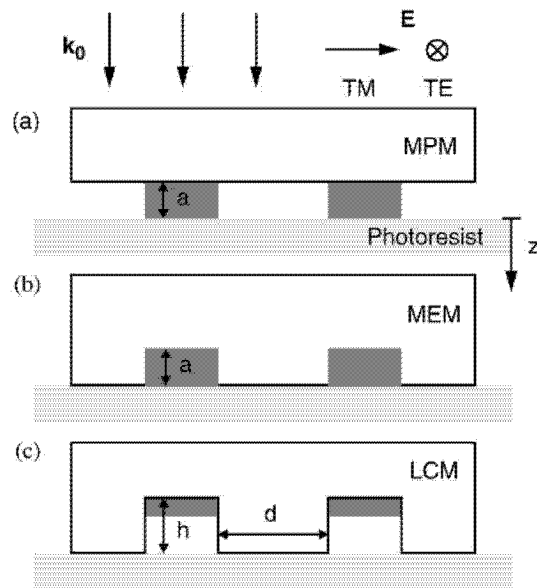


Fig. 1. Schematic view of the compared masks for contact lithography: (a) metal-protruding mask (MPM); (b) metal-embedded mask (MEM); (c) light-coupling mask (LCM).

boundary conditions at the interfaces between different materials, as well as at the edges of the computation window are perfectly and automatically fulfilled.

For our study we consider isolated lines with a line width of $d = 100$ nm and as absorber material in the mask we chose chrome or gold because these metals are most frequently used in experiments. The determinant parameter to characterize a given exposure is the intensity $I = \mathbf{E} \cdot \mathbf{E}^*$. The results presented here refer to a plane-wave illumination perpendicular to the mask surface with a vacuum wavelength of 248 nm. The intensity of the incident field is normalized to unity, and a circular polarization is used for all computations if not stated otherwise. The optical properties of the simulated material systems are assumed to be linear and isotropic. The relative permittivities at this wavelength are $\epsilon = 2.25$ for the mask background, $\epsilon = 2.5$ for the photoresist, $\epsilon = -3.4 + i3.6$ for chrome, and $\epsilon = -0.9 + i4.3$ for gold [10].

3. Results

We first compare the contrast that can be achieved by the different techniques. For this purpose we define the contrast C as

$$C = \frac{I_{\max} - I_0}{I_{\max} + I_0}, \quad (1)$$

where I_{\max} is the maximal intensity of the transmitted light and I_0 is the intensity of the light that leaks through the absorbers and forms the background for the exposure.

In Fig. 2 we compare MEMs and MPMs with chrome or gold absorbers as a function of the absorber thickness a . All curves show a strongly enhanced contrast with increasing absorber thickness, because the intensity I_0 of the light leaking through the absorbers decreases exponentially.

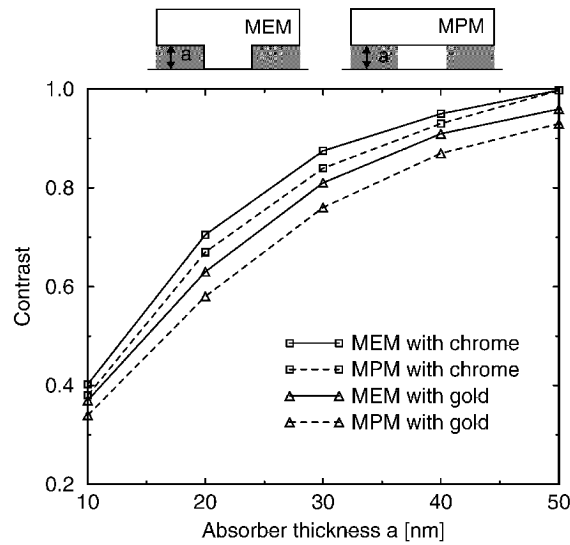


Fig. 2. Contrast as defined in Eq. (1) of MEMs and MPMs as a function of absorber thickness a at $z = 10$ nm. Chrome or gold is used as absorber material.

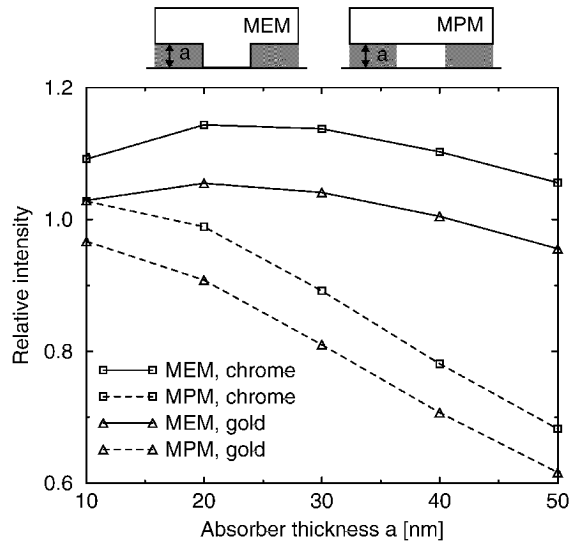


Fig. 3. Maximal intensity I_{\max} as a function of absorber thickness a at $z=10$ nm. MEMs and MPMs are compared using chrome or gold as absorber material.

In the limit of a thick absorber, C converges to 1 for all curves because the background I_0 in Eq. (1) becomes 0. Furthermore, the contrast of the chrome masks is greater than the contrast of the gold masks. The higher absorbance and higher reflectivity of chrome leads not only to a smaller background at the shadowed regions but also to a stronger field enhancement in the opening and, consequently, to a larger transmitted intensity. This fact is proved by Fig. 3, where the intensity I_{\max} for MEMs and MPMs is reported for different absorber thicknesses.

Figs. 2 and 3 also show that the contrast and the intensity of the MEM are slightly superior to those of the MPM, because reflections at the two interfaces mask substrate/air and air/photoresist lower the transmitted intensity [33% for the worst case of a $\lambda/4=62$ -nm thick air slab (not shown) and by 16% for a 30-nm thick air slab, Fig. 3].

Note that the intensities for the MEMs have a maximum at $a=20$ nm, which represents the tradeoff between two mechanisms: The transmitted intensity decreases, whereas the confinement of light becomes more efficient with increasing metal thickness.

The contrast increases similarly if we fill metal into the air gaps of an LCM with a fixed total protrusion height h , because the absorber significantly lowers the background I_0 . However, as a thicker metal also lowers the intensity transmitted into the resist, there is a tradeoff between good contrast and enough light passing through the mask. In the following we shall consider an LCM with a constant metal thickness of $a=20$ nm (corresponding to the optimum in Fig. 3) and study the influence of the lateral air gaps. Fig. 4 reports the contrast of LCMs with chrome or gold absorbers as a function of the total protrusion height h . Note that the total protrusion height h includes both the absorber thickness a and the remaining air gap. Again, chrome proves to be the metal that produces higher contrast. In Fig. 4 we also notice that C reaches a maximum at $h=75$ nm. This maximum corresponds to the maximal reflectivity of the metal/air slab, leading to a minimum of I_0 . Thus, by choosing the appropriate total protrusion height, the contrast can be increased by 15% for a gold absorber and by 10% for a chrome absorber. As this effect is solely related to the air gap of the LCM,

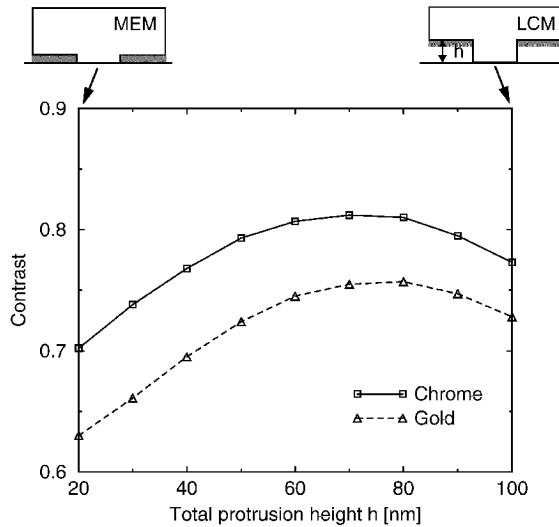


Fig. 4. Contrast of LCMs as a function of the total protrusion height h at $z=10$ nm. All masks have a 20-nm thick chrome or gold absorber. The leftmost values correspond to an MEM with $a=20$ nm.

it is independent of the absorber thickness a . For a thicker absorber (leading to a reduction of the background), a similar effect is observed and an optimal total protrusion height h can be found.

The intensity distribution should ideally show not only a large difference between the regions to be illuminated and the shadowed regions, but also a shape that accurately replicates the pattern in the resist. To assess this requirement as a function of the additional air gap we computed the electric field at different depths in the photoresist, $z=10$ nm, $z=100$ nm and $z=250$ nm, and determined the full width at half maximum (FWHM) of the intensity distribution. Fig. 5 presents line cuts through the

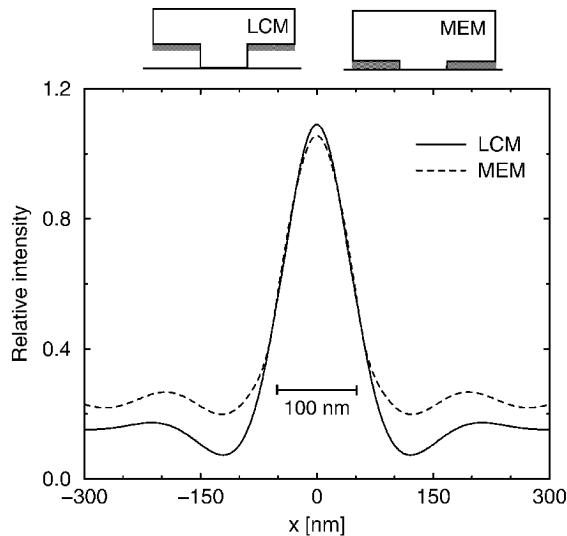


Fig. 5. Relative intensity distributions at $z=10$ nm for an MEM and an LCM. Both masks have a 20-nm thick gold absorber; the total protrusion height of the LCM is $h=80$ nm. The bar represents the original line width.

intensity distribution close to the mask ($z=10$ nm) for an LCM and an MEM. The masks have a 20-nm thick gold absorber, the total protrusion height h of the LCM is 80 nm, which is close to the optimum in Fig. 4. The FWHM of both line cuts is ≈ 90 nm, and the intensity at the edges of the mask has dropped to $I=0.6$. With the additional air gap of the LCM, however, the confinement of the transmitted light is improved, leading to a slightly greater maximal intensity. This effect is even more pronounced for the intensity distribution deeper in the photoresist. Fig. 6 shows line cuts of 100 and 250 nm depth in the photoresist. The shape of the intensity distributions becomes substantially more narrow and higher for the LCM. The FWHM decreases by $\approx 10\%$ at $z=100$ nm and even by $\approx 20\%$ at $z=250$ nm, compared to MEM. Concurrently, at both depths the peak intensity is 10% greater for LCM than for MEM. The air gap in the LCM improves the guiding of the light into the resist, resulting in greater directionality without the loss of intensity that would occur with thick full-metal absorbers. At the corners of the targeted line, 100 nm deep in the photoresist, the relative intensity is $I=0.6$ for both masks. This is still close to the value at $z=10$ nm (Fig. 5) providing steep edges of the developed resist. At $z=250$ nm the targeted line is defined only by the $I=0.5$ isointensity lines for both masks. Hence, this corresponds to the bottom region of the developed photoresist.

If we compare the intensity distributions of MEMs with MPMs having an identical absorber, the FWHMs of the MPMs are 14% greater close to the mask ($z=10$ nm) and 17% greater deeper in the photoresist ($z=100$ nm). Hence, not only a smaller portion of the illuminating light is transmitted, but the directionality provided by the mask opening is less efficient.

Until now computations were carried out for circularly polarized illumination. To show in more detail the influence of the mask composition on polarization, Fig. 7 reports the intensity distributions when a TE or TM-polarized illumination is used (see Fig. 1 for the definition of TE and TM). Again, an MEM with a 20-nm gold absorber is compared with an LCM with 20 nm of gold and a 60-nm air gap (total protrusion height $h=80$ nm). For both polarizations the LCM shows a slightly higher transmitted intensity. Owing to the orientation of the TE-polarized electric field vector the intensity is focused on the center of the opening, resulting in a narrow peak with an FWHM of ≈ 80 nm for both masks. In contrast, the TM electric field vector is perpendicular to the surfaces, and hence the

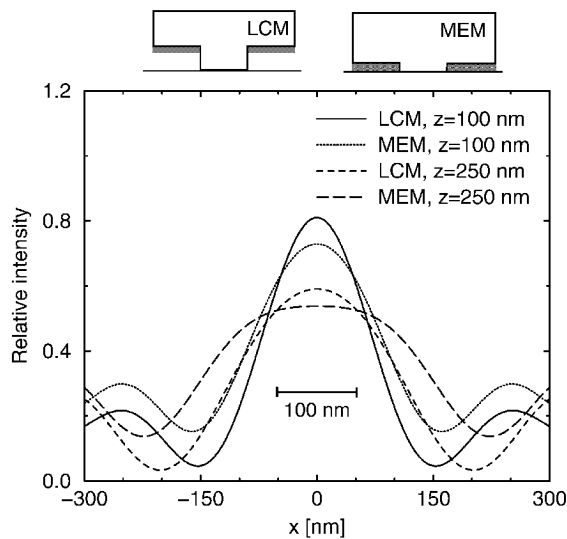


Fig. 6. Same as Fig. 5, but at a depth of $z=100$ and 250 nm.

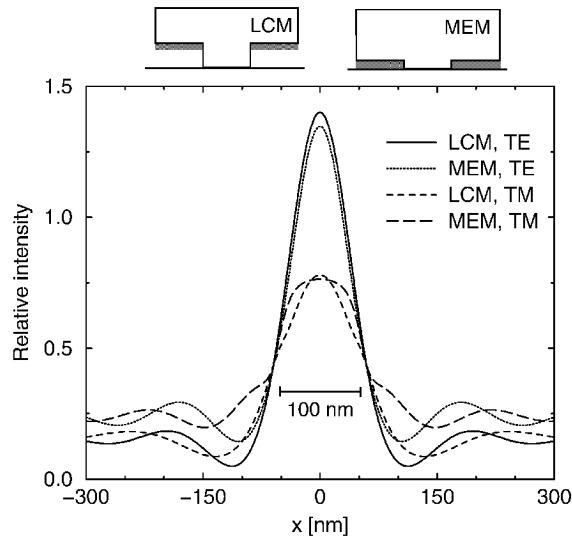


Fig. 7. Polarization-dependent relative intensity distributions for an MEM and an LCM at $z=10$ nm. TE or TM-polarized light is used as illumination (see Fig. 1). Both masks have a 20-nm thick gold absorber; the total protrusion height of the LCM is $h=80$ nm. The bar represents the original line width.

intensity distribution is wider with an FWHM of ≈ 110 nm for both masks. This broadening is based on the continuity of the displacement field $D = \epsilon E$, resulting in a high intensity at the edges of the opening. Furthermore, the electric field is extremely enhanced at the metal corners, leading to the broader intensity distribution of the MEM. This effect also depends on the absorber metal and can be enhanced when surface plasmons are excited in the metal.

Similar results are obtained for an MPM, where the FWHM is about 5% greater for both polarizations. However, in agreement with Fig. 3, the maximum peak values I_{\max} of the relative intensity decrease significantly to 1.07 and 0.74, respectively, for the TE and TM polarizations, respectively. Note that the dimensions used together with gold as absorber are not appropriate for a polarizing functionality.

4. Discussion

Following the laws of image formation in a lens system, the ultimate resolution Δ for pattern replication with optical lithography is given by the diffraction limit [11]:

$$\Delta \approx a \frac{\lambda_0}{NA}, \quad (2)$$

where a is a process parameter, λ_0 the vacuum wavelength and NA the numerical aperture. Whereas for projection lithography this relation restricts the ultimate resolution to $\Delta \approx \lambda_0/2$, for contact lithography this limit is further reduced. Since the refractive index n of the mask lowers the effective wavelength λ_{eff} , structures with a size $\Delta \approx \lambda_{\text{eff}}/2 = \lambda_0/(2n)$ can be realized. With the parameters used in this study (see Section 2) the resolution is enhanced to $\Delta \approx 248/(2 \cdot 1.5)$ nm = 80 nm. However,

even smaller structures can be replicated with the evanescent near field created by each opening in the mask [7].

All three considered mask types are capable of subwavelength resolution. However, the different contrast mechanisms imply different intensity distributions in the photoresist during exposure. For MEMs and MPMs a thicker metal absorber leads to an enhanced contrast (Fig. 2), but also lowers the intensity in the photoresist (Fig. 3) and, consequently, requires a more costly experimental setup. Especially with MPMs the amount of transmitted light is strongly reduced. The contrast can be further increased by an additional air gap below the metal absorbers (LCMs, Fig. 5). Since these air gaps improve the directional guiding of light, the intensity distribution remains better confined even deeper inside of the photoresist.

5. Summary

We used simulations based on the Green's tensor technique to precisely model and optimize the design of high-resolution contact lithography masks. Our calculations show that chrome is a superior absorber to gold because of its greater reflectivity and absorbance. We compared three different approaches to high-resolution contact lithography and studied the contrast mechanisms. We showed that embedding the absorbers in a transparent background material increases the transmitted light and enhances the contrast. An even further improvement at fixed metal thickness is achieved if topographically patterned masks are used, where the absorbers are recessed and the lateral air gaps lead to an enhanced confinement of the light.

Acknowledgements

The authors thank P. Seidler (IBM) and R. Vahldieck (ETH) for their support of the project and gratefully acknowledge the funding of the Swiss National Science Foundation.

References

- [1] H.I. Smith, Method for fabricating high frequency surface wave transducers, *Rev. Sci. Instrum.* 40 (1969) 729–730.
- [2] M.M. Alkaisi, R.J. Blaikie, S.J. McNab, R. Cheung, D.R.S. Cumming, Sub-diffraction-limited patterning using evanescent near-field optical lithography, *Appl. Phys. Lett.* 75 (22) (1999) 3560–3562.
- [3] U.C. Fischer, H.P. Zingsheim, Submicroscopic pattern replication with visible light, *J. Vac. Sci. Technol.* 19 (4) (1981) 881–885.
- [4] J.G. Goodberlet, Patterning 100 nm features using deep-ultraviolet contact photolithography, *Appl. Phys. Lett.* 76 (6) (2000) 667–669.
- [5] H. Schmid, H. Biebuyck, B. Michel, O.J.F. Martin, Light-coupling masks for lensless, sub-wavelength optical lithography, *Appl. Phys. Lett.* 72 (1998) 2379–2381.
- [6] J.A. Rodgers, K.E. Paul, R.J. Jackman, G.M. Whitesides, Using an elastomeric phase mask for sub-100 nm photolithography in the optical near field, *Appl. Phys. Lett.* 70 (20) (1997) 2658–2660.
- [7] S.J. McNab, R.J. Blaikie, Contrast in the evanescent near field of $\lambda/20$ period gratings for photolithography, *Appl. Opt.* 39 (1) (2000) 20–25.
- [8] O.J.F. Martin, N.B. Piller, H. Schmid, H. Biebuyck, B. Michel, Energy flow in light-coupling masks for lensless optical lithography, *Optics Express* 3 (1998) 280–285.
- [9] M. Paulus, O.J.F. Martin, Light propagation and scattering in stratified media: A. Green's tensor approach, *J. Opt. Soc. Am. A* 18 (4) (2001) 854–861.
- [10] O.S. Am, 2nd Edition, *Handbook of Optics*, Vol. II, McGraw-Hill, New York, 1995.
- [11] M. Born, E. Wolf, *Principles of Optics*, 6th Edition, Pergamon Press, Oxford, 1987.

P6

A fully vectorial technique for scattering and propagation in three-dimensional stratified photonic structures

Michael Paulus and Olivier J. F. Martin
Opt. Quant. Electron. **33**, 315–325 (2001)

A fully vectorial technique for scattering and propagation in three-dimensional stratified photonic structures

MICHAEL PAULUS^{1,2} AND OLIVIER J. F. MARTIN^{1,*}

¹*Electromagnetic Fields and Microwave Electronics Laboratory, Swiss Federal Institute of Technology,
ETH-Zentrum ETZ, CH-8092 Zurich, Switzerland*

²*IBM Research Division, Zurich Research Laboratory, CH-8803 Rüschlikon, Switzerland
(*author for correspondence: E-mail: martin@ifh.ee.ethz.ch)*

Abstract. We present a three-dimensional (3D) technique for computing light scattering and propagation in complex structures formed by scatterers embedded in a stratified background. This approach relies on the Green's tensor associated with the background and requires only the discretization of the scatterers, the entire stratified background being accounted for in the Green's tensor. Further, the boundary conditions at the edges of the computation window and at the different material interfaces in the stratified background are automatically fulfilled. Different examples illustrate the application of the technique to the modeling of photonic integrated circuits: waveguides with protrusions (single element 'grating') and notches. Subtle effects, like polarization crosstalks in an integrated optics device are also investigated.

Key words: computational technique, eigenmodes, Green's tensor, integrated optics, light propagation, polarization, scattering, stratified media, waveguides

1. Introduction

Most photonic integrated circuits (PICs) are built on a stratified background. This background, formed by a stack of layers with different permittivities, is used to confine and guide the light. The particular functions in the circuit (light source, switch, coupler, modulator, detector, etc.) are then incorporated as distinct components in this background (e.g., a quantum well in a stratified laser structure or a grating on top of a waveguide).

Different approaches can be used for the simulation of such PICs, for example eigenmode expansions (Herzinger *et al.* 1993; Willems *et al.* 1995; Derudder *et al.* 1998), finite difference time domain algorithms (Lee *et al.* 1992; Hayes *et al.* 1999), finite element methods (Davies 1993; Noble *et al.* 1998), beam propagation methods (Huang and Xu 1993; Hsueh *et al.* 1999; El-Refaei *et al.* 2000) or the method of lines (Helfert and Pregla 1999; Huang and Syms 1999). For a recent review, see e.g., Scarmozzino *et al.* (2000).

We recently proposed a new approach to this problem, based on the Green's tensor technique (Paulus and Martin 2001). It is a fully vectorial

model for three-dimensional (3D) structures based on the solution of the electric field integral equation. We will briefly outline this technique in Section 2 and illustrate in Section 3 its application to several 3D integrated optics systems. We will summarize our results in Section 4.

2. The Green's tensor technique

We consider a system formed by distinct 3D scatterers with permittivity $\varepsilon(\mathbf{r})$ embedded in a stratified background made up of L material layers with permittivities $\varepsilon_i, i = 1, \dots, L$ (Fig. 1(a)). Throughout this paper, we consider non-magnetic materials ($\mu = 1$) and assume a harmonic time dependence $\exp(-i\omega t)$ for the fields.

The core of our technique is the integral equation for the electric field,

$$\mathbf{E}(\mathbf{r}) = \mathbf{E}^0(\mathbf{r}) + \int_V d\mathbf{r}' \mathbf{G}(\mathbf{r}, \mathbf{r}') \cdot k_0^2 \Delta\varepsilon(\mathbf{r}') \mathbf{E}(\mathbf{r}'), \quad (1)$$

which gives the total scattered field $\mathbf{E}(\mathbf{r})$ when the system is illuminated with an incident field $\mathbf{E}^0(\mathbf{r})$ propagating in the stratified background (Tai 1994; Martin and Piller 1998).

In Equation (1), $k_0 = \omega/c$ is the wave number in vacuum; the dielectric contrast $\Delta\varepsilon(\mathbf{r})$ represents the polarizability of the scatterer compared to that of the background and is defined by

$$\Delta\varepsilon(\mathbf{r}) = \varepsilon(\mathbf{r}) - \varepsilon_\kappa \quad \text{for } \mathbf{r} \in \text{layer } \kappa. \quad (2)$$

The tensor $\mathbf{G}(\mathbf{r}, \mathbf{r}')$ is the Green's tensor associated with the stratified background. It contains the entire response of the stratified background and includes all reflections/refractions at any interface, as well as the radiation conditions at infinity.

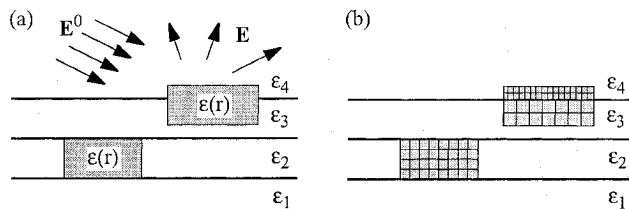


Fig. 1. (a) Typical structure under study: a stratified background formed by L layers of materials with different permittivities ε_i contains several scatterers $\varepsilon(\mathbf{r})$. The structure is illuminated with an incident field $\mathbf{E}^0(\mathbf{r})$ and our objective is to compute the total field $\mathbf{E}(\mathbf{r})$ in the system. Note that the first and last background layers represent semi-infinite media. (b) Only the scatterers must be discretized to solve the scattering problem numerically using the Green's tensor technique. A non-regular mesh, with higher refinement in the regions of high contrast is used.

This dyadic cannot be obtained analytically and must be computed numerically. This is best achieved by expressing $\mathbf{G}(\mathbf{r}, \mathbf{r}')$ in Fourier space and using the symmetry properties of the stratified background in that space. We recently detailed this procedure in Paulus *et al.* (2000) and refer the reader to this publication. In the present article, we will simply use $\mathbf{G}(\mathbf{r}, \mathbf{r}')$ to perform scattering calculations with Equation (1).

However, before doing so, we would like to illustrate the physical signification of the Green's tensor for a stratified background: for a given source–observer \mathbf{r}', \mathbf{r} pair, the 3×3 matrix representing the Green's tensor,

$$\mathbf{G}(\mathbf{r}, \mathbf{r}') = \begin{pmatrix} G_{xx} & G_{xy} & G_{xz} \\ G_{yx} & G_{yy} & G_{yz} \\ G_{zx} & G_{zy} & G_{zz} \end{pmatrix}, \quad (3)$$

gives the electric field radiated at \mathbf{r} by three orthogonal dipoles located at \mathbf{r}' .

For example, Fig. 2 illustrates the first column of $\mathbf{G}(\mathbf{r}, \mathbf{r}')$, corresponding to the three components of the electric field radiated by an x -oriented dipolar source. The source point is located at $\mathbf{r}' = (0, 0, 250 \text{ nm})$ in the stratified background corresponding to Fig. 3. The wavelength is $\lambda = 633 \text{ nm}$ (note that in Section 3 we consider a wavelength $\lambda = 1.55 \mu\text{m}$). The three components of the Green's tensor are computed along a vertical line in the stratified background, at a one wavelength lateral distance from the source point. One notices in Fig. 2 that both in the cap InP layer and in the InGaAsP layer, the electric field oscillates in a manner that corresponds to a stationary wave

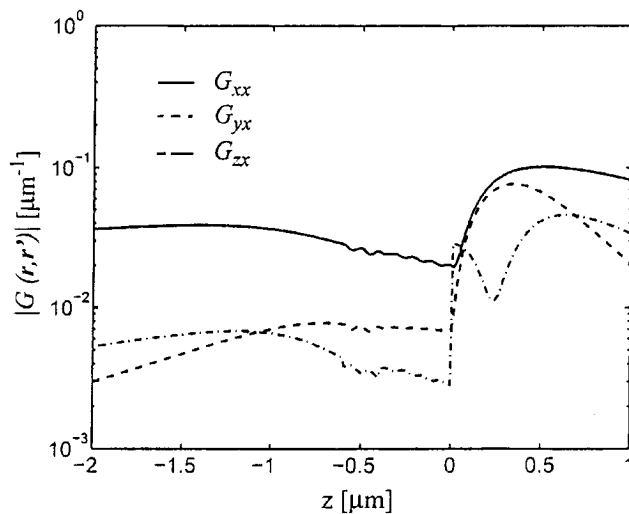


Fig. 2. Three components of the Green's tensor for the stratified background corresponding to the structure depicted in Fig. 3.

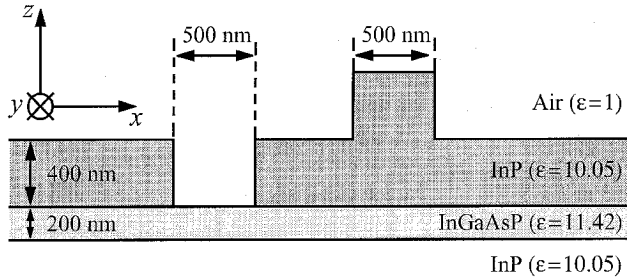


Fig. 3. Geometry and permittivity of the system: a notch is etched in, or a protrusion deposited on top of an InP/InGaAsP structure. The structure is illuminated with a TE_0 or a TM_0 mode propagating in x -direction and the scattered field is computed.

excited in the corresponding layer, with a shorter effective wavelength in the layer with the highest index (InGaAsP). The x and y electric field components are parallel to the interfaces and therefore continuous. On the other hand, the z component is normal to the material interfaces and therefore discontinuous, as is visible in Fig. 2. This figure illustrates the significant physical information contained in the Green's tensor.

To solve Equation (1) numerically, we define a mesh on the system with N discretized elements centered at \mathbf{r}_i with permittivity $\varepsilon_i = \varepsilon(\mathbf{r}_i)$ and volume V_i (Fig. 1(b)). The discretization volume V_i need not be constant and, in order to achieve a given accuracy, it is actually necessary to use a smaller mesh where the dielectric contrast is larger (Piller and Martin 1998). Each mesh must be entirely inside a layer and cannot sit astride a boundary between two layers (Fig. 2(b)).

We can formally write the discretized system of equations corresponding to Equation (1):

$$\mathbf{E}_i = \mathbf{E}_i^0 + \sum_{j=1}^N \mathbf{G}_{i,j} \cdot k_0^2 \Delta \varepsilon_j \mathbf{E}_j V_j, \quad i = 1, \dots, N. \quad (4)$$

It should be noted that a special treatment must be applied to the case $j = i$ since the Green's tensor diverges in that case. This procedure, which is detailed in Paulus and Martin (2001), leads to additional terms in Equation (4).

The system of Equations (4) is then solved numerically, e.g. with an iterative solver, to obtain the unknown discretized field \mathbf{E}_i for a given illumination \mathbf{E}^0 .

Let us finally note that Equation (1) can also be used for scattering calculations in an infinite homogeneous background (instead of a stratified background) by simply using the corresponding Green's tensor. In that case, $\mathbf{G}(\mathbf{r}, \mathbf{r}')$ takes a very simple analytical form (Martin and Piller 1998).

3. Results

To illustrate this technique, we consider the InP/InGaAsP waveguide structure depicted in Fig. 3. At the wavelength of $1.55\text{ }\mu\text{m}$, the InGaAsP guide can support two different modes: a transverse electric TE_0 mode, with the electric field polarized in the y -direction, and a transverse magnetic TM_0 mode, with the electric field in the (x, z) -plane.

Fig. 4 gives the total electric field amplitude (square root of $\mathbf{E} \cdot \mathbf{E}^*$) when the system is illuminated with a TE_0 mode propagating in the x -direction. An InP protrusion has been deposited on the structure. This single step ‘grating’ somewhat disturbs the propagation of the mode, leading to light scattered into the substrate. The interaction of this scattered light with the incident field produces an interference pattern on the left-hand side of the protrusion in Fig. 4(a). The diffraction of the incoming mode is particularly visible in the middle of the InGaAsP layer, where a depletion in the field amplitude appears just behind the protrusion (Fig. 4(b)), note that the grayscale is chosen to emphasize the structure of the field distributions, leading to different saturation values for the distribution in a (x, z) - or a (x, y) -plane). However, due to the limited lateral extension of the protrusion, this scattering effect remains localized and, quite rapidly, the incident mode is re-established in the structure. A similar behavior is observed when a TM_0 illumination is used (not shown).

Let us point out how perfectly the boundary conditions at the edges of the computation window and at the interface between the different layers are fulfilled. This at no additional computational costs, since these complex boundary conditions are already included in the Green’s tensor $\mathbf{G}(\mathbf{r}, \mathbf{r}')$.

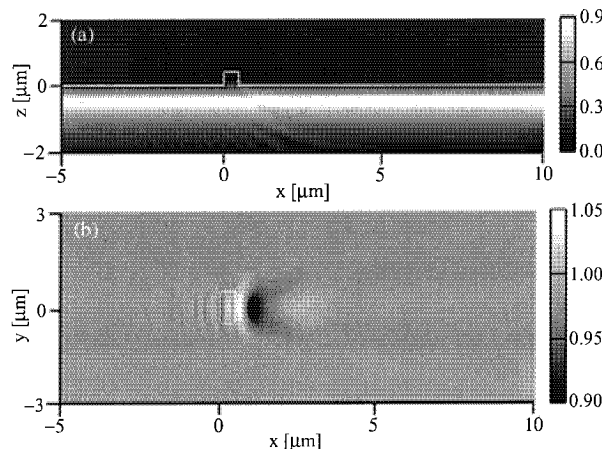


Fig. 4. Total field amplitude when a $x = 500\text{ nm}$, $y = 1\text{ }\mu\text{m}$ and $z = 400\text{ nm}$ InP protrusion is deposited on the structure. TE_0 illumination. (a) Side view ($y = 0$), (b) top view ($z = -550\text{ nm}$, the projection of the protrusion is shown).

The scattering increases when a second protrusion is deposited on the structure (Fig. 5). The field amplitude just inside the protrusion is now somewhat larger than in the case of a single protrusion. This field is the forerunner of the field that will be diffracted off the structure when a longer grating is deposited on the surface (Hunsperger 1991; März 1994). The light intensity diffused into the substrate also increases slightly, while the interaction of the field scattered by the two protrusions produces a more complex pattern inside the waveguide (Fig. 5(b)).

Since our approach is fully 3D, we can position protrusions on the structure arbitrarily, as illustrated in Fig. 6. In that case of two protrusions with a lateral offset, a fairly complex field distribution appears inside the waveguide. This pattern depends on the mode that is used to illuminate the structure: for TE_0 illumination, the field in the waveguide reaches a maximum just after each protrusion, followed by a field minimum (Fig. 6(a)). For TM_0 illumination, the diffraction pattern is broader, with a maximum field amplitude inside the protrusion (Fig. 6(b)). The interference pattern resulting from the interaction of the field scattered by the different elements is particularly visible for TM_0 polarization (Fig. 6(b)). Striking on that figure is the difference in the periodicity of the field in the forward direction and in the backward direction, the former being related to the interference of the light scattered by the protrusions and the latter being related to the ‘stationary wave’ resulting from the interaction of the incident field with the back-scattered field.

The difference of behavior observed in Fig. 6 for TE_0 and TM_0 excitations can be related to the different boundary conditions experienced by the electric field, depending on its orientation relative to the protrusion boundaries (Martin *et al.* 1994). A quantitative comparison of the scattering amplitudes

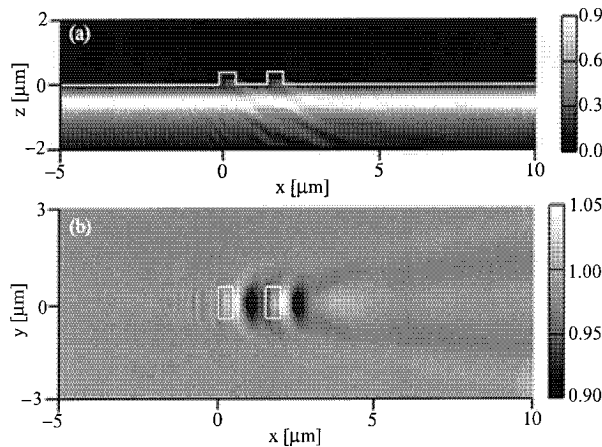


Fig. 5. Same situation as in Fig. 4 but with two similar protrusions.

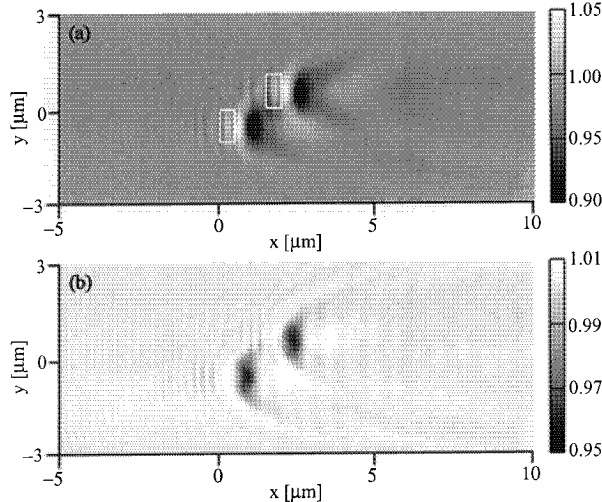


Fig. 6. Same situation as in Fig. 4 but with two protrusions offset in y -direction. The field is computed in the guiding layer ($z = -550$ nm) and the projection of the protrusions is shown: (a) TE_0 illumination and (b) TM_0 illumination.

shows that the interaction with the protrusion is stronger for the TE_0 mode than for the TM_0 mode.

The different scatterers placed in the background do not need to be aligned in a particular direction, as illustrated in Fig. 7, where the situation is similar to that of Fig. 6, but with a tilted protrusion. The scatterers can also extend over several background layers. This direct space discretization is therefore extremely versatile and can handle a broad range of physical systems.

A more dramatic effect on the guided wave is observed when a notch is etched inside the cap InP layer, as depicted in Fig. 8. Note that for this simulation the dielectric contrast $\Delta\epsilon$ in Equation (1) is negative since the scatterer permittivity (air, $\epsilon = 1$) is smaller than the permittivity of its surrounding layer (InP).

An important part of the incident TE_0 field is now scattered into the substrate (Fig. 8(b)). The back-scattered field is also larger, producing a marked interference pattern in the waveguide and in the substrate. Further, within the simulation window, the incident mode does not re-establish in the forward direction with the same intensity (compare Fig. 8(b) with Fig. 4(b)).

As a last example, we would like to briefly discuss the polarization coupling that can occur in the waveguide structure investigated in Fig. 8. Since our approach is fully vectorial, the electric field computed using Equation (1) includes all three components, even when the excitation \mathbf{E}^0 is only a scalar field. As an example, in Fig. 9(a), we consider a TE_0 incident field, i.e., an incident field with only a y -component. However, during the scattering process, a TM electric field, with x - and z -components, is generated.

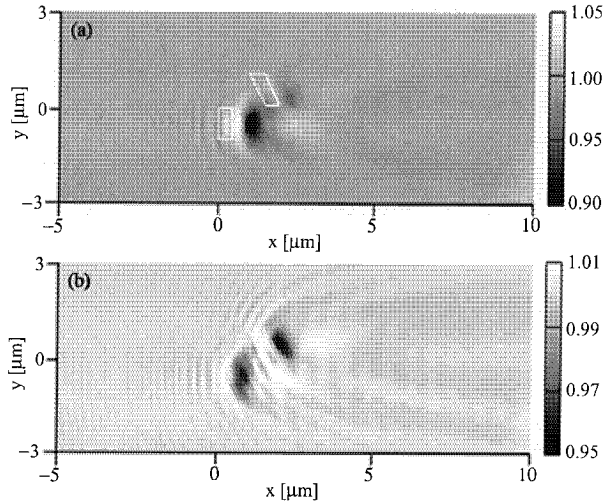


Fig. 7. Same situation as in Fig. 6, but now with one tilted protrusion. The field is computed in the guiding layer ($z = -550$ nm) and the projection of the protrusions is shown: (a) TE_0 illumination and (b) TM_0 illumination.

Its amplitude is represented in Fig. 9(a). Note the perfect symmetry of this field, related to the fact that the scatterer is symmetrical and the incident field propagates along one of its symmetry axis. The interference pattern in Fig. 9(a) originates from the finite extension of the scatterer (in the order of one wavelength). This interference pattern is similar in the forward and backward directions. This is because no TM components were present in the

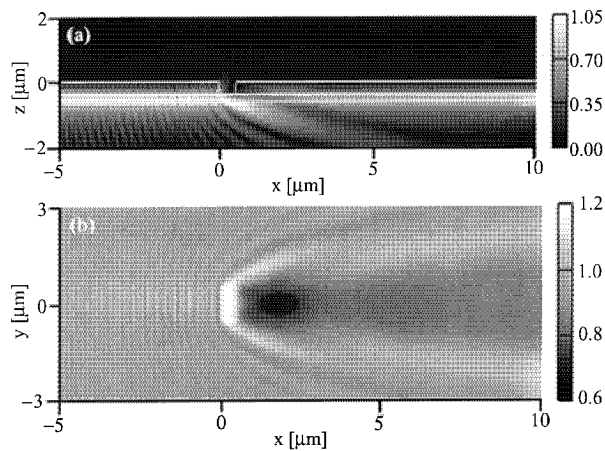


Fig. 8. Same situation as in Fig. 4 but now a notch with similar dimensions is etched through the InP layer.

incident field. Therefore no interferences between incident and reflected field can occur for this polarization component (compare with Fig. 8(a)).

A similar effect is observed when a notch is etched in the waveguide (Fig. 9(b)). For that geometry, the interaction is stronger and the amplitude of the TM field created during the scattering process is larger (notice the different amplitude scales in Fig. 9(a) and (b)).

Fig. 10 shows for the case of a waveguide with a notch (Fig. 9(b)) the real part of electric field components created during the scattering process: the z -component for a TE_0 incident field and the y -component for a TM_0 incident field.

These new field components correspond to a field generated at the location of the notch and propagating in both directions in the waveguide. A mode cross-polarized to the incident field is therefore established in the waveguide. As a matter of fact, an analysis of the generated field shows that its propagation constant is identical to the propagation constant which can be expected for a mode of that polarization (Fig. 10). Note however that the amplitude of this cross-polarized mode is much smaller than the amplitude of the original incident field. For the geometry of Fig. 9(a) (protrusion)

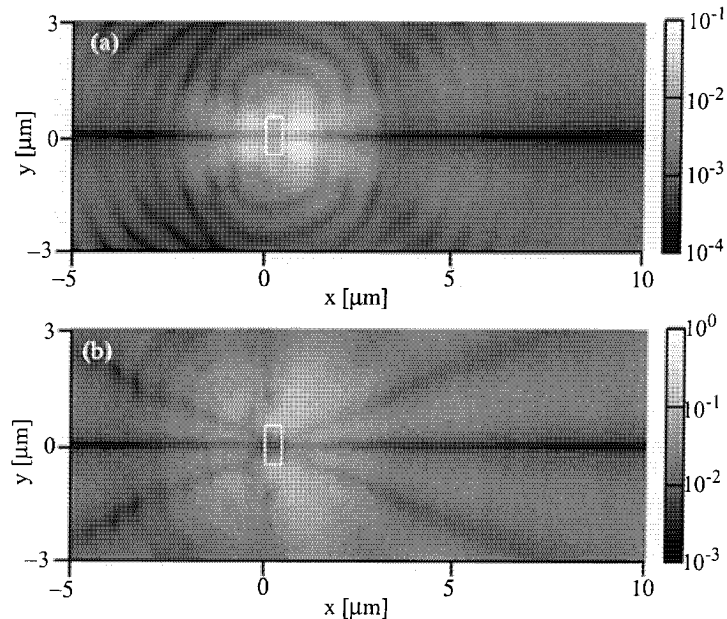


Fig. 9. (a) Same geometry as in Fig. 4; the field in the guiding layer ($z = -550 \text{ nm}$) is shown. The waveguide is excited with a TE_0 mode and the amplitude of the TM field is computed; this polarization, which was not present in the excitation, is created during the scattering process. (b) Same situation but with a notch (as in Fig. 8) instead of a protrusion. Note that in both figures a different logarithmic grayscale is used.

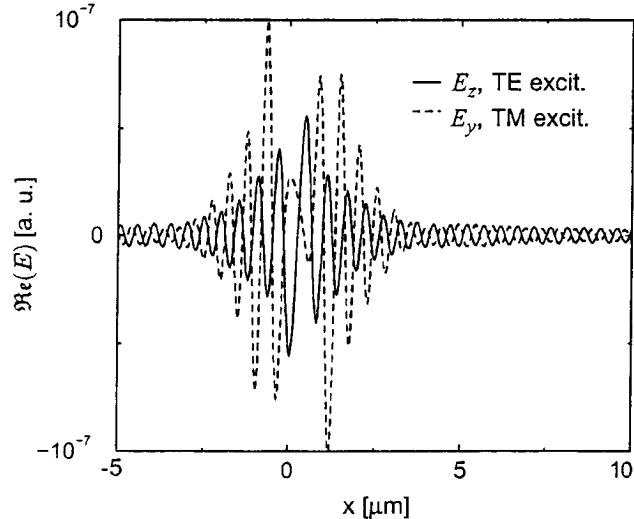


Fig. 10. Real part of the electric field components created during the scattering process depicted in Fig. 9(b) (notch): E_z , respectively E_y , are shown for a TE_0 , respectively TM_0 , excitation of the structure. These new field components, that were not present in the illumination field, are shown along the center of the structure ($y = 0$ in Fig. 9(b)).

similar behavior could not be observed because the perturbation of the incident field by the protrusion is not strong enough to generate a cross-polarized mode.

4. Conclusion

We have presented a fully vectorial 3D technique, based on the Green's tensor, for scattering computations in stratified media. In this approach, only the elements that differ from the stratified background must be discretized; the response of the background being taken into account by the Green's tensor. Further, the boundary conditions at the edges of the computation window, as well as at the different interfaces in the stratified background are automatically fulfilled.

The different examples presented have illustrated the versatility of this approach and its suitability for investigating subtle effects such as polarization crosstalks in a waveguide.

We believe that this technique can handle a broad range of complex systems, including integrated optical circuits and photonic band gap structures. However, since it is a fully 3D vectorial approach, the computational costs can become prohibitive for very large systems.

Acknowledgements

We thank B. Michel and R. Vahldieck for their support of the project and gratefully acknowledge funding of the Swiss National Science Foundation.

References

- Davies, J.B. *IEEE Trans. Magn.* **29** 1578, 1993.
 Derudder, H., D. De Zutter and F. Olyslager. *Electron. Lett.* **34** 2138, 1998.
 El-Refaei, H., D. Yevick and I. Betty. *IEEE Photon. Tech. L.* **12** 389, 2000.
 Hayes, P.R., M.T. O'Keefe, P.R. Woodward and A. Gopinath. *Opt. Quant. Electron.* **31** 813, 1999.
 Helfert, S.F. and R. Pregla. *Opt. Quant. Electron.* **31** 721, 1999.
 Herzinger, C.M., C.C. Lu, T.A. DeTemple and W.C. Chew. *IEEE J. Quant. Electron.* **29** 2273, 1993.
 Hsueh, Y., M. Yang and H. Chang. *J. Lightwave Technol.* **17** 2389, 1999.
 Huang, W. and R.R.A. Syms. *J. Lightwave Technol.* **17** 2658, 1999.
 Huang, W.P. and C.L. Xu. *IEEE J. Quant. Electron.* **29** 2639, 1993.
 Hunsperger, R.G. *Integrated Optics: Theory and Technology* 3rd edn, Springer, Berlin, 1991.
 Lee, J.-F., R. Palandech and R. Mittra. *IEEE Trans. Microwave Theory Technol.* **40** 346, 1992.
 Martin, O.J.F., A. Dereux and C. Girard. *J. Opt. Soc. Am. A* **11** 1073, 1994.
 Martin, O.J.F. and N.B. Piller. *Phys. Rev. E* **58** 3909, 1998.
 März, R. *Integrated Optics Design and Modeling*. Artech House, Boston, 1994.
 Noble, M.J., J.A. Lott and J.P. Loehr. *IEEE J. Quant. Electron.* **34** 2327, 1998.
 Paulus, M., P. Gay-Balmaz and O.J.F. Martin. *Phys. Rev. E* **62** 5797, 2000.
 Paulus, M. and O.J.F. Martin. *J. Opt. Soc. Am. A* **18** 854, 2001.
 Piller, N.B. and O.J.F. Martin. *IEEE Trans. Antennas Propag.* **46** 1126, 1998.
 Scarmozzino, R., A. Gopinath, R. Pregla and S. Helfert. *IEEE J. Sel. Top. Quant.* **6** 150, 2000.
 Tai, C.-T. *Dyadic Green Function in Electromagnetic Theory*. IEEE Press, New York, 1994.
 Willems, J., J. Haes and R. Baets. *Opt. Quant. Electron.* **27** 995, 1995.

How to tap an innocent waveguide

Michael Paulus and Olivier J. F. Martin

Opt. Express **8**, 644–648 (2001)

How to tap an innocent waveguide

Michael Paulus^{1,2} and Olivier J. F. Martin¹

¹ *Electromagnetic Fields and Microwave Electronics Laboratory
Swiss Federal Institute of Technology, ETH-Zentrum, ETZ
CH-8092 Zurich, Switzerland*

² *IBM Research, Zurich Research Laboratory
CH-8803 Rüschlikon, Switzerland*

paulus@ifh.ee.ethz.ch, martin@ifh.ee.ethz.ch
<http://www.ifh.ee.ethz.ch/~martin>

Abstract: We study the interaction of a mode propagating in a planar waveguide with a three-dimensional rectangular defect (protrusion or notch) in the structure. The scattering by the defect disturbs the propagation of the mode and light is coupled out of the waveguide. To investigate these phenomena we compute electric field distributions with the Green's tensor technique and show movies with varying defect geometries and different mode polarizations. These calculations should be useful for optimizing specific elements in complex photonic circuits.

© 2001 Optical Society of America

OCIS codes: (130.0130) Integrated optics; (230.0230) Optical devices; (260.3160) Interference; (260.5430) Polarization; (290.0290) Scattering.

References and links

1. R. G. Hunsperger, *Integrated Optics: Theory and Technology*, 3rd ed. (Springer, Berlin, 1991).
 2. T. Tamir and S. T. Peng, "Analysis and Design of Grating Couplers," *Appl. Phys.* **14**, 235–254 (1977).
 3. M. Paulus, P. Gay-Balmaz, and O. J. F. Martin, "Accurate and efficient computation of the Green's tensor for stratified media," *Phys. Rev. E* **62**, 5797–5807 (2000).
 4. M. Paulus and O. J. F. Martin, "Light propagation and scattering in stratified media: A Green's tensor approach," *J. Opt. Soc. Am. A* **18**, 854–861 (2001).
 5. D. Marcuse, *Light transmission optics*, 2nd ed. (Krieger, Malabar, 1989).
 6. M. Born and E. Wolf, *Principles of Optics*, 6th. ed. (Pergamon Press, Oxford, 1987).
-

1 Introduction

In many applications the coupling of optical energy out of or into a waveguide is obtained by a grating deposited on top of the structure [1]. The properties of such a grating like the coupling efficiency and the angular distribution of the radiated electric field strongly depend on the shape, the size and the periodicity of the individual elements forming the grating [2]. For a quantitative analysis the collective behavior of these elements must be taken into account. However, from a physical point of view, much can be learned from the reduced problem of a "grating" with a single element.

In this paper we focus on the scattering by a three-dimensional (3D) rectangular defect in the planar InP/InGaAsP waveguide structure depicted in Fig. 1. The extension of the scattering element in the x and the y directions is $0.5 \times 0.5 \mu\text{m}^2$ and held fixed. We deliberately choose a defect smaller than the wavelength to avoid any resonance effects and concentrate our study on the influence of the vertical extension of the defect. In the z direction we vary the defect height between $h = 500 \text{ nm}$ and $h = -800 \text{ nm}$. For positive z values the defect forms a protrusion on the waveguide structure whereas

negative z values correspond to a notch etched into the waveguide. We show electric field distributions calculated by computer simulations and discuss the effects associated with the height variation for different polarizations of the waveguide mode.

2 Model

An accurate calculation of the scattered electric field requires the solution of the vectorial wave equation with boundary conditions given at the different material interfaces. In our case the entire structure is formed by the 3D scattering element (protrusion or notch) embedded in the planar stratified waveguide (see Fig. 1). We recently proposed an approach to this problem based on the Green's tensor technique [3, 4]. This fully vectorial model provides a self-consistent and accurate solution of the electric field integral equation. The advantage of this approach lies in the fact that the boundary conditions at the different material interfaces, as well as at the edges of the computation window are automatically and perfectly fulfilled and artificial absorbing boundary conditions are not needed. Further, only the protrusion/notch must be discretized, the remaining of the structure being accounted for in the Green's tensor. We refer the interested reader to Ref. [4], where the specificities of this approach are discussed in detail and compared to alternative techniques for computational optics.

3 Results

At a wavelength $\lambda = 1.55 \mu\text{m}$ the planar InP/InGaAsP waveguide supports a transverse electric mode (TE_0 , electric field polarized in the y direction) and a transverse magnetic mode (TM_0 , electric field polarized in the xz plane). The corresponding propagation constants are $\beta_{\text{TE}_0} = 12.96 \mu\text{m}^{-1}$ and $\beta_{\text{TM}_0} = 12.92 \mu\text{m}^{-1}$ [5]. For both modes we present movies of the electric field amplitude (square root of $\mathbf{E} \cdot \mathbf{E}^*$) as a function of the defect height h . When $h = 0$ the defect vanishes and the total electric field is simply given by the excitation in the stratified background. In all cases we assume that the incident mode propagates in the positive x direction.

The movies in Fig. 2 show side views of the electric field distribution, when a TE_0 mode is used as excitation. Obviously, the field remains fairly unaffected by a protrusion [$h > 0$, Fig. 2(a)]. On the other hand, with a notch building up ($h < 0$), the incident mode is reflected at the waveguide/air interface and an interference pattern caused by the interaction of the incident field with the reflected one appears on the left-hand side of the notch. In the forward direction the propagation of the mode is disrupted and the field amplitude is depleted just behind the defect. However, this depletion remains

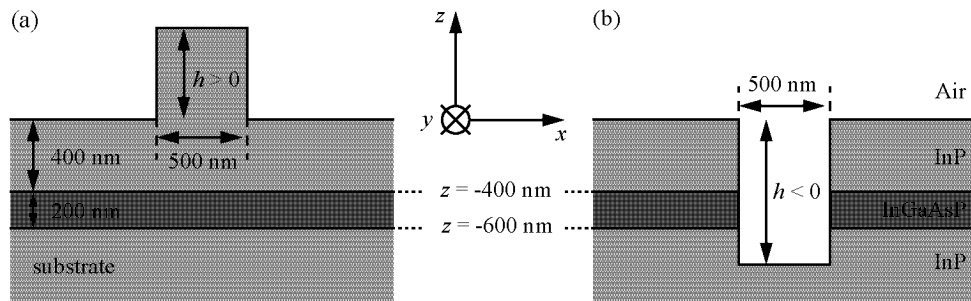


Fig. 1. Geometry of the investigated InP/InGaAsP planar waveguide structure (permittivities $\epsilon_{\text{InP}} = 10.05$, $\epsilon_{\text{InGaAsP}} = 11.42$, wavelength $\lambda = 1.55 \mu\text{m}$). Either (a) a protrusion with height $h > 0$ is deposited on or (b) a notch with depth $h < 0$ is etched through the structure. This scattering element has a finite lateral extension (500 nm) in both the x and the y directions.

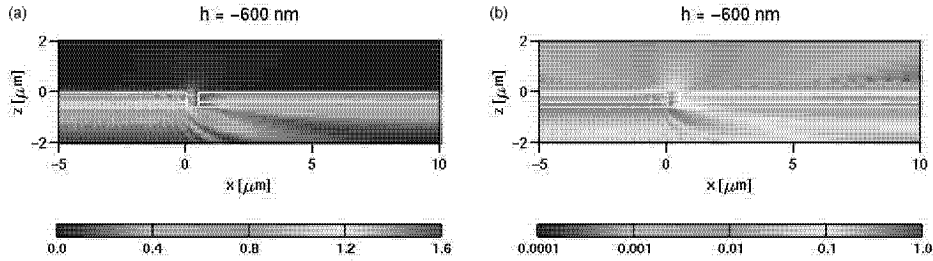


Fig. 2. Movies of the electric field amplitude for the investigated waveguide structure (Fig. 1) with varying defect height/depth h . A TE_0 mode propagating in the x direction is used as illumination. Side view through the center of the structure ($y = 0$) with a (a) linear (441 KB) and a (b) logarithmic (459 KB) color scale.

localized and even for the $h = -800 \text{ nm}$ notch (which completely disrupts the guiding layer) the mode re-establishes after $2.5 \mu\text{m} \approx 5\lambda_{\text{InGaAsP}} = 5\lambda/\sqrt{\epsilon_{\text{InGaAsP}}}$ because of the defect's finite lateral extension. Further, the scattering at a notch leads to a deflection of the incident mode towards the substrate at an angle which increases with the notch depth h .

Some light is also coupled out upwards into the air, which is emphasized in Fig. 2(b), where we use a logarithmic color scale. This representation evidences the mode scattering on the protrusion ($h > 0$) which produces an electric field distribution with two main lobes in the forward and the backward direction. These lobes are the forerunners of the field that would be coupled out of the structure if a long grating formed by many such elements was used. For a notch the interaction is stronger, with increasing depth h more light is coupled out and the two lobes merge into a single one.

With the logarithmic scale we can also observe remarkable interference patterns in air at a distance $z \approx 500 \text{ nm}$ above the InP layer. These patterns arise on both sides of the scattering element with different periodicities. They come from the interaction between the exponentially decaying electric field of the initial mode and the wave radiated in the air by the scattering element. For a quantitative analysis of this interference structure we report in Fig. 3 the electric field computed along a line 500 nm above the InP/air interface ($z = 500 \text{ nm}$) for a protrusion and for a notch. Corresponding to the different propagation constants ($k_{\text{air}} = 2\pi/\lambda$ for the radiated wave and β_{TE_0} for the mode) the

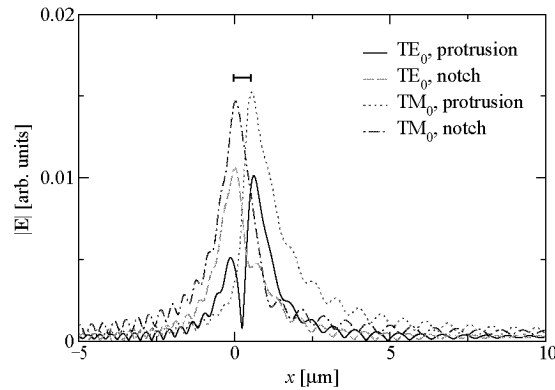


Fig. 3. Electric field amplitude in the symmetry plane ($y = 0$) 500 nm above the InP/air interface for two different defects (protrusion with $h = 100 \text{ nm}$ and notch with $h = -100 \text{ nm}$) and two different illumination polarizations. The bar represents the extension of the defect in the x direction.

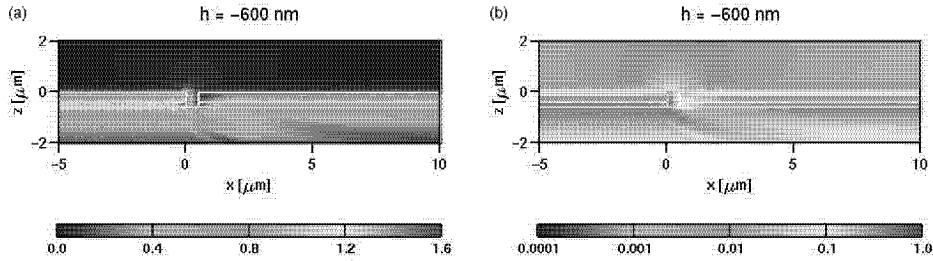


Fig. 4. Same situation as in Fig. 2 but with a TM_0 mode as illumination. The movies have a (a) linear (435 KB) and a (b) logarithmic (444 KB) color scale.

electric field amplitude is modulated with the periodicities $\Delta_{\text{fw}} = 2\pi/(\beta_{\text{TE}_0} - k_{\text{air}}) \approx 705 \text{ nm}$ in the forward direction and $\Delta_{\text{bw}} = 2\pi/(\beta_{\text{TE}_0} + k_{\text{air}}) \approx 369 \text{ nm}$ in the backward direction [6]. Our numerical results agree perfectly with these predicted numbers.

In the movies in Fig. 4 we show the same situation as in Fig. 2, but now with a TM_0 mode as excitation. With this polarization we can observe qualitatively the same features as in the TE case. However, now a protrusion also creates a field distribution with only one main lobe in forward direction. The periodicities of the interference patterns in air change only slightly since the propagation constants are similar for both modes: $\Delta_{\text{fw}} = 2\pi/(\beta_{\text{TM}_0} - k_{\text{air}}) \approx 709 \text{ nm}$ in forward direction and $\Delta_{\text{bw}} = 2\pi/(\beta_{\text{TM}_0} + k_{\text{air}}) \approx 370 \text{ nm}$ in backward direction.

Let us now study in greater detail the processes taking place inside the waveguide itself. The movies in Fig. 5 show top views of the electric field amplitude at $z = -525 \text{ nm}$, i.e. inside the guiding InGaAsP layer. Again, the field distribution remains nearly homogeneous in the case of a protrusion ($h > 0$) or a shallow notch ($h \lesssim 0$). With a deeper notch the scattering increases strongly, the region behind the defect becomes depleted and a complex interference pattern arises: The interaction of the incident field and the scattered field creates in the backward direction a dense system of fringes and in forward direction a field distribution which can be interpreted as the diffraction pattern of the defect. On the left-hand side of notches deeper than $h \approx -500 \text{ nm}$ one also observes an interference pattern with a period larger than that mentioned above. However, this is a Moiré pattern due to the finite number of computed field points without physical significance.

Away from the defect the electric field distributions in Fig. 5 are similar for a TE_0 or a TM_0 excitation. The different polarizations can however be distinguished inside the

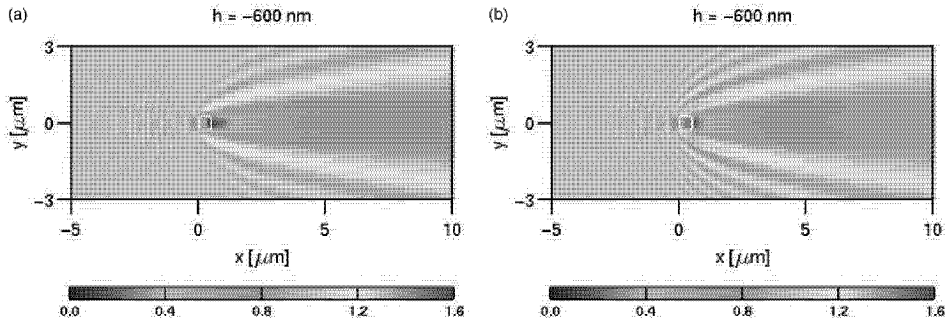


Fig. 5. Movies of the electric field amplitude in the InGaAsP layer ($z = -525 \text{ nm}$) for varying defect height/depth h . Top view for a (a) TE_0 (408 KB, see Fig. 2) and a (b) TM_0 illumination (415 KB, see Fig. 4). The white box represents the extension of the defect in the xy plane.

defect: The largest fields are created at the edges normal to the electric field vector of the excitation, especially close to the front side of the defect, where the incident field is backreflected. Hence, for a TE_0 illumination with the electric field in the y direction, we observe sharp peaks at the two left inner corners when the computation plane intersects the notches [$h < -525 \text{ nm}$, Fig. 5(a)]. On the other hand, for a TM_0 illumination with the electric field mainly in the z direction, the largest fields occur at the left y -directed edge of a notch. As a matter of fact, for $h = -550 \text{ nm}$ this edge being close to the computation plane, the corresponding figure shows a strong electric field enhancement [Fig. 5(b)].

4 Summary

In this paper we studied the scattering of a mode propagating in a planar InP/InGaAsP waveguide on a three-dimensional rectangular defect. Our simulations show in detail the dependence of the scattering strength on the vertical extension of the defect and provide insights into the local effects taking place when light is coupled out of a waveguide. However, our approach based on the Green's tensor technique is not only beneficial for the basic understanding of scattering phenomena but provides also solutions for technologically relevant problems in device development. For example, we can estimate an upper limit for the roughness in the layered waveguide system in dependence on the outcoupled energy and define process windows for the production and operation of the device.

Acknowledgements

It is a pleasure to acknowledge stimulating discussions with J. P. Kottmann and to thank B. Michel (IBM) for his support of the project. We gratefully acknowledge funding from the Swiss National Science Foundation.

P8

**Scattering experiments
with a diving cylinder**

Michael Paulus and Olivier J. F. Martin
Opt. Express **9**, 303–311 (2001)

Scattering experiments with a diving cylinder

Michael Paulus^{1,2} and Olivier J. F. Martin¹

¹ *Electromagnetic Fields and Microwave Electronics Laboratory
Swiss Federal Institute of Technology, ETH-Zentrum, ETZ
CH-8092 Zurich, Switzerland*

² *IBM Research, Zurich Research Laboratory
CH-8803 Rüschlikon, Switzerland*

paulus@ifh.ee.ethz.ch, martin@ifh.ee.ethz.ch
<http://www.ifh.ee.ethz.ch/~martin>

Abstract: We present numerical experiments of light scattering by a circular dielectric cylinder embedded in a stratified background, using the Green's tensor technique. The stratified background consists of two or three dielectric layers, the latter forming an anti-reflection system. We show movies of the scattered field as a function of different parameters: polarization, angle of incidence, and relative position of the cylinder with respect to the background interfaces.

© 2001 Optical Society of America

OCIS codes: (240.0240) Optics at surfaces; (260.3160) Interference; (260.5430) Polarization; (290.0290) Scattering; (310.1620) Coatings.

References and links

1. Lord Rayleigh, "On the Electromagnetic Theory of Light," *Philos. Mag.* **12**, 81–101 (1881).
2. T. C. Rao and R. Barakat, "Plane-wave scattering by a conducting cylinder partially buried in a ground plane. I. TM case," *J. Opt. Soc. Am. A* **6**, 1270–1280 (1989).
3. T. C. Rao and R. Barakat, "Plane-wave scattering by a conducting cylinder partially buried in a ground plane II: TE case," *J. Opt. Soc. Am. A* **8**, 1986–1990 (1991).
4. G. Videen and D. Ngo, "Light scattering from a cylinder near a plane interface: theory and comparison with experimental data," *J. Opt. Soc. Am. A* **14**, 70–78 (1997).
5. P. J. Valle, F. González, and F. Moreno, "Electromagnetic wave scattering from conducting cylindrical structures on flat substrates: study by means of the extinction theorem," *Appl. Opt.* **33**, 512–523 (1994).
6. A. Madrano and M. Nieto-Vesperinas, "Scattering of electromagnetic waves from a cylinder in front of a conducting plane," *J. Opt. Soc. Am. A* **12**, 1298–1309 (1995).
7. R. Borghi, F. Gori, M. Santarsiero, F. Frezza, and G. Schettini, "Plane-wave scattering by a perfectly conducting circular cylinder near a plane surface: cylindrical-wave approach," *J. Opt. Soc. Am. A* **13**, 483–493 (1996).
8. R. Borghi, M. Santarsiero, F. Frezza, and G. Schettini, "Plane-wave scattering by a dielectric circular cylinder parallel to a general reflecting flat surface," *J. Opt. Soc. Am. A* **14**, 1500–1504 (1997).
9. J.-J. Greffet, "Scattering of s-polarized electromagnetic waves by a 2d obstacle near an interface," *Opt. Commun.* **72**, 274–278 (1989).
10. M. A. Taubenblatt, "Light scattering from cylindrical structures on surfaces," *Opt. Lett.* **15**, 255–257 (1990).
11. F. Pincemin, A. Sentenac, and J.-J. Greffet, "Near field scattered by a dielectric rod below a metallic surface," *J. Opt. Soc. Am. A* **11**, 1117–1127 (1994).
12. N. P. Zhuck and A. G. Yarovoy, "Two-Dimensional Scattering from an Inhomogeneous Dielectric Cylinder Embedded in a Stratified Medium: Case of TM Polarization," *IEEE Trans. Antennas & Propag.* **42**, 16–21 (1994).
13. M. Totzeck and H. J. Tiziani, "Interference microscopy of sub-λ structures: A rigorous computation method and measurements," *Opt. Commun.* **136**, 61–74 (1997).

14. M. Paulus and O. J. F. Martin, "Green's tensor technique for scattering in 2D stratified media," *Phys. Rev. E* **63**, 066615.1–066615.8 (2001).
 15. O. J. F. Martin and N. B. Piller, "Electromagnetic scattering in polarizable backgrounds," *Phys. Rev. E* **58**, 3909–3915 (1998).
 16. J. D. Jackson, *Classical electrodynamics*, 3rd ed. (Wiley, New York, 1999).
 17. O. J. F. Martin, C. Girard, and A. Dereux, "Dielectric vs. topographic contrast in near-field microscopy," *J. Opt. Soc. Am. A* **13**, 1801–1808 (1996).
 18. C. F. Bohren and D. R. Huffman, *Absorption and scattering of light by small particles* (Wiley, New York, 1983).
 19. M. Born and E. Wolf, *Principles of Optics*, 6th. ed. (Pergamon Press, Oxford, 1987).
-

1 Introduction

The optical properties of cylindrical particles have generated a lot of interest, as they provide a simple model for specific physical systems. The scattering on a cylinder situated in an infinite homogeneous background was for example already treated by Lord Rayleigh in 1881 [1].

However, most real situations are more complex, the particles are located on a substrate or embedded in an even more complicated stratified background. To investigate such geometries many analytical and numerical approaches were developed. They include, for example, image methods [2–4], applications of the extinction theorem [5, 6], expansions of cylindrical waves [7, 8] or integral-equation methods [9–13]. Most of these methods only consider a background medium consisting of two half spaces [2–11] or restrict the choice of the material or geometry parameters [2–5, 7].

Recently, we presented a general technique for light propagation and scattering in two-dimensional (2D) structures formed by a stratified background with embedded scatterers [14]. This approach is based on the Green's tensor associated with the stratified background and provides a rigorous solution of the vectorial wave equation with the boundary conditions given at the different material interfaces.

In this paper we apply our approach to study the light scattered by a dielectric circular cylinder in the presence of a stratified dielectric background. We investigate the different phenomena that can occur, depending on the relative cylinder position with respect to the background interfaces, as well as on the illumination direction.

In Sec. 2 we briefly recall our computational approach and in Sec. 3 we show calculations of the total electric field amplitude $A = \sqrt{\mathbf{E} \cdot \mathbf{E}^*}$ as a function of different geometrical and illumination parameters. Our results are summarized in Sec. 4.

2 Model

Throughout the paper we consider a circular cylinder with radius $r = 150\text{ nm}$ and permittivity $\varepsilon_{\text{Cyl}} = 2$ embedded in a two- or three-layer background. This system is illuminated from the top with a plane wave under different angles of incidence Θ . The illumination wavelength is $\lambda = 633\text{ nm}$ and two different polarizations are considered: s polarization, with the electric field \mathbf{E}^0 in y direction, and p polarization with the electric field \mathbf{E}^0 lying in the xz plane.

Since the scattering geometry under study is translation invariant in y direction we can restrict the investigation to a cross section in the xz plane [14]. When such a system formed by a stratified background (L layers, permittivity ε_l , $l = 1, \dots, L$) with embedded scatterers is illuminated with an incident field $\mathbf{E}^0(\mathbf{r})$ propagating in the stratified background [we consider harmonic fields with time dependence $\exp(-i\omega t)$], the total field $\mathbf{E}(\mathbf{r})$ is given by the electric field integral equation:

$$\mathbf{E}(\mathbf{r}) = \mathbf{E}^0(\mathbf{r}) + \int_A d\mathbf{r}' \mathbf{G}(\mathbf{r}, \mathbf{r}') \cdot k_0^2 \Delta \varepsilon(\mathbf{r}') \mathbf{E}(\mathbf{r}'), \quad (1)$$

where $\mathbf{G}(\mathbf{r}, \mathbf{r}')$ is the Green's tensor associated with the stratified background, $k_0^2 = \omega^2 \epsilon_0 \mu_0$ the vacuum wave number and $\Delta\epsilon(\mathbf{r})$ the dielectric contrast:

$$\Delta\epsilon(\mathbf{r}) = \epsilon(\mathbf{r}) - \epsilon_\kappa, \quad \mathbf{r} \in \text{layer } \kappa. \quad (2)$$

Whereas the Green's tensor for an infinite homogeneous background can be expressed analytically [15], this is not possible when the background is stratified. In this case $\mathbf{G}(\mathbf{r}, \mathbf{r}')$ must be computed numerically with Sommerfeld type integrals [14].

Since the integration in Eq. (1) runs only over the scatterer section A, the discretization is limited to this volume, the stratified background being accounted for by the Green's tensor. Another advantage of this method is that the boundary conditions at the different material interfaces, as well as at the edges of the computation window are perfectly and automatically fulfilled [14, 15].

3 Results

3.1 Homogeneous space

Before studying complex effects that can arise when the cylinder is placed in a stratified background, it is educational to review the simpler case of the scattering by a cylinder in an infinite homogeneous space $\epsilon_H = 1$. Figure 1 shows the total electric field amplitude in such a system for both s and p polarizations, when the cylinder is illuminated with an incident electric field \mathbf{E}^0 propagating in $-z$ direction:

$$\mathbf{E}^0(x, z) = \mathbf{A}^0 \exp(i\mathbf{k}\mathbf{r}) = \mathbf{A}^0 \exp(ik_z z), \quad (3)$$

where \mathbf{A}^0 is the amplitude vector with $|\mathbf{A}^0| = 1$, $\mathbf{k} = (k_x, k_z)$ is the wave vector of the incident wave and $k_z = -|\mathbf{k}|$. (For all the calculations we normalize the electric field amplitude of the incident field $|\mathbf{A}^0| = (\mathbf{E}^0 \cdot \mathbf{E}^{0*})^{1/2} = 1$.)

Some features of the field distributions in Fig. 1 are common to both polarizations: in backward direction stationary waves are created due to the interference of the incident and the reflected waves. In the forward direction we recognize the diffraction pattern of the cylinder. However, the near field distribution at close vicinity of the cylinder strongly depends on the polarization of the incident field. For s polarization a maximum of the intensity can be observed inside the cylinder whereas for p polarization two peaks occur on the left and right sides of the scatterer. This behavior can be explained with the

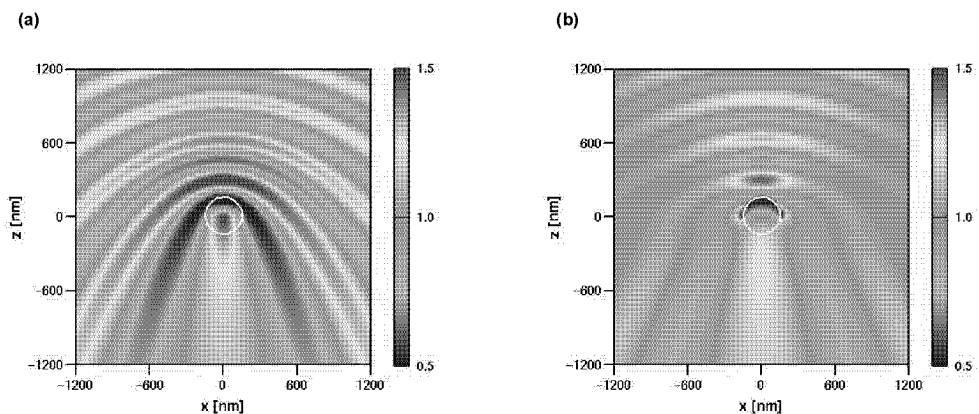


Fig. 1. Electric field amplitude distribution for the scattering by a cylinder in an infinite homogeneous background. Two different polarizations are investigated: (a) s polarization, (b) p polarization.

boundary conditions resulting from Maxwell's equations. When the electric field \mathbf{E} is parallel to a material interface it must be continuous [16]. When it is normal to the interface, it is the displacement field $\mathbf{D} = \epsilon \mathbf{E}$ which must be continuous. Hence, for a p-polarized excitation the total electric field amplitude is discontinuous by a factor $\epsilon_{\text{Cyl}}/\epsilon_{\text{H}}$ wherever the incident field is normal to a material interface (i.e. on the left and right sides of the cylinder in Fig. 1(b)). Such depolarization effects do not occur at the top and bottom sides of the cylinder for p polarization [Fig. 1(b)] or on the entire circumference for s polarization [Fig. 1(a)], since in those locations the incident field is parallel to the material interfaces [17].

As a consequence of the depolarization effects for a p-polarized excitation, the forward scattered light is focussed by the cylinder and reaches a maximum at $z \approx -300$ nm. For s polarization, on the other hand, the field maximum is situated inside the cylinder.

The total scattering cross section of a dielectric circular cylinder is greater for s polarization than for p polarization, the difference increasing with a larger dielectric contrast [18]. As a matter of fact, we observe in Fig. 1(a) a more pronounced interference pattern than in Fig. 1(b). This polarization dependence of the total scattering cross section is also observable for all further configurations under study.

3.2 Scattering in the presence of a surface

Now we divide the background into two half spaces $\epsilon_1 = 1$ ($z \geq 0$) and $\epsilon_2 = 2$ ($z < 0$), in such a way that the lower layer has the same permittivity as the cylindrical scatterer, $\epsilon_2 = \epsilon_{\text{Cyl}}$.

The movies in Fig. 2 show the response of the system under normal incidence ($\Theta = 0$) for s- and p-polarized illumination. Each movie frame corresponds to a given distance h between the cylinder center and the material interface.

Since the incident wave is now reflected back at the plane interface, the illumination electric field becomes in the top layer

$$\mathbf{E}^0(x, z) = \mathbf{A}^0 [\exp(ik_{1z}z) + R \exp(-ik_{1z}z)], \quad z \geq 0, \quad (4)$$

and in the bottom layer

$$\mathbf{E}^0(x, z) = \mathbf{A}^0 T \exp(ik_{2z}z), \quad z < 0, \quad (5)$$

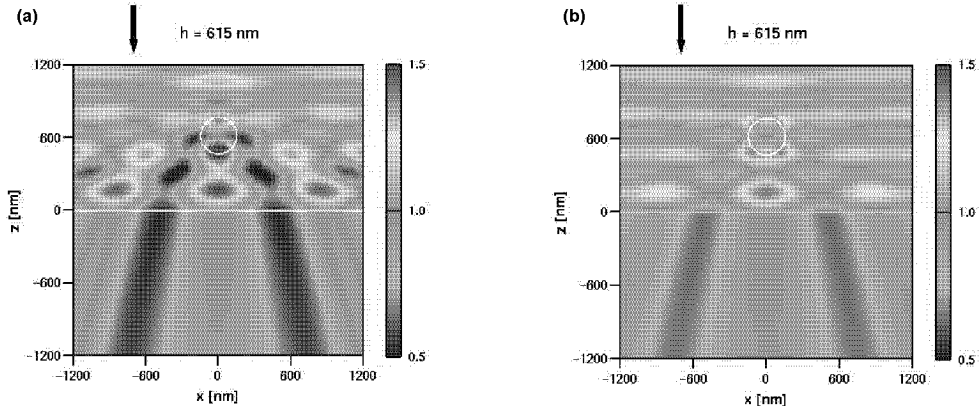


Fig. 2. Electric field amplitude distribution for the scattering by a cylinder above a dielectric surface with same permittivity, as a function of the distance h between the cylinder center and the interface. Normal incidence ($\Theta = 0^\circ$, the arrow represents the propagation direction of the illumination wave) (a) s polarization (528 KB), (b) p polarization (479 KB).

where k_{iz} , $i = 1, 2$, is the z component of the wave vector in layer i , R is the Fresnel reflection coefficient and T the corresponding transmission coefficient for normal incidence [19]:

$$R = \frac{\sqrt{\varepsilon_1} - \sqrt{\varepsilon_2}}{\sqrt{\varepsilon_1} + \sqrt{\varepsilon_2}}, \quad (6)$$

$$T = \frac{2\sqrt{\varepsilon_1}}{\sqrt{\varepsilon_1} + \sqrt{\varepsilon_2}}. \quad (7)$$

Note that R and T are real for absorptionless media. The negative reflection coefficient obtained in our system leads to a phase shift of 180° for the reflected field.

The illumination amplitude in the upper half space reads now

$$A = (\mathbf{E}^0 \cdot \mathbf{E}^{0*})^{\frac{1}{2}} = |\mathbf{A}^0| [1 + R^2 + 2R \cos(2k_{1z}z)]^{\frac{1}{2}}, \quad z \geq 0, \quad (8)$$

and a stationary wave with period $\Delta = \pi/k_{1z} = \lambda/2$ is created in the upper half space (Fig. 2). Because of $R < 0$ the amplitude is minimal directly at the interface.

The cylinder is not anymore illuminated by a homogeneous plane wave but moves in the field of the stationary wave. Hence, in the top layer the total field distribution is a superposition of the stationary wave and a diffraction pattern similar to that in Fig. 1. This pattern determines also the field distribution in the bottom layer depending on the transmittance of the interface.

As in the case of the homogeneous background the near field of the cylinder depends on the polarization of the excitation. Additionally, the location and strength of the scattered field maxima are modulated by the cylinder altitude h .

The stationary wave itself is further amplified in the region between the cylinder and the interface. This is caused both by the focusing provided by the cylinder and by multiple reflections between the surface and the cylinder. Note also that the interaction between the excitation and the field scattered by the cylinder creates an interference pattern in x direction.

For $h = -15$ nm, when half of the cylinder is included in the surface, most of the back-scattering disappears in a narrow sector of the upper halfspace. Finally, for $h = -165$ nm the cylinder is entirely immersed in the lower layer with identical permittivity, and the total electric field is simply given by the excitation in the stratified background. Since without the cylinder s and p polarization are indistinguishable for normal incidence, the field distributions are identical in both frames.

Let us now rotate the angle of incidence Θ with respect to the surface normal. Figure 3 shows again the scattering as a function of the cylinder altitude h , but for $\Theta = 30^\circ$.

In this case, the illuminating electric field in the top layer becomes

$$E_\alpha^0(x, z) = A_\alpha^0 [\exp(ik_{1z}z) + R_\alpha \exp(-ik_{1z}z)] \exp(ik_x x), \quad z \geq 0, \quad \alpha = x, y, z, \quad (9)$$

where the reflection coefficients correspond to the polarization of the given component: $R_x = -R^p$, $R_y = R^s$, and $R_z = R^p$. In this case of non-normal illumination, the Fresnel coefficients $R^{s/p}$ depend on the polarization of the incident wave [19]:

$$R^s = \frac{k_{1z} - k_{2z}}{k_{1z} + k_{2z}}, \quad (10)$$

$$R^p = \frac{\varepsilon_2 k_{1z} - \varepsilon_1 k_{2z}}{\varepsilon_2 k_{1z} + \varepsilon_1 k_{2z}}. \quad (11)$$

The illumination amplitude in the upper half space is then

$$\begin{aligned} A = & \{A_x^0 [1 + R^p]^2 - 2R^p \cos(2k_{1z}z)] + A_y^0 [1 + R^s]^2 + 2R^s \cos(2k_{1z}z)] \\ & + A_z^0 [1 + R^p]^2 + 2R^p \cos(2k_{1z}z)\}^{\frac{1}{2}}, \quad z \geq 0. \end{aligned} \quad (12)$$

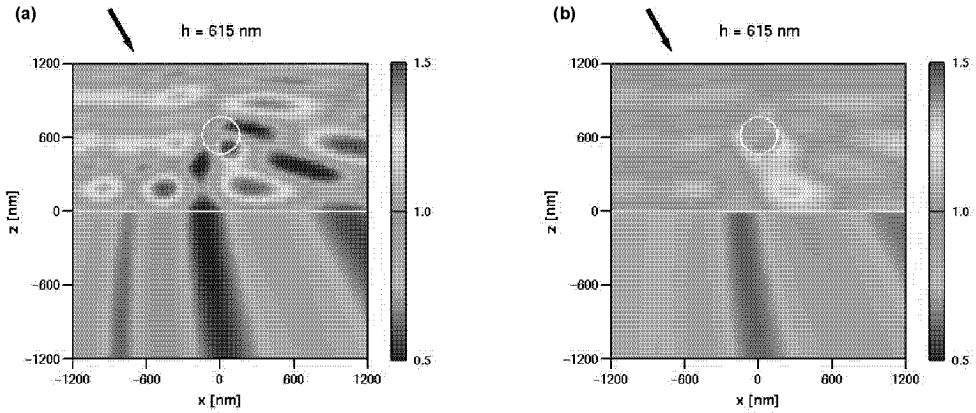


Fig. 3. Same situation as in Fig. 2, but now the illumination field is incident at a $\Theta = 30^\circ$ angle. (a) s polarization (530 KB), (b) p polarization (452 KB).

Again, a stationary wave excites the cylinder, but the period is now increased to $\Delta = \pi/k_z = \lambda/(2 \cos \Theta) = \lambda/\sqrt{3}$.

The diffraction patterns and position of the near field maxima rotate accordingly to the change of the incidence angle (compare Figs. 2 and 3). For p polarization, one of the two field maxima previously visible on the lateral sides of the cylinder (Fig. 1) disappears and only a maximum is now visible on the right, in the direction of the illumination momentum (Fig. 3).

The computer experiments reported in Fig. 3 also illustrate the polarization dependence of the boundary conditions at the interface between the two layers: for s polarization the electric field must be continuous, whereas p polarization enforces a discontinuity proportional to the ratio $\varepsilon_1/\varepsilon_2$.

To further investigate the effect of the angle of incidence Θ , we show in Fig. 4 movies for a fixed cylinder altitude $h = 615$ nm and a varying illumination angle Θ .

As expected, the period of the stationary wave increases for larger angles Θ and the diffraction pattern becomes more and more twisted (Fig. 4). Since the reflection coefficients $R^{s/p}$ of the interface approach 1 in the limit $\Theta = 90^\circ$, the field transmitted

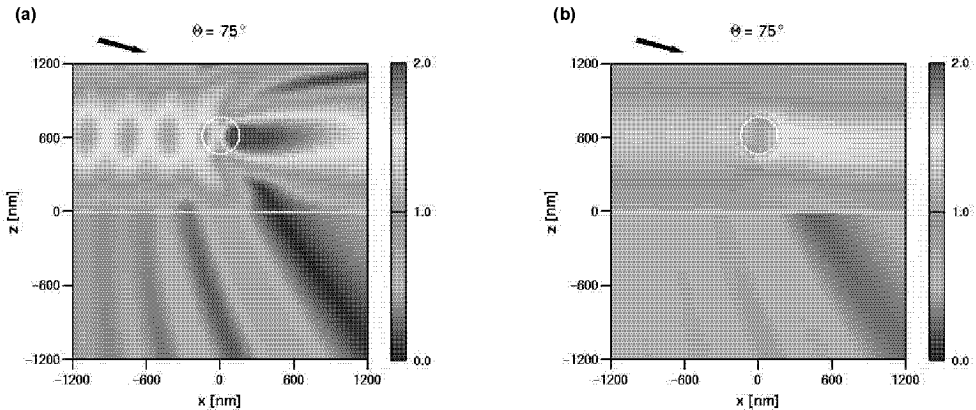


Fig. 4. Electric field amplitude distribution for the scattering by a cylinder above a dielectric surface with same permittivity, as a function of the illumination angle Θ (the arrow indicates the propagation direction of the illumination field). The cylinder position is kept fixed: $h = 615$ nm. (a) s polarization (227 KB), (b) p polarization (204 KB).

into the lower half space vanishes for larger angles and the amplitude maxima of the stationary wave converge towards their upper value for total reflection $A = 2$ (see Eq. (12) with $k_z \rightarrow 0$ and $R^{s/p} \rightarrow 1$). This produces a strong scattering both in forward and in backward direction when the maximum of the stationary wave coincides with the cylinder altitude ($\Theta = 75^\circ$, Fig. 4).

At first sight, it may be surprising that in the case of p polarization the stationary wave in the top layer vanishes for $\Theta \approx 40^\circ\text{--}60^\circ$, and only the field scattered by the cylinder can be observed [Fig. 4(b)]. Depending on the angle, two different mechanisms contribute to this behavior. First, for $\Theta = 45^\circ$ the x and z components of the p-polarized illumination electric field are identical, $A_x^0 = A_z^0$, and Eq. (12) becomes

$$A = |\mathbf{A}^0| (1 + R^{p^2})^{\frac{1}{2}}. \quad (13)$$

Hence, the z dependence of $\mathbf{E} \cdot \mathbf{E}^*$ is cancelled out.

To illustrate the second mechanism we report in Fig. 5 the amplitude A_{refl} reflected by a plane interface between two half spaces $\varepsilon_1 = 1$ and $\varepsilon_2 = 2$, as a function of the angle of incidence Θ . At $\Theta \approx 55^\circ$, the Brewster angle of the material system under study, $A_{\text{refl}} = 0$. At this angle, the reflectivity vanishes for p-polarized plane waves and all the energy of the incident field is transmitted into the lower half space. Note however that zero reflectivity does *not* imply that the amplitude of the transmitted light T in the bottom layer is 1 [19]. A straightforward calculation gives $T = \sqrt{\varepsilon_1/\varepsilon_2}$, which yields in our case $T \approx 0.75$, in perfect agreement with our calculations. Both above-mentioned phenomena do not exist for s polarization.

In Fig. 5 we can further observe that on the entire angle range s polarization leads to a larger reflectivity. This behavior is similar to the polarization dependence of the scattering on a cylinder (see Sec. 3.1).

3.3 Anti-reflection layer

In the following, we add a third layer to create a structure with $\varepsilon_1 = 1$, $\varepsilon_2 = 1.334$, and $\varepsilon_3 = 1.78$. This structure represents an air/water system, separated by an intermediate slab acting as anti-reflection layer [19]. For normal incidence on the material interfaces, the reflectivity is indeed strictly zero only if the permittivities are connected by

$$\varepsilon_2 = \sqrt{\varepsilon_1 \varepsilon_3} \approx 1.334, \quad (14)$$

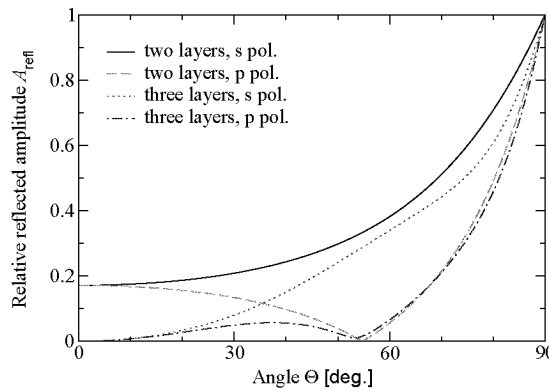


Fig. 5. Relative reflected amplitude A_{refl} for a two-layer medium with $\varepsilon_1 = 1$, $\varepsilon_2 = 2$, and a three-layer medium with $\varepsilon_1 = 1$, $\varepsilon_2 = 1.334$, $\varepsilon_3 = 1.78$, as a function of the angle of incidence Θ . Incident s and p polarizations are compared. The minima for p polarization correspond to the Brewster angle.

and the thickness d of the slab is

$$d = \left(n + \frac{1}{2} \right) \frac{\lambda}{2\sqrt{\varepsilon_2}}, \quad n = 1, 2, 3, \dots \quad (15)$$

Taking $n = 2$ in Eq. (15), we use for our calculations $d = 411 \text{ nm}$, so that the cylinder fits within the antireflection layer.

The movies in Fig. 6 clearly illustrate that, independent of the cylinder location, there is no stationary wave in the top layer due to reflection of the illuminating field by the slab. Striking in these movies is the fact that the antireflection layer remains very efficient, even in the presence of the cylinder. Again, it is the s-polarized illumination which produces a weak interference pattern. To explain this behavior, in Fig. 5 we also report the reflected amplitude A_{refl} for the three-layer system under study. Similar to the case of the single interface, s polarization leads to a stronger scattering for all angles Θ and, consequently, to an enhanced backreflection of the field components scattered by the cylinder and impinging at non-normal incidence on the interface. Note also that $A_{\text{refl}} = 0$ for $\Theta = 0^\circ$ since we designed the slab to be reflectionless. Further, in Fig. 5 we observe that for p polarization the Brewster angle is slightly shifted to $\Theta \approx 53^\circ$, and the corresponding reflected amplitude does not vanish completely for that three-layers system.

4 Summary

When a cylindrical particle is located in a stratified background, the resulting electric field distribution is determined by the interaction between the cylinder and the different material interfaces. In this paper, we used the Green's tensor technique to illustrate the scattering phenomena occurring in such structures. The Green's tensor technique is very well adapted to this kind of geometry because the optical processes in the layered material system are accurately described by the Green's tensor. Further, only the cylinder needs to be discretized, irrespective of the number of layers forming the stratified background. Our calculations illustrate the complexity of the phenomena that can occur in such a rather simple system, depending on the relative position of the cylinder to the different material interfaces.

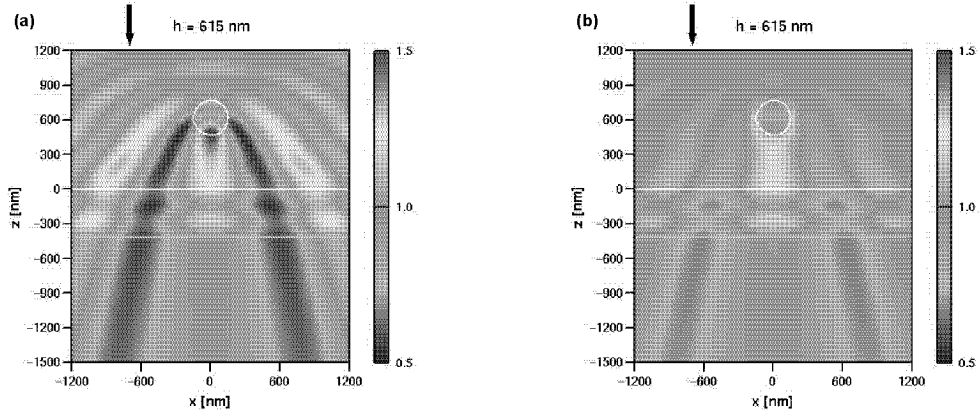


Fig. 6. Electric field amplitude distribution for the scattering by a cylinder in a three-layer system, including an anti-reflection slab, as a function of the cylinder altitude h above the top interface. Normal incidence ($\Theta = 0^\circ$, the arrow represents the propagation direction of the illumination wave). (a) s polarization (1052 KB), (b) p polarization (959 KB).

Acknowledgments

It is a pleasure to thank B. Michel (IBM) for his support of the project. We gratefully acknowledge funding from the Swiss National Science Foundation.

